BRNO UNIVERSITY OF TECHNOLOGY
VYSOKÉ UČENÍ TECHNICKÉ V BRNĚ

FACULTY OF MECHANICAL ENGINEERING
FAKULTA STROJNÍHO INŽENÝRSTVÍ

INSTITUTE OF MATERIALS SCIENCE AND ENGINEERING
ÚSTAV MATERIÁLOVÝCH VĚD A INŽENÝRSTVÍ

METAL MATRIX COMPOSITES PREPARED BY POWDER METALLURGY ROUTE
KOMPOZITY S KOVOVOU MATRICÍ PŘIPRAVENÉ CESTOU PRÁŠKOVÉ METALURGIE

DOCTORAL THESIS
DIZERTAČNÍ PRÁCE

AUTOR PRÁCE / AUTHOR
Ing. Igor Moravčík

AUTHOR AUTOR PRÁCE	Ing. Igor Moravčík
SUPERVISOR ŠKOLITEL	prof. Ing. Ivo Dlouhý, CSc.

BRNO 2017

Abstract

Conventionally, the alloy design, alloy production, and alloy selection are almost strictly confined to single element or one compound concept. Consequently, this alloy concept imposes a significant limit to the degrees of freedom in alloy's composition and thus limits the development of special microstructure and properties. In the last decade, it has become particularly obvious that materials science and alloy engineering are still not fully explored due to an appearance of new class of alloys – usually called high entropy alloys (HEA). This exclusively new class of alloys caught significant scientific attention for the novelty of its approach to alloy design, as they do not contain a single base element, but rather at least 5 elements in very close atomic portions. In the recent years medium entropy alloys (MEA) appeared as a variant of HEAs with only three or four elements. The work is contributed to the research of feasibility of production of HEA and MEA alloys and composites by utilization of powder metallurgy (PM) manufacturing route, the combination of mechanical milling (MA) of elementary powders, followed by pressure or field assisted densification.

Altogether three compositions have been studied: $AlCoCrFeNiTi_{0.5}$, $Co_{1.5}Ni_{1.5}CrFeTi_{0.5}$ and CoCrNi, as well as B_4C metal matrix composite (MMC) with CoCrNi as matrix phase. Deep microstructural and mechanical analyses including transmission electron microscopy and tensile testing have been performed. During the whole study, the problems with the contamination of powders with oxygen have been observed, however the oxides formed relatively homogenous dispersion in all manufactured materials and they did not impair significant mechanical property reduction.

$AlCoCrFeNiTi_{0.5}$ exhibited relatively high hardness over 800 HV, but rather low ductility. The attempt has been made to improve the ductility with heat treatment procedure, but to no avail. The formation of in-situ TiC dispersion has been recorded, due to the utilization of carbon containing methanol as a process control agent during milling, that reacted with the present elemental Ti. In this manner metal matrix composite has been effectively produced. Additionally, the same procedure, the milling in the controlled amount of carbon containing medium, may be used also to produce other advanced composites with dispersion of in-situ formed TiC.

On the other hand, CoCrNi alloy possessed very high tensile ductility (26%) and ultimate strength over 1000 MPa. Microstructure was composed of major FCC phase and BCC precipitates. The CoCrNi alloy has been due to the high ductility chosen as the best candidate for the subsequent production of metal matrix composites. The introduction of B_4C resulted in the displacement reaction of Cr element with B_4C, resulting in the formation of Cr_5B_3 boride phase. The composite possessed nano-grained microstructure and high tensile strength over 1400 MPa. However, the tensile ductility decreased to 1.9%.

The $AlCoCrFeNiTi_{0.5}$ alloy achieved the best combination of tensile ductility (4%) and remarkable strength over 1300 MPa, bearing pure FCC microstructure with extremely fine grain size.

Therefore, the PM production route has proven to be a feasible way for the production of HEAs and MEAs, as well as HEA and MEA based metal matrix composites with remarkable combination of mechanical properties. Furthermore, the utilization of PM process offers a control of microstructure features and material design freedom by a simple change of process parameters, unmatched by any other manufacturing method.

Abstract

Ve všeobecnosti, poznatky o design slitin, jejich výrobě a výběru legujúcich prvků sú omezené na slitiny s jedním základním prvkem. Tento fakt ale výrazně limituje možnosti a volnost výběru prvků pro dosáhnuti speciálních vlastností a mikrostruktur. V poslední dekádě se ukázalo, že materiálová věda a inženýrství nejsou ještě zdaleka prozkoumané v důsledku objevu nové třídy materiálů nazvané vysoko entropické slitiny (HEA high entropy alloys). Jejich objev upoutal pozornost vědecké komunity. Základní koncept pro jejich design je, že namísto jednoho, nebo dvou základních prvků obsahují minimálně 5 prvků v podobných atomových koncentracích. V posledních letech se objevila skupina materiálů odvozená od HEA, nazvaná slitiny so střednou entropii (MEA medium entropy alloys). Na rozdíl od HEA ale obsahují 3, nebo 4 prvky. Táto práce je věnovaná studiu přípravy a charakterizaci HEA, MEA a jejich kompozitů s pomocí metod práškové metalurgie.

V této práci byli dohromady zkoumány tři kompozice: $AlCoCrFeNiTi_{0.5}$, $Co_{1.5}Ni_{1.5}CrFeTi_{0.5}$ a CoCrNi, kompozity s kovovou matricí (MMC metal matrix composites) vyztužené částicemi B_4C s CoCrNi jako matricí. Hloubková mikrostrukturní a mechanická analýza těchto materiálů byla provedena pomoví metod rastrovací a transmisní elektronové mikroskopie spojené s tahovými a ohybovými zkouškami. V průběhu celé studie se objevovaly problémy s kontaminací kyslíkem, co se projevilo vznikem značného množství oxidů v připravených materiálech.

U Slitiny $AlCoCrFeNiTi_{0.5}$ byla naměřena tvrdost přesahující 800 HV. Její houževnatost ale byla velice omezena. V její mikrostruktuře byly identifikovány částice in-situ TiC v důsledku přítomnosti organického, anti-aglomeračního činidla (metanolu) v mlecí misce. Tato reakce může být použita v budoucnu k přípravě MMC se záměrnou disperzí TiC.

Na druhé straně, slitina CoCrNi ukázala vysoké hodnoty tažnosti (26%) a meze pevnosti přes 1000 MPa. Mikrostruktura obsahovala majoritní FCC fázi s BCC precipitáty. Tahle slitina byla z důvodu vysoké tažnosti zvolena pro přípravu kompozitu s výztuží B_4C. V průběhu slinování ale došlo k reakci mezi přítomným Cr a B_4C, které výsledkem byl Cr_5B_3 borid. Tento kompozit mel pevnost v tahu 1400 MP a extrémne jemnozrnnou strukturu. Celková tažnost ale klesla na 1.9 %.

Slitina $AlCoCrFeNiTi_{0.5}$, která mela strukturu složenou jen z FCC tuhého roztoku dosáhla nejlepší kombinaci mechanických vlastností s pevností přesahující 1300 MPa a dostatečnou tažností 4%.

Prášková metalurgie se ukázala jako vhodná metoda pro přípravu HEA a MEA slitin a jejich kompozitů, s dobrou kombinací pevnosti a tažnosti. Tato metoda dovoluje měnit mikrostrukturní parametry připravených materiálů jednoduchou úpravou parametrů procesu.

Keywords: mechanical testing, high entropy alloy, medium entropy alloy, strength, ductility, mechanical alloying, milling, composites.

Bibliographic citation:

MORAVČÍK, I. *Kompozity s kovovou matricí připravené cestou práškové metalurgie.* Brno: Vysoké učení technické v Brně, Fakulta strojního inženýrství, 2017. 149 s. Vedoucí dizertační práce prof. Ing. Ivo Dlouhý, CSc.

“Science, in all its greatness, is still subject to human creativity. It starts the first moment a child tries to reach up and grab at the clouds. Soon, the child learns that his own hands cannot reach the sky, but his hands are not the limit of his potential. For the human brain observes, considers, understands, and adapts. Locked within the mind is infinite possibility.’’

Yukito Kishiro

Acknowledgements

I would like to offer my sincere gratitude to my PhD supervisor prof. Ivo Dlouhy and my advisor specialist Dr. Jan Cizek for their continuous counselling, guidance and support throughout the world of material science.

I would like to express my sincerely gratitude to my family for the amazing care and support throughout my entire life.

Special thanks to Larissa de Almeida Gouvea, for her essential help with the formal aspects of the thesis.

I would also like to thank Dr. Vladimir Girman from Safarik University in Kosice Slovakia, Dr. Jozef Vesely and Dr. Peter Minarik from Charles University in Prague, Ivo Kubena and Vit Hornik from Institute of Physics of Materials in Brno for their vital help with TEM characterization of my materials.

Also, I would like to thank Zdenek Spotz, Petra Hanusova, Jan Cupera and Jozef Zapletal from Brno University of Technology in Brno for their help with XRD, SEM analysis and mechanical testing.

I am grateful also for the support and guidance of Dr. Sheng Guo from Chalmers University of Technology in Gotheborg that gave me the opportunity to work in his High Entropy Alloys Group and his PhD student Saad Sheikh for his help with my research there.

I would like to thank Zuzana Kovacova, Michael Kitzmantel and Dr. Erich Neubauer from RHP-Technology GmbH in Seibersdorf, Dr. David Salomon, Tan Hua from CEITEC in Brno and Radek Musalek from Institute of Plasma Physics in Prague for their help with the densification experiments.

I would also like to thank everyone else which contributed directly or indirectly to the production of this thesis.

The research was co-funded by the Ministry of Education, Youth and Sports within the „National Sustainability Programme I“ (NETME CENTRE PLUS - LO1202). Support to Czech Science Foundation project GACR 13-35890S is further acknowledged.

Declaration

I hereby declare that I am the sole author of this work and that I have compiled it in my own words. The work was made under the supervision of Prof. Ing. Ivo Dlouhý CSc. and Ing. Jan Cizek PhD.

Brno………… ……………………….
Ing. Igor Moravcik

Content

1 Introduction

Conventionally, the alloy design, alloy production, and alloy selection are almost strictly confined to single element or one compound concept [1, 2]. Consequently, this alloy concept imposes a significant limit to the degrees of freedom in alloy's composition and thus limits the development of special microstructure and properties. In the last decade, it has become particularly obvious that materials science and alloy engineering are still not fully explored thanks to an appearance of new class of alloys – usually called high entropy alloys (HEA) - following the original work of J. W. Yeh and Cantor [1, 3]. This exclusively new class of alloys caught significant scientific attention for the novelty of its approach to alloy design, as they do not contain a single base element, but rather at least five elements in very close atomic proportions. Another new group of materials inspired by the HEA idea are medium entropy alloys (MEA) containing only three elements with equiatomic proportions.

Composites are another group of materials which is gradually receiving substantial scientific and industrial attention. They represent combined materials containing at least two components with remarkably different properties. As such, they pose a way to solve some of the most challenging engineering problems [4, 5], where classic alloys meet their service limits.

The above mentioned HEAs are usually produced by traditional casting manufacturing route. The employment of Powder metallurgy (PM) manufacturing route for these alloys preparation, as an additional method, appears to be promising. Especially the combination of mechanical milling (MA) of elementary powder mixtures, followed by pressure or field assisted densification, has yielded the most promising results in the preparation of the full density high entropy materials and their composites [6].

The nature of PM process may solve several problems usually associated with traditional casting procedures, e.g. segregation, chemical heterogeneity, etc. PM alloys usually possess higher strengths than their cast and wrought counterparts, stemming from fine grained homogenous microstructure [7]. PM manufacturing route also possesses another advantage, namely relatively easy and efficient production of a wide scope of advanced materials, including composites, that would be extremely demanding to produce by the conventional metallurgical methods [8].

Accordingly, the metal matrix composites with high or medium entropy alloy matrix phase can be produced. The creation of composite materials with such alloys as the matrix may result in a completely new branch of advanced materials, with a unique combination of strength and fracture resistance.

This work will be dedicated to the study of feasibility and challenges of subsequent production of HEA, MEA and their respective composites by PM route.

2 Evolution of alloys from binary to multi-component systems

Phase diagrams could be described according to the amount of components, i.e. binary for two components, ternary for three components, etc. [9, 10]. The deep knowledge and understanding of these diagrams, including quantitative relations and consequences of microstructural and phase composition have become an integral part of materials science and engineering.

In the regular alloy design approach, a single element is always selected as a base of the alloy, with regards to its primary properties. Then, by further alloying with additional elements, intentional changes in the secondary properties of the material are induced.

With the knowledge of the phase diagrams and theory of phase transformation mechanisms, the approximate properties of a new system could be anticipated. For instance, with the use of an appropriate alloying element selection and additional eventual heat treatments, it is possible to induce precipitation strengthening in different alloys to increase their load bearing capability.

Same as in the case of steels, generally, research was oriented almost exclusively on binary alloys with very small amounts of additional alloying elements, usually in the range of few percent (either weight or atomic percent). The addition of significantly higher elements content to the systems was usually avoided (exception to this are high alloyed Cr-Ni steels). Basically, all commercial alloys were developed in this way.

Cantor et al. [3] pointed out to the fact that, at the present time, an enormous amount of theoretical and experimental knowledge about phase transformations, physical and mechanical properties with the respect to processing conditions and microstructures have been acquired for alloys based only on one or two elements. The alloy's systems containing more than three elements with equi-atomic or near equi-atomic concentrations have not been explored significantly. Up to date, investigations have usually been focused only on the corners of ternary or quaternary phase diagrams, as marked by green color in Fig. 1 for better elucidation. The middle part of these diagrams has, in most instances, remained - more or less - a mystery. This fact suggests that there is still a considerable room for future alloy development.

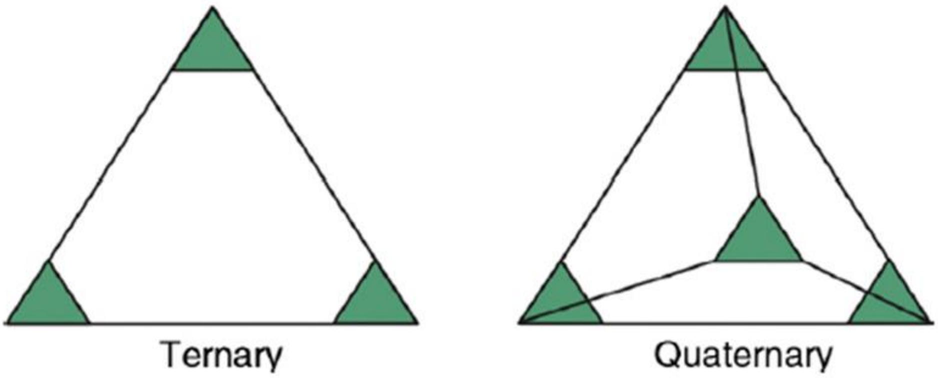

Fig. 1 Ternary and quaternary phase diagrams with thoroughly explored areas marked by green color, whereas, in most of the systems, the white space usually remained unexplored [10].

The examination of alloys with one base element and low concentration of others, e.g. steels, is considerably easier when taking into account the properties' prediction, in contrast to multi-component systems. On the latest, it is important to notice that there is a high probability of formation of very complicated microstructures, furthermore complicating the properties' prediction.

According to the Gibbs phase rule, the number of equilibrium phases (F) that could coexist in a microstructure - under the condition of a constant pressure - is given by equation [11]:

$$F = \mathrm{N} - \mathrm{V} + 1. \tag{1}$$

In this relation, N refers to the number of components in the system and V is the maximum number of thermodynamic degrees of freedom. For instances when $\mathrm{V} > 1$, the thermodynamic conditions may be altered without causing changes in the equilibrium state. In case of an invariant reaction in a five component system, the maximum number of coexisting phases can be up to six.

For instance, a typical microstructure of a nickel-base superalloy, containing Cr, Co, Fe and C elements,is composed of a disordered face centered cubic (FCC) solid solution, an ordered FCC intermetallic phase ($L1_2$ type) with Ni_3Al stoichiometry and $M_{23}C_6$ carbide (lattices in Fig. 2) is presented [12]. Except for these phases with a beneficial effect on the superalloys performance, a number of other intermetallic phases with topologically close packed lattices (TCP phases like σ, μ and P phase) can nucleate and grow into the microstructure. The complicated structures of these phases usually result in a limited number of slip systems and long Burger`s vectors of the present dislocations. Therefore, inherent brittleness of such phases is to be expected, as well as embrittlement of the microstructure containing these phases. The research of the mutual relations of microstructure, properties and manufacturing process for complicated systems is, therefore, extremely difficult.

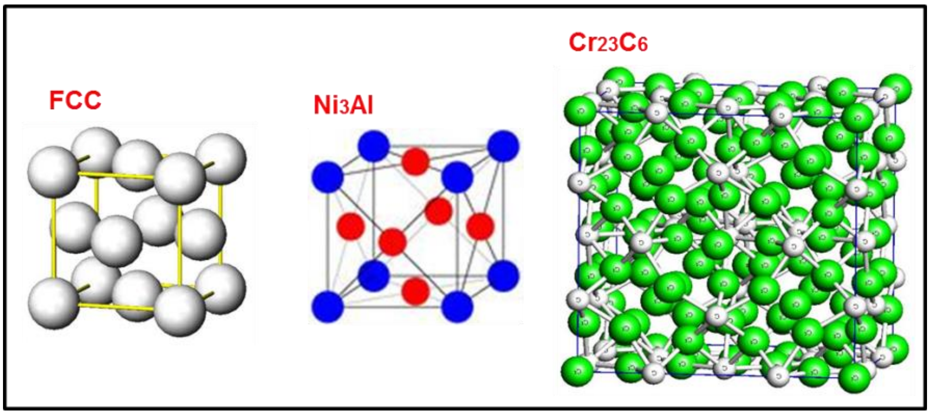

Fig. 2 Crystal lattices of typical phases in nickel-based superalloys [12].

The issues cited above were, initially, expected also for new multi-principal element alloys. For that reason, Cantor and Yeh [2][3] started simultaneous investigations on these systems. Their efforts ultimately led to the creation of a completely new family of advanced materials, which were named as High Entropy Alloys (HEAs, also referred to as multi-principal element alloys, MPEA).

Several definitions of HEAs appeared. One of the most frequently used was proposed by Yeh et al. [1] and refers to high entropy alloys, as described by multi-elements systems with the structure of simple solid solutions composed of more than five elements with near equiatomic ratios. The common property of these new alloys is their high calculated configurational entropy, i.e. the magnitude of a system disorder.

2.1 High entropy effects

There are, essentially, four core effects presented and attributed to the comprehensive behavior of high entropy alloys, including the principles governing their microstructural evolution. These main effects will be further described below.

High entropy effect

According to the Gibbs phase rule (equation 1), the number of thermodynamically stable, co-existing phases in systems with multiple present elements that may appear in the microstructure of HEA is rather high. In the light of this preposition, it is surprising that the only phase usually observed in CoCrFeMnNi equiatomic alloy – widely considered as a model HEA - is single FCC solid solution. The mechanism underlying such phase composition was denoted as high entropy effect [2]. According to the basic equation for phase stability, in general [11, 13]:

$$\Delta\mathrm{G} = \Delta\mathrm{H} - \mathrm{T}\Delta S, \tag{2}$$

where ΔG is the Gibbs free energy in J mol^{-1}. T is given as thermodynamic temperature in Kelvins, ΔS correspond to a change in the entropy and ΔH is a change in the enthalpy. The increase of the thermodynamic stability of any phase present leads to the increase of negative values of ΔG. ΔG is distinguished as the stored energy that the system is able to release. Therefore, the decrease of its corresponding total energy has, as consequence, the ascendance to a more energetically stable state. For solid solution phases, where elements are distributed randomly, the value of ΔG is denominated as ΔG_{mix} (Gibbs free energy of mixing). ΔG_{mix} is attributed to the decrease in the system energy upon the formation of random solid mixture of its respective elements, with corresponding values as ΔH_{mix} and ΔS_{mix}.. The change in the enthalpy of mixing is calculated as [14]:

$$\Delta\mathrm{H}_{mix} = \left(\sum\nolimits_{i=1, j\neq i}^{n} \beta_{ij} c_i c_j\right). \tag{3}$$

In the presented equation, c_i is the atomic fraction of the i-th element; $\beta_{ij} = 4\ \Delta H_{AB}$ in J mol^{-1}, while ΔH_{AB} refers to change of mixing enthalpy of binary blend, calculated with the use of values which have been tabulated by Takeuchi [15][2]. These values have been derived with the use of the modified Miedema's macroscopic model [15].

It should be noted that, in most examples provided in the literature, ΔS_{mix} is calculated only as configurational entropy, ignoring the fraction of the thermal entropy. The configurational entropy is, in its very nature, an evaluation of the number of states in which a particular system is able to exist in. In the case of the solid crystalline phases, different states of the system are understood as different crystal configurations, i.e. different elements occupying variable spaces within one crystallographic system. Consequently, the configurational entropy is, in essence, the number of ways that the atoms can be randomly arranged in a single lattice type with the absence of any chemical affinity amongst the elements [13]. On the other hand, the thermal entropy is understood as the number of ways that the energy is distributed among the atoms, which is significantly more difficult to determine. ΔS_{mix} in J K^{-1} could be calculated by [16]:

$$\Delta S_{mix} \cong klnW, \tag{4}$$

where k is the Boltzmann's constant (1.38×10^{-23} J K^{-1}.mol^{-1}) and W is the number of states of the system. For a materials description, it is much more convenient to use the equation in its modified version, with the elemental concentrations as [17]:

$$\Delta S_{mix} \cong -R_g \sum_{i=1}^{n} c_i ln c_{i\,,} \tag{5}$$

where R_g is the gas constant (8.314 J K^{-1} mol^{-1}). From the latter discussion, one can assume that the entropy is, in general, a thermodynamic quantity which can be understood as a measure of the system's disorder. It is clear, from equation 2, that the positive increase in the change of entropy of any phase leads to an increase of the stability of the corresponding phase as well, i.e. it promotes the decrease of ΔG, as mentioned previously. Enthalpy is, on the other hand, referring to a certain chemical attraction (affinity) between elements that may result in the formation of appropriate configurations of the valence electrons, in order to decrease the energy of the system [17]. The more negative the values of ΔG means the more energy is available to be released in this manner. As a result, if the atomic pairs of the elements with very negative mixing enthalpy are present in the alloy, there is a high the probability of the formation of ordered phases. The ordered phases possess very low values of the configurational entropies (approaching zero in instances where the perfectly ordered lattice is reached). In summary, the low mixing enthalpy favors the formation of the ordered phases, e.g. carbides, nitrides and intermetallics, while increasing the entropy supports the appearance of disordered solid solutions.

The described inner competition between two thermodynamic quantities - entropy and enthalpy of different phases - in conjunction with diffusion kinetics, determines the final microstructures of the alloys. The highest values of entropy are achieved when all the elemental components of an alloy are present within the single solid solution phase (elements in equiatomic ratios, as presented in Fig. 3) [3][4]. This is the very basic concept of the HEAs design, as well as a significant quality which distinguish them from the rest of the alloys.

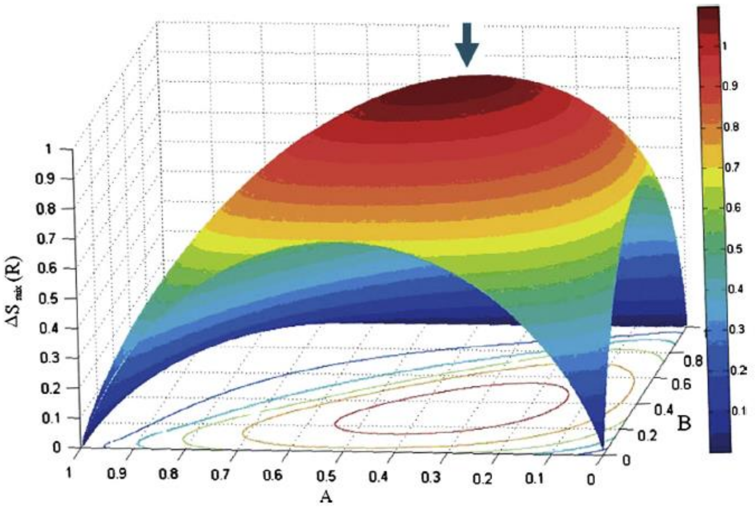

Fig. 3 The influence of the atomic ratios (concentrations) of elements in 3 component system on overall configurational entropy (atomic ratios on X and Y axis) [10].

Sluggish diffusion effect

The sluggish diffusion effect is typically believed to be the main phenomenon governing the precipitation of nano-sized particles in HEAs (example of such particle is displayed in in Fig. 4) as opposed to coarser precipitates in most of traditional alloys [10]. Due to the slow diffusion intrinsic to HEAs, the formation of the initial precipitate nuclei and their constitutive growth is severely retarded.

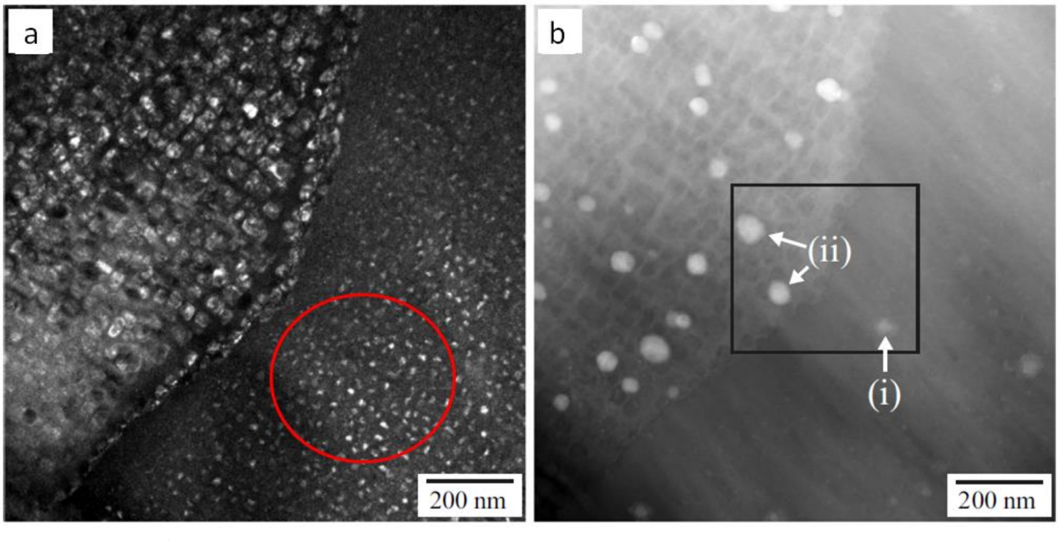

Fig. 4 a) TEM dark field image revealing nanosize particles denoted by red circle present in FCC solid solution phase of $Al_{0.5}$CrFeCoNiCu HEA; b) STEM image of ordered particles denoted as (i) and (ii) [10].

Consequently, the HEAs' microstructural stability during elevated temperatures exposure is rather high [10]. Tsai et al. [18] have investigated the mechanisms of vacancy formation and the influence of the chemical composition change in systems bearing single FCC microstructures, such as in CoCrFeMnNi HEAs, various austenitic stainless steels and pure elements. They observed that the values of diffusion coefficients (*D*) may be compiled in a sequence presented as follows:

$D_{\text{HEA}} < D_{\text{stainless steelAISI 304}} < D_{\text{pure elements}}$

The decrease of the diffusion coefficient is associated to the increase of the activation energy needed for diffusion in HEAs, in respect to the rest of alloys and pure elements – as illustrated in Fig. 5. The increase in activation energy is directly correlated with the number and type of elements present in a crystal lattice of a solid solution.

The elements present in the lattices bear certain differences in their respective atomic radii. The diffusion in metals is carried out by jumps of atoms or vacancies, respectively, in the direction of the atomic concentration gradient present within the microstructure. This is the most prominent, and energetically most efficient, diffusion mechanism [19]. The differences in atomic radii are suppressing the jumps of atoms due to the geometrical constraints, i.e. larger atoms move slowly in the lattices, as their size is inappropriate for smaller vacancies. The atomic radii difference also creates a first order lattice stress (also related to the third high entropy effect of lattice distortion described in the following sub-section). Due to the need to overcome the increased lattice stress, higher energetic barriers are present for individual jumping atoms, further slowing down their diffusion kinetics [18].

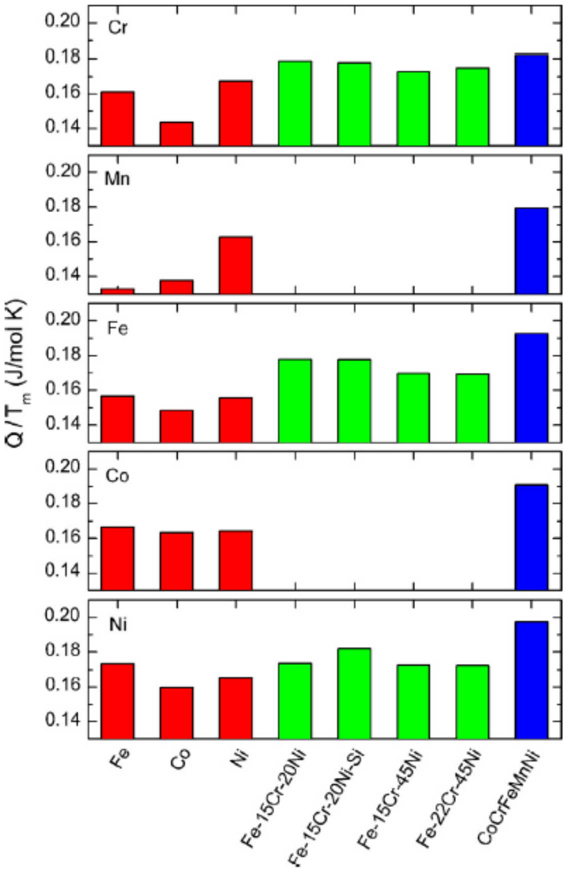

Fig. 5 Differences in normalized activation energy of atoms of Co, Cr, Fe, Ni and Mn elements in FCC pure metals and their alloys [18].

Severe lattice distortion effect

The severe lattice distortion effect is explained by the comparison of HEAs and the systems based on single dominant elements. In the substitutional solid solutions, the solute atoms of the alloying elements are occupying positions in the substitutional sites of the original lattice of a base element. In HEAs with single solid solution nature, the probability of occupying lattice sites is exactly the same for each element, i.e. there is no base element, if we omit any tendencies for chemical ordering stemming given by the negative values of mixing enthalpy ΔH_{AB} of the pertaining atomic pairs of the system. A comparison between a pure element lattice and a high entropy solid solution is presented in Fig. 6 a, b.

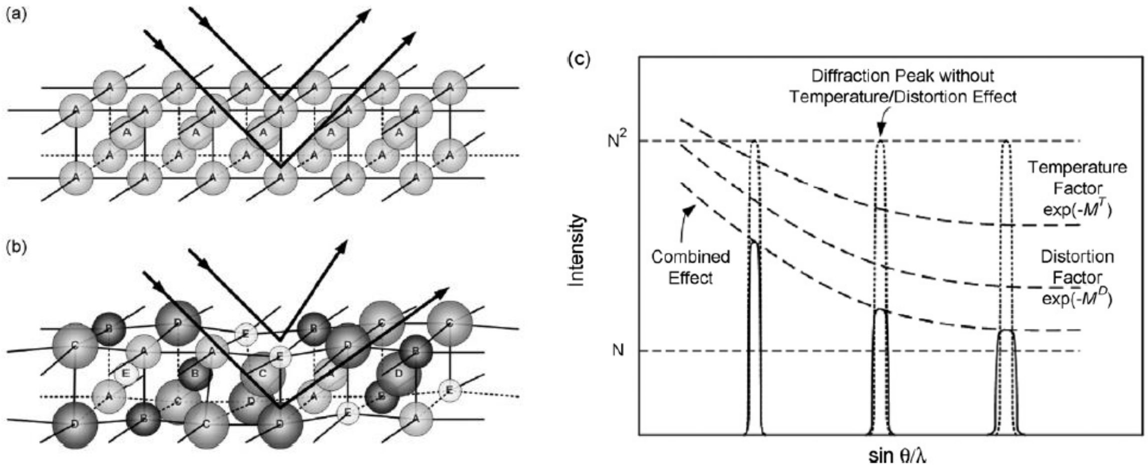

Fig. 6 Lattice configurations and diffracted radiation in a) FCC pure metal: b) high entropy FCC solid solution c) the influence of thermal effects and lattice distortion on the shapes of diffraction peaks of diffractogram of alloys in general [21].

The difference in atomic radii of the elements cause an increase in the local lattices stresses, impeding the movement of redundant dislocation loops by increasing the Peirls-Nabarro stress, i.e. the stress needed for dislocation core rearrangement during a single dislocation glide. This is principally a special case of an extreme substitutional solid solution strengthening, to the point that there is no distinguishable difference between the base atoms and the solute atoms. In this fashion, the high strength properties of some BCC HEAs are outlined [20].

The severe lattice stress has a significant influence also on the diffraction behavior of metals. The materials with atoms arranged in Bravais lattices are composed of periodically alternated atomic planes with a precise arrangement of atoms. During the electromagnetic radiation emission at 0 K temperature, smooth and well-defined Braggs diffraction planes are guaranteed (seen in Fig. 6 b in N^2 levels). With the increase in the temperature, the oscillation of atoms in the lattice around their equilibrium position is increasing as well, causing evident coarsening of the reflecting diffraction planes – therefore, also causing a slight drop in the diffractogram peaks' intensities. A higher directional scatter of the radiated photons is the fundamental reason behind this, which has been presented in Fig. 6 c as a temperature-factor effect. Consequently, this phenomenon came to be known as the temperature effect [21].

The decrease in the peak intensity and peak broadening (increased scattering) is also supported by the presence of additional lattice strains. A study on the influence of the number of present elements on diffraction peak intensities in CuAlCoCrFeNiSi system has been carried out [21]. The authors observed changes in peak intensities with the systematic addition of pure elements to a single-phase alloy. The alloys were composed from two to eight elements in equimolar ratios. They observed an anomalous decrease in peak intensities with every new added respective element, as well as their slight broadening, which is a very similar phenomenon to the temperature effect mentioned earlier. The final fundamental phenomenon underling this behavior is connected with the significant scatter of lattice parameter between the present elements, i.e. severe lattice distortion.

The synergic effect of severe lattice distortion and temperature increase is visible in Fig. 6 c above as a combined effect.

Cocktail effect

Cocktail effect is used to explain the observation of unexpected and, in many cases, abnormal properties in alloys, where a number of different elements is blended together, while neither of the utilized elements bears the additional properties when used separately. The technical term “cocktail effect” was invented by Ranganathan [22]. For example, the alloy $NbTiVTaAl_{0.25}$ exhibits a combination of strength and ductility, retained even at high temperatures, surpassing any of the elements in its composition. The microstructure of the alloy is composed of a single body centered cubic (BCC) solid solution from room temperature to the melting point of the alloy, thus making it a promising future high temperature material [23] (any phase transformation is very undesirable in any high temperature materials). The alloy properties may be adjusted by the alternation of elemental concentrations by the addition of small amounts of other elements, e.g. by the same procedure as for traditional metallic materials.

The basic rule for the HEA design and alloying elements selection may be compiled as follows: the bigger is the difference in atomic radii of potentially selected elements and the more negative are the tabulated values of binary mixing enthalpy (ΔH_{AB}) of these elements, the more significant change will be induced. Fig. 7 denotes the influence of the relative atomic concentration of selected elements on compressive strength and ductility of AlCoCrFeNi HEA, prepared with the same processing conditions [24, 25]. A significant increase in the strength is observed in both cases, imposed by the increase of the atomic radii mismatch δ and the lattice strain, as both added elements - Nb and V respectively - possess larger atomic radii, with the respect to the average value for AlCoCrFeNi composition [24, 25]. The formation of ordered intermetallic phases in the alloy microstructures has been observed for concentrations exceeding 0.25 in atomic fraction, further increasing the ultimate compressive strength, but with the cost of impediment of plastic properties [24, 25].

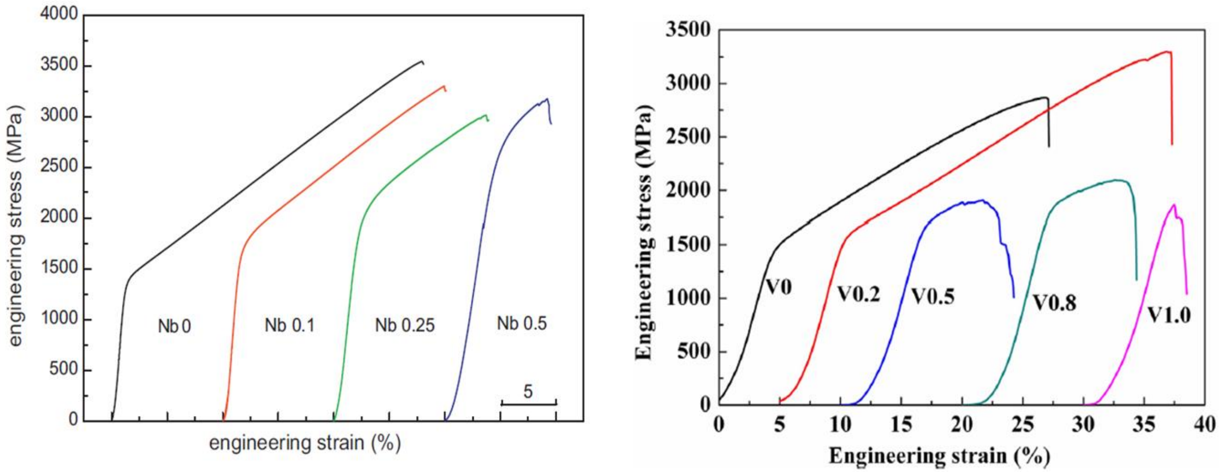

Fig. 7 The influence of the amount of niobium and vanadium on the compressive properties of AlCoCrFeNi alloy, prepared by electric arc melting [24, 25].

2.2 Multi–phase microstructure and high entropy effects

At this point, it is increasingly important to clarify on the role of multi - phase microstructures on the previously mentioned HE effects, as many reported HEA systems are not single phase. These HE effects are, sometimes, believed to be the main reason behind the interesting properties of HEAs. In the original concept proposed by Yeh [2, 26], the single solid solution phase in the microstructure was anticipated. However, after a dedicated literature review, one may observe that most of the produced alloys bear multi-phase microstructures, i.e. microstructures that are usually composed of solid solution phase and at least one additional ordered phase, e.g. σ phase, Laves phase, etc [10, 27]. With the implication of these findings, many scientists started to refer to such multi-phase alloys as compositionally complex alloys (CCA) or multi-principal element alloys (MPEA), due to their deviation from the original single solid solution concept [28].

Only a negligible difference is observed if the calculated total configurational entropy ΔS_{mix} of a single phase CoCrFeMnNi alloy is compared with a double phase $Al_{1.5}$CoCrFeNi alloy (total ΔS_{mix} calculated for $Al_{1.5}$CoCrFeNi as single phase in Table 1). The same calculations have been carried out in the articles [13, 29]. In those works, the fact that the $Al_{1.5}$CoCrFeNi alloy is (according to Wang [30, 31]) comprised of two different phases, namely FCC solid solution and B2 ordered phase, with lattice configuration same as NiAl intermetallic, is often neglected. The configurational entropy should be calculated for every phase separately, based on the respective chemical composition of the selected phases, as presented in Table 1. It can be seen that the configurational entropy of the FCC solid solution decreases, if one calculates for each phase separately, whereas the value for the ordered B2 phase should be approaching to zero. As in this case, there is usually only one configuration of atoms for ordered phase.

If, for instance, the amount of B2 phase is approximated to be around 50 volume % (as observed from the microstructure images in [31]), the rule of the mixture proves that the calculated total configurational entropy for the system could be around 6.45 K^{-1} mol^{-1}. For this reason, the concept of the above mentioned high entropy effect, i.e. suppression of ordered phase formation, is not applicable in multi-phase systems. However, the calculated value of

ΔS_{mix} for solely FCC phase is still surprisingly high - 12.7 K^{-1} mol^{-1}. As a result, the remaining effects (sluggish diffusion, severe lattice distortion and cocktail effect) may still play a significant role in the properties of the FCC solid solution phase within the microstructure of $Al_{1.5}CoCrFeNi$.

The questionability of the original high entropy effect is further supported by the latest studies [32, 33],which proves that complex phases may precipitate under certain conditions, even in models of FCC high entropy alloys, such as CoCrFeMnNi, which was believed to be intrinsically single phased.

Table 1 Calculated configurational entropies ΔS_{mix} values of two (single phase, double phase) HEA systems.

Alloy	**Structure**	**ΔS_{mix} ($J\ K^{-1} mol^{-1}$) Total**	**ΔS_{mix} ($J\ K^{-1}\ mol^{-1}$) FCC phase**	**ΔS_{mix} ($J\ K^{-1}\ mol^{-1}$) B2 phase**
$Al_{1.5}CoCrFeNi$	FCC+B2	13.25	12.70	~ 0
CoCrFeMnNi	FCC	13.38	13.38	-

2.3 Microstructural composition predictions

In the present time, the application of the methods based on thermodynamic calculation - CALPHAD (CALculation of Phase Diagrams) - has become a common practice in the field of microstructural and phase transformations prediction. However, for an accurate performance of such complex calculations, a vast number of thermodynamic parameters is necessary. The sheer compositional complexity, combined with a broad range of possible elemental concentrations, is making such calculations extremely complicated. Another reason that makes the CALPHAD calculation inefficient, stems from usual lack of sufficient verified data in the commonly used thermodynamic databases, resulting in significant differences in the calculated and experimentally determined results of HEA phase compositions [28]. For instance, even though the special HEA database for CALPHAD software Thermocalc© has been introduced recently, it still lacks in the number of available elements used in calculations,e.g. lack of C, N elements.

As a countermeasure for these issues, a number of new methods and parameters have been established with the development of new researches about HEAs. These methods are usually based on a systematic analysis of the experimental results and subsequent formulation of generalized theories for the complex systems predictions. With these new methods, it is possible to approximately determine the anticipated microstructures of very complicated systems in extremely short periods of time – thus making the HEA alloy design slightly less overwhelming.

The parameter that became the very basic principle for phase predictions of most alloys and, arguably the most reliable one, is atomic size difference δ, based on verified Hume - Rothery rules [17, 34, 35]:

$$\delta = 100\sqrt{\sum_{i=1}^{n} c_i \left(1 - \frac{r_i}{\bar{r}}\right)^2} \, . \qquad (6)$$

In this equation, c_i is the atomic concentration (fraction), r_i presents the atomic radius of i-th element and $\bar{r}$ is the average atomic radius of a given system, determined as [17, 34]:

$$\bar{r} = \sum_{i=1}^{n} c_i \, r_i \; . \qquad (7)$$

Fig. 8 illustrates the influence of atomic size difference and mixing enthalpy ΔH_{mix} for different types of alloys, with experimentally determined microstructures. It is clear that for formation of solid solution, a relatively small difference in atomic size is needed. The atomic size difference is governing also the type of solid solution lattices. According to a study undertaken by Kao [36] on AlCoCrFeNi alloys, the lattice of the solid solutions is changing from FCC through a mixture of FCC and BCC to pure BCC with increasing Al content [36]. This phenomenon was explained by a closed packing nature of the FCC structure when compared to the BCC one. The addition of an atom with significantly larger atomic size with respect to other present elements has, as a consequence, the increase in the lattice distortion and strain, resulting in elevation of the value of total internal energy, since Al possess much larger atoms than Co, Cr, Fe and Ni. At some point, the formation of BCC lattice is energetically more favorable, due to its lower packing factor and subsequently lower stress (there is literally more free space for accommodation of larger atoms in BCC, as compared to FCC lattice).

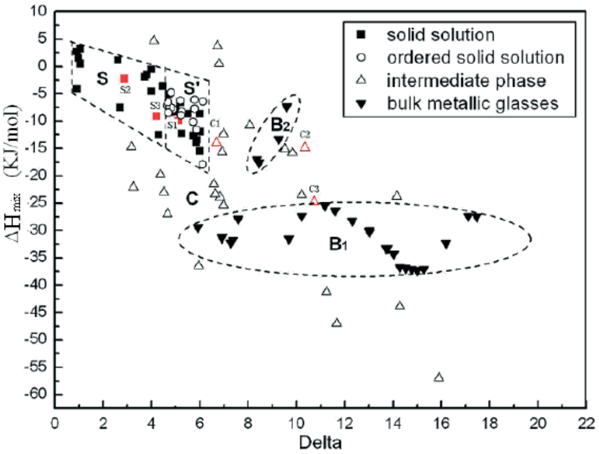

Fig. 8 The influence of atomic size difference δ in % and mixing enthalpy on phase composition of a variety of alloys bearing different microstructures [17].

Guo et. Al. [29] have studied the relationships between microstructural composition of the alloys with experimentally determined phases and the previously mentioned parameters ΔH_{mix}, ΔS_{mix}, δ. Additionally, they also have observed an influence of difference in electronegativity of the elements. Based on these parameters, they formulated a few generalization rules for alloys containing solid solutions. According to their findings, solid solutions are present in the microstructure when $-22 \leq \Delta H_{mix} \leq 7$ kJ mol^{-1}, $0 \leq \delta \leq 8.5$ % and $11 \leq \Delta S_{mix} \leq 19.5$ J K^{-1} mol^{-1}, calculated for the total average chemical composition.

Over the time, a modified condition has been proposed for alloys where only a single solid solution microstructure with no additional phases is demanded [37]: $-10 \leq \Delta H_{mix} \leq 5$ kJ mol^{-1}, $\delta \leq 4$ % and $\Delta S_{mix} \geq 13.38$ K^{-1} mol^{-1}.

In order to further assess the influence of free electrons in a metal, Guo et al. have utilized a new parameter, named as valence electron concentration (VEC) [29]:

$$VEC = \sum_{i=1}^{n} c_i VEC_i \tag{8}$$

VEC_i is the number of valence electrons for the i-th element. The VEC_i incorporates all electrons, including d electrons for transition elements. By means of VEC, it is possible to predict the lattice of designed solid solution alloys. FCC lattice is expected if the calculated VEC value is higher than 8. On the other hand, BCC is observed when VEC is lower than 6.86. The transition interval between 6.87 and 8 is characterized by a formation of FCC/BCC complex microstructure.

Yang et. al [13] proposed a method on the account of the natural competition between ΔH a ΔS, connecting these two thermodynamic parameters into a new one - **Ω**.

$$\Omega = \frac{T_m \ \ \Delta S_{conf.}}{|\Delta H_{mix}|}. \tag{9}$$

In the equation, T_m corresponds to an approximate temperature of melting in Kelvins, determined as an average value of the present elements. T_{mi} is a temperature of melting for respective elements and is described as:

$$T_m = \sum_{i=1}^{n} c_i T_{m_i} \tag{10}$$

With the calculated **Ω** value, the approximation of the alloy phase composition is very trivial. From the equation (9), it can be assumed that the **Ω** value is always positive, while the formation of disordered microstructures is believed to take place for a condition of $\Omega > 1$. The distribution of alloys type in conjunction with the **Ω** and δ parameters is presented in a plot of Fig. 9. A relatively good agreement of experimental observations and previously introduced parameters is evident.

Even with the use of mentioned parameters, the determination of a theoretical alloy microstructural composition closely resembling the experimental one is still extremely complicated, since the fundamental thermodynamic mechanisms underlying the microstructural evolution in alloys cannot be generalized so easily. The phase composition of the alloys is significantly modified as the intentional, or non-intentional, far from equilibrium processing conditions are applied. The influence of processing technology even for the same chemical compositions has to be further acknowledged.

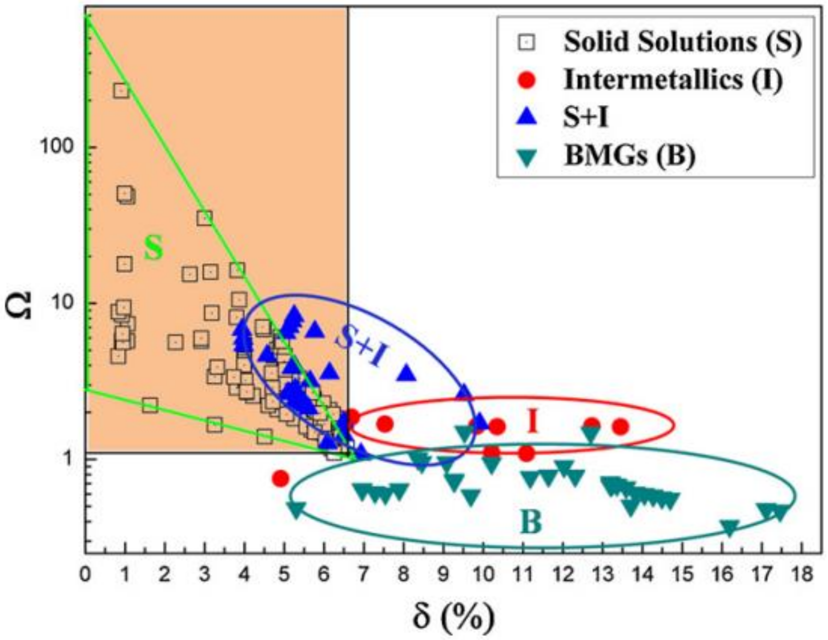

Fig. 9 The map of microstructures of known alloys based on Ω and δ parameters [13].

Schuch et al. evaluated the behavior of the originally single phase CoCrFeMnNi alloy during high pressure torsion and subsequent recrystallization treatments [38]. They observed an extreme grain refinement and improved strength levels – thanks to grain boundary strengthening. However, after annealing at 450 °C, an unexpected prospective increase in strength coupled with pronounced embrittlement took place. It was concluded that the precipitation of nano-sized Mn, Ni and Cr enriched brittle intermetallic phases was the source of this behavior (Fig. 10). This finding had an exceptional impact on HEA community and HEA design concepts, as it was believed firmly that the CoCrFeMnNi alloy is a very basic example of single phase HEA, at least according to the previous experimental observations and calculations [38]. There is, yet, another example of the prominent role of the processing conditions consideration.

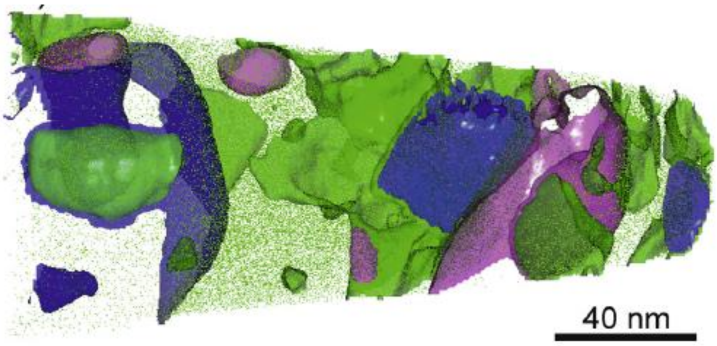

Fig. 10 3D atom probe tomography reconstruction of CoCrFeNiMn alloy nanostructure after high pressure and intermediate annealing on 450 °C, Cr enriched phase denoted by pink, blue and green colors are denoting Mn and Ni rich phases respectively [38].

2.4 Properties of High Entropy Alloys

In the following sections, the mechanical, chemical and physical properties of selected attractive HEAs will be discussed, with the aim of making a proper comparison with the conventional metallic materials. The future prospects of their application and future development directions will be briefly introduced.

2.4.1 Selected mechanical properties

The term “mechanical properties” includes a set of materials features connected to their performance under mechanical loading, namely: elastic moduli, strength properties, deformation behavior, fracture behavior, fracture resistance and fatigue properties. These properties are the most vital for load bearing materials used in supporting constructions and parts – currently, one of the most promising applications for HEA.

HEAs frequently exhibit a prominent combination of strength and fracture resistance [20, 39-43].

Fig. 11 a) and b) represents the results of tensile and fracture toughness tests on CoCrFeMnNi alloy. The alloy exhibits very good combination of the ductility and fracture toughness, proportionally increasing as the test temperature decreases. The values of fracture toughness K_{IC} for all temperatures surpassed 200 MPa.m$^{-1/2}$

Such good combination of the strength properties and fracture resistance is most probably a result of their simple solid solution microstructures. FCC and BCC lattice structures combined with non-directional metallic bonding is the origin of the materials ductility. Due to a multiple slip system available and short Burger`s vectors of dislocations, dislocation movements and resulting plastic deformation are carried out relatively easily [1, 10]. Simultaneously, the severe lattice distortion and resulting lattice stresses make the dislocation movement more energy consuming, due to the increase in lattice friction, therefore increasing the material overall strength and hardness, although with no deleterious effect on the overall ductility. The simultaneous increase in strength and ductility in CoCrFeMnNi alloy were attributed to the onset of deformation twinning phenomenon at cryogenic temperatures, as an additional deformation mechanism [44].

Gludovatz et al. [45] made an attempt to further improve the low temperature fracture toughness of a CoCrFeMnNi HEA. They have examined its variant using only three elements: Co, Ni, and Cr, as they believed Fe and Mn usually cause a reduction in low temperature properties as a result of transition behavior. The alloy was designated as Medium Entropy Alloy (MEA) due to a decrease in configurational entropy as a consequence of the presence of only three elements. Surprisingly, the CoCrNi alloy bearing pure FCC solid solution microstructure exhibited a combination of strength, fracture toughness and tensile ductility unrivalled by any other known HEA before, provided in Fig. 11 c, d together with CoCrFeMnNi alloy.

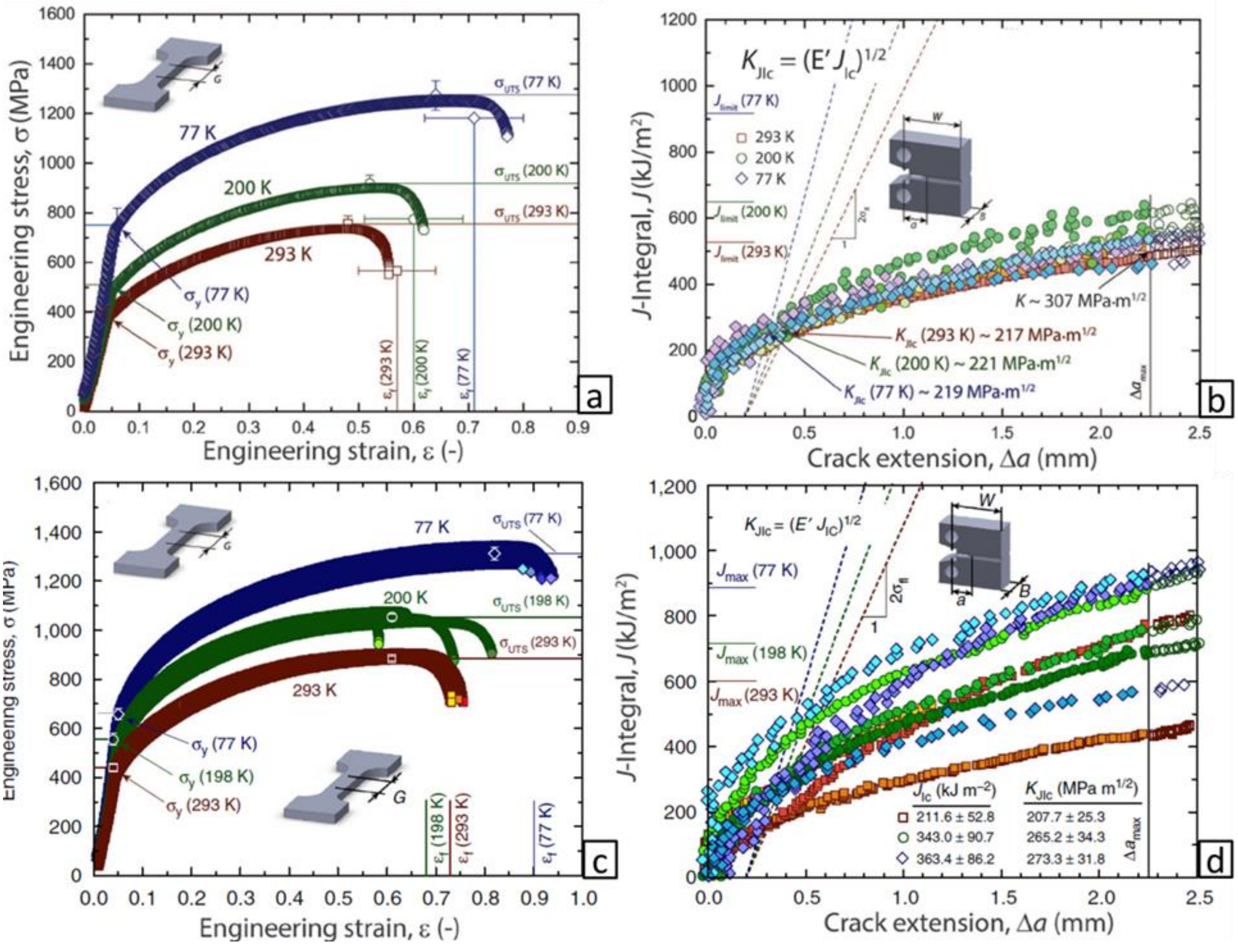

Fig. 11 Influence of temperature on tensile properties and fracture toughness of a, b) CoCrFeMnNi alloy and c, d) CoCrNi alloy - showing simultaneous increase in strength and ductility with decreasing temperature [44, 45].

The better properties of CoCrNi alloy are believed to come from the observed deformation nano-twinning upon straining at room temperature, unlike in CoCrFeMnNi HEA, where deformation nano-twinning was observed only at cryogenic temperatures. As the testing temperature decreases, the scale of deformation twinning increases. They also proposed the idea that not only the high configurational entropy, but also the appropriate element selection is essential for improvements in the properties of HEAs and MEAs as well as a special role of Cr element in these systems. Cr element, according to them, impair improvement in higher properties, as compared to other elements, without significant influence on the phase composition, as it promotes more severe lattice distortion effect [46].

In a few of several studied FCC systems, the deformation twinning has been observed as well (Fig. 12) [47, 48]. Deformation twinning is an additional deformation mechanism to the usual dislocation slip, increasing the ability of the material to accommodate subsidiary strain, i.e. stress relaxation, thus increasing the overall ductility of the alloy [49]. Consequently, it postpones the onset of plastic instability occurrence during tensile loading [48, 50, 51] . The deformation twinning is believed to be a result of low stacking fault energy (SFE) of selected alloys. In this context, the twinning boundary represents a case of extremely wide stacking fault.

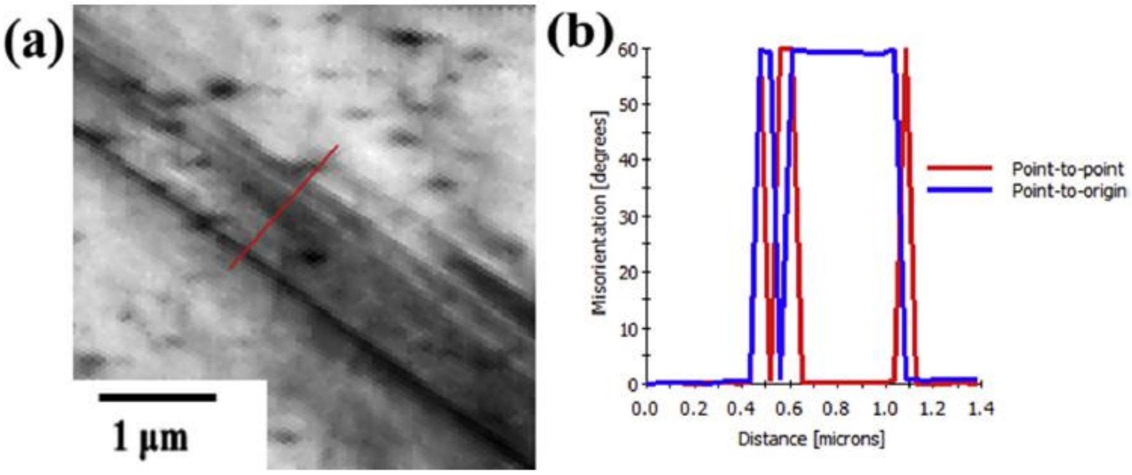

Fig. 12 Deformation twining revealed by HR EBSD analysis in CoCrFeMnNiC$_{0.5}$ alloy at 77K a) High-magnification Kikuchi pattern quality map; b) corresponding misorientation as a function of distance for the red line [47].

Based on ab-initio stacking fault energy calculations and deformation behavior observations, the mechanisms behind the CoCrFeMnNi alloy increase in both strength and ductility, with temperature change from 293 to 77 K was finally comprehensively explained (presented before in

Fig. 11) [44, 52]. At the room temperature, the deformation is preferentially carried out by normal dislocation slips in close packed planes. With the temperature reduction, the SFE in this system is being decreased as well (as shown in Fig. 13.). This leads to a change in the principal deformation mechanism, as soon as the formation of stacking faults suddenly becomes more energetically favorable than dislocation slip, i.e. twin boundaries formation consumes less energy than new grain boundaries formation respectively, as the dislocation slip is responsible for new grains formation.

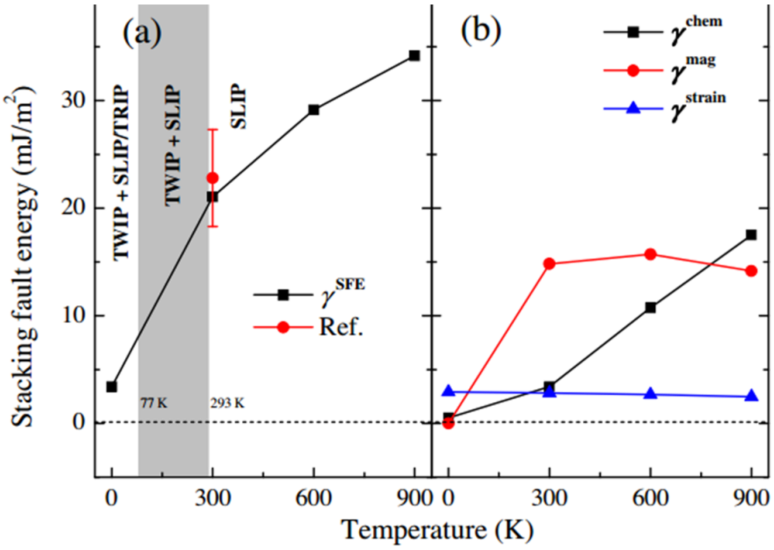

Fig. 13 a) calculated stacking faults energy change based on temperature in CoCrFeMnNi alloy, with prevailing deformation mechanisms denoted (TRIP – transformation induced plasticity TWIP – twinning induced plasticity); b) the influence of three components of SFE levels [52].

This behavior corresponds to the previously mentioned TWIP effect. If the stacking fault energy decreases even further, an effect called as Transformation Induced Plasticity (TRIP) appears. The TRIP effect is associated with the strain induced phase transformation from the FCC to HCP lattice, accomplished by the movement of Shockley partial dislocations on every second close packed plane [52], i.e. formation of stacking faults on every second plane in FCC. This phenomena is denoted as strain induced transformation to ε martensite [53]. TRIP and TWIP effects are both resulting in the increase of fracture toughness by retarding the crack growth kinetics.

In order to employ TRIP and TWIP phenomena, Deng et al. designed $Fe_{40}Mn_{40}Co_{10}Cr_{10}$ alloy, again by the utilization of the first principles' calculations, to adjust the stacking fault energy [54]. They observed mechanical twinning in the alloy at room temperature (properties displayed in Fig. 14). They also succeeded in the reduction of the amounts of expensive elements, and, therefore, increased the application's potential of the material. However, the measured properties did not reach the levels of equi-atomic CoCrFeMnNi alloys, probably due to the decrease of solid solution strengthening.

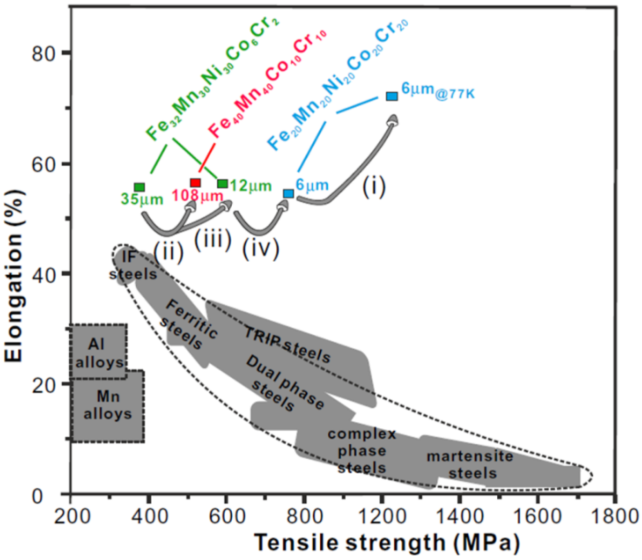

Fig. 14 The comparison of tensile properties of $Fe_{40}Mn_{40}Co_{10}Cr_{10}$ and FeCoCrMnNi alloys with different grain sizes and conventional materials [54].

The alloys with BCC lattice exhibit usually intrinsically much higher strengths, but lower ductility. The $AlCoCrFeNiTi_{0.5}$ alloy, with the BCC solid solution structure and precipitates of coherent B2 phase, displayed an extraordinary combination of mechanical properties [37, 55]. The alloy has a compressive strength of over 3000 MPa with 23 % maximum strain and 120 GPa elastic modulus. Such properties are even more striking, if its low density of 6.77 g cm^{-3} is taken into consideration. These properties are comparable with the high-strength materials, e.g. such as maraging steels and titanium alloys. For a better illustration, Fig. 15 clarifies the comparison of strength to weight ratios and elastic moduli of different materials. Occasionally, only the strength and ductility of the materials is taken into consideration. Nonetheless, for structural materials, also a high value of elastic modulus is essential for a successful application, as it is a guarantee of the structural stiffness.

However, it should be taken into account that a comparison presented in Fig. 15 is only an approximation, due to different types of tests used for the measurements of mechanical properties, as materials intrinsically exhibit different values of strength and ductility in compression and tension.

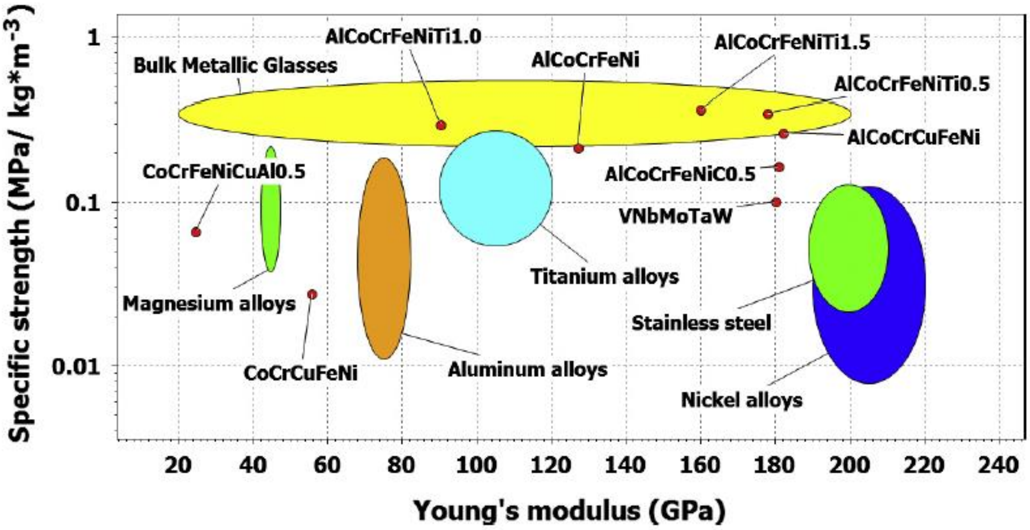

Fig. 15 Comparison of specific strength (strength to density ratio) and elastic moduli of different materials [10].

2.4.2 Wear resistance

The tribological and the wear properties play an essential role for an efficient performance of a number of advanced materials applied in structures, where intensive materials contact and friction occurs. This is another possible area of application for HEAs, partially owing to their high strength properties.

One of the best examples of wear resistant HEA are the $Co_{1.5}Ni_{1.5}CrFeAl_xTi_y$ alloys developed by Chuang et al. [56]: x and y correspond to varied addition of Al and Ti elements. They examined the adhesive wear resistance properties of these HEAs with the utilization of pin on disc method, followed by a comparison of results of the most common wear-resistant materials. Unquestionably better wear properties of $Co_{1.5}Ni_{1.5}CrFeAl_{0.2}Ti$ alloy are apparent from Fig. 16 (SUJ2 and SKH51 are equivalents for EN ISO 100Cr6 and HS 6-5-2 steels). This alloy bears the microstructure of FCC solid solution and hexagonal ordered η phase possessing Ni_3Ti chemical composition. Due to a precipitation strengthening effect of a significant volume fraction of η phase in FCC matrix, a high strength of 717 HV is achieved for $Co_{1.5}Ni_{1.5}CrFeAl_{0.2}Ti$. However, the hardness of the later is lower than that of SKH51 steel, while still bearing better adhesive wear properties. Therefore, some additional mechanism must be responsible for its improved wear resistance. It may be the ability of the alloy to form stable oxides upon local temperate increase on contact surfaces (where the temperature may locally rise to 800 °C) causing the decrease of friction coefficient and also better resistance to thermal softening [56].

The increased wear and hardness properties of some HEAs could be employed in combination with a softer, ductile substrate for manufacturing diverse advanced coatings with additional properties.

Huang et al. [26] prepared Plasma Sprayed coating with $AlSiTiCrFeNiMo_{0.5}$ and $AlSiTiCrFeNiCoMo_{0.5}$ chemical compositions. In a state directly after deposition, the coating contained a major single BCC solid solution phase with its average hardness around 500 HV. After an intermediate temperature annealing at 800 °C, the hardness further increased up to almost 900 HV. The wear resistance of both coatings was exceptionally good as compared to common steels, as seen in Fig. 17.

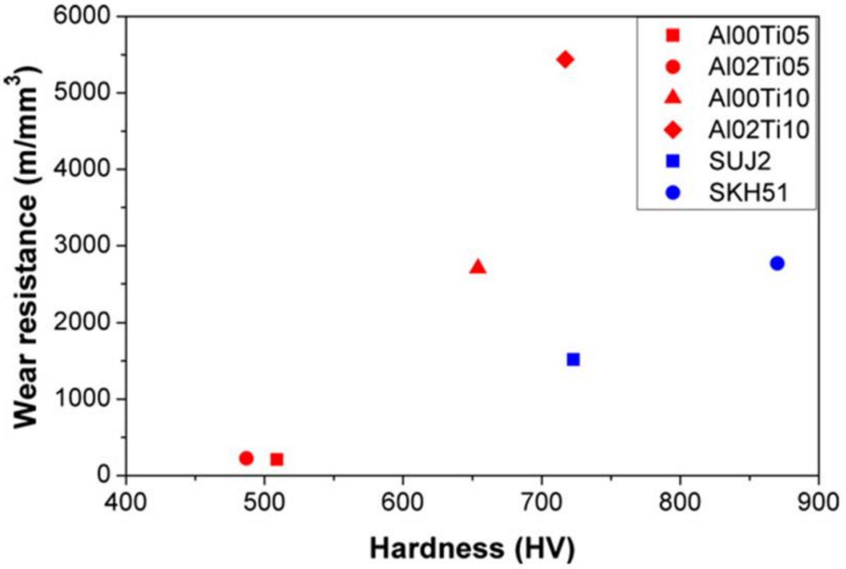

Fig. 16 The adhesive wear resistance and hardness of $Co_{1.5}Ni_{1.5}CrFeAl_xTi_y$ alloy compared to conventional wear resistant steels by pin on disc method [56].

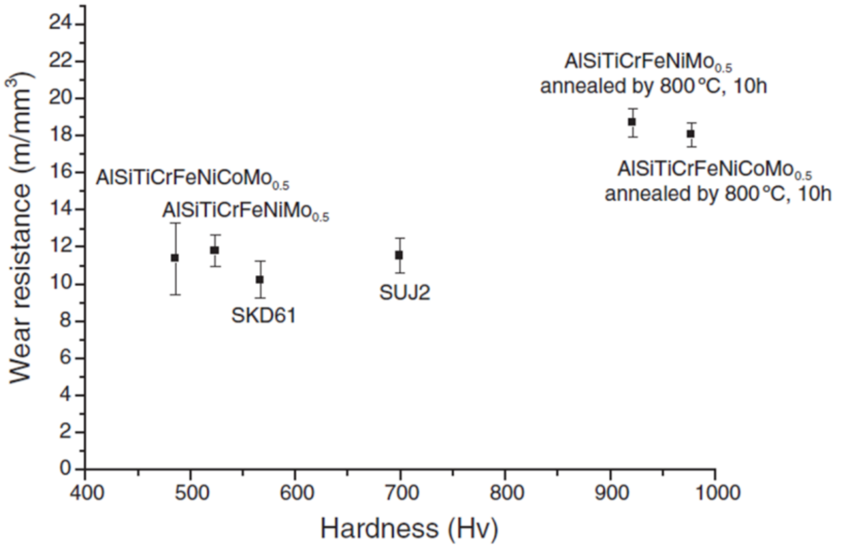

Fig. 17 The adhesive wear resistance and hardness of $AlSiTiCrFeNiMo_{0.5}$ and $AlSiTiCrFeNiCoMo_{0.5}$ thermal spray coatings as compared to steels [26].

2.4.3 Chemical and electrochemical properties

Most of the HEAs contain relatively high atomic fractions of Al, Cr, Si, Mo elements, i.e. elements forming a passivation oxide layer on their surfaces, protecting them from further excessive oxidation upon oxygen atmosphere exposure – especially at elevated temperatures. Based on this fact, it is reasonable to expect a good oxidation resistance for most HEAs, comparable to those of stainless steels or nickel base superalloys, stemming from comparable amounts of Al and Cr. For example, electrochemical corrosion resistance of AlCoCrFeNiCu alloys in both NaCl and H_2SO_4 solutions is higher than those of conventional austenitic stainless steel AISI 304 [57, 58].

Zhia et al. [59] published a comprehensive review on the HEA's electrochemical properties in water solutions. They implied that the properties of some HEAs are better than even the best stainless steels (corrosion rates are lower than 1mm per year) as shown in Fig. 18. Some alloys also exhibit a good high temperature oxidation resistance. For instance, the $Co_{1.5}Ni_{1.5}CrFeAl_{0,3}Ti_{0,2}$ alloy exhibit an oxidation behavior comparable to the Inconel 718 nickel base superalloy [39, 60]. The main source of its good properties is the formation of compact layer of stable Cr_2O_3 on the alloys surface. The combination of corrosion resistance, the high temperature hardness and strength of this alloy system makes it one of the most the promising HEAs of today.

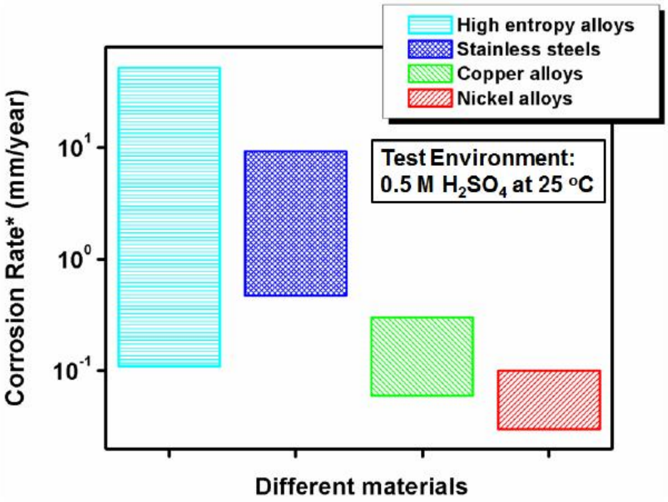

Fig. 18 Calculated electrochemical corrosion rates of HEAs as compared to traditional corrosion resistant materials [58].

2.4.4 High temperature strength

The basic properties expected for elevated and high temperature materials are: high microstructural stability (phase composition stability), high temperature strength and good creep properties, as well as high oxidation resistance. Finding such properties' combination in a single material is usually not an easy undertaking. Considering the slow diffusion kinetics, presence of strengthening intermetallic phases and stable oxide formation for HEA systems, it is safe to assume that the prospective potential of HEAs for high temperature applications is vast [28]. Therefore, they may be considered as candidates for future replacement of Co and Ni based superalloys.

For instance, the $Al_{10}Co_{25}Cr_8Fe_{15}Ni_{36}Ti_6$ alloy, developed by Daud et al., with the support of thermodynamic calculations [61], has a microstructure composed of FCC solid solution phase (γ) and extremely fine coherent precipitates of ordered $L1_2$ phase (γ′ phase) after heat treatment; the exact same type of microstructure as that of Ni based alloys. The heat treatment was composed of homogenization annealing at 1220 °C for 20 hours with air cooling and subsequent aging for 50 hours at 900 °C. The alloy treated in this way had a higher tensile strength during high temperature testing than Inconel 617L and Alloy 800H in the whole range of temperatures from 20 to 1000 °C. The same group also developed a number of HEAs with interesting high temperature properties with γ/γ′ phase microstructures [62, 63]. They are presented in Fig. 19.

The already mentioned $Co_{1.5}Ni_{1.5}CrFeAl_xTi_y$ system may also be promising, bearing in mind its good wear properties [56]. With the change of Al and Ti ratio (x/y), or different heat treatment conditions, the phase composition can be adjusted to suit to particular application's needs [39]. The formation of three different types of ordered precipitates dispersed in the FCC matrix can be achieved: already mentioned γ′ phase, η phase (Ni_3Ti bearing HCP lattice) and β phase ((Ni, Co)Al with ordered B2 lattice). The most prominent seems to be a combination of fine γ′ and η phase in FCC matrix. Fig. 20 elucidates the comparison among high temperature hardness of different HEAs, as well as Ni based superalloy Inconel 718, as an example of common material.

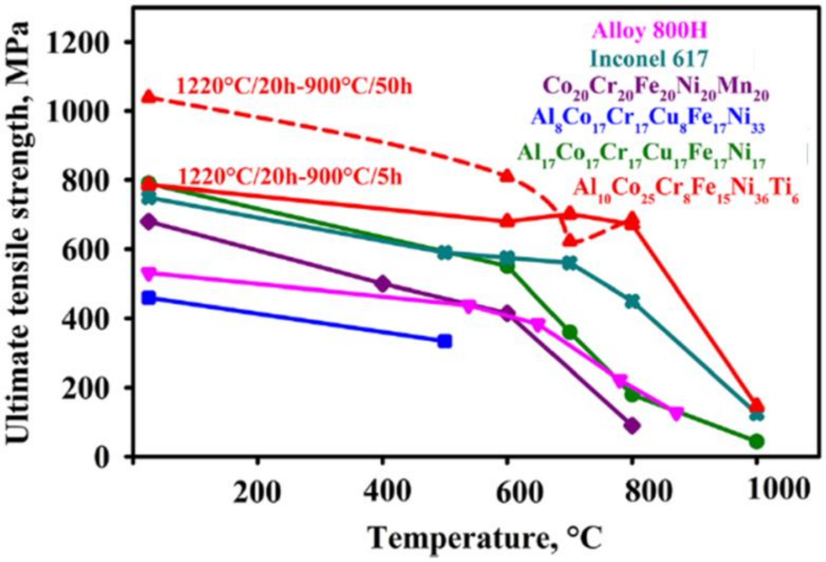

Fig. 19 High temperature tensile strength of different HEAs and nickel base superalloys [61].

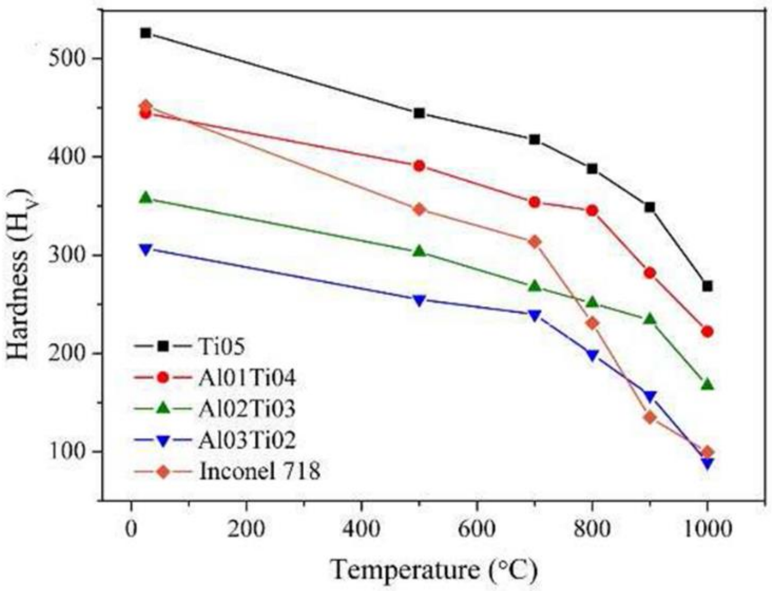

Fig. 20 High temperature hardness of $Co_{1.5}Ni_{1.5}CrFeAl_xTi_y$ alloys compared to Inconel superalloy [60].

3 Selected strengthening mechanisms in metals and metal matrix composites

For the efficient design of the materials, there is an indispensable need to fully understand the mechanisms responsible for the properties' alterations that occur during manufacturing and operation [64]. As the load bearing constructions are the primary interest in mechanical engineering, the most prominent property is unquestionably strength.

The strength is closely connected to the materials plastic deformation - or rather the plastic deformation prevention - which is further associated with the dislocation movements in the most favorable slip systems. Therefore, if the resistance to permanent deformation of metals should be increased, it is necessary to employ mechanisms intrinsically responsible for the reduction of dislocation movements [64]. Additionally, different strengthening phenomena act at varied length scales.

3.1 Composite materials

Composite, is usually understood as a material combined from at least two types of materials with distinguishable interface, bearing significant differences in mechanical, physical or chemical properties [65] of the separate components. In the resulting material, a combinatorial effect is taking place, i.e. the gathering of the best properties of all incorporated materials, while the negative properties are suppressed to some extent. However, this synergy of properties, resulting in achievement of qualities positively deviating from the rule of mixture, is plausible only if the proper composite design and material selection is applied [66]. Therefore, it is of great importance to understand the true nature of the physical phenomena determining the overall properties.

As opposed to conventional materials (alloys), in which the components form by a thermodynamic phase transformation and possess at least some level of chemical similarity, the constituents in composite may be of diametrically different nature (e.g. metal-plastic composites). As a consequence, most of the composites are very hard to prepare by spontaneous processes [65].

The design of a composite material is always bonded to the required structural part and application. According to this, the adequate material system is designed, as opposed to usual materials, where the parts are manufactured from already commercially available materials. Therefore, the improvement in properties of a composite over the traditional material must be significant enough to compensate the increase of the composite's manufacturing costs.

After a deep investigation, one can assume that all the natural materials with supporting or protective functions, e.g. bone, nacre, wood, are in fact composites with highly hierarchical spatial arrangements, that sometimes surpasses the individual properties of their base materials by orders of magnitude [67].

The major component of the composite is referred to as matrix – it usually comprises the highest volume fraction of the composite. The other components usually induce strengthening and, therefore, are called reinforcements [68]. Composites are most often divided in three groups, depending on the used matrix as: polymer matrix composites (PMC), ceramic matrix composites (CMC) and metal matrix composites (MMC) [65]. Every group bears its characteristic properties coming from the intrinsic properties of the utilized matrix material.

3.1.1 Metal matrix composites

The metal matrix composites provide a number of benefits with respect to conventional monolithic materials - usually higher strength, stiffness and high temperature properties, sometimes coupled with additional physical properties, when combined with ceramic reinforcements. The presence of reinforcements has also a significant influence on the additional properties, like heat and electric conductivity, and coefficient of thermal expansion (CTE) [68].

Except for the dominating material defining the matrix properties, the different types of MMCs are divided according to the type or geometry of the used reinforcements. Three types of composites arise as the most used: fiber skeletal and particulate composites. The fibers in composites provide a genuinely efficient strengthening as a consequence of the nature of the stress transfer and due to some additional toughening phenomena (e.g. crack bridging by the fibers). They are generally divided by the length of the fiber to composites with:short and long fibers, and also based on the fiber arrangement to randomly arranged or aligned fiber reinforced composites in one or more directions [69]. The skeletal composites are composed of load bearing porous skelet, usually infiltrated by matrix metal, used as a binder to increase the fracture resistance. In spite of their relatively lower mechanical properties (with respect to fiber and skeletal MMCs), the most common type of MMCs are the particulate composites due to their relatively easier and cheaper manufacturing technologies. In these, the reinforcement in the spherical shape is more or less evenly distributed in the matrix, providing the barriers for the subsequent dislocation movements [69]. Apart from the isotropic properties, the success of the particulate composites arise from the possibility to employ already established conventional, or slightly modified manufacturing routes [68, 70]

3.2 Strengthening in metals

The different strengthening phenomena present in metals usually act on an order of size comparable to lattice parameters of the metal atoms. As such, the strengthening is the result of the interaction of lattice defects and present atoms in the multitude of different ways.

3.2.1 Hall - Petch strengthening

Hall - Petch strengthening phenomenon is very well known as its theory is successfully applied for all poly-crystalline materials. It is based on the approximation of the interactions of moving dislocations with existing grain boundaries. The grain boundaries are 2D crystal defects composed of dislocation segments acting as barriers for moving dislocations. The stress needed for the accumulated dislocations to pass this boundary (for low angle grain boundaries), or to induce dislocation movement in neighboring grains is the basis for the equation. The increase of yield strength, being reversely related to the grain size is described as follows [71, 72]:

$$\sigma_y = \sigma_0 + \, k_y \, d^{-\frac{1}{2}} \, . \qquad (12)$$

In the formula, σ_0 is the lattice friction stress (including all active strengthening mechanism - recalculated for tensile loading with respect to shear friction stress $\Delta\tau$ that will be described later) in MPa, k_y is a constant material value (MPa m$^{-1/2}$) determined for given material, and *d* is the average grain size.

3.2.2 Interstitial and substitutional strengthening

The presence of atoms of one element in the lattices of other element results in two separate effects. The solvent (basic metal) and solute atoms may be different in either atomic size or elastic properties - producing the atomic misfit and elastic misfit interaction, respectively. For the majority of cases, these two interactions act simultaneously.

As the dislocations present in the metal travel within the lattice containing solute atoms of different atomic size, a misfit interaction take place due to the lattice distortion which corresponds to the elastic misfit problem parallelly associated with inserting a ball in a smaller hole [64].

However, there is a difference in the behavior corresponding to the solute atoms with small size differences - substitutional atoms replacing the atoms of base elements in the lattice sites, and atoms with much more significant size difference (much smaller atoms) of interstitial elements that occupy the space between solvent atoms (e.g. C atoms in empty space within the α-Fe BCC lattice). Substitutional atoms, such as Cr in Fe, give rise to a completely symmetrical spherical distortion in the lattice and consequently only pure hydrostatic stresses are induced. Based on this fact, the substitutional solute atoms are able to interact only with edge dislocations, as the nature of the stress field of edge dislocations is also purely hydrostatic; there is a tensile stress field attracting the bigger substitutional atoms and compressive stress fields on opposite side of dislocation core attracting smaller substitutional atoms.

Screw dislocations, in contrast, induce a stress field of a pure shear character - the hydrostatic component of a screw dislocation is zero [64]. That is the reason why substitutional atoms (possessing only hydrostatic stress), are not able to interact with screw dislocation. On the other hand, interstitial atoms generate stress fields with both hydrostatic as well as shear nature due to their tetragonal distortion of lattices. Therefore, interstitial atoms are able to interact with both edge and shear dislocations as opposed to substitutional atoms, leading to a more effective dislocation impediment and increased strengthening (just as in case of carbon and nitrogen atoms in α iron BCC lattice) [64].

Interstitial atoms have also the tendency to occupy the free space in dislocation cores, pinning the dislocation movement even further and evocating additional changes to the material (Portevin - Le Chatelier effect, sharp yield point) [73].

The other type of interaction, referred to as elastic misfit interaction, is stemming from the valence electron arrangement of different elemental atoms. As a result, they also possess different bonding energies, causing different elastic properties around these atoms which directly influence passing dislocations. This is sometimes referred as a formation of “softer” and “harder” zones [64].

As mentioned previously, the presence of substitutional and interstitial atoms will inevitably lead to solid solution strengthening. This is generally defined by the increase of shear stress $\Delta\tau$, needed to induce the movement of dislocation segment (lattice friction) of the grain. A simple empirical equation is used for the evaluation [64]:

$$\Delta\tau = Kc^N, \tag{11}$$

where K is the constant influenced by the nature of solute and solvent atoms and dislocation properties, c is the solute atomic concentration and N is exponent in the interval from 1/3 to 2/3. Solid solution strengthening is the fundamental source of properties of high entropy materials, as was mentioned in 2.1. In composites, it acts as a matrix strengthening phenomenon.

3.3 Strengthening in metal matrix composites

The strengthening phenomena acting in metal matrix composites, or rather any type of material with the dispersion of at least one type of strengthening phase can be described as follows:

3.3.1 Zener type strengthening

In the metal matrix composites containing stable ceramic reinforcements, due to the grain boundary pinning by dispersed particles, the grain growth at high temperatures is severely retarded (displayed in Fig. 21). For materials working at elevated and high temperatures, the grain growth suppression is an essential quality. It is closely associated with previously mention Hall-Petch strengthening. Even in materials used at room temperatures, the grain growth inhibition will manifest at the processing temperatures, causing reduced grain size and better mechanical properties in the resulting product. With the increasing amounts of reinforcement, the grain coarsening inhibition is increasing as well, as the more grain boundaries are pinned by present ceramic particles, with the condition of a constant reinforcement particle size. This phenomenon is, therefore, sometimes referred to as Zener-type strengthening, named by its founder. Zener prescribed a relation for the final grain size d_m of the matrix of manufactured MMC as [70]:

$$d_m = \frac{4A_n\, d_p}{3v_p}\,, \tag{13}$$

where A_n is a proportionality constant, $d_p$is the average reinforcement particle size in and v_p is reinforcement volume fraction in matrix.

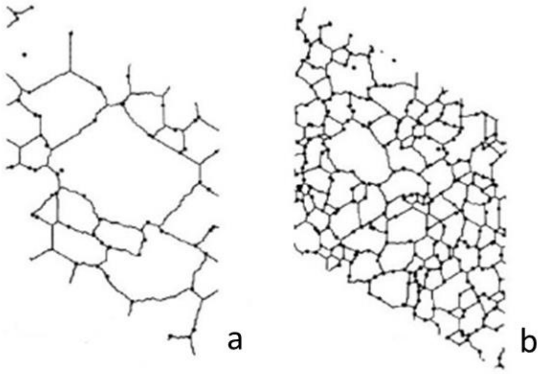

Fig. 21 The influence of the reinforcement fraction on grain size of composites a) 1 volume % fraction; b) 5 volume % fraction [70].

3.3.2 The load transfer strengthening

The load transfer strengthening becomes evident in cases of strong interface bonding among softer, malleable matrix and harder, stiffer reinforcements. The mechanical load is transferred not only through the matrix, but also to the reinforcements. The result is the increase in the material load bearing capacity as a whole. For description of this type of strengthening, Mardon and Prew prescribed a general model usually applied for particle reinforced composites, where improvement in strength $\Delta\sigma_l$ is [74]:

$$\Delta\sigma_l = v_p \sigma_m \frac{(l+t)A}{4l}\,, \tag{14}$$

where v_p is volume fraction of reinforcement, σ_m is the yield strength of matrix, l is the reinforment phase dimension parallel to the loading direction, t is the thickness of particles in perpendicular dimension and $A = l/t$. For spherical particles, further simplification may be used, based on the spherical particle symmetry. The equation goes as:

$$\Delta\sigma_l = 0.5\, v_p \sigma_m\ . \tag{15}$$

3.3.3 Orowan strengthening

The Orowan’s strengthening describes the influence of any present particles (reinforcement particles) on the strength of a material. It is an acting phenomenon in double phase systems, with the preposition of the non-coherent matrix/particle interface - e.g. reinforcement and matrix lattice types are completely different by either size or atomic ordering, or the respective lattices are close to being identical, but the reinforcement particle size is excessive [75]. The physical model is based on the assumption of homogenously dispersed particles and intrinsic inability of passing dislocations to cross right through them (the particles are approximated as perfectly non-deformable barriers that the dislocations are not able to penetrate). The dislocations loops passing through matrix are therefore bended around the particles, due to the influence of applied stress. The length of dislocation loops is increasing as the bending proceeds. The energy consumed by this process is provided from external, stress inducing forces. In the last stage, the dislocation segments around the particles join, creating a new dislocation loop pinned around the particle, while the original dislocation segment is moving further to other particles (denoted in Fig. 22). Orowan strengthening σ_{Orowan} can be calculated as [76, 77]:

$$\sigma_{Orowan} = M \frac{0.4Gb}{\pi(1-\mu)^{1/2}} \frac{\ln(\bar{d}/b)}{\lambda}, \tag{16}$$

$$\bar{d} = \sqrt{\frac{2}{3}d_p}\ , \tag{17}$$

$$\lambda = \bar{d}\sqrt{\frac{\pi}{4v_p - 1}}, \tag{18}$$

$$G = \frac{E}{2(1+\mu)}\ . \tag{19}$$

In the equations, M is the orientation factor, G is shear elastic modulus, b is the dislocation burgers vector, μ is Poissons constant, d_p is particle diameter and λ interparticle spacing. The interparticle spacing λ is determined directly by the geometry measurements or from the reinforcement volume fraction.

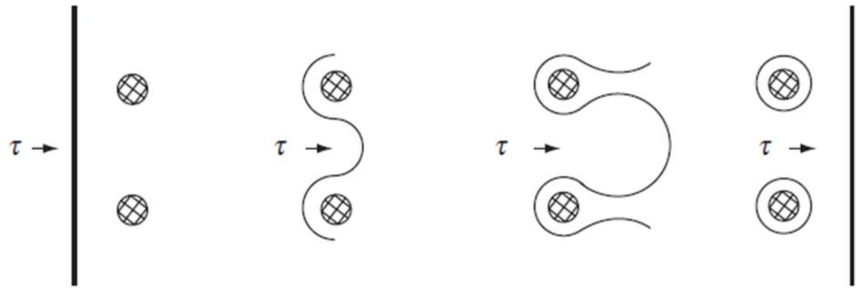

Fig. 22 The reinforcement particles are passed by a matrix dislocation, due to the applied sheer stress τ resulting in creation of closed loops around particles [75].

3.3.4 CTE and EM difference strengthening

In the multi-phase materials with the presence of hard reinforcement particles in softer matrix, the differences in mechanical properties induce the change in matrix behavior in the vicinity of the particle. Differences in the coefficient of thermal expansion (CTE) and elastic moduli (EM) of the two phases introduce interfacial residual stresses, with any temperature change that the solid material is subjected to. Consequently, provided that the matrix is ductile enough, geometrically necessary dislocations (GND) are generated in the matrix around every reinforcement particle, as a way of stress relaxation. The dislocation density is highest at the interface area and is rapidly decreasing with increasing distance from the interface. This effect is comparable to the strain hardening process [74]. Even if the matrix phase is not ductile (GNDs are not formed), the stresses remain in the material and result in the same level of strengthening. The stresses are generated in the material as it is cooled from the processing temperature, which is always much higher than operation temperature, regardless of the production route. This is especially significant for the materials produced by powder metallurgy (PM) and casting.

Taylor [78] noticed a relationship between dislocation density and the strength (especially yield or proof strength), in all kinds of materials. This equation, therefore, applies for the GNDs generated by the matrix and reinforcement differences of CTE and EM as well. The equation accounting for the contribution of CTE mismatch to the increase of strength is given by modified Taylors equation as [79]:

$$\sigma_{dCTE} = K\beta Gb\sqrt{\rho^{CTE}}. \tag{20}$$

In the formula, K refers to Taylor`s constant depending on the lattice type (usually in the range from 0.1-0.3), β is constantly given as 1.25, ρ^{CTE} is a calculated dislocation density given by:

$$\rho^{CTE} = \frac{Z\Delta\alpha\Delta T v_p}{bd(1 - v_p)}, \tag{21}$$

where $\Delta\alpha$ is taken as CTE mismatch value, ΔT is the difference in processing and operation temperature. Z is a geometrical constant defining the reinforcement geometries, with value ranging from 10 to 12 [77].

Elastic modulus mismatch strengthening is calculated in similar way as:

$$\sigma_{dEM} = \sqrt{3}BGb\sqrt{\rho^{EM}}, \tag{22}$$

with B being the constant value (usually taken as B = 0,5) and ρ^{EM} is the EM mismatch dislocation density, characterized by the equation as [80] [81]:

$$\rho^{EM} = \frac{6v_p}{\pi d^3}\varepsilon\ . \tag{23}$$

The parameter ε is referring to uniform deformation value in the vicinity of the particle. It should be also noted that the residual stress field, due to CTE an EM mismatch in materials with low plasticity, strongly affect crack propagation trajectory, once the crack is running across the vicinity of the reinforcement particle. Depending on the matrix-reinforcement system, the crack tip is either deflected by the present particles, or attracted by them.

3.4 Synergy of strengthening mechanisms

The resulting increase in strength of the material (either metals or MMCs) is an average value of the mentioned strengthening contributions, described in the previous section. In particular cases, additional types of strengthening contributions may be added to the equation (short range ordering, TRIP effect etc.) [71, 76] :

$$\Delta\sigma = \sqrt{(\Delta\sigma_l)^2 + \left(\sigma_y\right)^2 + (\sigma_{Orowan})^2 + (\sigma_{dCTE})^2 + (\sigma_{dEM})^2}\ \ . \tag{24}$$

With the knowledge of the previously mentioned strengthening effects and experimentally determined constants for different materials, it is possible to determine the approximated increase in strength of the composite material. The comparison of the experimentally determined and calculated data for reference MMC is given in Fig. 23. There are still some visible deviations between the experimental and calculated results. Nevertheless, the calculations are particularly useful for predictions of the influence of reinforcement size and type on the resulting strength properties [74], usually serving as a tool for advanced composite design and property adjustment.

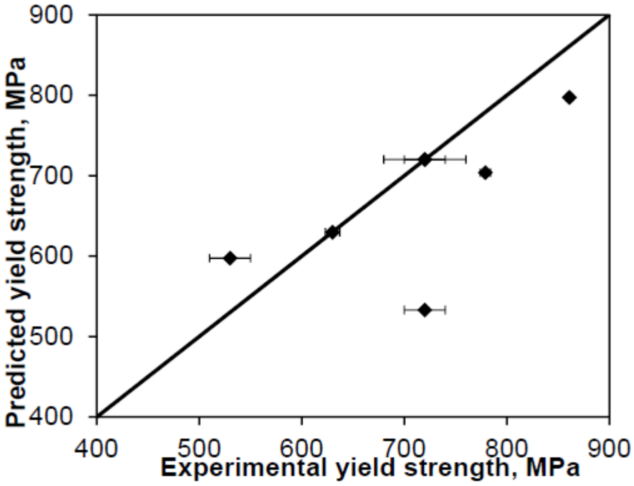

Fig. 23 Comparison of experimental and predicted values of yield strength for Ti/Y_2O_3 nanocomposite [75].

Fig. 24 denotes the different strengthening effect contributions: Hall-Petch strengthening, Orowan strengthening, thermal mismatch strengthening and load bearing effect as a function of reinforcement particle size and volume fraction for Ti / Y_2O_3 composite system. It is evident that the Hall–Petch strengthening due to reduced grain size (equation 12) of the composite is the most prominent factor for reinforcement particles size of 1 μm. The second most pronounced contribution is CTE mismatch, followed by Orowan strengthening and load transfer effect [74]. The total value of strengthening contributions may change for different material systems; however, the comparison of scale of contributions should be applicable generally.

It should be pointed out that all the strengthening mechanisms are dramatically increased with the reinforcement size reduced to 30 nm, as a consequence of the reduced interparticle spacing, considering that a similar volume fraction of reinforcement is present. If the reinforcing particles diameter is decreased, the effect of CTE mismatch and Orowan strengthening is much more pronounced to the point where, at volume fraction of over 0.02, the CTE mismatch contribution prevails over the Hall Petch strengthening contribution. It seems also that, for volume fractions slightly higher than 0.04, the Orowan strengthening contribution outmatches the latter as well.

Therefore, to boost the strengthening, the particles should be as small as possible. In principle, these very same mechanisms also apply for skeletal and fiber composites. Hence the reason for the outbreak of research on composites with nanosized reinforcements in the last decades.

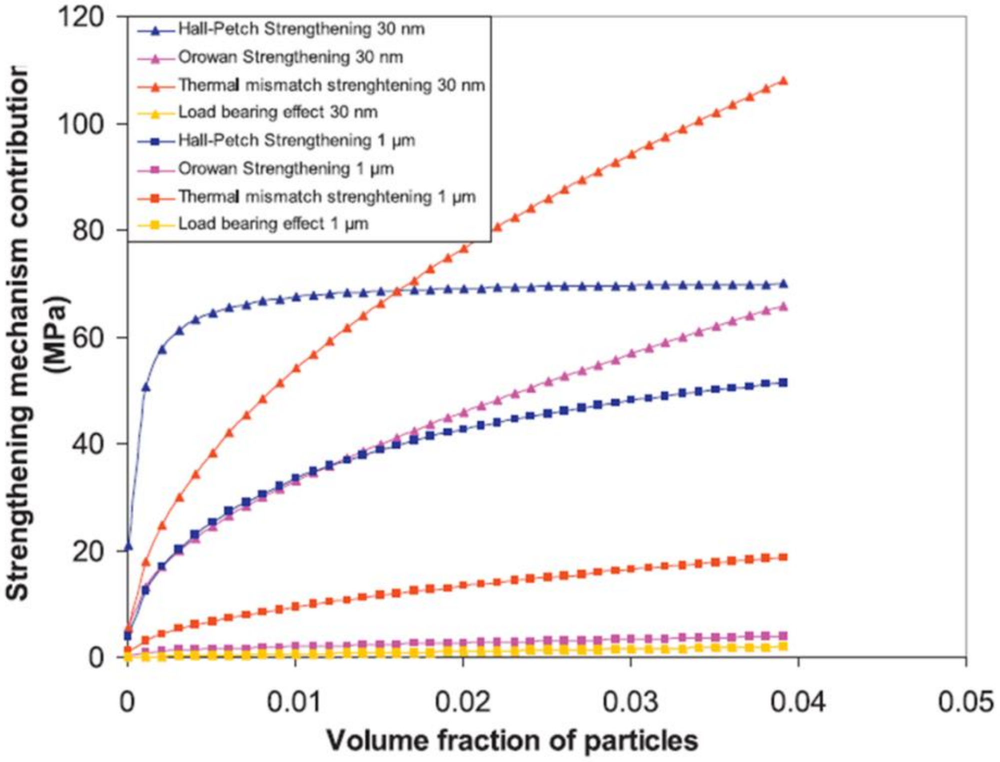

Fig. 24 Calculated influence of size and volume fraction of reinforcement particles on the intensity of different strengthening contributions in Ti/Y_2O_3 composite system [74].

Following the previously mentioned findings, the magnitude of strengthening may be adjusted by setting the volume fraction of the reinforcement, reinforcement grain size, but consequently also the by the reinforcement type – due to the differences in physical properties of the reinforcement in respect to the properties of matrix.

In general, the higher the difference in CTE and EM misfit of the reinforcement and matrix, the higher the strengthening effect will be imposed. The equivalent effect will be evocated by the increase of the difference between processing and operation temperatures – as given by the equation 21.

Fig. 25 displays the effects of the use of different reinforcement particles in Al based composites. The use of B_4C particulate reinforcement, possessing lower CTE and higher EM as compared to Al_2O_3, results in higher strengthening of the material [81]. This is explained by a higher difference between CTE and EM values of B_4C in respect to aluminum matrix.

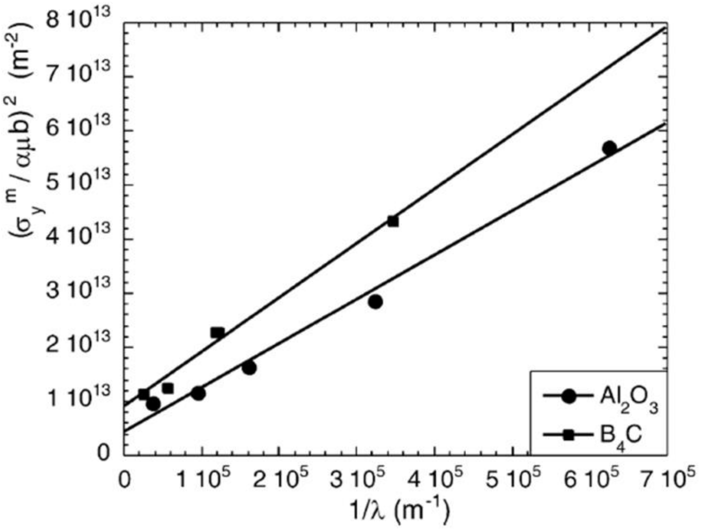

Fig. 25 Influence of the reinforcement fraction given as change in interparticle spacing λ of used ceramic reinforcement on yield strength $\sigma^{m}{}_{y}$ of Al / Al_2O_3 and Al / B_4C composites [80].

The influence of the presence of secondary strengthening phases, either particles or fibers, on the improvement of strength is well documented in scientific publications, as well as in real applications. Another issue that must be accounted for is the resistance of the strengthened materials to crack propagation. While the strength is improved relatively easily, most of the reports are pointing out to the significant reduction of ductility, toughness and fracture properties, for the majority of such materials [82, 83]. Even the reduction of reinforcement size to nano-scale seems to be inefficient, for the preservation of sufficient ductility levels in composites with homogenous dispersion of reinforcement [84]. As a result, the hope of materials science community is switching to advanced composites, with non-homogenous distribution of second phase, nano-laminates, hierarchical structures, etc.; many of them inspired by the natural structures, that will be able to vanquish the traditional ductility/strength trade-off [4, 66]. Selected examples will be further discussed later in the contribution. One of the methods to produce such materials is the powder metallurgy.

4 Powder metallurgy as a way for composites fabrication

Manufacturing processes from powdered materials include, invariably, at least two steps: the first part is powder manufacturing itself and then subsequent powder consolidation, to form bulk materials (or coatings).

A variety of technologies is available for the needs of powder manufacturing, based on mechanical, physical and chemical processes. In the contribution, only the ones directly associated to the dissertation thesis topic will be described.

4.1 Mechanical alloying

Mechanical alloying (MA) is one of the methods that utilizes mechanical principles to process powders. The MA process itself starts with blending of powders (either metallic or ceramic), succeeded by very intensive, long term milling to induce excessive plastic deformation to the powders. Therefore, nanocrystalline materials (with a crystallite size of few nanometers, usually < 100 nm) are usually produced by MA of powder mixtures in this fashion.

Additionally, it has been recognized that this technique can be used to induce chemical displacement reactions in powder mixtures at room temperature or at temperatures comparably lower than normally required to synthesize pure metals [85].

About 1–2 wt. % of a process control agent (PCA - stearic acid, methanol etc..) is frequently added to prevent excessive cold welding amongst the powder particles, as well as sticking of powders to the milling media and milling bowl walls, assuming that the powders of ductile metals are milled.

The powder mixture is milled to the desired condition, which usually refers to the state, with homogenous distribution of alloying elements inside the powder particles, i.e. every single powder particle holds the same chemical composition as the desired material [86]. Mechanical alloying process has many forms and variations; thus the desired powder microstructure depends on the application. For example, if the process is stopped in its early stage, when the powders have a flake morphology, the flakes may be utilized to produce advanced laminated composites [84].

4.1.1 Mechanical alloying principle

During a high energy ball milling process, powder particles are crushed and then cold welded together in the milling bowl walls by repeated impacts of milling balls (Fig. 26) [87].

During every impact of two balls, or ball and milling bowl wall, some powder material is trapped in between. The repeated impacts result in severe plastic deformation of the powders and, therefore, significantly increase of dislocation density. The hardness of the particles is increasing, however their plasticity decreases to a point of total depletion [86]. After this, the particles are unable to withstand the impacts and start to fracture. This results in the creation of new surfaces that enable new cold welding.

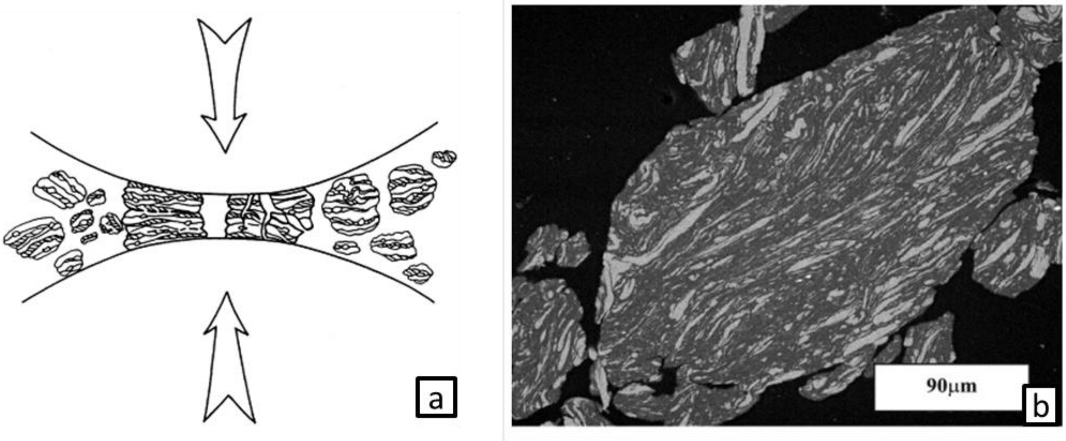

Fig. 26 formation of lamellar powder microstructure in the early stage of mechanical alloying process a) impact of two milling balls flattening and cold welding powder particles b) lamellar microstructure of Ni-Al alloy powder [86].

At the start of the milling of metal materials, powder particles are usually soft, with high ability for plastic deformation and cold welding. In these stage, particles are usually flattened (Fig. 27 part to b) and their size rise significantly (sometimes particles can grow to three times the original size). A lamellar microstructure appears composed of alternating layers of original powders – the first stage of mechanical alloying.

The second stage of the process is characterized by increasing plastic deformation of the powders. This results in the increase in hardness and brittleness, ultimately ending in fracturing of particle (fatigue mechanism). The rate of particle joining is lower than particle fracturing and the average particle size is rapidly reduced (Fig. 27 b to c part). Therefore, the lamellar structure becomes finer. Then, high dislocation density together with the heat generated by impacts cause the increase in diffusion rates. After some time, homogenous dispersion of elements in the powders is achieved, forming homogenous powders with no need for the powders annealing.

Due to the constant ball impacts, the crystallite size of the powder is more and more refined; however, the average particle size is relatively stable. At this time, the process has reached its third, final stage. The particle morphology becomes spherical. The milling time needed to reach this stage is significantly varied, based on the type of mill used as a consequence of different milling energies and intensities. By the intensive milling, it is possible to obtain nano-grained powders with relative ease [85, 88, 89].

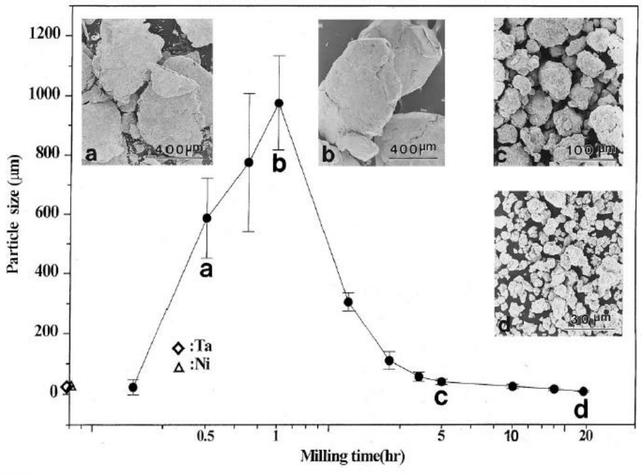

Fig. 27 Typical influence of milling time on powder particle size and morphology [85].

4.1.2 Quantitative description of processes during mechanical milling

The quantification of mechanical milling process is a very challenging issue, due to a great number of parameters with direct influence on final the powder properties, especially considering that even relatively small changes in the applied milling parameters induce significant phase and morphological changes to the powders. One of the most widely used type of milling device used for high energy milling, enabling to control above mentioned parameters, is planetary ball mill.

Milling bowls of planetary mills containing powder materials and milling media are placed on a rotating disc. The centrifugal forces caused by the rotation of the supporting disc and autonomous turning of the bowl act on the milled materials. Since the turning directions of the supporting disc and the vial are opposite, the centrifugal forces alternately are synchronized and opposite as well. Therefore, the milling media and the powder charge roll on the inner wall of the milling bowl, and then are lifted and thrown off across the bowl at high speed (depending on the speed of rotation), as schematically presented in Fig. 28 [85]. This process is repeated continuously. In this way, the process becomes very efficient. The milling speed has to be adjusted accurately; the milling balls are thrown off to powders only at certain speed (they lose contact with inner walls for a moment). Otherwise, the balls will only circulate around the milling jar.

For the description of the milling process, an equation based on the calculation of milling ball speed (V_b in ms^{-1}) is used [87]:

$$V_b = \frac{2\pi}{60}\left[Rp^2\Omega^2 + (R_v - R_b)\omega^2(1 + 2\frac{\omega}{\Omega})\right]^{0.5}, \qquad (24)$$

where R_p, R_v and r_b are the radii of the plate, bowl and ball, respectively. Value ω and Ω are the angular velocity of the bowl and plate on which the vial is fixed respectively, as seen in Fig. 28

Kinetic energy E_b (J) of the single ball is expressed with the equation:

$$E_b = 0.5 m_b v_b^2 \quad , \qquad (25)$$

in the equation, m_b refers to the weight of single milling ball. The end parameter that is used for process quantification is milling intensity I_t (given for 1 gram of milled powder):

$$I_t = \frac{\emptyset E_b N_b tm}{W_p} \quad , \qquad (26)$$

where N_b accounts for number of the milling balls, t_m is total milling time, W_p is a total weight of milled powder. Efficiency factor $\emptyset$ incorporates into the expression the presence of large number of grinding balls in the jar (usually equals 0.95).

In general, the efficiency of milling is better when the milling jar is filled less, due to the restriction of ball movement in cases when too many balls are present inside. Therefore, the milling jar should never be filled completely, usually it’s filled only to 1/3 of the total capacity ($\emptyset$=0.95).

The milling process can be altered by many other parameters (milling atmosphere, process control agent). Nevertheless, the milling intensity describes the milling process sufficiently, and becomes very useful for comparison of milling conditions from an energy point of view. The following calculations were successfully used for Fritsch Pulverisette type mills [88].

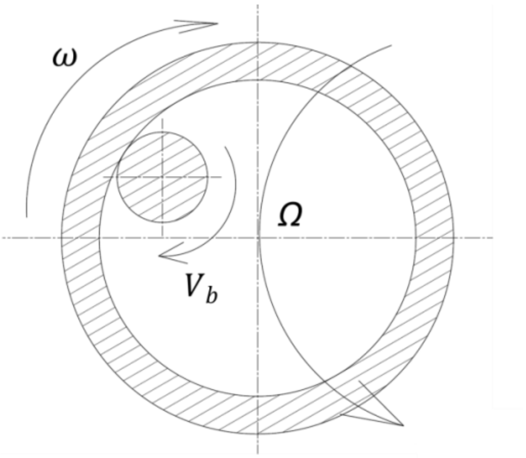

Fig. 28 Principle of planetary ball mill geometry and parameters of milling kinetics.

4.2 Sintering with simultaneous application of pressure

For the preparation of the bulk structural components, a proper densification technology must be selected with respect to the desired properties. If the aim is the achievement of full density (or near full density), the use of densification process that includes the application of external pressure and high temperature is necessary [7].

One of such processes which fulfills this condition appears to be Spark Plasma Sintering (SPS). It is a powder consolidation technology, based on the simultaneous application of pressure and pulse (on-off) of direct electrical current. The combination of a very rapid heating by Joules heat generated from electric current and high pressure (up to 100 MPa), enables very high densification rates (usually full density is achieved in minutes compared to tens of hours in conventional pressureless sintering or hours in hot pressing). Such high densification rate prevents the excessive diffusion-driven grain growth during the sintering. The SPS process is very efficient for production of extremely fine-grained materials, as opposed to conventional sintering, where excessive grain growth occurs [90, 91]. To certain point it is even possible to retain fine grained microstructure of the mechanically milled powders. Over the years, SPS has proven capable of production of materials with special properties such as dispersion strengthened alloys, nano-grained ceramic as well as powder metallurgical HEAs [92-94].

SPS process flow

Fig. 29 depicts a sketch of the SPS process. The powder is placed in a die with desired dimensions. In order to make the process functional, the die must be made from a material at least partially electrically conductive and mechanically resilient enough to withstand the application of pressure - the most commonly used material is graphite. To prevent powder contamination by carbon or any undemand reactions, a protective graphite foil covered with boron nitride coating is inserted between the die walls and the powder charge.

With the upper and lower punch, the force is applied to the powders during the whole process. At the same time, a pulsed direct current is generated, flowing through both punches of the conductive die into the powders. The heat is generated in the die by the electrical loses due to die resistance. Then, the powders are heated up by heat conduction from the hot die and also by electric current in case of conductive charge. The highest level of electric resistance (higher the resistance is, the higher are electric losses and generated heat) is on the particles contacts - the same principle that is applied in resistance welding. The cause of this is the extreme increase of electric current density on particles contacts due to very small surface of contact areas. The presence of an oxide layer on all surfaces of metals exposed to air is further increasing the electric resistance. This phenomenon causes the prevalent heating of particle contact areas and subsequent particle joining with increased kinetics [91].

An external thermocouple is connected directly to the die, which serves for an accurate process of monitoring and control.

The whole setup is placed in sealed a vacuum chamber. Special gasses may be introduced to the chamber in the case of special processing requirements (e.g. nitrogen, argon etc.).

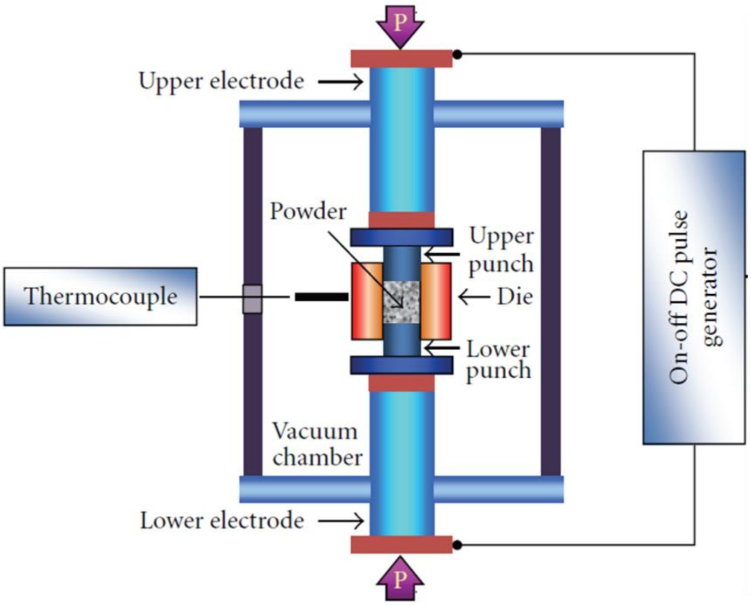

Fig. 29 – Spark plasma sintering process schematics [91].

4.3 Selected advanced PM composites

One of the uppermost advantages of powder metallurgy is its ability to produce composite bulk materials, which would not be possible to manufacture in any other way [7, 86]. After a careful selection of the used materials, utilizing previously mentioned strengthening principles and new design strategies, and bearing in mind processing technology limitations, advanced materials with exceptional properties can be manufactured. In the following section, selected examples will be presented.

Al/Al_2O_3 nanolaminate

One of the most intriguing examples of the successful advanced composite production by PM is the Al/Al_2O_3 nanolaminates**.** They were be prepared by the method of flake powder metallurgy, as a result of bio-inspired design strategy. This Al-based laminated composite achieved an impressive combination of strength and ductility (ultimate tensile strength of 276 MPa with 23% total elongation, with density around 2.3 g cm^{-3}), measured in the direction parallel to lamination [84]. The produced composite microstructure has been inspired by the arrangement of collagen and lime in mollusk shells. The manufacturing procedure is explained in Fig. 30. The powders of pure aluminum with very narrow size distribution and almost spherical morphology were milled for 2 hours. Due to the impacts of milling balls, the powder particles got flattened to the shape of flakes (hence the reason for the term flake powder metallurgy). This method was named as micro-rolling. Stearic acid was added to the powders to prevent cold welding of the flakes, due to very soft nature of the pure aluminum powders. Powders were then taken out of the milling bowl and annealed on the air. The stearic acid evaporated and native alumina (Al_2O_3) layer was formed on the particles surfaces, as a result of natural aluminum affinity towards oxygen. Powders were the cold pressed in steel die with uniaxial pressure. The flakes powders naturally arranged themselves to the forms of overlapping layers with longest dimension of flakes perpendicular to the pressing axis (Fig. 31). After sintering, the layered microstructure of alternating layers of aluminum and alumina is retained, which possesses the substantial mechanical strength and natural ability to deflect propagating cracks – significantly improving the fracture toughness of the structure.

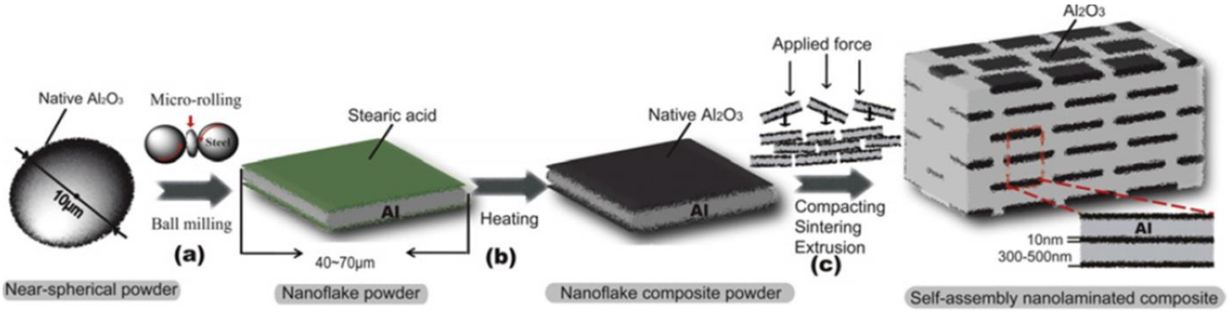

Fig. 30 Manufacturing process of nano-laminated composite of Al/Al_2O_3 a) milling in ball mill to obtain flake powder morphology; b) creation of native Al_2O_3 layer by heating; c) densification by uni-axial pressure and resulting laminated microstructure [84].

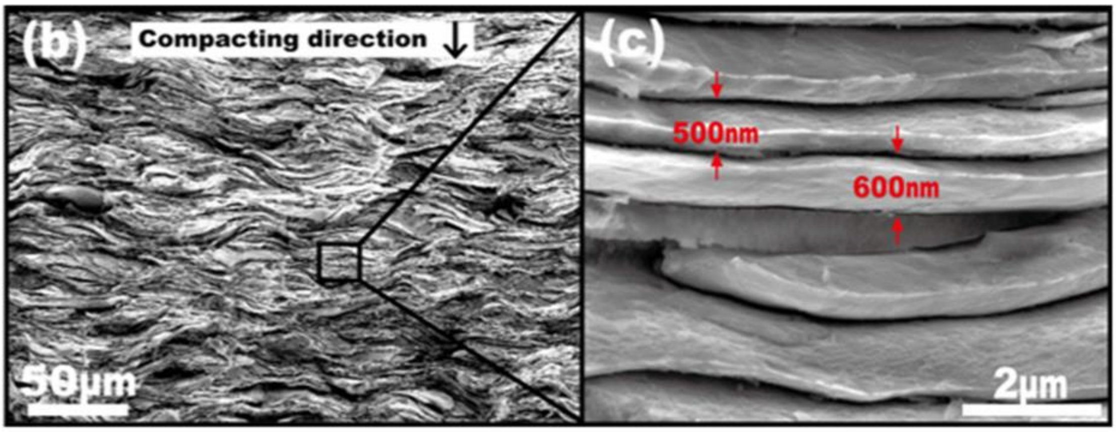

Fig. 31 natural arrangement of flakes in uniaxially pressed compacts of Al/Al_2O_3 composite [84].

Composites possessing trimodal grain size

Trimodal grain size (TGS) composites are advanced materials designed to obtain a good combination of mechanical properties - strength and ductility ratios. The concept of TGS composite is relatively new, but very interesting for anticipated industrial applications. The main reason lies in the vast possibility of properties' adjustment by simple changes in the processing conditions altering the hierarchical arrangement of different grain sized areas [95, 96]. The concept is mimicking the natural materials in the hierarchical arrangement components. In the recent commercially produced metallic materials, the microstructures are composed of many different phases (solid solutions, carbides, intermetallics etc.). As opposed to that, in natural materials, the supporting parts are composed usually of only two basic components (for example hydroxyapatite and collagen in bones) arranged in a number of different forms [67]. This arrangement determines the properties.

Al/B_4C trimodal composites consisting of areas with nanograin, coarse grain and ceramic reinforcement areas have been manufactured by Ye et al. [96].

The composites were manufactured by extrusion of three different types of powders. Normal high purity aluminum powders, nano-grain sized powders made by high energy cryo - milling of pure aluminum powders and composite powders manufactured by milling of B_4C ceramic and aluminum together. In this fashion, coarse grains areas, nano-grained areas and reinforced areas have been formed within one bulk sample respectively, as seen in Fig. 32. The material has a good mechanical strength, due to the presence of nano grains and ceramic reinforcement, as well as good plastic properties as a consequence of toughening effect of softer, coarse grained areas. The trimodal composite exhibited better tensile strength and elongation, when compared with the bulk sample manufactured in same condition, but with homogenous reinforcement dispersion. The properties are so satisfying that the composite is already experimentally used for ballistic armor plates [95].

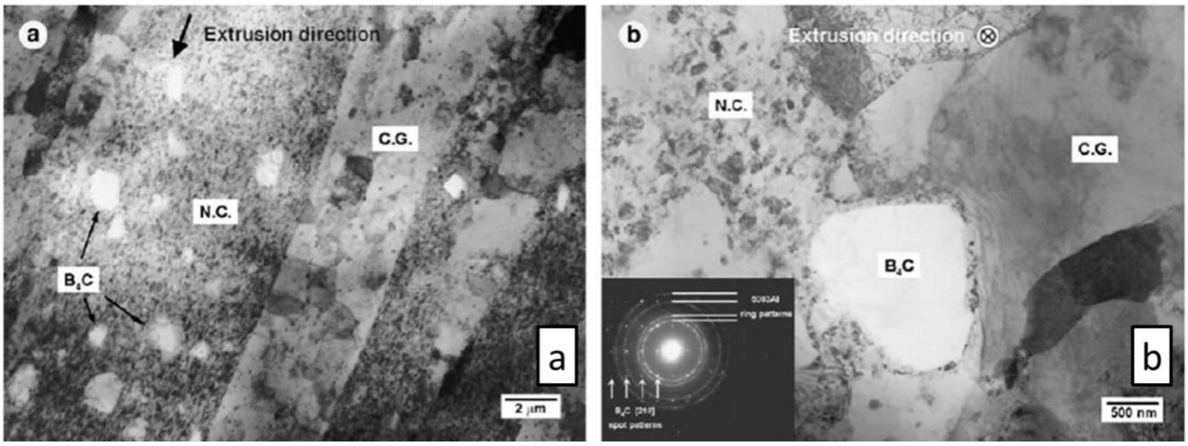

Fig. 32 microstructure of Al/ B_4C composite a) perpendicular to the extrusion direction b) parallel to extrusion direction [96].

4.4 HEAs produced by combination of MA + SPS

There are a few examples where mechanical alloying and spark plasma sintering have been utilized for the production of HEAs, with good mechanical properties, mostly as a consequence of grain refined nature retained after the sintering. The materials always exhibit high compressive strengths and hardness, however lack in plastic properties [51, 97].

Up to date, the best properties have been achieved by $Al_{0.6}CoNiFeTi_{0.4}$ and $Al_{0.7}FeNiCrCo_{0.3}$ alloys; compressive stress-strain curves displayed is Fig. 33 [92, 98]. $Al_{0.6}CoNiFeTi_{0.4}$ alloy reaches 2732 MPa yield strength, compressive strength of 3172 MPa with total strain of $\varepsilon = 10.2$ %. The measured hardness is as high as 721 HV. $Al_{0.7}FeNiCrCo_{0.3}$ alloy exhibits slightly lower properties, namely 2033 MPa yield strength, compressive strength of 2635 MPa with $\varepsilon = 8.12$ % strain. The measured hardness is lower again - 624 HV. The microstructure of both alloys is composed from combination of FCC solid solution and ordered B2 phase. In the $Al_{0.6}CoNiFeTi_{0.4}$ alloy, the presence of nano-twins within the FCC grains has been detected – possibly the source of comparably better properties of this alloy, as compared to $Al_{0.7}FeNiCrCo_{0.3}$. As mentioned before, the high strength and hardness are a consequence of extremely refined grain size that was retained from the mechanical alloying process (powders were milled for 45 hours).

In both cases, the fracture behavior was strictly brittle with intergranular crack propagation. This may present a problem for HEAs application as structural materials, where ductility is a critically important property for manufacturing of damage tolerant structures, e.g. structures that will fail in a predictable and relatively reliable manner, in case of overload. As such, there is a need to produce HEA with sufficient ductility values. So far, this has not been achieved to the author's best knowledge in materials produced by PM.

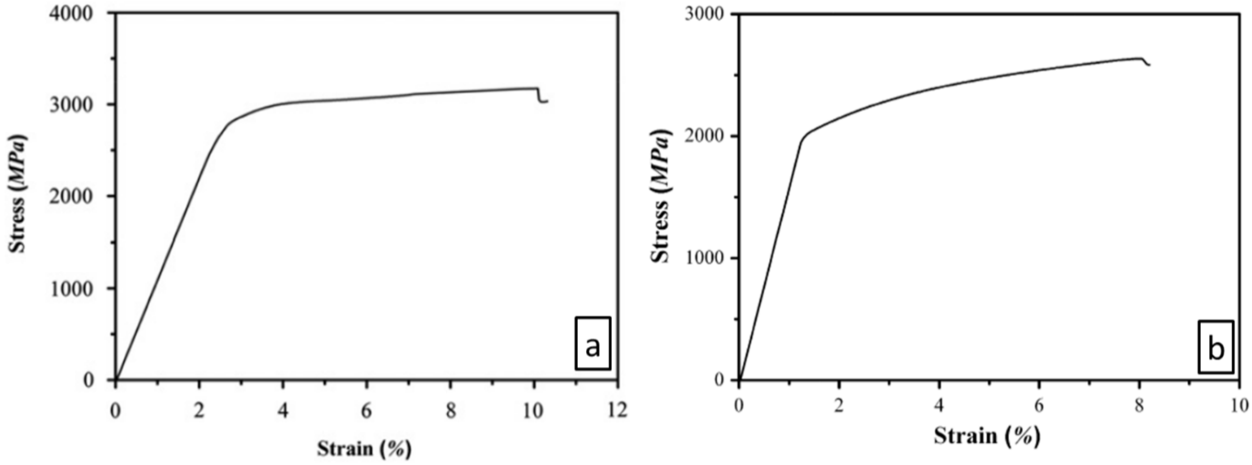

Fig. 33 - The records from compressive tests on cylindrical specimens a) alloy $Al_{0.6}CoNiFeTi_{0.4}$; b) alloy $Al_{0.7}FeNiCrCo_{0.3}$ [92, 98].

5 Aim of the work

Bearing a wide variety of interesting properties, HEAs are presumably perspective materials for several applications. In most cases, these new materials are being manufactured by traditional casting procedures and studied in as cast state. However, due to relatively complicated chemical compositions, additional issues with casting may arise (elements segregation, structural inhomogeneity, etc.). For instance, it is extremely complicated to prepare alloys containing high amounts of aluminum and chromium (melting point difference 1247 ºC). as excessive evaporation of aluminum can take place; consequently, the final chemical composition of the material may be significantly altered (especially in industrial scale production in induction or arc melting furnaces).

The powder metallurgy route may be an alternative way of production of various HEAs, with perfect chemical homogeneity and the absence of casting defects. Additionally, powder metallurgy processing would enable a very feasible way of MMCs manufacturing with HEAs or MEAs as the matrix materials. Therefore, the objectives of the presented dissertation thesis were given as:

1. Investigate the aspects of mechanical alloying process for production of HEA powders;
2. Confirm the possibility of production of ductile bulk HEAs and MEAs by powder metallurgy route, especially by the combination of mechanical alloying and spark plasma sintering;
3. Microstructural and phase characterization of the produced materials;
4. Characterization of basic mechanical properties of bulk materials (hardness, strength, ductility);
5. Explore the possibility of MMCs production with previously obtained HEAs or MEAs as a matrix material.

6 Experimental

6.1 Precursor powders

All the powders in this study, utilized for the preparation of bulk materials, were prepared from elemental powders by mechanical alloying process.

The feedstock (elemental) powders were supplied by GTV VerschleibSchutz GmbH, Germany, and Sigma-Aldrich Corporation, United States. Details of the feedstock powder morphologies and chemical compositions are presented below:

Chromium

Chromium powders with particle size under 44 μm have been used. The powder morphology is presented in Fig. 34. It seems that the powder was manufactured by mechanical crushing method. According to EDS analysis, the powder contains 96.8 at. % of Cr, 1.68 at. % of Al and 1.12 at. % of Fe. The measured purity is sufficient for the needs of mechanical alloying.

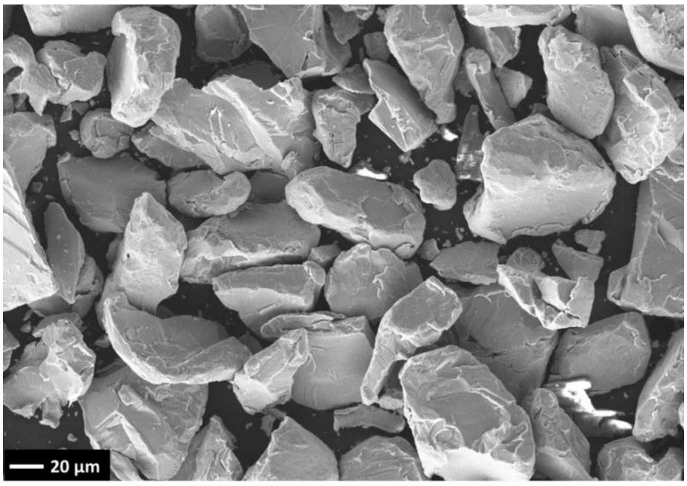

Fig. 34 Morphology of the used Cr powder.

Iron

The iron powder used for the experiments was manufactured by Sigma Aldrich through carbonyl reduction. Its morphology is presented in Fig. 35. It has almost perfect spherical morphology with particle size under 5 μm. The purity measured by EDS method was 100 at.% Fe.

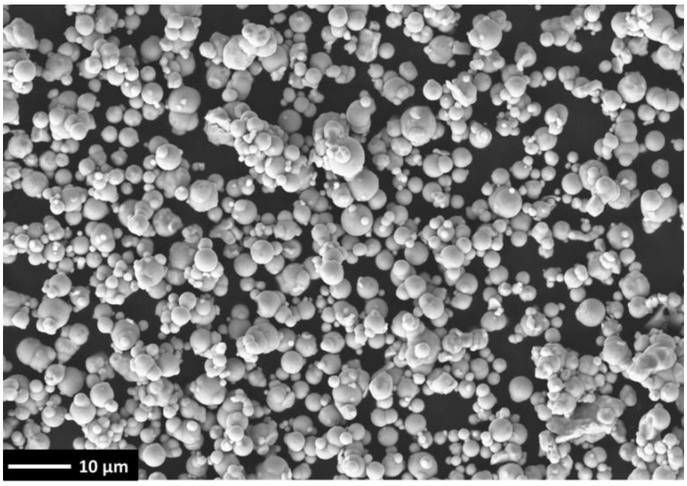

Fig. 35 Morphology of the used Fe powder.

Nickel

The nickel powder utilized in the study was manufactured by GTV VerschleibSchutz GmbH Germany by inert gas atomization. The almost perfect spherical morphology is presented in Fig. 36. Particle's size is in the range from 15 to 53 μm with 100 at. % Ni of chemical purity, as measured by EDS.

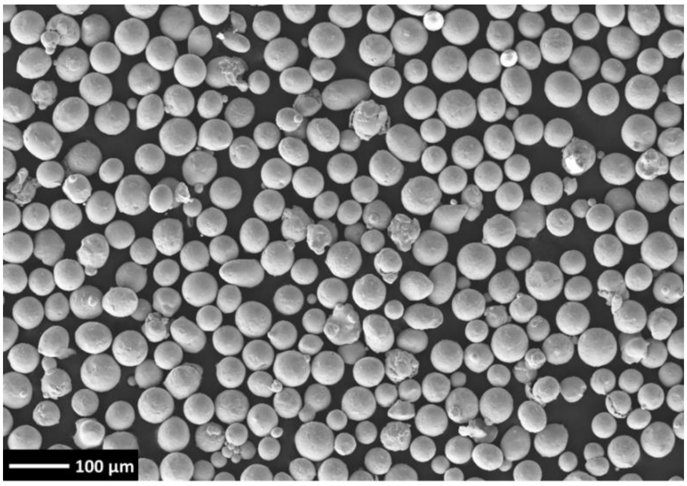

Fig. 36 Morphology of the used Ni powder.

Cobalt

The cobalt powder used in the study was manufactured by Sigma Aldrich, with particle size under 150 μm. The morphology of the powder presented in Fig. 37 reveals that the powder is composed of agglomerated smaller particles. Therefore, the powder was manufactured most probably by chemical reduction process. According to EDS analysis, it contains 99.81 at. % of cobalt and 0.19 at. % of Si.

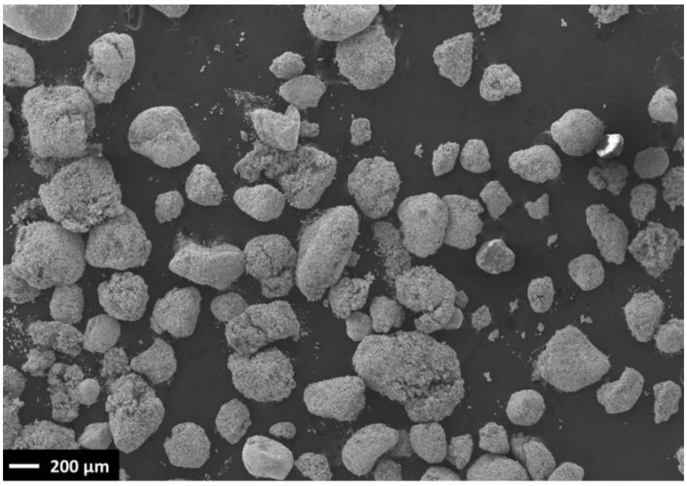

Fig. 37 Morphology of the used Co powder

Titanium

The titanium powder was produced by Sigma Aldrich, with particle size under 44 μm and irregular morphology, presented in Fig. 38. The powder contains 100 at. % of Ti, as measured by EDS analysis.

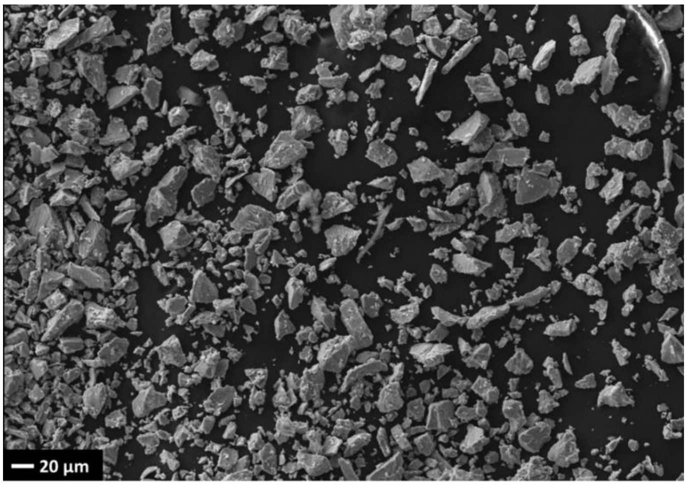

Fig. 38 Morphology of the used Ti powder.

Aluminum

The aluminum powder was manufactured by GTV company by gas atomization process. The particle size is under 44 µm. The purity of the powder according to EDS is 100 at. % of Al. However, a slight oxidation of the powder has been revealed by EDS mapping.

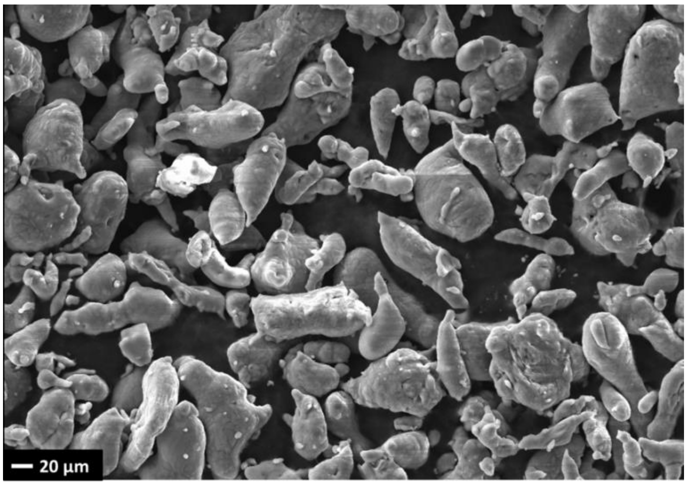

Fig. 39 Morphology of the used Al powder.

Boron carbide – B_4C

Boron carbide utilized for production of experimental composite materials was supplied by Sigma Aldrich. The powder has irregular morphology, bearing particle size bellow 5 µm (provided in Fig. 40).

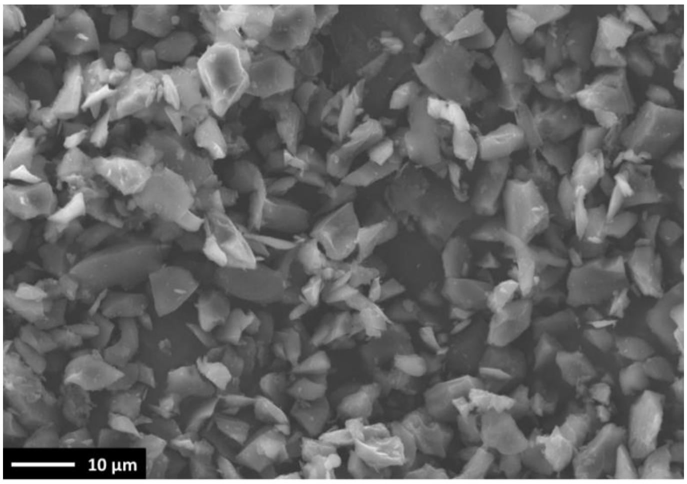

Fig. 40 Morphology of the used B_4C powder.

6.2 Experimental materials preparation

All the experimental powder materials used in this study were prepared by feedstock powder processing by mechanical alloying. The process was carried out in an in-house made EN 1.2379 (X120CrMoV 12-1) hardened tool steel bowl. Into the bowl, the powders were sealed together with hardened EN 1.3505 (100Cr6) steel balls. The sealed vial was, then, placed in a high energy planetary ball milling (Fritsch Pulverisette 6). After the milling, the powders were removed from the milling vial and dried in air. The image of the milling experimental setup is provided in Fig. 41. The mechanically alloyed powders were subsequently densified by SPS technology to obtain bulk alloy samples. The parameters of mechanical alloying process and the SPS device and parameters utilized for the preparation of the experimental materials were different for different compositions, and will be described separately in the following section.

Fig. 41 - Ball milling equipment a) planetary ball mill Fritsch Pulverisette 6 (milling bowl denoted by red arrow) b) detail of milling bowl.

6.2.1 Mechanical alloying process parameters evaluation

As the first step of the study, the necessity to evaluate the influence of different milling parameters on the resulting powder properties has arisen. The main evaluation parameters were the powder homogeneity and morphology. Therefore, a set of different milling parameters has been chosen to apply on elemental powders mixed with nominal composition of AlCoCrFeNiTi$_{0.5}$ (in atomic proportion). The alloy composition AlCoCrFeNiTi$_{0.5}$ was chosen with the consideration of possessing a good combination of strength and ductility, reported in the literature [37]. Elemental powders of Fe, Ni, Cr, Al, Co and Ti were mechanically alloyed under Ar atmosphere (4.6 purity – 99.996 % Ar). The total powder weight was 30 g for all milling procedures, while 2 ml of methanol was poured to the powders to prevent excessive cold welding. The milling plan of the powders is presented in Table 2. Eight separate milling procedures have been carried out, with two different milling speeds (RPM – revolutions per minute of turning speed), two different milling times and two milling ball sizes. Additional milling procedure, designated as milling number 9, has been performed later in the study, in order to evaluate the influence of methanol presence and it will be discussed separately.

Table 2 milling conditions and calculated milling parameters.

Milling number	**RPM**	**BPR**	**Time**	**Ball D [mm]**	**PCA**	**Mil. Intensity I_t [J/g]**
1	250	1:10	10	10	Methanol	**834**
2	250	1:10	24	10	Methanol	**2002**
3	250	1:10	10	15	Methanol	**784**
4	250	1:10	24	15	Methanol	**1883**
5	400	1:10	10	10	Methanol	**2135**
6	400	1:10	24	10	Methanol	**5125**
7	400	1:10	10	15	Methanol	**2009**
8	400	1:10	24	15	Methanol	**4822**
9	400	1:10	24	15	**-**	**4822**

6.2.2 AlCoCrFeNiTi$_{0.5}$ alloy preparation

The bulk alloys were prepared from AlCoCrFeNiTi$_{0.5}$ alloy powders by subsequent SPS densification. The chosen powders milled with presented conditions were utilized:

- Milling number 4 - 250 RPM for 24h and 15mm balls designated as $AlCoCrFeNiTi_{0.5}$ alloy A
- Milling number 8 - 400 RPM for 24h and 15mm balls designated as $AlCoCrFeNiTi_{0.5}$ alloy B
- Milling number 9 - 400 RPM for 24h and 15mm balls without methanol designated as $AlCoCrFeNiTi_{0.5}$ alloy C

Powders milled with a set of three different conditions were used for densification, to observe the differences in properties of identical materials (chemically), induced by the varied milling conditions. Densification by SPS (Thermal Technology LSS model 10-4) in 30mm graphite die was conducted at the Institute of Plasma Physics, Czech Academy of Sciences. For easy removal graphite foils were placed between powders and the die walls. The temperature of 1100 ºC with 60 MPa pressure and 8 minutes soaking time were used. A typical process parameters diagram can be seen in Fig. 42. The proper densification conditions have been selected according to previous test runs, with the aim to obtain 100 % density and retain fine grain sizes. Temperature profile during sintering and piston position were observed as indication of densification progress (the lower the piston is, the smaller space the powders are occupying, i.e. the higher the sample density). The heating from room temperature to 1000 ºC was performed with a heating rate of 100 ºC.min^{-1}. From 1000 ºC to 1100 ºC, the heating rate was then reduced to 50 ºC min^{-1} to ensure the best possible densification conditions. The resulting products were cylinders with the diameter of 30mm and approximately 6 mm of height.

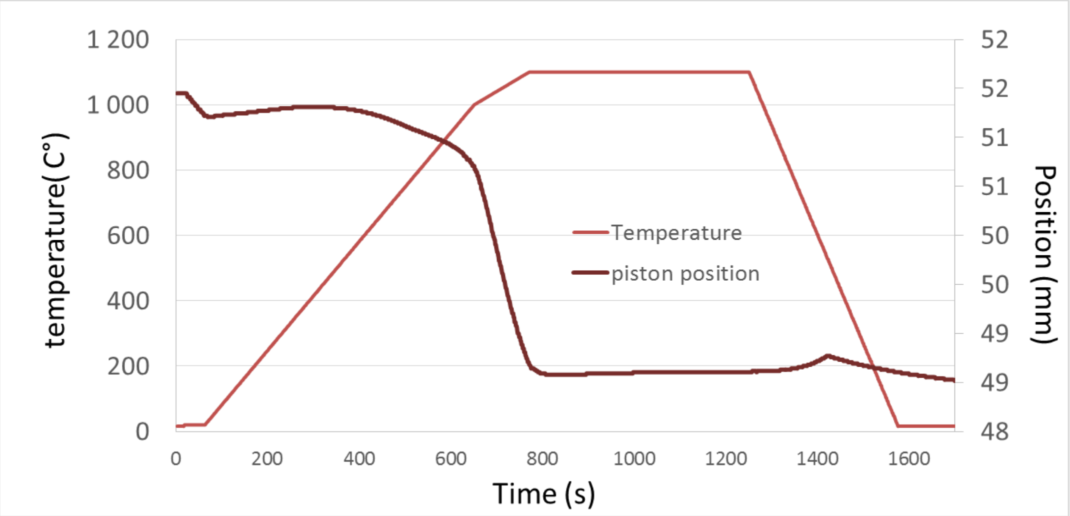

Fig. 42 Typical process diagram of SPS densification of the powders (densification rate visible from piston position).

6.2.3 $Co_{1.5}Ni_{1.5}CrFeTi_{0.5}$ alloy preparation

Elemental powders of Co, Cr, Ni, Fe, and Ti were mixed in desired atomic ratios and mechanically alloyed. A mixture of 15 mm and 20 mm balls in 10:1 total ball to powder weight ratio was used and milled with high purity nitrogen (6.0) atmosphere for the powder surface protection against oxidation during milling. Nitrogen gas was utilized as compared to argon used for $AlCoCrFeNiTi_{0.5}$ alloys due to higher available purity Nitrogen 6.0 as compared to argon 4.6. The total amount of densified powder was 100 g. The powders were dry milled (without the addition of any organic process control agent to prevent formation of carbides) at speeds of 250 rpm for 30 hours. Consequently, additional 2 hours of wet milling in toluene was carried out. Even through it could cause small carbon contamination, 2 hours of wet milling was absolutely necessary to remove the powder stuck to the milling media and decrease its particle size. Milling conditions have been chosen after a previous optimization procedure.

The ball milled powders were subsequently consolidated in RHP Technology GmbH by SPS in a 50 mm-inner-diameter graphite die at 1150 °C for 10 minutes. The sintering was performed in vacuum (residual cell pressure < 8 Pa) at a constant pressure of 30 MPa. For an easy removal and reduction of a potential surface contamination, graphite foils coated with boron nitride layer were placed between the die and the powders. The sintering had been controlled by a preset heating program. The heating from RT to 1000 °C was done at a heating rate of 100 °C min^{-1} , with 15 minutes' dwell time at temperature of 550 °C, to ensure removal of any prospective organic compounds,e.g. residual toluene from the wet milling. From 1000 °C to 1100 °C, the heating rate was reduced to 50 °C min^{-1} and further to 20 °C min^{-1} in the final sintering range of 1100 – 1150 °C to ensure the best possible densification conditions. The process parameters diagram can be seen in Fig. 43. After sintering, the pressure from pistons and the electric current were removed and the whole setup was left to cool down to RT in the vacuum encapsulation. The resulting specimen was a 50 mm diameter cylinder with thickness of 7 mm.

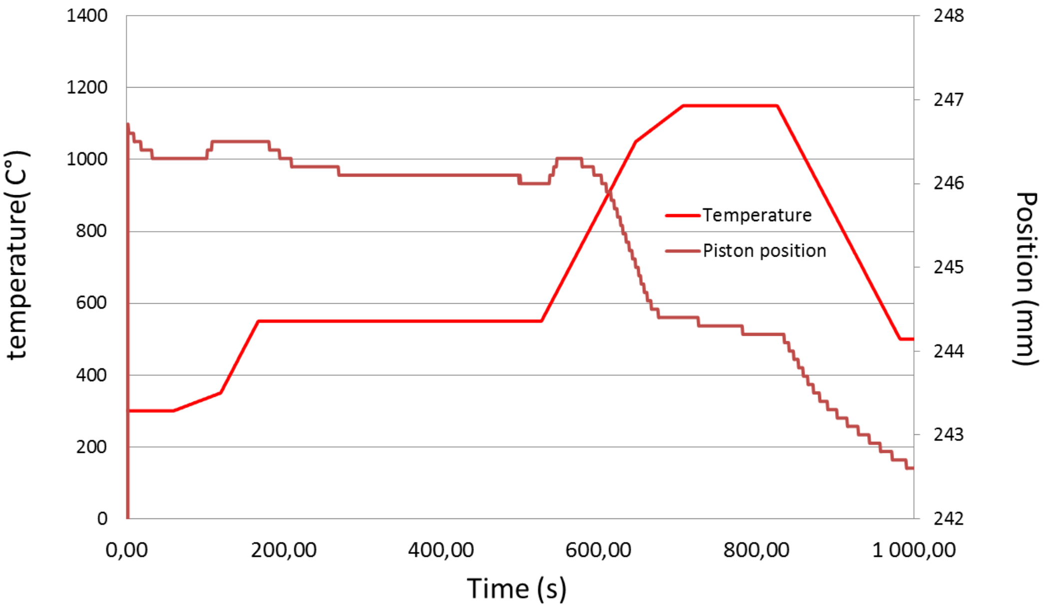

Fig. 43 $Co_{1.5}Ni_{1.5}CrFeTi_{0.5}$ alloy process diagram from SPS densification (densification rate visible from piston position).

6.2.4 CoCrNi alloy preparation

The composition of the investigated alloy was CoCrNi (expressed in atomic ratio). A mixture of 15 mm and 20 mm milling balls, with 10:1 total ball to powder weight ratio was used. High purity nitrogen atmosphere (6.0) was utilized for powder protection. Milling was conducted at a speed of 250 rpm for 30 h. To remove the powder stuck to the milling balls surfaces, toluene was further added and such wet milling has been performed for additional 5 hours. The powders were then removed from the milling bowl and dried in air. A longer milling time in toluene was needed as compared to 2 hours for $Co_{1.5}Ni_{1.5}CrFeTi_{0.5}$ alloy, as there were significantly more powders stuck to milling bowl walls in case of CoCrNi alloy.

The ball milled powders were subsequently consolidated by SPS in RHP-Technology GmbH by SPS in 50 mm inner diameter graphite die at 1180 °C for 10 minutes. The sintering was performed in a vacuum atmosphere with a constant piston pressure of 30 MPa. The heating from room temperature to 1000 °C was done with the heating rate of 100 °C min^{-1} with 10 minutes' dwell time at a temperature of 550 °C. The dwell time was included in order to remove any organic compounds potentially present in the powders – toluene used in the milling. From 1000 °C to 1100 °C, the heating rate was reduced to 50 °C.min-1 and further to 20 °C min^{-1} in the final sintering range of 1100 °C - 1180 °C.

After the final sintering dwell time, the pressure from pistons was released, the electric current was cut-off and the set up was left to slowly cool down in the evacuated chamber. In this way, cylindrical sample with 50 mm diameter and thickness of 6 mm was prepared.

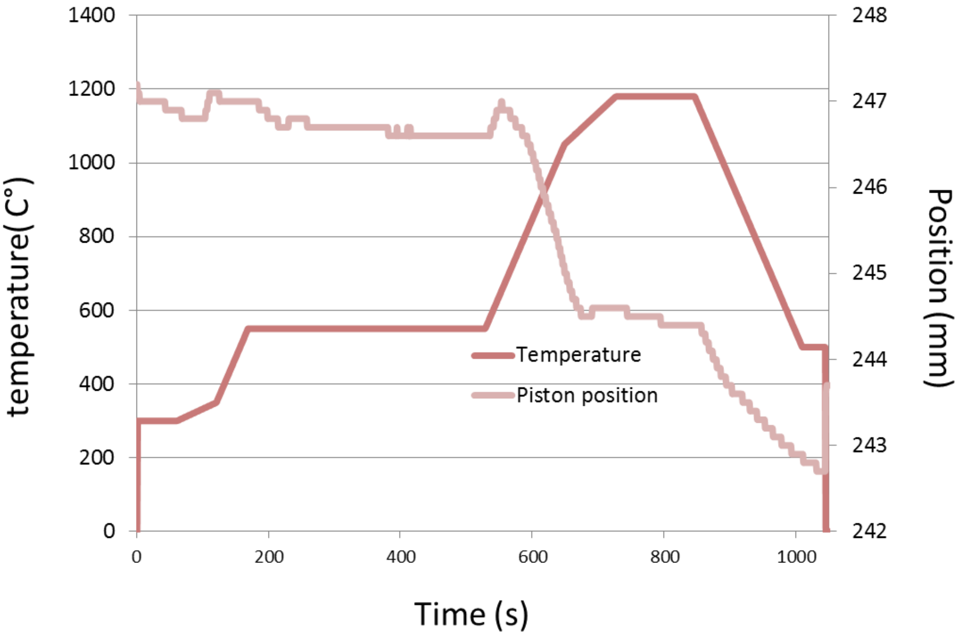

Fig. 44 CoCrNi alloy process diagram from SPS densification (densification rate visible from piston position).

6.2.5 CoCrNi / B_4C composite

The composition of the investigated alloy was CoCrNi (expressed in atomic ratio) with 7.5 volume % of B_4C introduced into the milling bowl. A mixture of 15 mm and 20 mm milling balls, 10:1 total ball to powder weight ratio, was used. High purity nitrogen atmosphere (6.0 – 99.9999%) was utilized for powder protection. The milling was conducted at a speed of 250 rpm for 35 h. To remove the powder stuck to the milling balls surfaces, toluene was further added and such wet milling has been performed for additional 15 minutes. The powders were, then, removed from the milling bowl and dried in air. The consecutive densification has been performed in Sumitomo Coal Mining, Dr. Sinter SPS machine in Central European Institute of Technology (CEITEC). For an easy removal, graphite foils were placed between the powders and die walls. The temperature of 950ºC with 60 MPa pressure and 10 minutes soaking time were used for the densification. Heating rate of 50 ºC min^{-1} has been utilized. The process diagram is not shown in Fig. 45. The piston position was not recorded, due to the error of the machine software.

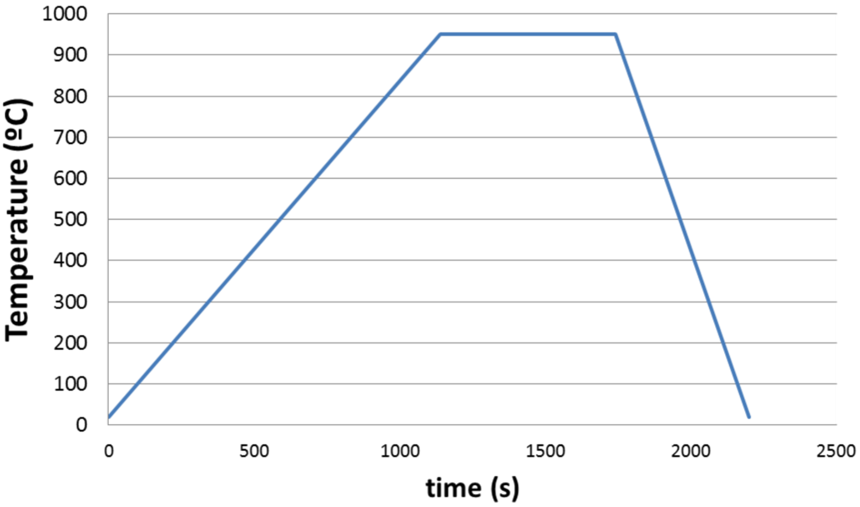

Fig. 45 CoCrNi / B_4C composite process diagram from SPS densification.

6.3 Characterization methods

Preparation of bulk and powder samples for microstructural observation was mostly carried out by hot mounting in a polymeric resin. The samples were then mechanically ground with SiC emery papers of different particles sizes down to 1200 grit size. Subsequently, the samples were polished using diamond paste with 3 µm and 1 µm particle size. The last step of sample preparation was performed by mechano-chemical polishing, using Struers OPS suspension, to obtain perfectly flat, scratch free surfaces.

Scanning electron microscopy (SEM)

The scanning electron microscope (SEM) characterization of powders, bulk materials, and fracture surfaces after the mechanical testing was carried out using Zeiss Ultra Plus microscope at accelerating voltages of 10 kV and 20kV in secondary and backscattered electrons (BSE) mode respectively. Electron channeling contrast imaging (ECCI) mode of BSE was used in cases of single phased microstructures, for plastically deformed materials. Electron backscattered diffraction (EBSD) mode was used for the evaluation of grain size of single phase microstructures, as well as to obtain the lattice parameters of selected phases.

Energy dispersive X-ray microanalysis studies (EDS) have been performed to evaluate the chemical composition of the materials.

X-ray diffraction analysis (XRD)

X-ray diffraction analysis (XRD) of the phase composition of the materials was carried out using different diffractometers operated at 40 kV with Cu K_α radiation, Cr K_α and Co K_α radiation (the type of radiation depended on the machine used, which changed during the study). Most of the results were characterized by Philips X´Pert Pro diffractometer machine. Subsequent XRD patterns analysis was performed in X´Pert High Score Plus software. Rietveld analyses have been performed on selected patterns to calculate the amount of phases. The different diffractometers were used as a consequence of the works being done at different institutes, or changes on the used equipment throughout the four years of the study. As the software utilized for the analyses is able to take into account the changes in the used equipment, the performed analyses were always fully comparable.

Transmission electron microscopy (TEM)

Thin foil specimens were prepared for Transmission Electron Microscopy (TEM) observation of microstructures and Selected Area Electron Diffraction (SAED) analysis by material grinding and Precision Ion Polishing System (PIPS). The observation was carried out using Jeol 2200 microscopes in Institute of Physics of Materials, Czech Academy of Sciences and Department of Physics of Materials, Faculty of Mathematics and Physics of Charles University.

Differential scanning calorimetry (DSC)

Differential scanning calorimetry (DSC) measurements were performed with Netzsch Jupiter® TGA-DSC and Setaram Set Sys DSC devices, with 10 K min^{-1} heating and cooling rate in protective argon atmosphere, on samples with dimension approximately 2 × 2 × 2 mm. The analysis has been performed in Institute of Materials Sciences and Enginnering, Brno University of Technology and Institute of Manufacturing Technology, Chalmers University of Technology in Goteborg, Sweden.

Thermo-mechanical analysis

For the CoCrNi alloy, a thermo-mechanical analysis (TMA) - consisting of a measurement of one directional dimensional change of the tested sample, with heating and cooling rates of 5 °C.min^{-1} from 20 °C to 1100 °C has been performed for the observation of phase changes and for the measurement of the coefficient of thermal expansion (CTE), respectively.

Indentation experiments

Measurement of Vickers hardness, according to ISO 6507-1:2005, throughout the whole study was carried out using LECO LM 274 AT hardness tester, with applied loads of 0.2 kg and 0.3 kg. The presented values are an average of at least 7 measurements.

Nanoindentation experiments were performed using a Nanoindenter G 200 machine with the Berkovich indenter in individual indentations mode at Institute of Materials, Slovak Academy of Sciences in Kosice, Slovakia. The samples were measured with a maximum force of 50 mN, with time to load/unload of 15 s and hold period of 10 s.

Elastic modulus determination

The elastic modulus measurements were carried out on samples produced for bending tests, according to ASTM E 1876-09 standard, by impulse excitation of vibration on Grindosonic MK5i machine, with 10 measurements or by resonant ultrasound spectroscopy (RUS) method [99] for. Resonant frequencies and the corresponding modal shapes of the first 20 resonant modes of the free elastic vibrations of the bar were recorded. The RUS spectrum was, then, complemented by pulse-echo measurements of longitudinal wave velocity in the direction perpendicular to the largest face of the samples.

Bending test

The room temperature bending strength (R_{mb}) was, then, measured using three-point bending jig on Zwick Z020 universal tensile test machine, with the loading span of 18 mm and a crosshead speed of 1 mm min^{-1}. The samples had nominal dimensions of 22 × 6 × 4 mm. To decrease the influence of surface roughness on the measured values, the samples were polished to mirror finish. The 4 × 22 mm face of these samples corresponded to the direction perpendicular to the SPS pressing direction. The value of bending stress R_b were calculated from the applied load, considering the dimension of the samples.

Tensile test

The tensile strength test was performed using cylindrical samples with two different types of geometry. The samples were cut from the SPS samples by the electric discharge machining (EDM) method.

First specimen geometry had a gauge length of 12.5 mm and 3.5 mm in diameter, tested with cross head speed of 0.2 mm min^{-1} (i.e. strain rate of 0.25×10^{-4} according to EN ISO 6892) on Instron 8801 testing machine at room temperature. The elongation has been measured on the gauge length of the samples.

Second specimen geometry used a gauge length of 7.6 mm with 2 mm in diameter, tested with universal testing machine Zwick Z250. The elongation has been determined by the extensometer clipped on the sample holders in the close vicinity of the gauge length.

The utilization of two different types of tensile specimen geometry is the result of different available setup used throughout the study.

The differential Crussard-Jaoul analysis was performed to determine the strain hardening exponent n, supposing Hollomon equation, quantifying the uniform deformation of tensile curve [100].

Heat treatment experiments

A tube furnace Carbolite Gero STF with protective argon gas atmosphere has been used for all the heat treatment experiments on $AlCoCrNiFeNiTi_{0.5}$ alloy presented in the study. Two hours' dwell time on 1100 °C and 1250 °C has been used. After the end of dwell time, the tube was opened, samples were removed and cooled in water to prevent phase changes.

Density determination

The calculated density for the materials was given by the rule of mixture of the respective elements present in all alloy compositions. However, given by the differences in elemental lattices, this method should be taken only as approximate. The approximate density of materials was always determined by observation of SEM micrographs. For the $Ni_{1.5}Co_{1.5}CrFeTi_{0.5}$ and CoCrNi alloys, the density was determined additionally by Archimedes method as well, in RHP Technology.

7 Results

7.1 Mechanical alloying process parameters evaluation

The evaluation of the induced modifications in the MA powders with changing the milling parameters, have emerged as very important aspect for the efficient future production of MA powders. The $AlCoCrFeNiTi_{0.5}$ alloy composition (in atomic fraction) has been selected for the starting experiments, due to its very good combination of mechanical properties mentioned in 2.4.1, and, therefore, its high application potential for future development. Fig. 46 shows the XRD patterns of mixed $AlCoCrFeNiTi_{0.5}$ powders milled for two different times with the use of two different milling balls diameter, milled with methanol - designated before in Table 2 as milling 1-8. It should be noted that the milling process number 9 without methanol will be described separately later in the study. In the XRD patterns, after 10 hours of milling with 250 RPM, peaks of the present elements, visible in only blended powders (0 h of milling) start to join together while their intensity decreases. This process can be considered as a start of a solid solution forming reaction [92]. After 24 hours of milling, only the peaks corresponding to BCC elements (iron and chromium) remains. Therefore, all the other remaining elements dissolved in the lattice of Fe and Cr, forming one solid solution. The peaks are visibly broadened – as the consequence of refining the powder crystallite size by repeated cold deformation from milling balls. Apparently, the milling balls size has only negligible influence on the phase composition of the powders (patterns for 10 mm and 15 mm balls size are basically identical).

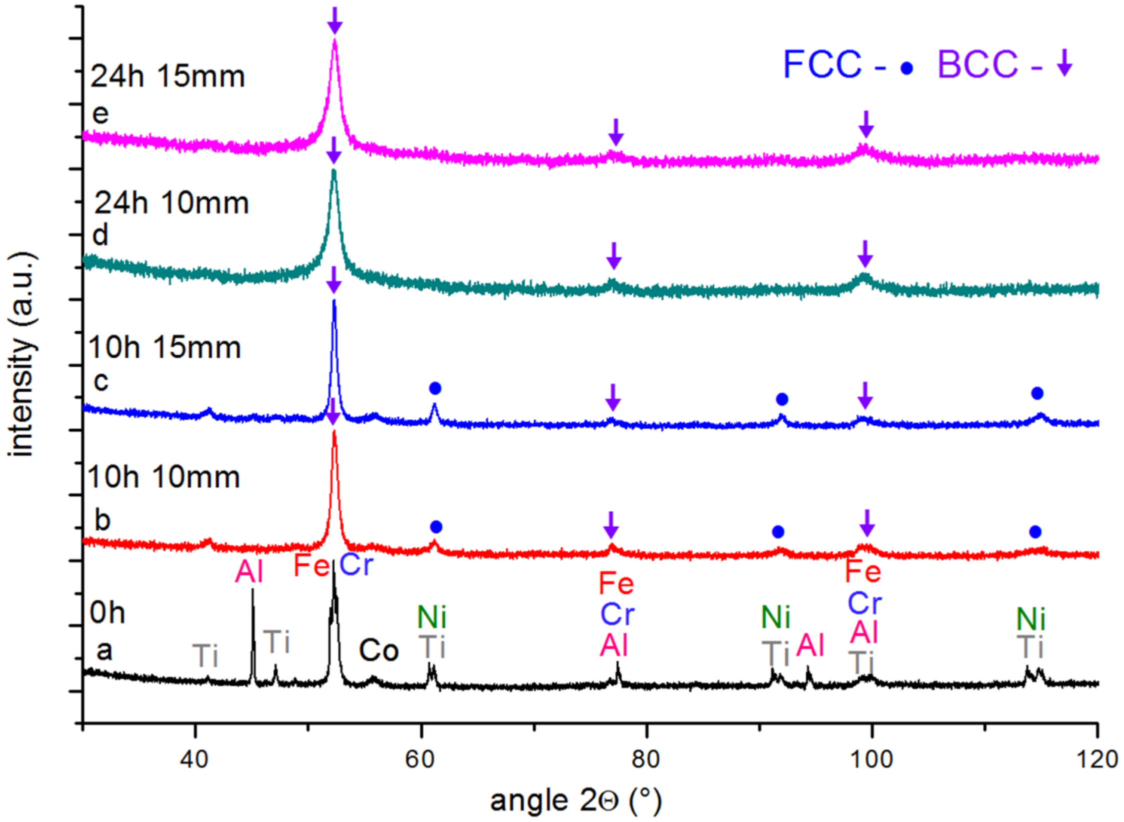

Fig. 46 XRD patterns of $AlCoCrFeNiTi_{0,5}$ powders after different milling times and balls diameters at 250 RPM of a) blended powder 0h; b) 10 h, 10 mm balls; c) 10 h, 15 mm balls; d) 24 h, 10 mm balls; e) 24 h, 15 mm balls.

Fig. 47 represents the XRD patterns of the same powders milled with a higher speed of 400 RPM. In this case, the formation of BCC solid solution occurred already after 10 hours of milling. It is not surprising, considering relatively comparable milling intensities (Fig. 47) of powders milled for 10 hours at 400 RPM and 24 hours at 250 RPM – 2135 as compared to 2002 J kg^{-1} respectively. The peaks in case of 400 RPM are even broader than in case of 250 RPM use, pointing out to more intensive alloying. No apparent differences are observed for the use of 10 mm and 15 mm milling balls again. Therefore, it seems that, the use of different milling balls diameter does not induce any significant differences to the phase composition of the MA powders in this particular case.

The mechanical milling may induce solid phase reactions is some materials. During milling of some materials, intermetallic phases, carbide or amorphous phases are formed [101]. However, this is not the case for $AlCoCrFeNiTi_{0,5}$ elemental powders. The only reaction of the present elements during milling was their dissolution and formation of single BCC solid solution, i.e. it is possible to refer to it as high entropy solid solution. No other interim phases were formed.

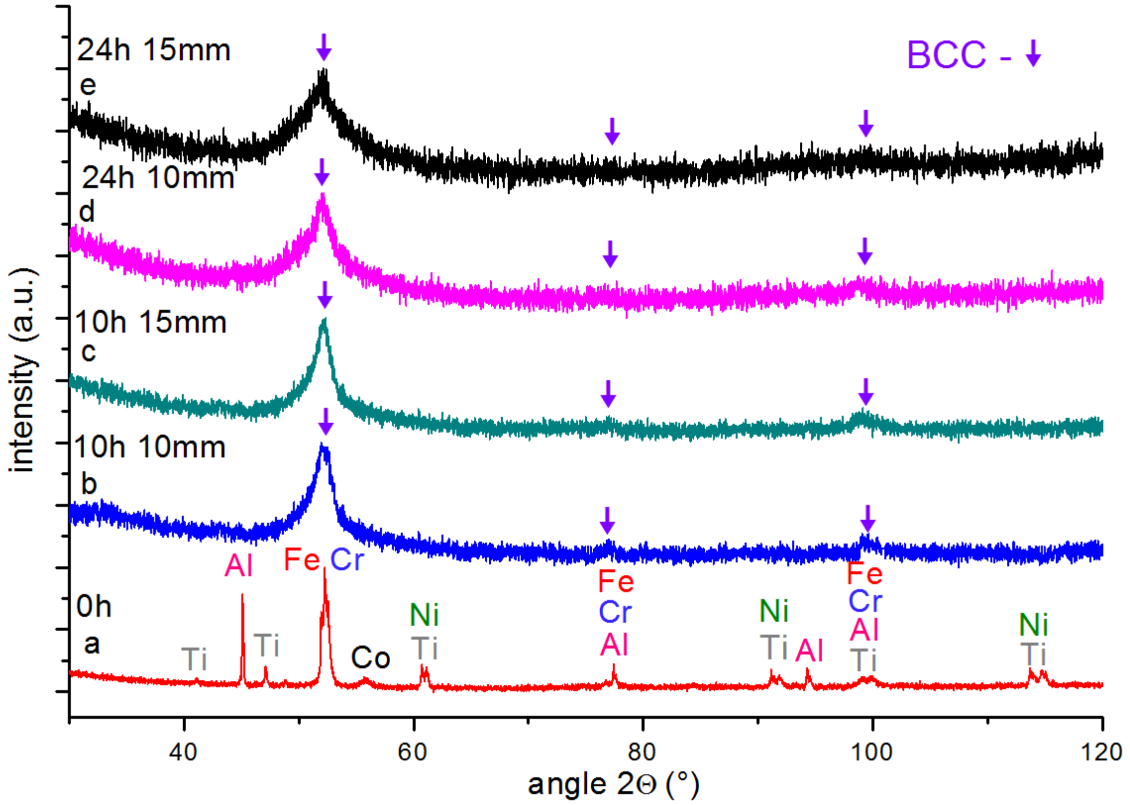

Fig. 47 XRD patterns of $AlCoCrFeNiTi_{0.5}$ powders after different milling times and balls diameters at 400 RPM a) blended starting powder b) 10h, 10mm balls c) 10h, 15mm balls d) 24h, 10mm balls e) 24h, 15mm balls.

The powder morphologies milled with different parameters are displayed in Fig. 48. The milling at 250 RPM for 10 hours produces a flake-like morphology with very poor chemical homogeneity (presented in appendix in Fig. A 1), where it is still possible to see the flattened original powder particles. This is usually referred to as first stage of mechanical alloying process (see paragraph 4.1.1.)

One can observe that in the powders milled at 250 RPM and for 24 hours, a pronounced change in morphology as well as homogeneity is visible. The alloying process reached its third stage (deduced from the spherical powder morphology). In this case, the differences in the use of 10 mm or 15 mm milling balls are observed. 10 mm balls seem to cause smaller particle sizes.

As expected, the utilization of higher RPM leads to better overall powder homogeneity, given by higher milling intensity in the shorter time periods. However, it seems that the average particle size is also significantly increased. With higher RPM, the speed at which the balls are moving is increasing. Therefore, the energy for one impact is increasing as well. One would expect that it would cause a higher powder fracturing, but it seems that the higher impact energy increases the ability of powders to form stronger cold welded contacts, or simply much more of them. Therefore, in the higher RPM range, the ability of powders to cold weld overcomes the powder fracturing – thus the increase of average particle size. The use of 10 mm milling balls appears to induce the increase in powder particle size - in contrary to the previous observation with 250 RPM, where the utilization of 10 mm ball caused lower particle size.

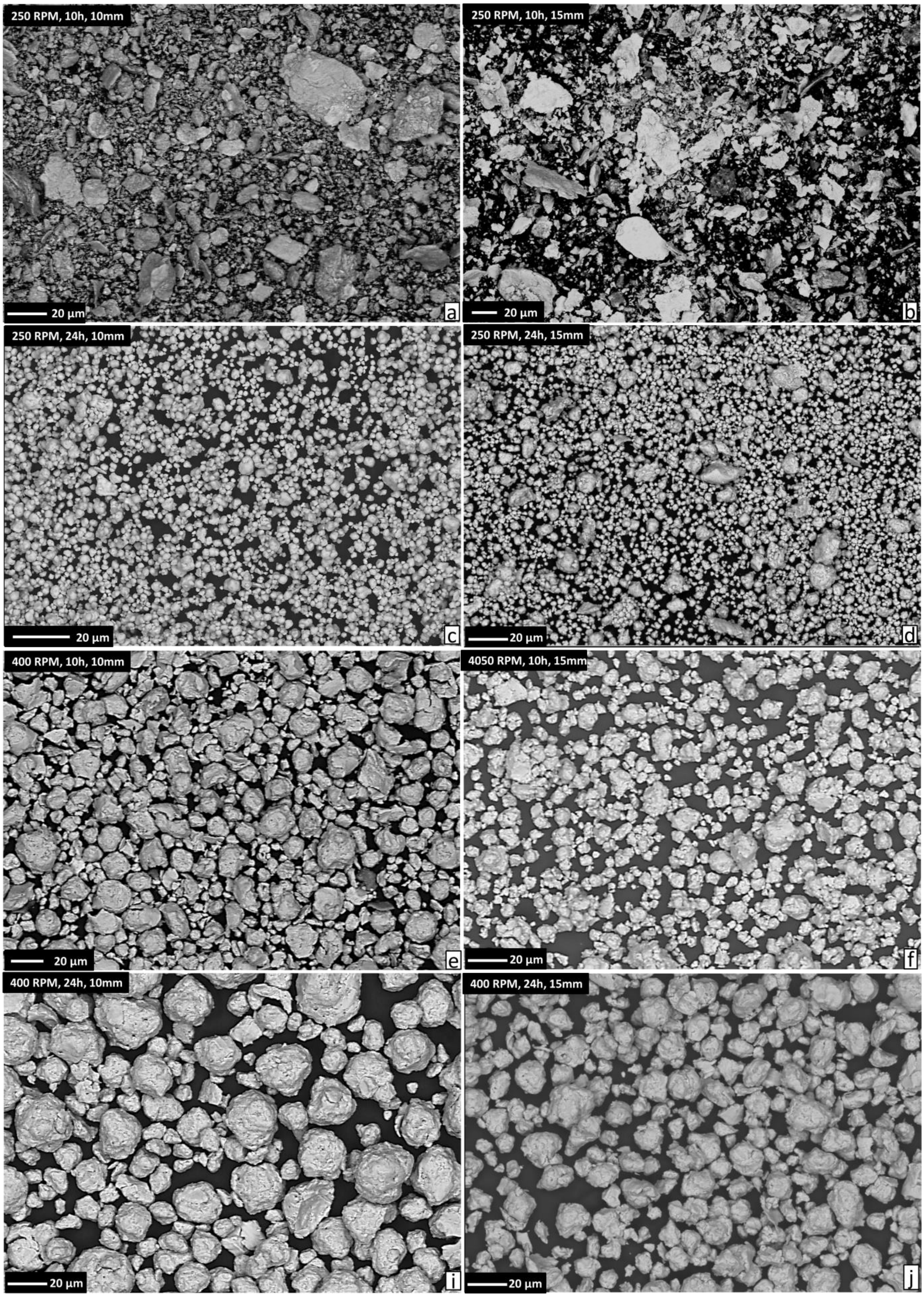

Fig. 48 SEM images of AlCoCrFeNiTi$_{0.5}$ alloy milled powder morphologies in BSE mode with parameters of a) 250 RPM, 10 h, 10mm balls b) 250 RPM, 10 h, 15mm balls c) 250 RPM, 24 h, 10 mm balls d) 250 RPM, 24 h, 15 mm balls e) 400 RPM, 10 h, 10 mm balls f) 400 RPM, 10 h, 15 mm balls i) 400 RPM, 24 h, 10 mm balls j) 400 RPM, 24 h, 15 mm balls.

The significant influence of milling parameters on powder morphology and particle size is evident. Depending on the desired properties of the powder, the parameters may be adjusted to fit the needs of particular application. For instance, in pressureless sintering, the best densification is obtained when particle size is as small as possible (due to higher number of particle contacts and more efficient die filling). For pressure assisted processes, like spark plasma sintering, high chemical homogeneity is desirable bearing in mind very short sintering times - limited diffusion.

7.2 AlCoCrFeNiTi$_{0.5}$ alloy

7.2.1 AlCoCrFeNiTi$_{0.5}$ alloy A bulk

The XRD pattern of the AlCoCrFeNiTi$_{0.5}$ alloy A, prepared from powders milled with 250 RPM, 24 h and 15 mm balls is presented in Fig. 49b. The milled powder pattern is added for better comparison. Only the peaks attributed to a BCC solid solution phase with 2.87 Å lattice parameter, i.e. close to Cr and Fe, are visible in the milled powders.

Apparently, the BCC phase formed by mechanical alloying process is highly unstable, and upon high temperature exposure during SPS densification (short, but dramatic increase in diffusion rates). A subsequent phase transformation to more stable products takes place; the mixture of 4 phases is observed in the bulk alloy pattern – B2 NiAl-like bearing lattice parameter of 2.89 Å phase with clearly visible superlattice (100) peak, , a disordered FCC phase with lattice parameter of 3.59 Å, a tetragonal σ phase with a=8.81 Å, c=4.56 Å, and, lastly, an evident FCC structured phase closely resembling titanium carbide (TiC). As compared to the milled powder pattern, the peaks are much sharper, suggesting an increase in crystallite size of the phases. The calculated volume fraction of phases by Rietveld method are 42.2 % of FCC phase, 42.3 % of B2 phase, 9.9 % of σ phase and 5.7 % of TiC.

The chemical composition of the bulk samples obtained by area EDS analysis (Fig. 50) almost perfectly matches the desired composition of the alloy. Therefore, the SPS process did not cause any significant alternation of the alloys chemical composition.

The appearance of TiC phase is very interesting, especially considering that no intentional addition of carbon to the powders was made. Its presence is attributed to the addition of methanol (CH_3OH) to the powders as a PCA (Process Control Agent). During the milling process, methanol was most likely trapped between the powder particles that were cold welded together. Subsequently, it decomposed and dissolved to the lattices of the powders. After sintering, the high affinity of carbon to titanium resulted in the formation of the TiC phase.

By a careful calculation of the amount of used methanol, as well as the needed amount of titanium, the observed in-situ formation of TiC can be employed to manufacture TiC reinforced composites with high entropy alloy as a matrix phase. By this method, there is no need to add any TiC ceramic powder to the milling bowl before MA process.

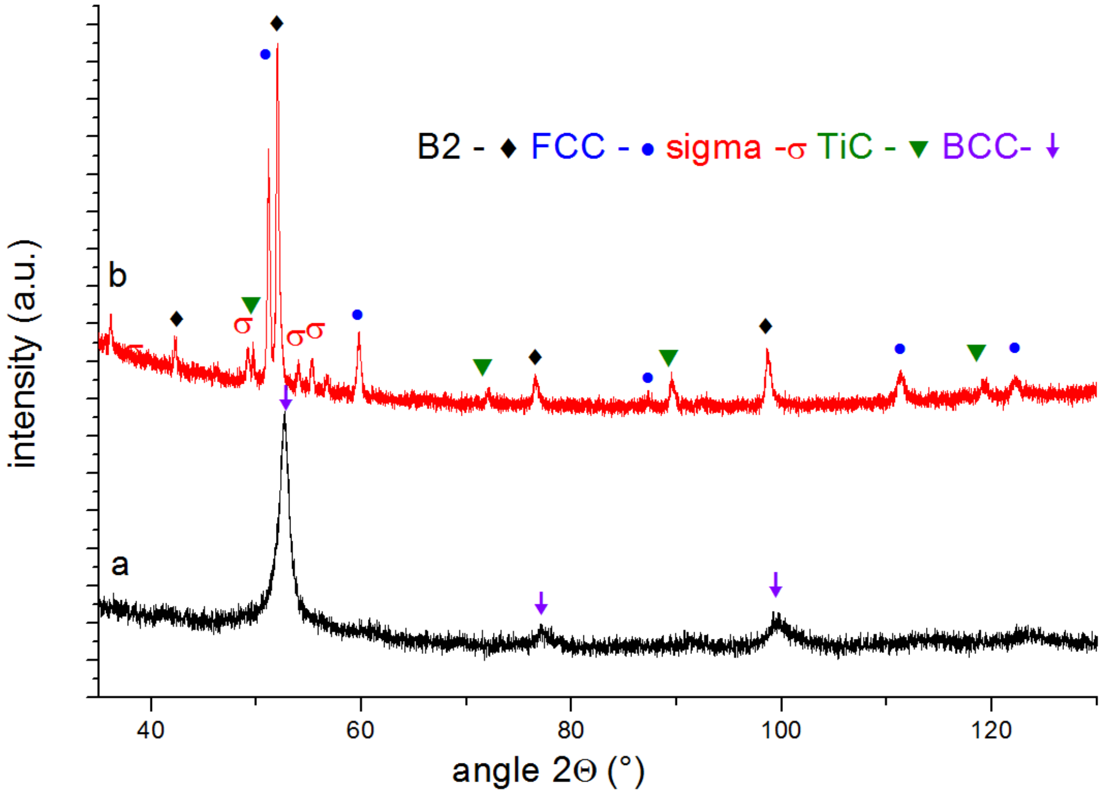

Fig. 49 – XRD pattern of a) AlCoCrFeNiTi$_{0.5}$ powder milled with 250 RPM, 24h and 15mm balls b) bulk alloy A after SPS.

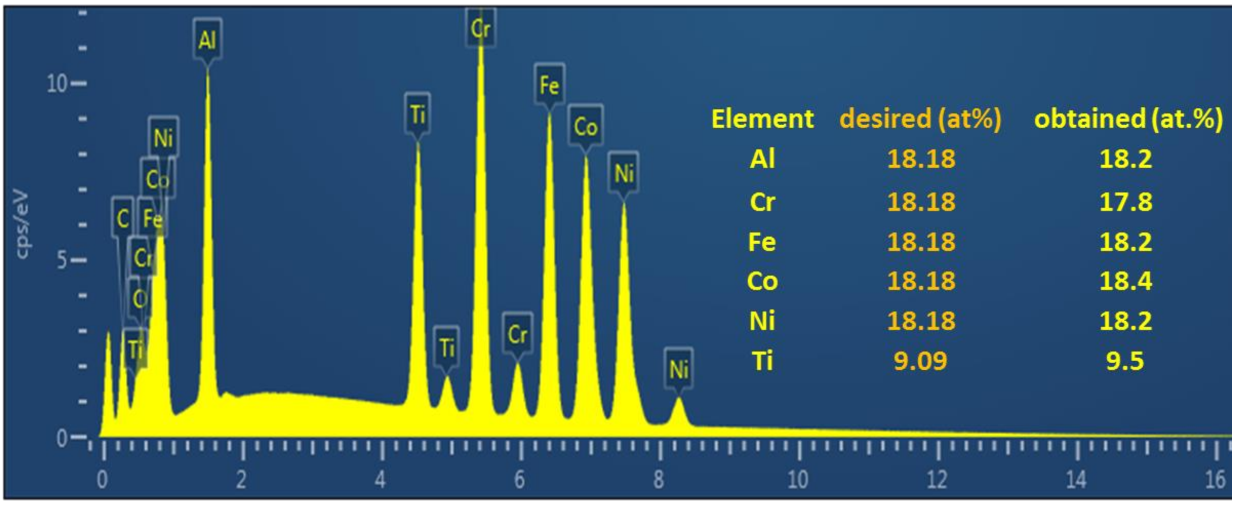

Element	desired (at%)	obtained (at.%)
Al	18.18	18.2
Cr	18.18	17.8
Fe	18.18	18.2
Co	18.18	18.4
Ni	18.18	18.2
Ti	9.09	9.5

Fig. 50 chemical composition of AlCoCrFeNiTi$_{0.5}$ alloy A bulk material.

Fig. 51 presents the micrographs of the AlCoCrFeNiTi$_{0.5}$ alloy A microstructure (with obtained chemical composition from different phases in Table 3. As analyzed by SEM observations, a full density material has been obtained by SPS with only few pores present, visible as the black dots in Fig. 51.

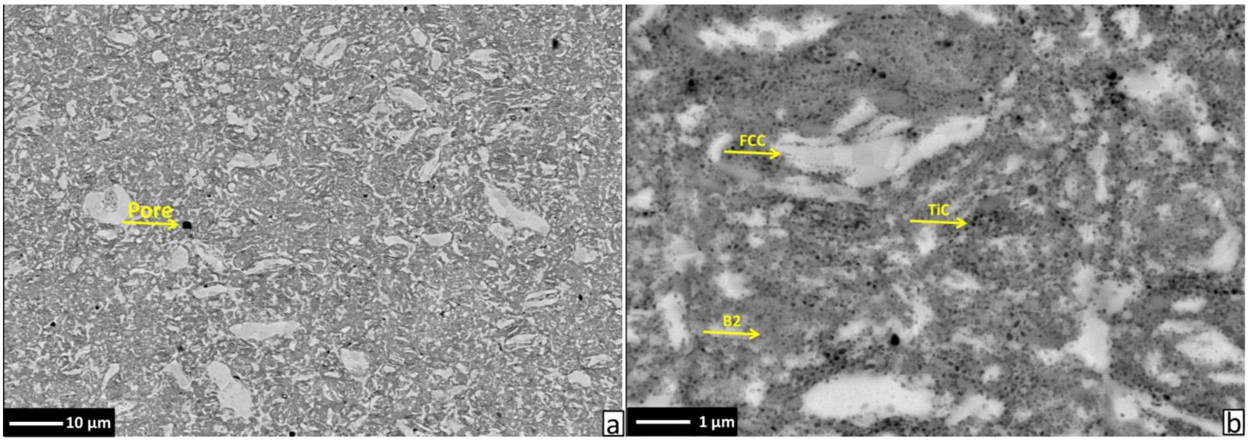

Fig. 51 AlCoCrFeNiTi$_{0.5}$ bulk alloy A microstructure a),b) SEM micrographs in back scattered mode (BSE) with marked phases

The results of TEM diffraction (Fig. 52) analysis are in good agreement with the results from XRD analysis. The microstructure is composed of the two major phases, i.e. FCC high entropy solid solution phase enriched in iron and chromium (visible as lighter contrast phase in SEM BSE micrographs) and an ordered B2 phase enriched in nickel and aluminum (darker grey phase). Small black dots correspond to nano-sized dispersion of in-situ formed TiC. In the SEM micrographs, it is impossible to distinguish tetragonal σ phase, due to its very close chemical composition with FCC phase, as seen in Table 3. However, its presence was revealed by electron diffraction (Fig. 52 e). As a consequence of powder surfaces contamination by air exposure, aluminum oxide particles were identified. From the present elements, aluminum has the highest affinity to oxygen. Therefore, other oxides present before milling on original elemental particles surfaces (chromium, titanium etc.), transformed during sintering to the oxide with highest thermodynamic stability - aluminum oxide.

Table 3 TEM EDS chemical composition of the phases present in AlCoCrFeNiTi$_{0.5}$ A alloy after SPS (atomic %).

	Al	Ti	Cr	Fe	Co	Ni
FCC	1.8	0.7	**26.3**	**31.3**	24.6	15.4
B2	**24.9**	5.2	4.1	11.6	24.1	**30.2**
σ phase	-	-	26.4	34.6	31.8	6.1

The calculated values of the previously mentioned parameters for microstructural prediction for the alloy A: chemical composition δ, ΔH_{mix}, ΔS_{mix}, Ω and VEC are 6.67 %, -17.91 kJ mol^{-1}, 14.7 K^{-1} mol^{-1}, 1.4 and 6.9 respectively. Based on the comparison of these results with the proposed criteria for HEA materials ($\delta \leq 4$ %, $-10 \leq \Delta H_{mix} \leq 5$ kJ.mol^{-1} and $\Delta S_{mix} > 13.38$ J.mol^{-1} is needed for single solid solution formation), the microstructure in alloy A should be most probably composed of mixture of solid solution phase and an ordered intermetallic, as a consequence of δ being higher and ΔH_{mix} lower than the optimal values for formation of pure solid solution microstructure. Therefore, the observed microstructure relatively well coincides with the predictions.

The FCC and B2 phases present in the alloy are in good agreement with materials in the references bearing very close chemical composition [92, 102, 103]. However, comparing the results of exactly the same $AlCoCrFeNiTi_{0.5}$ alloy produced by casting, the two-phase microstructure composed of BCC and B2 mixture has been documented [55, 104], as opposed to 4 phase FCC, B2, σ and TiC mixture in produced Alloy A of this study.

One reason for this discrepancy of phase composition may be the significant difference in the processing conditions. The SPSed material has been cooled naturally in the graphite die - relatively slowly compared to the cast material cooled by cold copper mold used in the study [104]. Usually, the σ phase precipitation kinetics takes relatively long time as it was shown to precipitate from solid solution phases in HEA before [31]. Consequently, the precipitation of the σ phase may have been suppressed in cast materials by much more rapid cooling.

The presence of FCC phase in the alloy A, instead of BCC phase in its cast counterparts, may also be associated with the formation of TiC. Upon the formation of TiC, the total amount of titanium present in the remaining phases surrounding TiC is decreased. Therefore, it seems that, with the decrease of titanium concentration in the remaining phases in the alloy A, the thermodynamic conditions change in a way that FCC solid solution formation is more favorable than the BCC one. The same phenomena may apply for aluminum, as some part of it may be trapped in the form of oxides as well. The change in major solid solution phase from BCC to FCC with decreasing concentration of aluminum has already been reported before [36].

The measured hardness for the bulk alloy was 762 ± 41 HV0.2. This value is relatively high for metallic materials. It is, supposedly, result of the presence of hard intermetallic and ceramic phases in bulk alloy. To confirm this, nanoindentation experiment has been performed. The increased size of some FCC grains (observable in Fig. 51 b) allowed the performance of nanoindentation measurements on this phase separately. The results are presented in Table 4.

As expected, the obtained hardness of 4.1 GPa HIT and elastic modulus EIT of 138.6 GPa for the FCC solid solution phase were significantly lower than the corresponding values of the measurements on the surrounding phases (areas around the white phase composed of mixture of B2, σ and TiC), possessing 9.1 GPa HIT and EIT of 190 GPa, respectively.

The original idea to use the selected alloy composition was to obtain a good combination of strength and ductility. However, due to its relatively high hardness, presence of small amount of porosity and also slight microstructural inhomogeneity, the ductility of obtained alloy seemed questionable. To improve the anticipated ductility level and observe the annealing behavior, the execution of heat treatment procedure was decided, prior to any further mechanical testing.

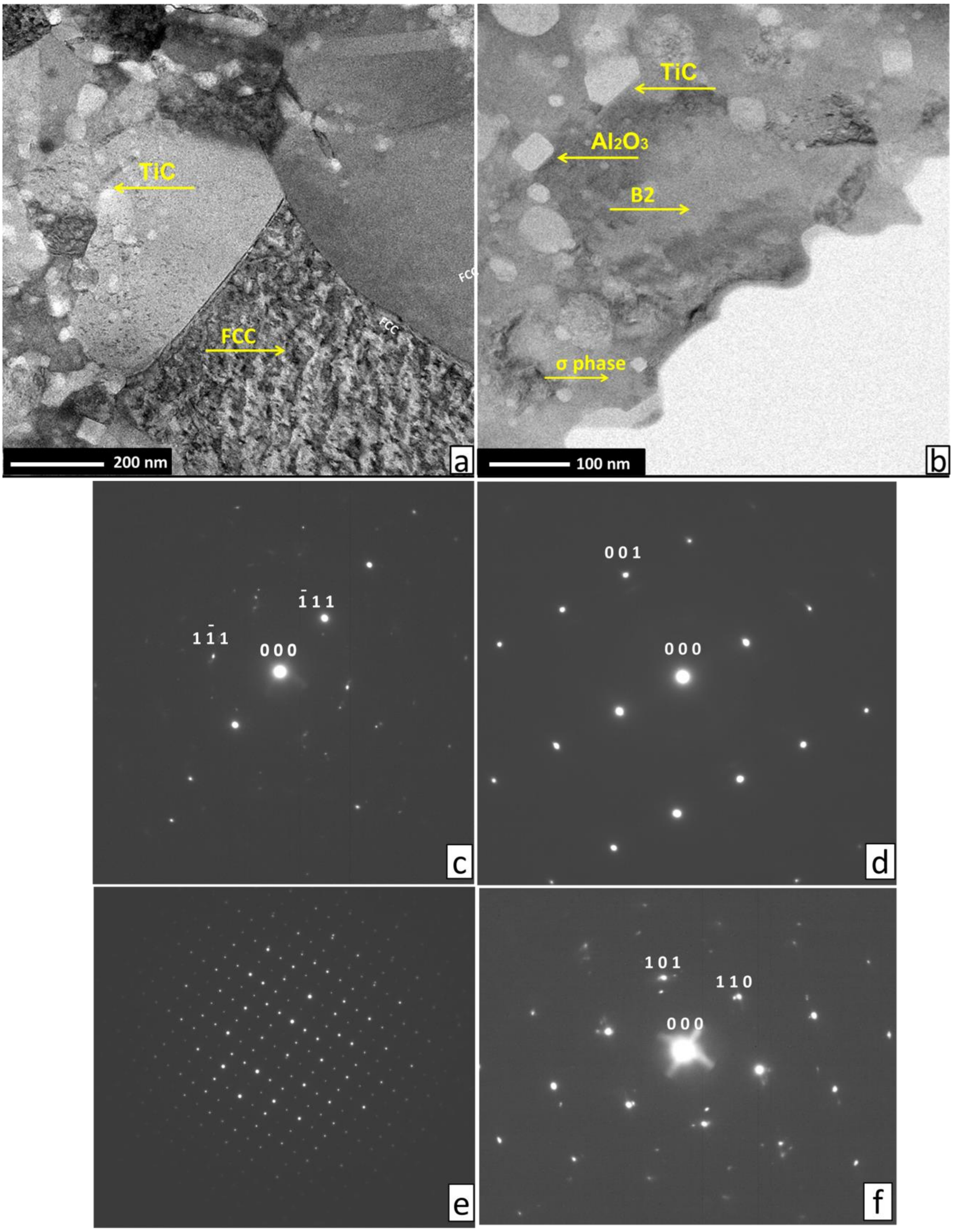

Fig. 52 TEM micrographs of AlCoCrFeNiTi$_{0.5}$ bulk alloy A a) b) microstructure with marked phases; c) diffraction pattern of TiC; d) diffraction pattern of FCC phase, e) diffraction pattern of σ phase; f) diffraction pattern of B2.

Table 4 Average hardness of the phases in $AlCoCrFeNiTi_{0.5}$ A alloy after SPS.

	Elastic modulus (GPa)	**Hardness (GPa)**
FCC	135.6	4.1 ± 20
B2 + σ + TiC average	160.0	9.1 ± 1

To obtain accurate information about the nature and temperatures of phase transformations in the alloy, Differential Scanning Calorimetry (DSC) measurement was performed.

Fig. 53 depicts the results from DSC analysis of bulk $AlCoCrFeNiTi_{0.5}$ alloy A, which was carried out to determine the phase transformation temperatures. The first significant change in the discontinuity of the curve starts is at 1040 ºC. This endothermic peak refers to the first phase transformation in the alloy, followed by a second peak at 1215 ºC. After this, the melting of the alloy starts at around 1280 ºC, with the melting peak at 1324 ºC. It is impossible to accurately determine phase transformations with only the DSC measurements, in completely new materials, such as the alloy A. However according to the previous results from references [31, 105], it may be postulated that, the first peak at 1040 ºC could correspond to the σ phase dissolution, while the second peak could correspond to either the change in the ordered B2 phase or the FCC phase.

Therefore, the heat treatment temperature has been chosen in intervals, where prospective phase transformations have already occurred (1100 °C and 1250 °C denoted by red lines in Fig. 53, with 2h dwell time performed in a tube furnace under argon atmosphere). After the annealing, rapid quenching to water has been utilized, as an attempt to retain high temperature microstructure present at annealing temperature, i.e. preventing any prospective phase transformations during cooling.

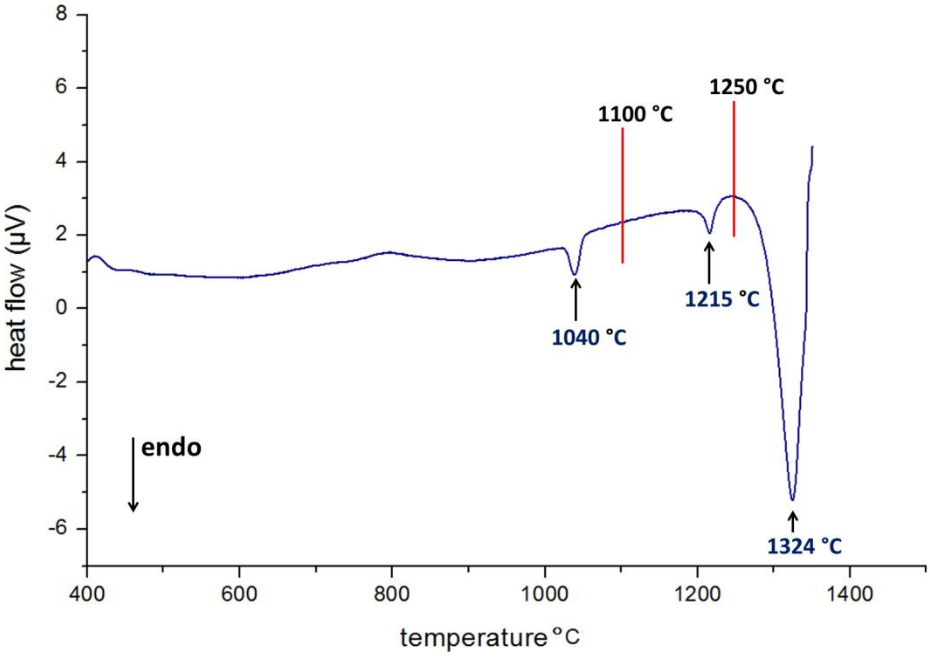

Fig. 53 Differential scanning calorimetry measurement of heat flow during $AlCoCrFeNiTi_{0.5}$ A bulk alloy sample heating.

Table 5 presents the result of Vickers hardness measurement after different heat treatment temperatures, as compared to the original hardness obtained directly after the SPS densification. As expected, the hardness values gradually decreased with increasing the annealing temperatures. However, even though the last annealing temperature step was relatively close to the start of alloy melting, the hardness after 2 hours of dwell time still remained on 533 ± 34 HV. This is pointing out to a relatively high microstructural stability of the powder alloy.

Table 5 Hardness change of AlCoCrFeNiTi$_{0.5}$ A bulk alloy after heat treatment procedures at different temperatures.

	After SPS (without HT)	**1100 °C**	**1250 °C**
Hardness (HV0.2)	762 ± 41	603 ± 35	533 ± 34

The results of XRD analysis of the materials after the applied heat treatment procedure are denoted in Fig. 54. The XRD patters after different heat treatment temperatures appear to be almost identical. New phases have not been formed, as the angular positions of the peaks corresponding to respective phases remained unchanged (with respect to those directly after SPS). The amount of the phases calculated from XRD patterns remained unchanged as well. The only observable difference in phase composition is the disappearance of σ phase.

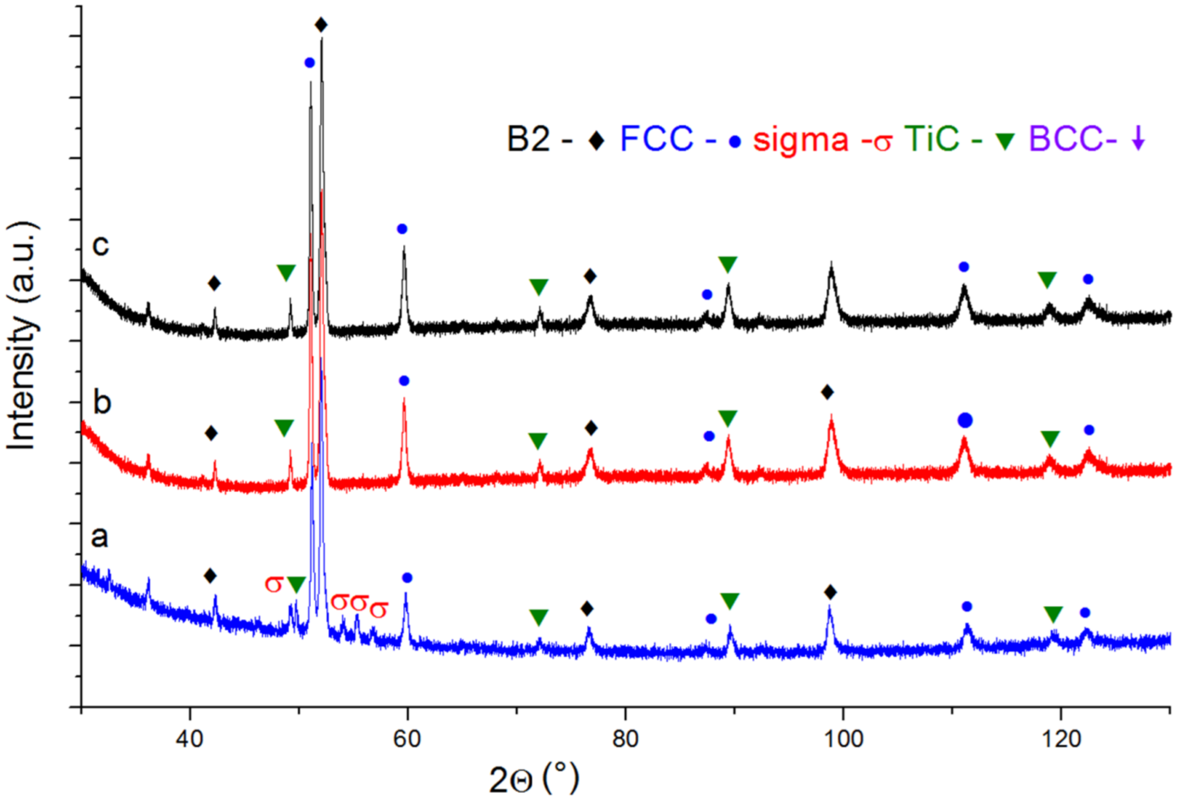

Fig. 54 XRD pattern of a) AlCoCrFeNiTi$_{0.5}$ bulk alloy A (after SPS); b) alloy A heat treated at 1100 °C; c) alloy A heat treated at 1250 °C.

Therefore, the first of the peaks in DSC curve should correspond to σ phase dissolution. The increased cooling rate after the annealing prevented its precipitation, supposedly from FCC solid solution phase (as it was observed to precipitate from it before in similar alloy in ref [31]). The σ phase is a tetragonal topologically closed packed phase (TCP phase), which is formed in austenitic stainless steels and nickel base superalloys, upon the selection of incorrect processing conditions [105, 106]. This phase is well-known for its detrimental effect on mechanical properties, due to its extreme brittleness. Consequently, its disappearance should be beneficial for the desired increase of ductility of PM $AlCoCrFeNiTi_{0.5}$ alloy.

Comparing the microstructures of the alloys after the heat treatment (Fig. 55) with the as SPSed alloy A (Fig. 51), significant morphological changes are visible, even though its phase composition seems to remain almost similar (judging from the grey-white contrast of the phases in SEM back scattered mode that remained unchanged with respect to state before HT).

The most notable is the change in the grain size of the phases. As expected, with the increased temperature, the diffusion rates increased as well, causing the grain growth. The observed grain growth is most probably the main reason for decreased hardness after HT, together with the disappearance of σ phase.

Annealing at 1100 ºC, however, caused only small changes in grain size (as observed from Fig. 55). It is, therefore, plausible to anticipate that the annealing treatment at temperatures lower than 1100 ºC would probably cause almost insignificant changes to the microstructure.

The microstructural changes in the sample annealed at 1250 ºC are much more pronounced. The reason for this phenomenon is the exponential elevation of diffusion rates with increasing temperature. Therefore, a difference in annealing temperature of 150 ºC in the high temperature range induces significant changes (as seen from Fig. 55). The grains of TiC (usually believed to be very a stable phase) present in the microstructure before HT in the form of extremely fine dispersion with the size in nm, grew to the size almost 1μm after the annealing at 1250 °C.

As seen in Fig. 55 d, a new feature has appeared in the microstructure, denoted as undetermined phase. Due to the extremely fine lamellar morphology, or insufficient volume fraction, this phase was not observed in XRD patterns. For same reasons, it was impossible to perform accurate EDS SEM chemical analysis on this phase. This can be observed only in samples heat treated on 1250 ºC. The mentioned phase arguably precipitated during the high temperature dwell from the surrounding B2 phase. The very fine, plate like morphology suggests a close crystallographic relation between B2 and undetermined phase. Therefore, the interfacial area should exhibit a coherent, or semi-coherent nature.

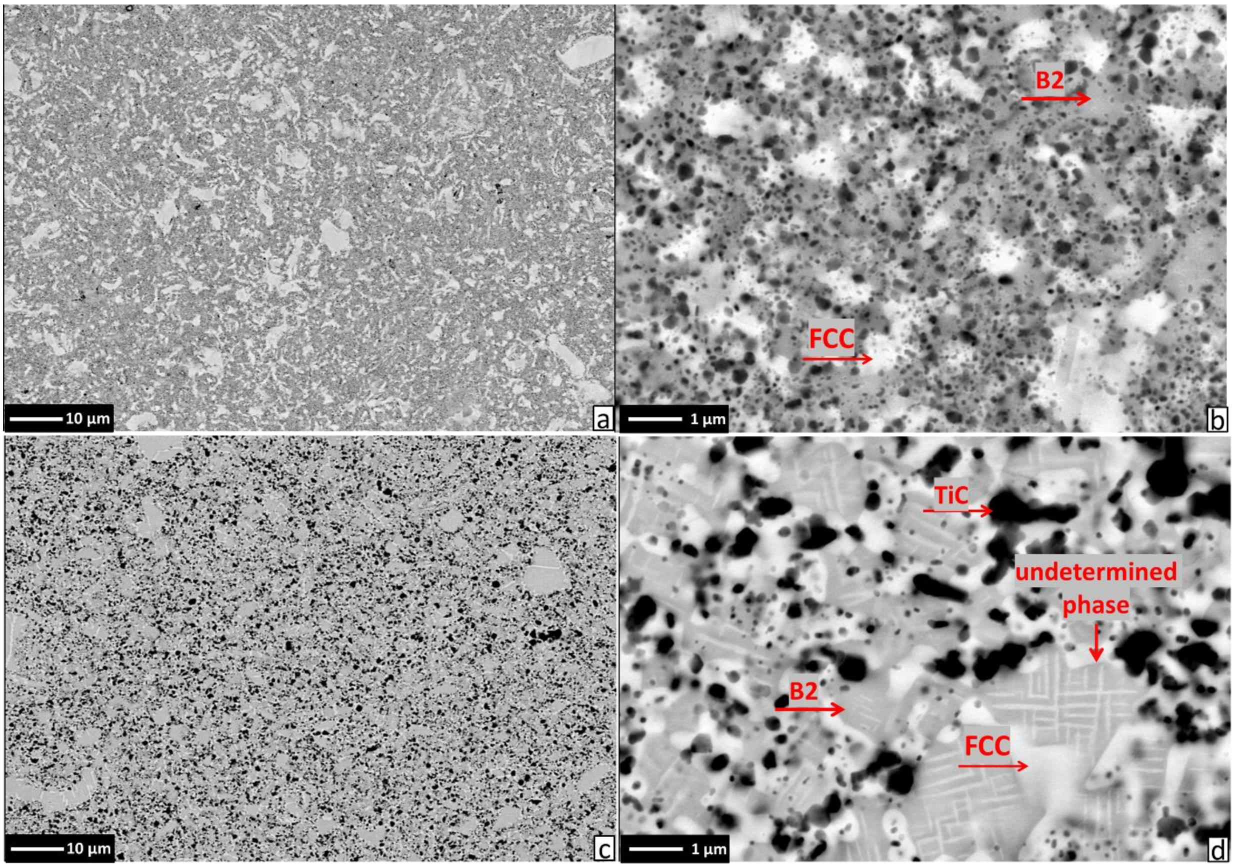

Fig. 55 SEM micrographs in back scattered mode (BSE) with marked phases of AlCoCrFeNiTi$_{0.5}$ bulk alloy A microstructure after heat treatment on a) b)1100 ºC; c) d) 1250 ºC.

The small pores observed in the material after SPS by SEM (Fig. 51 a) has been successfully removed. The porosity in the material increases the total internal energy of the material as a consequence of increased surface energy (energy of pore surfaces). Therefore, there is a pronounced thermodynamic drive to close the remaining pores by diffusion processes. In this manner, the heat treatment procedure was successful, in order to eliminate the small remaining porosity due to the increased diffusion rates.

The applied HT procedure induced desired changes to the material properties, most notably the decrease of hardness and closure of the pores, which may serve as crack initiation site.

AlCoCrFeNiTi$_{0.5}$ Bulk Alloy A Bending Test

The room temperature bending strength (R_{mb}) was measured on 4 samples, 2 of them in state after SPS, while the other 2 after heat treatment at 1250 ºC. The results are presented in Fig. 56 and Table 6, respectively.

The first visible feature common for all bending curves is the absence of any plastic deformation before the fracture, which is typical for brittle fracture behavior. The samples were broken by cleavage in the elastic loading region, as seen from stress – displacement curve (line) and samples fracture surfaces in Fig. 57.

Values of the elastic modulus determined from the load forces remained very similar for all samples, regardless of the used HT. It may be the consequence of the very similar phase composition, only slightly affected by the conducted heat treatment i.e. disappearance of σ phase. Even through the grain size has increased by the performed HT, it did not affect the elastic modulus as the changes in grain size do not affect the elastic modulus of metallic materials in general [107].

The strength values of the first two specimens, corresponding to the state of alloy A, directly after SPS exhibit extremely different values. This phenomenon is typical for materials with brittle fracture mode (similar to ceramic materials). It is associated with the defect driven fracture, as the crack growth occurs rapidly with small energy dissipation. Most probably, pore, or some other type of microstructural defect was present in sample 2, causing the premature failure.

Unexpectedly, the employed heat treatment on 1250 ºC did not affect the strength and plasticity values considerably, in spite of the fact that the hardness values decreased significantly.

At any rate, the measured levels of bending strength are still relatively high, especially taking into account the fact that the alloy density is considerably lower (calculated density 6.44 g.cm^{-3}) than density of comparable steels.

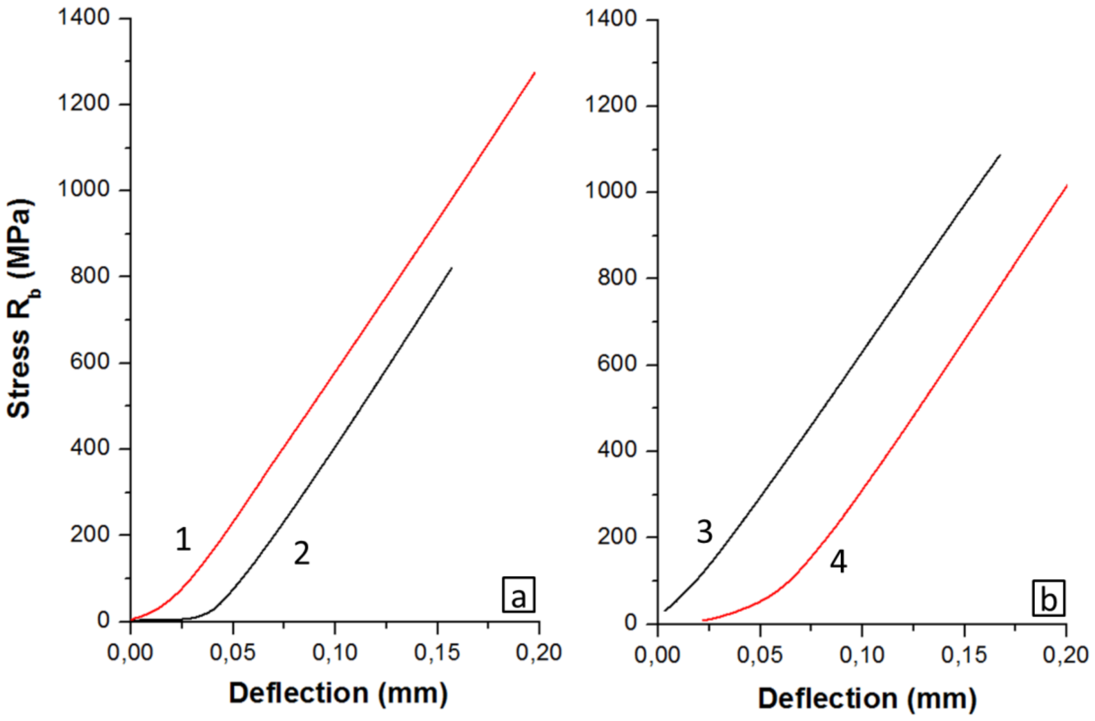

Fig. 56 Stress – deflection curves from three-point bending test of $AlCoCrFeNiTi_{0.5}$ bulk alloy A (the sample annotations 1-4 correspond to the ones illustrated in Table 6 at room temperature for a) samples directly after SPS; b) samples heat treated on 1250 ºC.

Table 6 Results of three-point bending test on $AlCoCrFeNiTi_{0.5}$ bulk alloy A after SPS and heat treatment.

Sample Nr.	**R_{mb} [MPa]**	**E [GPa]**	**Max. deflection [mm]**
1 after SPS	1275	99.4	0.2
2 after SPS	820	98.4	0.156
3 SPS + HT 1250 ºC	1117	94.7	0.167
4 SPS + HT 1250 ºC	1255	97.6	0.18

Fig. 57 represents typical fracture morphologies of the as-SPSed and SPS+heat treated broken specimens (arranged so that the sample side that is subjected to tensile loading is in the top, while the side subjected to compression in the bottom). The fracture of the alloy A, in the state after SPS (shown in Fig. 57 a, c, e), has no distinctive initiation site. On the upper edge of the sample corresponding to the side loaded by tensile stress, radiating valleys and ridges are present. The fracture initiated on several locations within the cross section at the same time. Only then at some point of the fracture process, the crack tips crossed and connected to form a magistral crack. The fracture surface is extremely fine, as a result of the extremely fine-grained microstructure. Conspicuous cleavage facets (denoted by yellow arrow) are visible at the surface. Considering their size, they should correspond to transgranular fracture of ordered brittle phases (most likely the B2 phase or the σ phase).

Another specific features, present in the fracture surfaces, are dimple-like formations (green arrow), most probably appertaining to ductile tearing of plastic FCC solid solution phase. The fracture surface of the sample after applied heat treatment (Fig. 57 b, d, f) has a visible initiation site at a needle like facet - presumably a remnant of brittle phase that may have formed from a local microstructural inhomogeneity, denoted by red arrow in Fig. 57 b. The fracture features are, in general, much coarser, as opposed to the state after SPS, corresponding to the observed coarsened microstructure after HT procedure. Again, distinctive areas with cleavage steps (marked by yellow arrow) and dimples (marked by green arrow) are visible; presumably corresponding to present brittle B2 ordered phase and FCC solid solution, respectively.

Distinguishable particle-like features (denoted by purple arrow) may have formed due to the presence of the coarsened TiC phase. During the fracture process, interfacial decohesion between TiC and the neighboring phase took place, leaving bare TiC on the fracture surface.

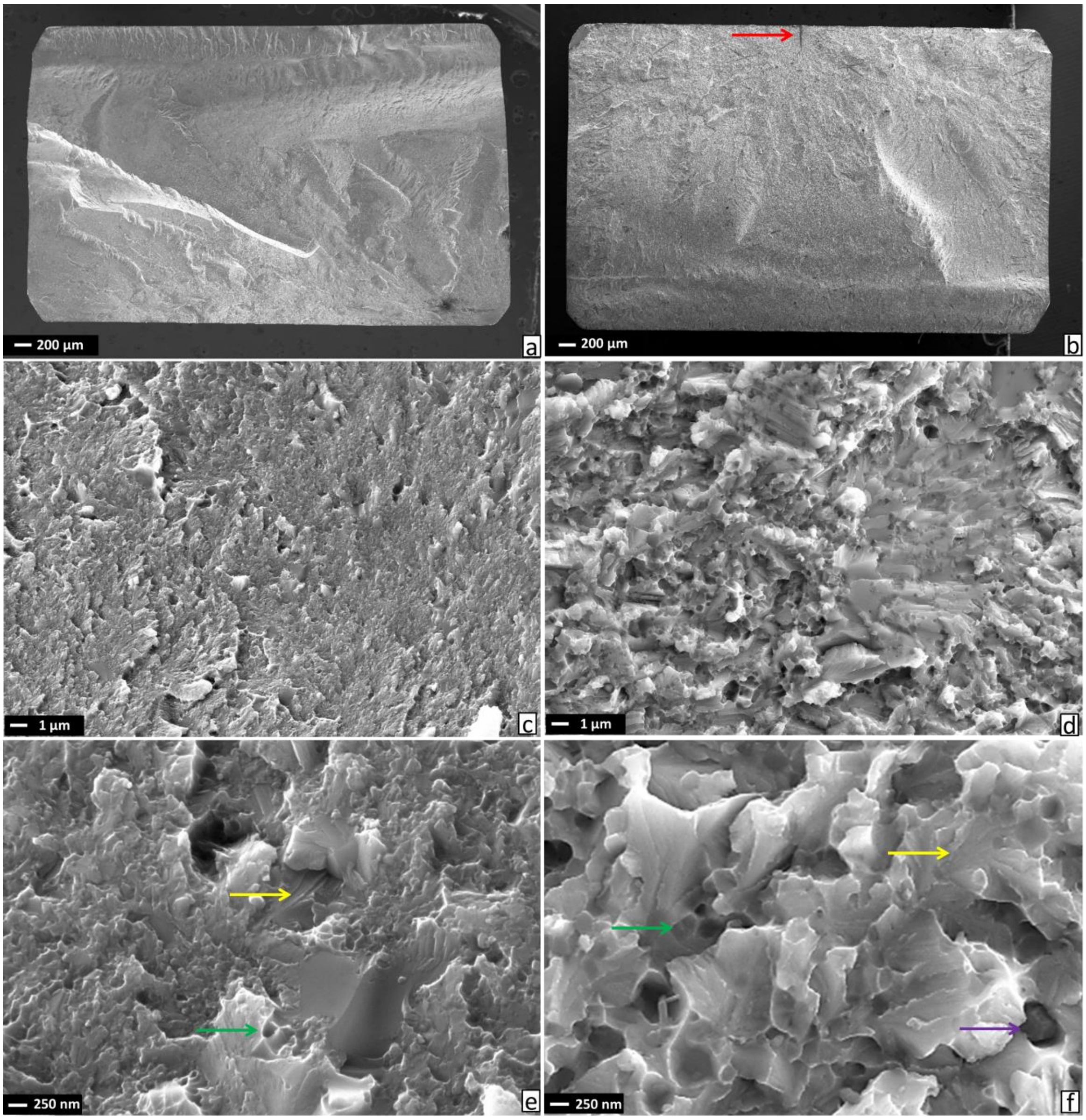

Fig. 57 SEM micrographs of fracture surfaces of bending specimens of bulk alloy A a, c, e) directly after SPS; b, d, f) after heat treatment at 1250 °C.

$AlCoCrFeNiTi_{0.5}$ alloy B bulk

For better overall powder homogeneity, the powders milled with higher intensity have been densified as well (400 RPM as compared to previous 250 RPM in alloy A). The XRD pattern of the $AlCoCrFeNiTi_{0.5}$ powders milled with 400 RPM 24 hours and 15 mm balls) is presented in Fig. 58 (hereby designated as alloy B). The patterns of the bulk SPSed alloy B, produced from these powders, is present together with bulk alloy B after heat treatment at 1250 ºC. The same condition of SPS and heat treatment as in the previous case of alloy A were applied. Heat treatment only at 1250 ºC temperature has been chosen, in order to obtain more material for subsequent mechanical testing.

The bulk alloy B powder, as-SPSed material and after HT at 1250 ºC are composed of the same phases i.e. FCC Fe and Cr enriched solid solution, B2 ordered phase enriched in Ni and Al and in-situ formed TiC. In contrast to alloy A, which was produced from powders milled with 250 RPM (Fig. 49), alloy B in the state directly after SPS does not contain σ phase in its XRD patterns. The calculated volume fraction of the present phases is: 26.5% of FCC phase, 58 % of B2 phase, and 15.5 % of TiC (as compared to alloy A containing 42.2 % of FCC phase, 42.3 % of B2 phase, 9.9 % of σ phase and 5.7 % of TiC). This different phase composition, especially the change in the amount of B2 phase and σ phase disappearance, may be attributed to the difference in the chemical composition, as presented in Fig. 59, and also to different milling conditions. The measured amount of present Fe element is considerably higher with respect to desired alloy's chemical composition. Therefore, it may have altered the phase composition of the alloy. The increase in the amount of TiC phase is however very hard to explain. There is a possibility that, due to more intensive milling, a higher amount of methanol PCA dissolved in the powders, consequently rising the C concentration available for TiC formation.

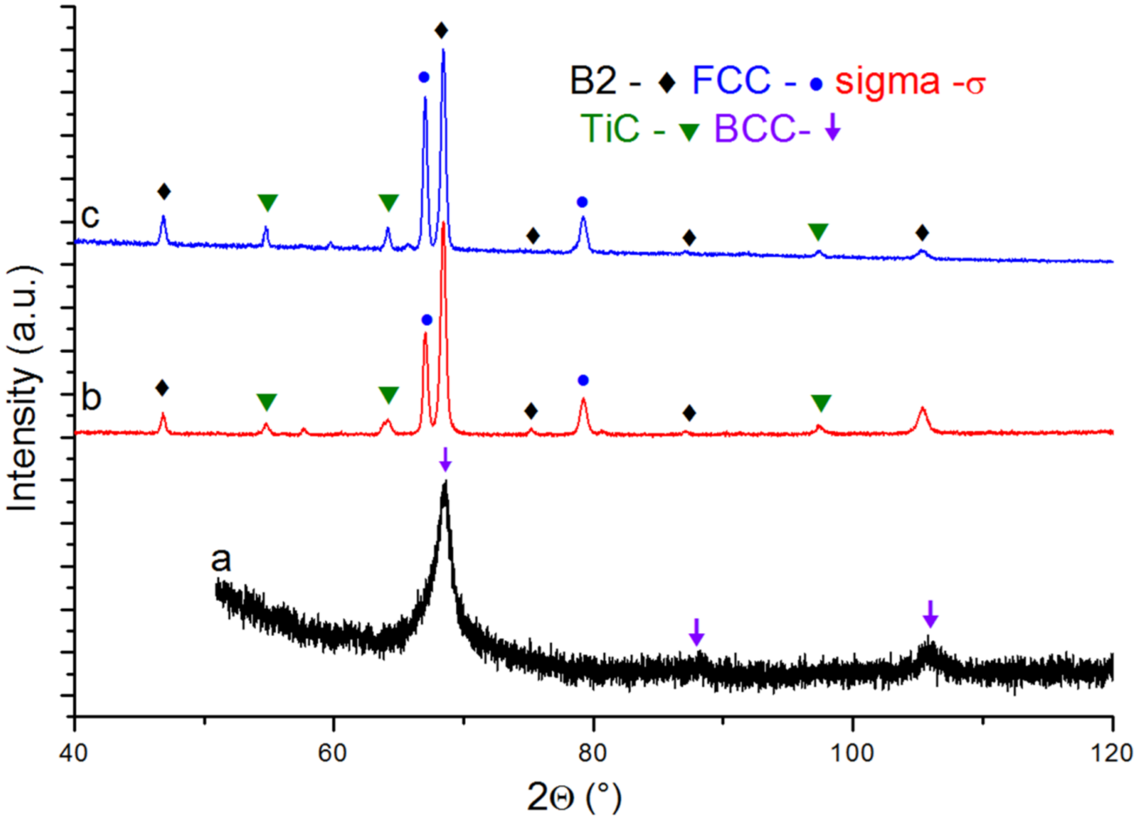

Fig. 58 – XRD pattern of a) $AlCoCrFeNiTi_{0.5}$ powder milled with 400 RPM, 24h and 15mm balls; b) SPSed bulk alloy B c) SPSed alloy B after heat treatment at 1250 ºC.

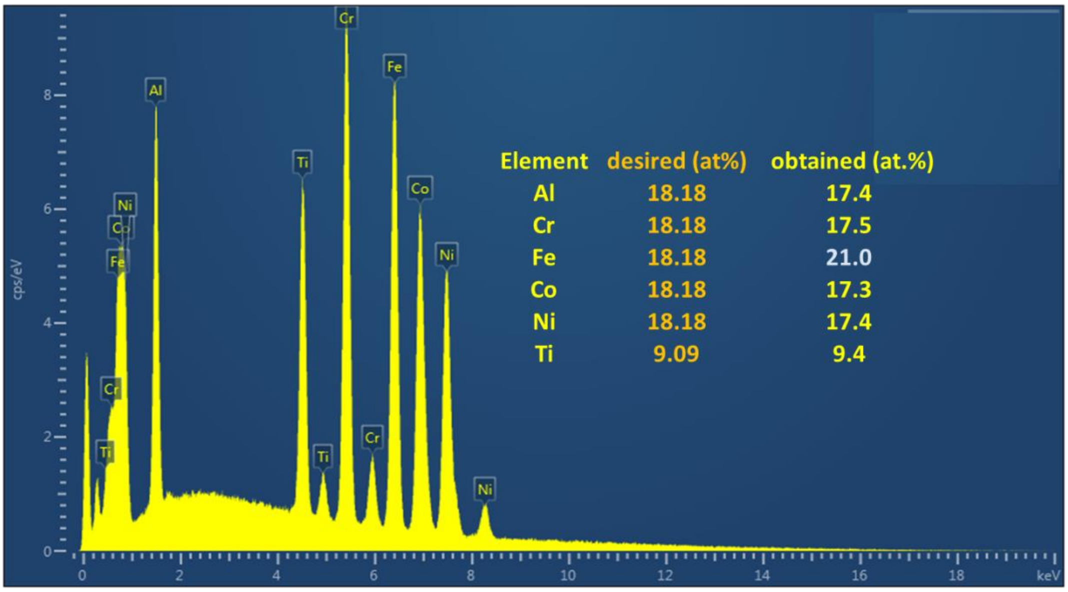

Element	desired (at%)	obtained (at.%)
Al	18.18	17.4
Cr	18.18	17.5
Fe	18.18	21.0
Co	18.18	17.3
Ni	18.18	17.4
Ti	9.09	9.4

Fig. 59 chemical composition area EDS SEM spectrum of $AlCoCrFeNiTi_{0.5}$ (400RPM) bulk alloy B.

The assumption of phase modification of phase composition due to change in iron concentration is supported by results of Tsai et al [106], that claimed the disappearance of σ phase from the HEA microstructure when the ratio of Fe and Cr element is other than 1:1. The increase in Fe concentration is probably a result of higher milling intensity. Due to high milling speed and long milling time, a significant wear of the steel milling balls probably took place, increasing the total amount of Fe in the milled powders. An increase in Fe concentration by around 3 at. % is evident already in the milled powders (EDS measurement provided in appendix Fig. A 2).

The measured hardness of the alloy after SPS (803 ± 40 HV0.2 presented in Table 7) was even higher than in previous case of the alloy A. There is a possible explanation to this attributed to higher milling intensity and nature of the SPS process. The higher milling intensity led to more significant grain refinement during milling as compared to powder milled with only 250 RPM (observable from broader XRD peaks in Fig. 47). This severe grain refinement was partially preserved even after SPS, due to relatively short sintering times, leading to smaller grains in the SPSed condition and, therefore, higher hardness. The hardness increase may be also associated with the increase in the amount of TiC phase, measured by XRD pattern. The heat treatment at 1250 ºC caused hardness decrease to 564 ± 33 HV0.2.

The explanation of the more grain-refined microstructure of SPSed sample, produced from powder milled with higher intensity, is further confirmed by SEM microstructural observations, presented in Fig. 60 a and b, corresponding to SPSed powder alloy B. According to the EDS chemical analysis, the phase composition remained unchanged after the HT procedure, which is in good agreement with XRD results from Fig. 58. It seems that the remains of original powder particles are still distinguishable in the microstructure of alloy B after SPS (for better clarity denoted by red circles in Fig. 60 a), with very fine FCC, B2 and TiC phase mixtures. These "islands" are surrounded by much coarser, brighter FCC phase. The microstructure seems rather homogenous, with very small porosity present.

The microstructure after the HT procedure is coarsened; however, the remnants of the original particle boundaries are still visible: they correspond to the arrangement of the FCC phase. The TiC phase particles inside the original ”islands” have slightly coarsened to the size of hundreds of nanometers. The morphology and size distribution of TiC phase after HT, however, seems more homogenous than in the alloy A. In general, the microstructure of alloy B in all states appears to be better arranged as compared to alloy A. Consequently, the bending test has been carried out again.

Table 7 Hardness change of $AlCoCrFeNiTi_{0.5}$ B bulk alloy after heat treatment procedure.

	After SPS (without HT)	**1250 °C**
Hardness (HV0.2)	803 ± 40	564 ± 33

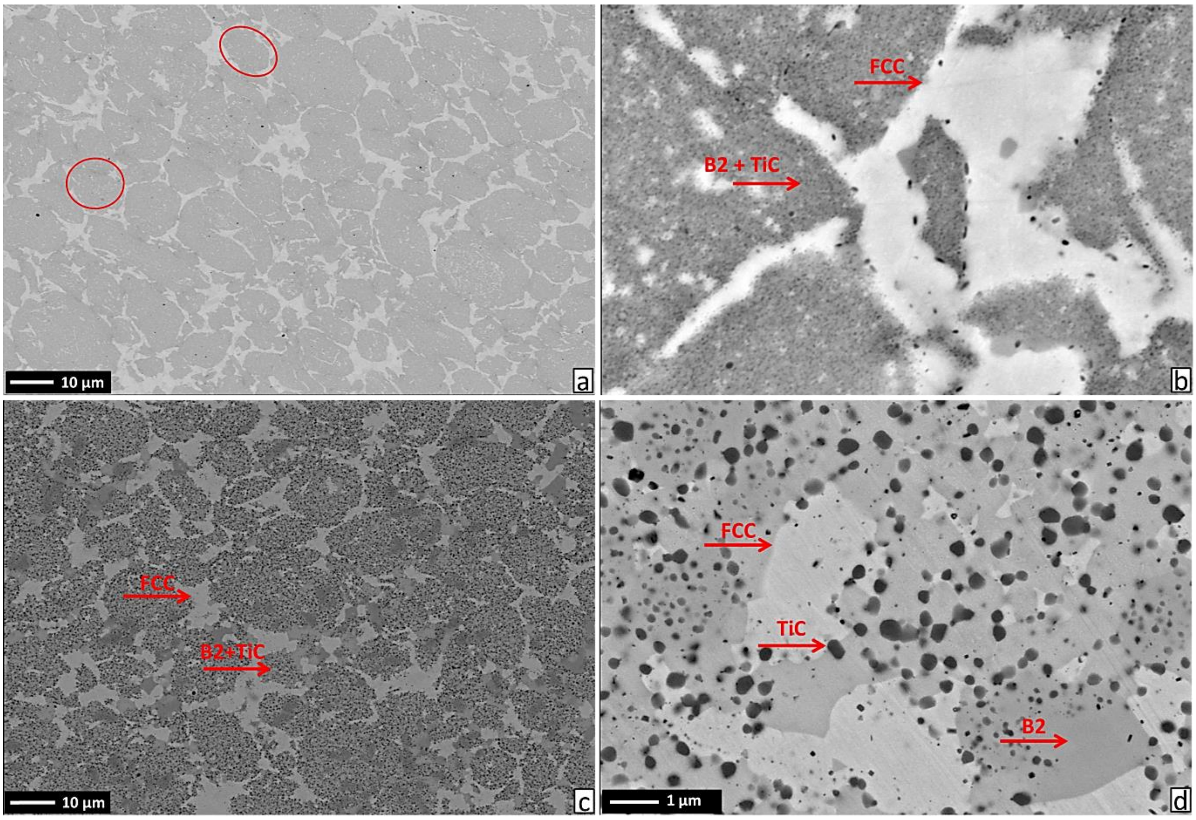

Fig. 60 SEM micrographs in back scattered mode (BSE) with marked phases of $AlCoCrFeNiTi_{0.5}$ bulk alloy B microstructure; a) b) after SPS densification, c) d) after heat treatment at 1250 °C.

$AlCoCrFeNiTi_{0.5}$ Bulk Alloy B Bending Test

Because of the limited amount of available experimental materials for production of the bending specimens, only the condition after the heat treatment at 1250 °C was tested, i.e. it was not possible to perform the bending test of the as-SPSed state of alloy B. Four samples were tested altogether, as opposed to only two for alloy A. The conditions of the testing were identical to the previous case.

The obtained results are presented in Fig. 61 with Table 8, respectively. The measured bending strength of the material was significantly improved as compared to case of alloy A, reaching almost 2 GPa, with lower value scatter as well. This may be ascribed to a more homogenous microstructure. The obtained value of elastic modulus is similar to the previous case. However, a brittle fracture has been observed again, with no significant plastic deformation preceding the fracture.

Fig. 62 a, b and c denotes the fractured surfaces of the broken bending specimen of the SPSed alloy B, heat treated at 1250 °C. The initiation site of the fracture was probably a surface defect from which the fracture rapidly propagated throughout the specimen cross – section. The specimen was cracked in a brittle fracture manner. Transgranular fracture features with visible cleavage facets (denoted by yellow arrow) are visible. In particular places on fracture surface (Fig. 62 c), the areas with brittle fracture are surrounded by ductile dimples (marked by green arrow). This arrangement of fracture morphology well corresponds to hard "islands" of B2/TiC phase mixture surrounded by intrinsically ductile FCC phase, observed on polished samples cross section.

SEM micrographs taken from a polished bending specimen side (in direction perpendicular to fracture surface) are presented in Fig. 62 d and e. Secondary cracks located near the magistral crack below the fracture surface are visible.

The cracks growth occurs preferentially in the regions of B2/TiC phase mixture, that are seemingly very brittle in nature (denoted by red arrow and red ellipse of Fig. 62 d). While the B2/TiC islands are already cracked, the ductile FCC phase grains are being plastically deformed, causing the crack bridging phenomenon. In this fashion, FCC grains are retarding the propagating cracks, causing the extrinsic toughening effect in the material. This ductile phase crack bridging may be the one of the reasons for the significantly increased values of the bending strength compared to previous case of alloy A, where this phenomenon was not observed.

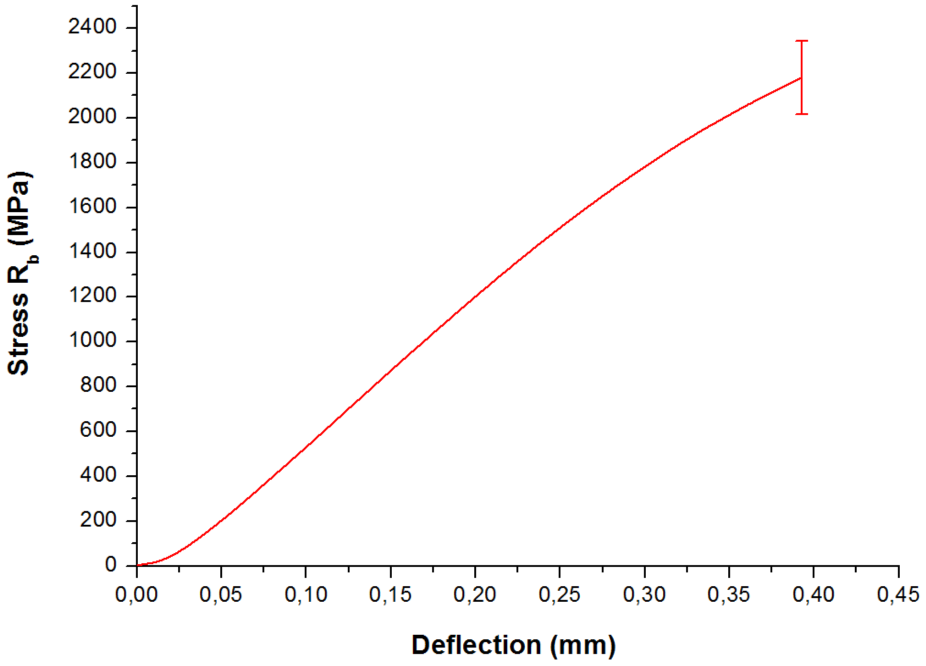

Fig. 61 Stress - deflection curves from three point bending test of AlCoCrFeNiTi$_{0.5}$ (400 RPM powder) bulk alloy B at room temperature for heat treated on 1250 °C.

Table 8 results of three point bending test on $AlCoCrFeNiTi_{0.5}$ bulk alloy B (400RPM powder) after SPS and heat treatment.

Sample	R_{mb} [MPa]	E [GPa]	Max. deflection [mm]
SPS + HT 1250 ºC	**1992** ± 164	99.4	0.4 ± 0.2

The complex microstructure composed of harder "islands" surrounded by ductile FCC phase seems promising for further alloy development. However, the fact that the secondary cracks appeared in the broken specimen is usually a sign of brittle state of the material. It has been observed that, by utilization of methanol as a milling PCA, the formation of in-situ carbides is promoted. The TiC does not form, if the methanol is omitted from milling process, as explained in 7.2.2. However, to obtain the material with higher ductility level, it seemed necessary to further decrease the presence of brittle phases, such as TiC, to discount their negative influence on fracture behavior. As a result, an attempt has been made to produce the same alloy composition without the presence of methanol to avoid the TiC formation, as well as to get insight about its influence on phase composition.

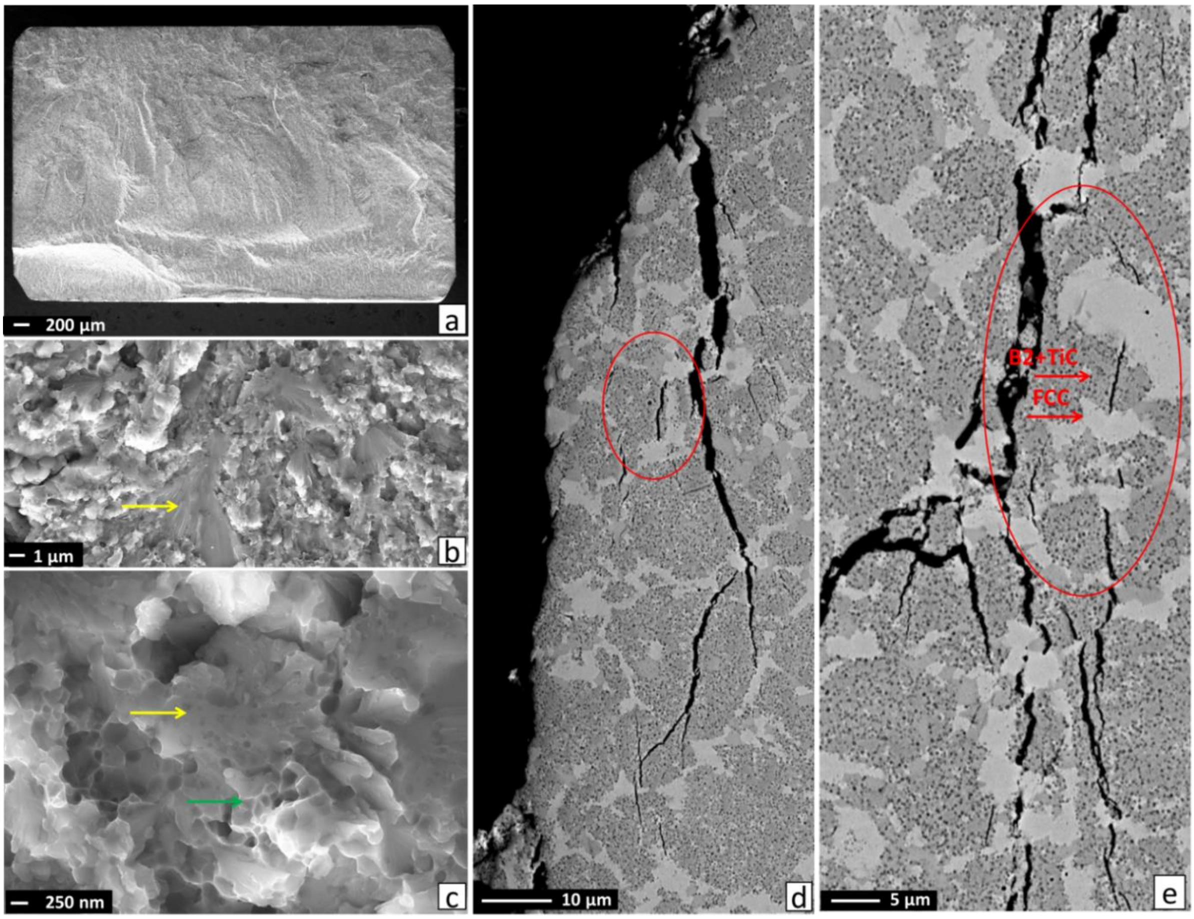

Fig. 62 SEM micrographs of bulk alloy B a, b, c) fracture surfaces of SPSed and 1250 °C heat treated bend test specimens; d,e) side view of polished fractured specimen revealing crack propagation mechanism.

7.2.2 $AlCoCrFeNiTi_{0.5}$ alloy C

For the production of this material, the same milling conditions as in previous case of alloy B has been utilized (e.g. 400 RPM, 24 hours of milling) as well as same conditions for SPS densification. However, due to the absence of a process control agent (PCA) in the form of methanol, the process went very poorly as almost all of the powder remained stuck to the milling media and milling vial surface.

The XRD pattern of the produced alloy C milled powder did not show any significant changes, compared to the milled powder used for alloy B preparation. However, the phase composition after the SPS process was significantly affected (Fig. 63). The microstructure of the materials is composed almost solely of ordered B2 and σ phases, with no FCC solid solution present. The amount has been calculated as follows: 60.4 % of B2 phase and 39.6 % of σ phase.

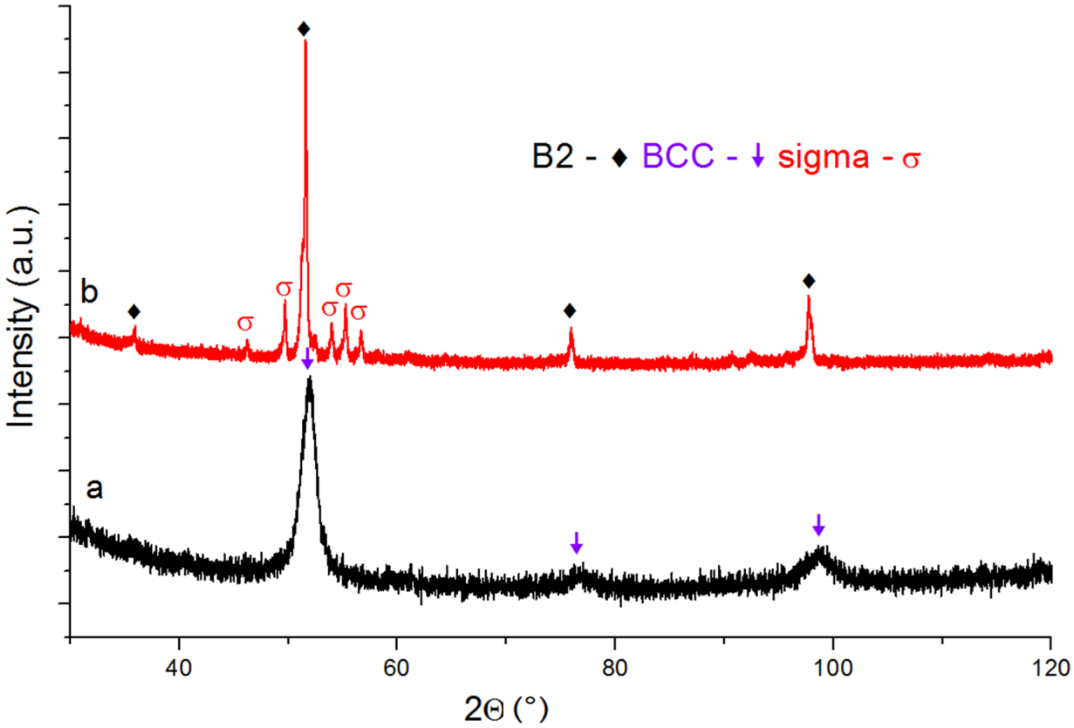

Fig. 63 XRD pattern of a) $AlCoCrFeNiTi_{0.5}$ powder milled with 400 RPM, 24 h and 15 mm balls without the presence of methanol; b) SPSed powder bulk alloy C from same powder.

The observation of a completely different phase composition in alloy C (as compared to alloy A and B) was confirmed by SEM observations as well (presented in Fig. 64). The bright phase present in the microstructure, composed almost solely from Fe and Cr as revealed by the EDS analysis, corresponds to σ phase from XRD pattern (EDS results are provided in Table 9). The darker contrast phase present is supposedly B2 phase enriched in Ni and Al. Darker small spots are oxide inclusions. The microstructure had, in general, very good homogeneity, with no pores present.

A material that is composed from such combination of ordered phases - especially the high amount of σ phase - should possess very high hardness levels. Therefore, it was not surprising that measured hardness value has been the highest in the whole study – 889 ± 15 HV0.3.

However, the alloy was extremely brittle, to the point that the full density sample 30 mm in diameter was broken in half during the sample preparation by compression stresses induced by the sample holder (during sample cross section cutting).

It seems that, the presence of comparably higher amount of unbounded Ti element (i.e. not bonded to C in the form of TiC as in alloy A and B) resulted in the detrimental change of alloy phase composition and, consequently, in extreme embrittlement by the σ phase.

After the analysis of the previous results, it became obvious that, in order to obtain a material with sufficient ductility, a chemical composition change of the produced alloys was essential. Hence the $Co_{1.5}Ni_{1.5}CrFeTi_{0.5}$ composition was selected.

Table 9 EDS SEM chemical composition of the phases present in $AlCoCrFeNiTi_{0.5}$ alloy C after SPS (atomic %).

	Al	**Ti**	**Cr**	**Fe**	**Co**	**Ni**
B2	**26.7**	14.3	5.4	12.3	20.3	**22.0**
σ phase	6.0	2.2	**38.4**	**32.2**	12.6	1.2

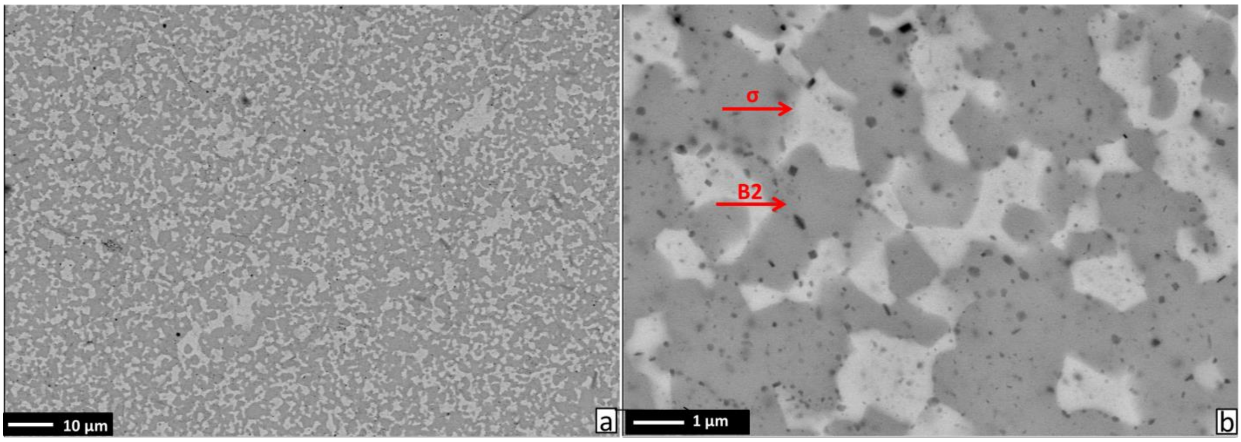

Fig. 64 SEM micrographs in back scattered mode (BSE) with marked phases of $AlCoCrFeNiTi_{0.5}$ bulk alloy C microstructure produced without methanol.

7.3 $Co_{1.5}Ni_{1.5}CrFeTi_{0.5}$ alloy

The selected alloy composition has been previously mentioned in the section dedicated to properties of HEAs (2.4.2, 2.4.3, 2.4.4). The microstructure of the corresponding cast alloys from the previous studies [39] was presented as a mixture of FCC solid solution phase and an ordered γ` phase ($L1_2$ lattice type) or η phase ($D0_{24}$ lattice type). Therefore, the alloy should provide adequate ductility derived from the presence of FCC solid solution and strength due to the dispersion of coherent intermetallic phase.

7.3.1 $Co_{1.5}Ni_{1.5}CrFeTi_{0.5}$ alloy powders

The measured XRD patterns of blended and mechanically alloyed powders are provided in Fig. 65. In the powder blend, all major peaks of the five respective elements were identified (Fig. 64 a). The MA procedure (Fig. 65 b) caused the formation of three phases: one BCC phase with lattice parameter of 2.87 Å, i.e. close to Cr and Fe, and two distinctive FCC phases with lattice parameters of 3.52 Å and 3.58 Å, respectively, both close to Ni. The milling process and repeated plastic deformation introduce extremely high concentration of defects to the powder microstructure, including vacancies. The latest phenomenon plays a major role in the diffusion process kinetics. Also, a certain amount of heat is generated, further supporting the diffusion of elements, causing the dissolution of elements in the lattice of Cr and Fe, thus forming the BCC phase. The diffusion of elements into Ni probably formed the remaining FCC phases. The elements that diffused mostly are, probably, Co and Ti, as their respective peaks disappeared from the XRD pattern. The peaks corresponding to BCC may actually be the peaks of two different overlapping BCC phases that formed by dissolution of other elements in the Cr and Fe powders. The evident peak broadening suggests either lattice distortion due to the induced strains, resulting in an increased X-ray beam scatter, or an excessive grain refinement induced by the repeated cold deformation, thereby increasing the volume of grain boundaries, triggering the same scatter effect. Due to the nature of the milling process, a combination of both phenomena probably contributed to the observed XRD peaks broadening.

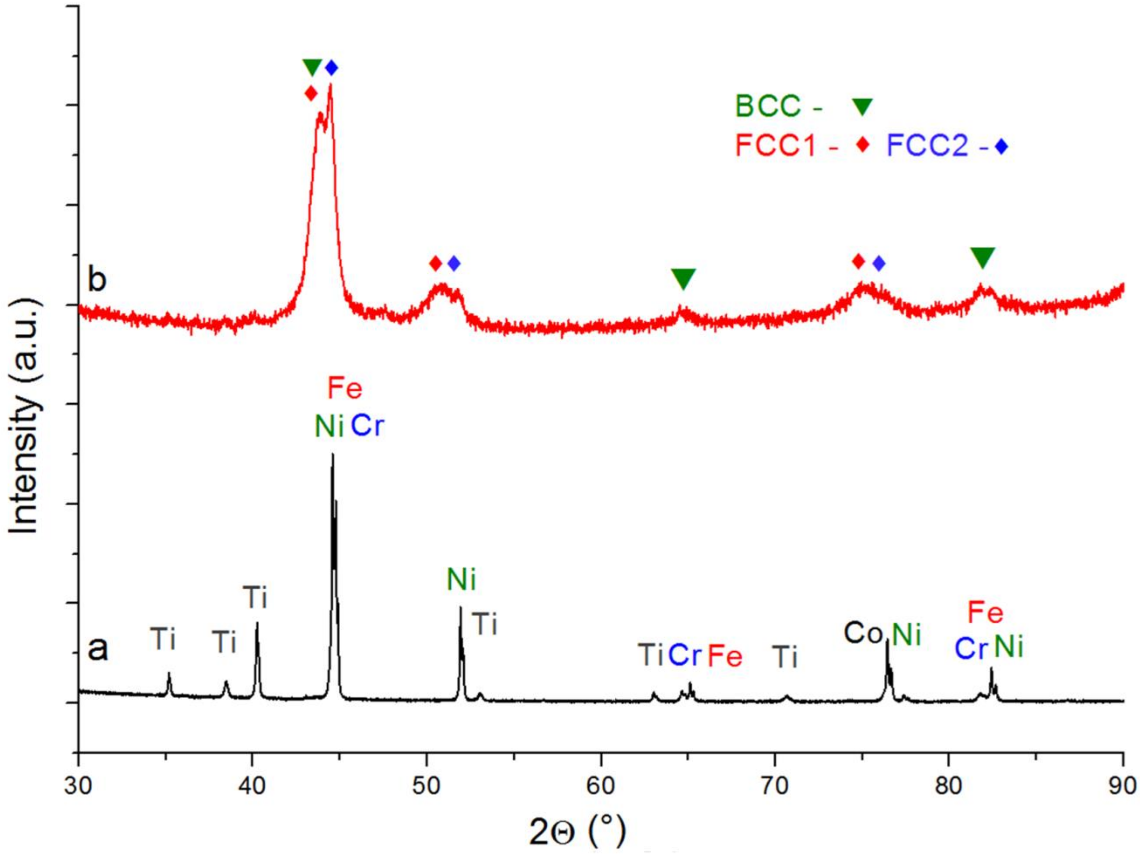

Fig. 65 – XRD pattern of a) Co$_{1.5}$Ni$_{1.5}$CrFeTi$_{0.5}$ blended powder b) Co$_{1.5}$Ni$_{1.5}$CrFeTi$_{0.5}$ mechanically alloyed powder.

The powder particle morphology after the MA procedure is demonstrated in Fig. 66 a, together with the polished powder cross-section (Fig. 66 b), added for better visualization of the microstructure. Eminent powder homogeneity has been achieved by the MA process, i.e. no traces of the original elements are observed in the chemically sensitive BSE SEM mode. It seems that, even though three phases should be present in the MA powders - as determined by the XRD analysis - it is not possible to clearly distinguish them in the powder particles cross-section (microstructure). This could be caused by the miniscule size of these phases, below the threshold for the SEM method - a claim supported by the XRD broadened peaks referring to extremely fine crystallite size. The second explanation may be the high degree of chemical similarity, induced by already mentioned solid phase diffusion.

The as-milled powder particle cross-section images unveil additional phases, visible as small black dots. They refer to Cr and Al oxide inclusions, exemplified in Fig. 66 c by red and yellow arrow, as revealed by EDS mapping. During the mechanical alloying process, oxides naturally present on the elemental powder surfaces disperse in the powder particles cross section, by the process of repeated cold re-welding and subsequent fracturing; ODS (oxide-dispersion strengthened) steels are manufactured in a similar fashion for instance [85].

The presence of Al oxide (Al_2O_3) originates from minor Al concentration in the used Cr feedstock powder (as presented in paragraph 6.1).

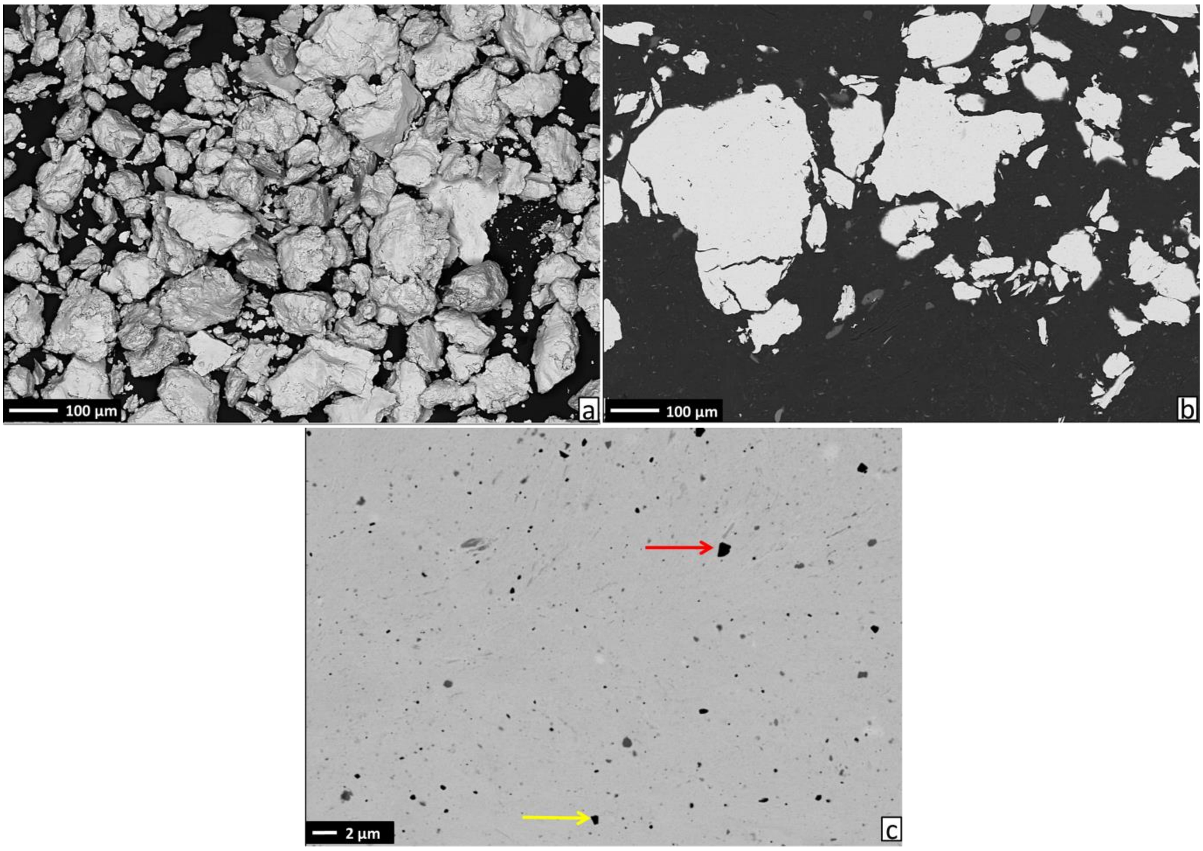

Fig. 66 SEM micrographs in BSE mode of $Co_{1.5}Ni_{1.5}CrFeTi_{0.5}$ milled powders: a) powder morphology b) powder cross-section; c) powder cross-section with denoted Cr oxide particles (red arrow) and Al oxide particles (yellow arrow).

7.3.2 $Co_{1.5}Ni_{1.5}CrFeTi_{0.5}$ alloy bulk

XRD patterns of the bulk $Co_{1.5}Ni_{1.5}CrFeTi_{0.5}$ alloy after SPS densification are provided in Fig. 67, together with the XRD patterns of milled powder, that were utilized in sintering process. Upon high temperature exposure during SPS densification, the phases present in the powders were transformed to a thermodynamically more stable FCC solid solution of all elements present within a single lattice bearing, possessing a parameter of 3.57 Å. The diffraction peaks are much sharper (as compared to the milled powders), suggesting an increase in the crystallite size.

Values of δ, ΔH_{mix}, ΔS_{mix}, Ω and VEC are 5.04 %, -10.71 kJ $\mathrm{mol^{-1}}$, 12.86 $\mathrm{K^{-1}}$ $\mathrm{mol^{-1}}$, 2.2 and 8.9 respectively (when $\delta \leq 4$ %, $-10 \leq \Delta H_{mix} \leq 5$ $\mathrm{kJ.mol^{-1}}$ and $\Delta S_{mix} > 13.38$ $\mathrm{J.mol^{-1}}$ single solid solution is formed as explained in 2.3). The theoretical density, calculated by rule of mixture, is 7.80 g $\mathrm{cm^{-3}}$. According to prediction, the microstructure should be, most probably, composed of a mixture of solid solution FCC and ordered intermetallic phase. However, the determined alloy microstructure is composed solely of a single solid solution. This discrepancy in the predicted and experimentally observed microstructural evolution may lie in the simplification of the proposed prediction parameters. These parameters were successfully employed for the predictions of microstructures of cast alloys. It seems that the differences in alloy preparation method, - e.g. intensive plastic deformation during MA - may cause the deviation from proposed prediction model.

As compared to cast alloys, the lower processing temperature of SPS densification has caused the alteration in diffusion kinetics that may have resulted in different phase composition, as it was already observed in $\mathrm{AlCoCrFeNiTi_{0.5}}$.

The bulk $\mathrm{Co_{1.5}Ni_{1.5}CrFeTi_{0.5}}$ alloy possesses chemical composition (Fig. 68) with very minor deviations from the desired theoretical composition. Therefore, the divergence in chemical composition is not responsible for the observed unexpected phase formation.

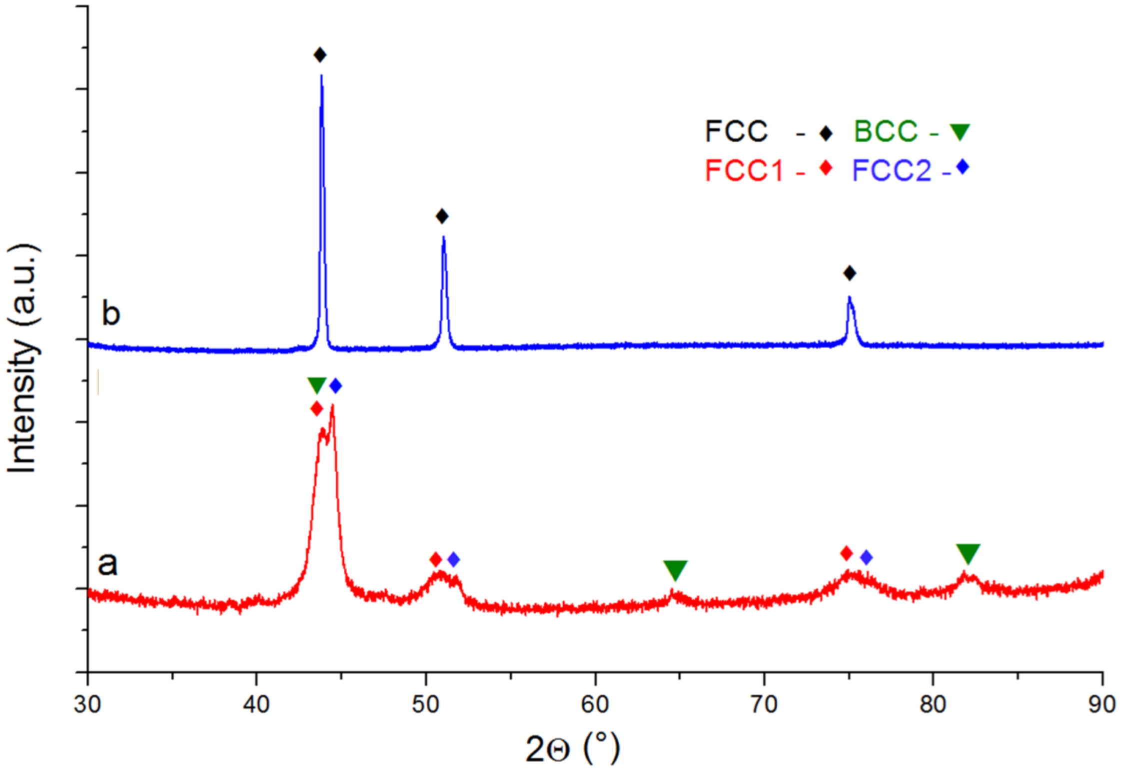

Fig. 67 XRD pattern of a) $\mathrm{Co_{1.5}Ni_{1.5}CrFeTi_{0.5}}$ MA powder; b) $\mathrm{Co_{1.5}Ni_{1.5}CrFeTi_{0.5}}$ sintered bulk alloy.

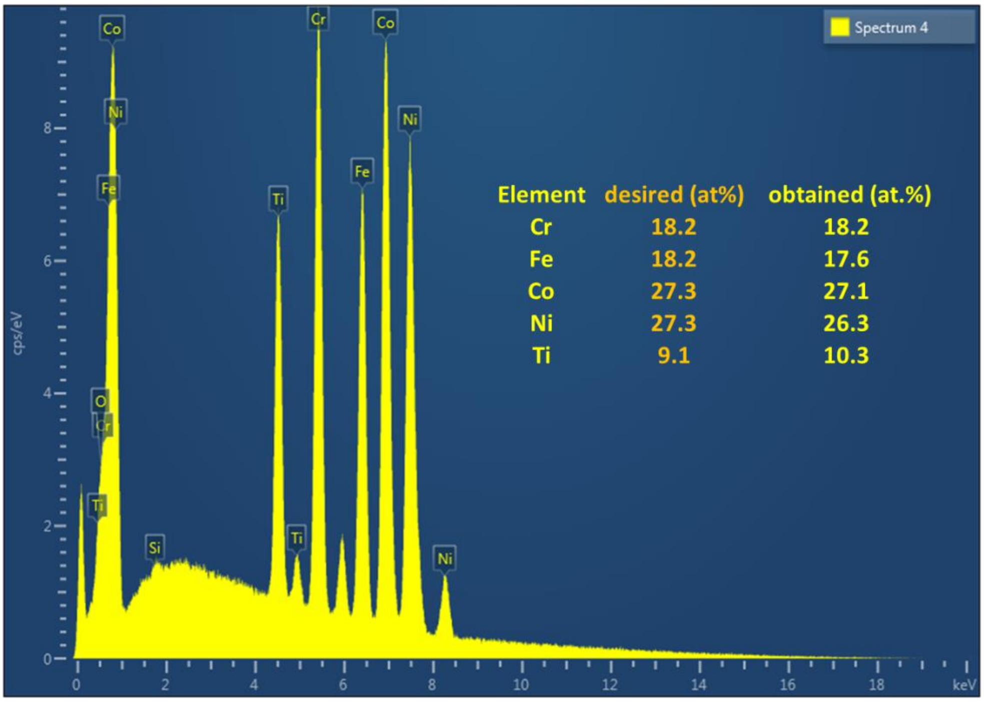

Element	desired (at%)	obtained (at.%)
Cr	18.2	18.2
Fe	18.2	17.6
Co	27.3	27.1
Ni	27.3	26.3
Ti	9.1	10.3

Fig. 68 Chemical composition of $Co_{1.5}Ni_{1.5}CrFeTi_{0.5}$ bulk alloy measured by area SEM EDS.

The microstructure of the alloy in BSE SEM mode is demonstrated in Fig. 69. The first striking microstructural feature visible on the images is the extremely fine grain size of the present single FCC phase. The size of the most grains was measured to be well under 1 µm, as measured later by EBSD. Even finer annealing twins are present within the grains, suggesting the possibility of low stacking fault energy (SFE) levels of the present FCC phase.

Second visible microstructural components are the black contrast dots. These black areas do not pertain to porosity, as 100% density of the bulk material was observed. No pores were observed by SEM and the density, measured by Archimedes method, exceeded 100 % of the theoretical one, that is 7.80 g cm^{-3}. Instead, they represent oxides with diverse sizes revealed by the EDS measurement to be mostly containing Al and Ti elements. Only the nature of oxide particles possessing the largest size was measured, due to the resolution limit of SEM EDS. The oxides of Cr, previously detected in the milled powders, were not observed in the microstructure. During the high temperature sintering, the diffusion rates were sufficient to induce the displacement reaction between the Cr oxides and present metallic elements, resulting in the change of nature and slight coarsening of the oxide particles. The formation of Ti and Al oxides is thermodynamically more favorable, due to the higher affinity of mentioned elements towards oxygen. The same phenomena have been observed previously in $AlCoCrFeNiTi_{0.5}$ alloy composition.

The present oxide phases were not detected by the XRD analysis. The substantial explanation for this may be the insufficient total amount of these phases to produce distinguishable diffraction peaks in the XRD pattern i.e. 3-5 % of volume fraction is generally taken as the resolution limit of XRD. The oxides of different elements, also different metal to oxide ratios, crystalize in wide array of crystallographic systems, depending on their chemical compositions. Also, the oxides with mixed nature may appear in systems composed of several similar metals, e.g. spinels. Consequently, they may have produced relatively high number of non-overlapping XRD peaks, hidden in the background noise of XRD.

The extremely fine grain sized nature of the produced bulk alloy, later quantified by the EBSD, is the result of extreme grain refinement i.e. severe plastic deformation that the powders were subjected to during the MA process. Even through some level of grain coarsening took place during SPS densification – as observed from broader XRD peaks in state after MA, as compared to as-SPSed. The processing time of SPS densification is short enough to prevent excessive grain coarsening during the high temperature dwell time. The oxide particles may have played a significant role in the grain growth suppression too, due to their pinning effect on moving grain boundaries.

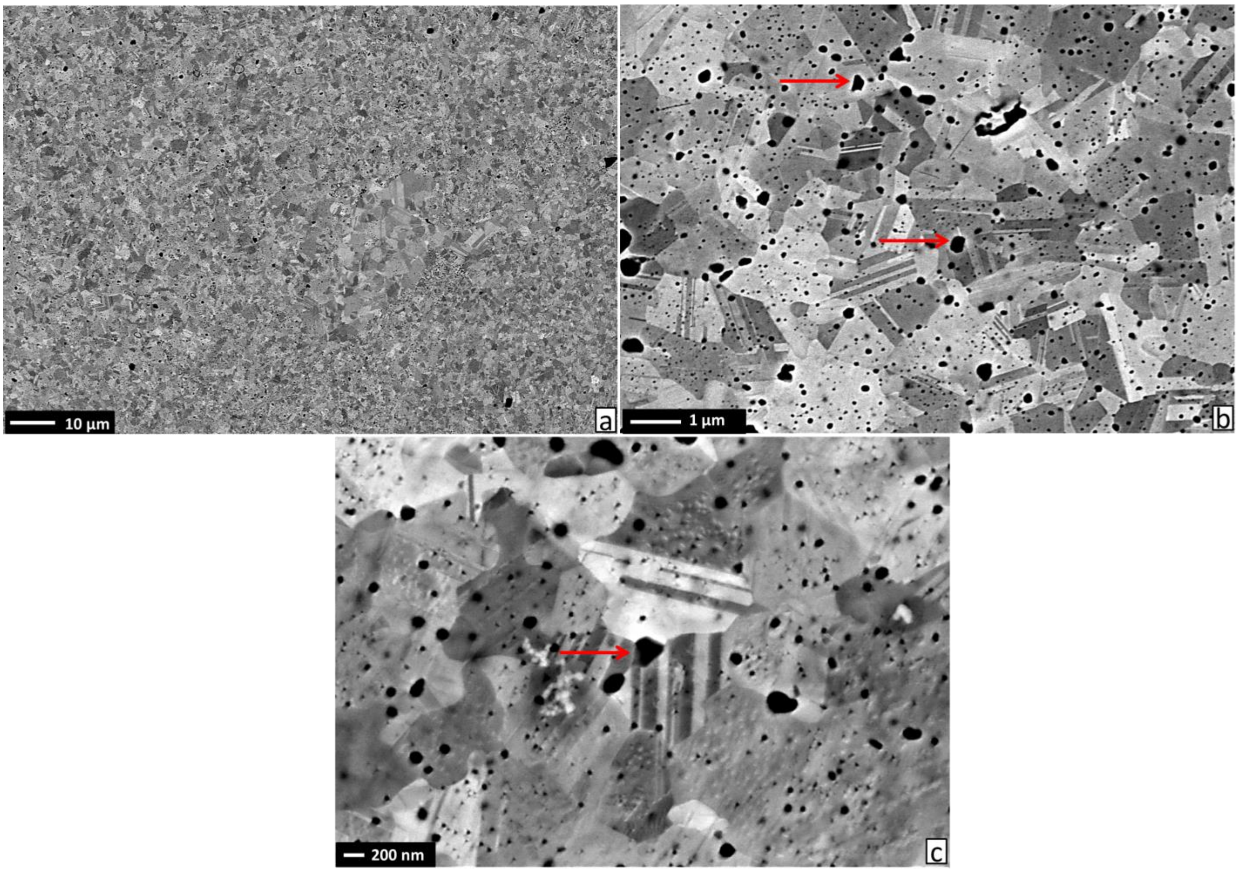

Fig. 69 SEM micrographs in back scattered mode (BSE) of $Co_{1.5}Ni_{1.5}CrFeTi_{0.5}$ bulk alloy in different magnification, with Al and Ti oxide particles marked by red arrows.

For a more accurate determination of the phase composition and consecutive grain orientation and size analysis, EBSD measurement has been performed with the results presented in Fig. 70.

The microstructure is composed of sole FCC phase grains (with corresponding Kikuchi diffraction pattern presented in Fig. 70 c), with lattice parameter matching the parameter measured by XRD analysis - 3.57 Å. The orientation map and attached pole figures reveal the lack of any preferential orientation of the FCC phase grains. The absence of any form of texture in the bulk alloy is relatively unexpected phenomena, considering the mechanism of SPS densification. During the SPS process, an uniaxial pressure is applied to the densified powders (section 4.2), causing plastic flow of material mostly in directions perpendicular to the pressing direction. As a consequence, certain degree of preferential orientation of grains was expected. It can be assumed that the applied pressure - 30 MPa - is not sufficient to evocate the considerable change of grains lattice orientation, while any remaining orientation was probably removed due to consecutive dynamic recrystallization process that acted during the densification dwell time and cooling.

The determined average grain size is - as expected – extremely small, 1.05 μm. This value is on the boundary lying between the nano and fine-grained materials as 1 μm is usually taken as the limit grain size, under which the materials are referred to as nano grained [85]. The size distribution presented in Fig. 70 b is pointing out to relatively non – uniform grain size, e.g. 80% of the present grains is bearing the diameter bellow 0.5 μm, with few larger grains of higher diameter, that increase the total value of average grain size, calculated as a weighted average value.

A large volume of annealing twins was detected by the EBSD method as well. Twining boundaries with typical miss-orientation angle of 60° are highlighted by wider black lines in Fig. 70 a. It should be noted that, the apparent density of the twins appears somewhat lower with respect to the images in Fig. 69 b and d, as the finest twins are not highlighted due to resolution constraints.

For the purposes of deep microstructural analysis, especially focused on the evidence of the single phase nature of the bulk alloy, TEM observation has been performed. The results are demonstrated in Fig. 71.

The observation confirmed the previous findings, i.e. the microstructure of the alloy is composed of single FCC phase and oxide inclusions of diverse size and chemical nature. Intermetallic precipitates are not present, despite the theoretical predictions. The FCC grains contain rather high volume of annealing twins. Some of the twin lamella size is in range of tens of nanometers, for instance denoted by yellow arrow in Fig. 71 a).

The observed oxides may be divided in two categories (observed by both, SEM and TEM): grain boundary oxides and the oxides dispersed inside the FCC grains, respectively. Grain boundary oxides are, in general, much coarser. The reason for this is the significantly higher diffusion flow on the grain boundaries as compared to the diffusion inside the grains. The higher diffusion rates generate more favorable condition for the consecutive coarsening of oxide particles during the high temperature exposure. On the contrary, the oxides present inside the individual grains form homogenous dispersion of extremely fine particles, highlighted by yellow circular area in Fig. 71 b). Such particles act as obstacles for the movement of dislocations, i.e. providing the Orowan strengthening effect. The arrangement of dislocation loops pinned on the oxide particles is observed on several places in the microstructure, denoted by red arrows in the images of Fig. 71.

The oxide strings, denoting the original boundaries of the milled and densified powder surfaces, sometimes present in PM bulks, were observed only on few occasions, as seen later in Fig. 75 d).

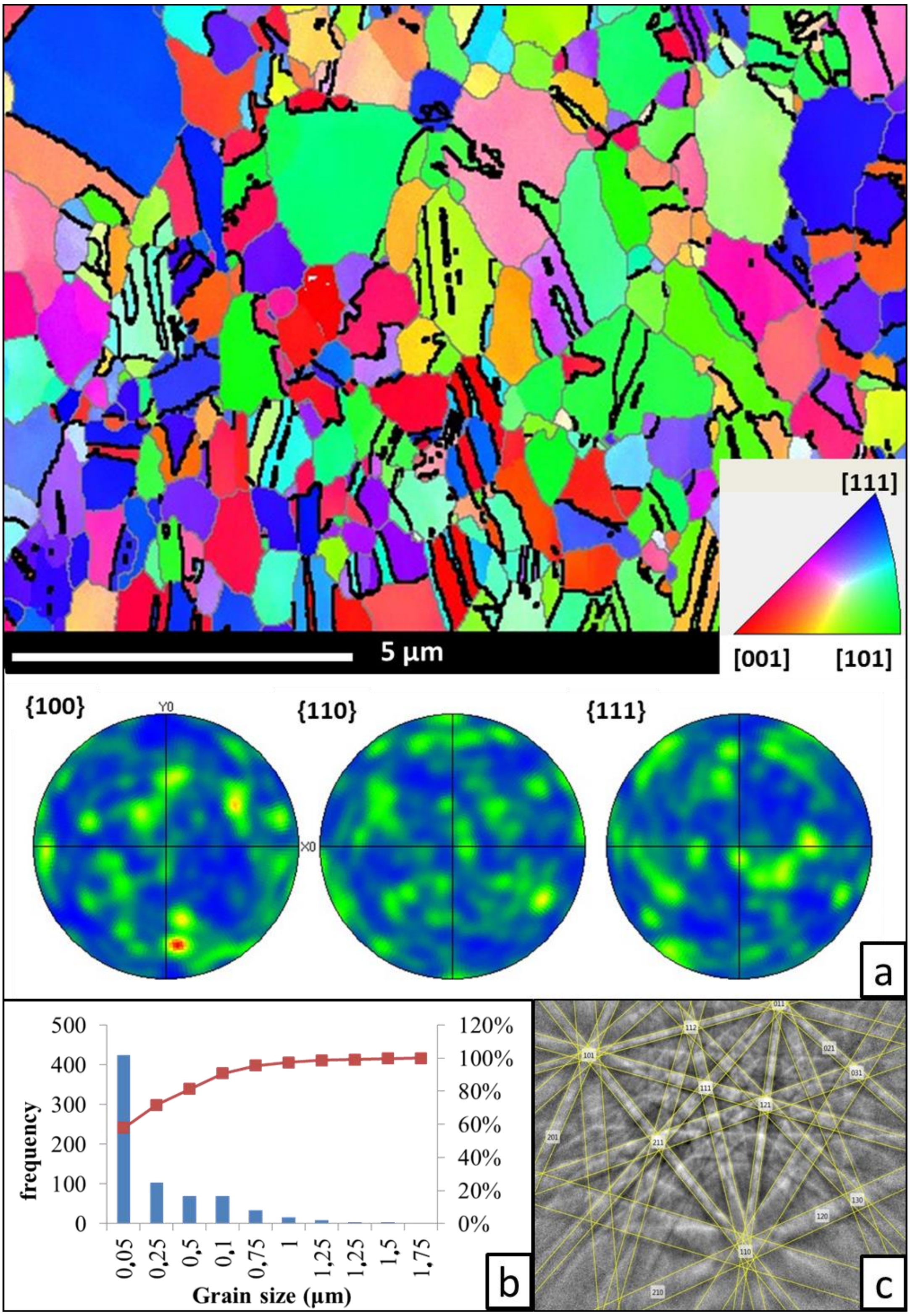

Fig. 70 SEM EBSD analysis results of Co$_{1.5}$Ni$_{1.5}$CrFeTi$_{0.5}$ bulk alloy representing: a) color orientation map with pole figure revealing single phase FCC bulk material with twin boundaries denoted by black lines showing no significant preferred orientation of grains; b) grain size distribution; c) diffraction pattern corresponding to FCC phase.

As observed by TEM EDS analysis, the microstructure is chemically very homogenous with all elements evenly distributed in the FCC grains. The oxides of diverse sizes present in the microstructure are revealed to contain Ti and Al elements – corresponding to SEM findings with the TEM EDS maps are provided in appendix Fig. A 3. The higher fraction of oxide particles belongs to Ti.

Fig. 72 represents the results of TEM SAED analysis. The diffraction pattern of single grain is presented in Fig. 72 b, matching the diffraction spots for FCC lattice. The diffraction of single oxide particle lying on the edge of TEM foil has been identified to match the calculated hexagonal α-Al_2O_3 pattern (denoted by red dots).

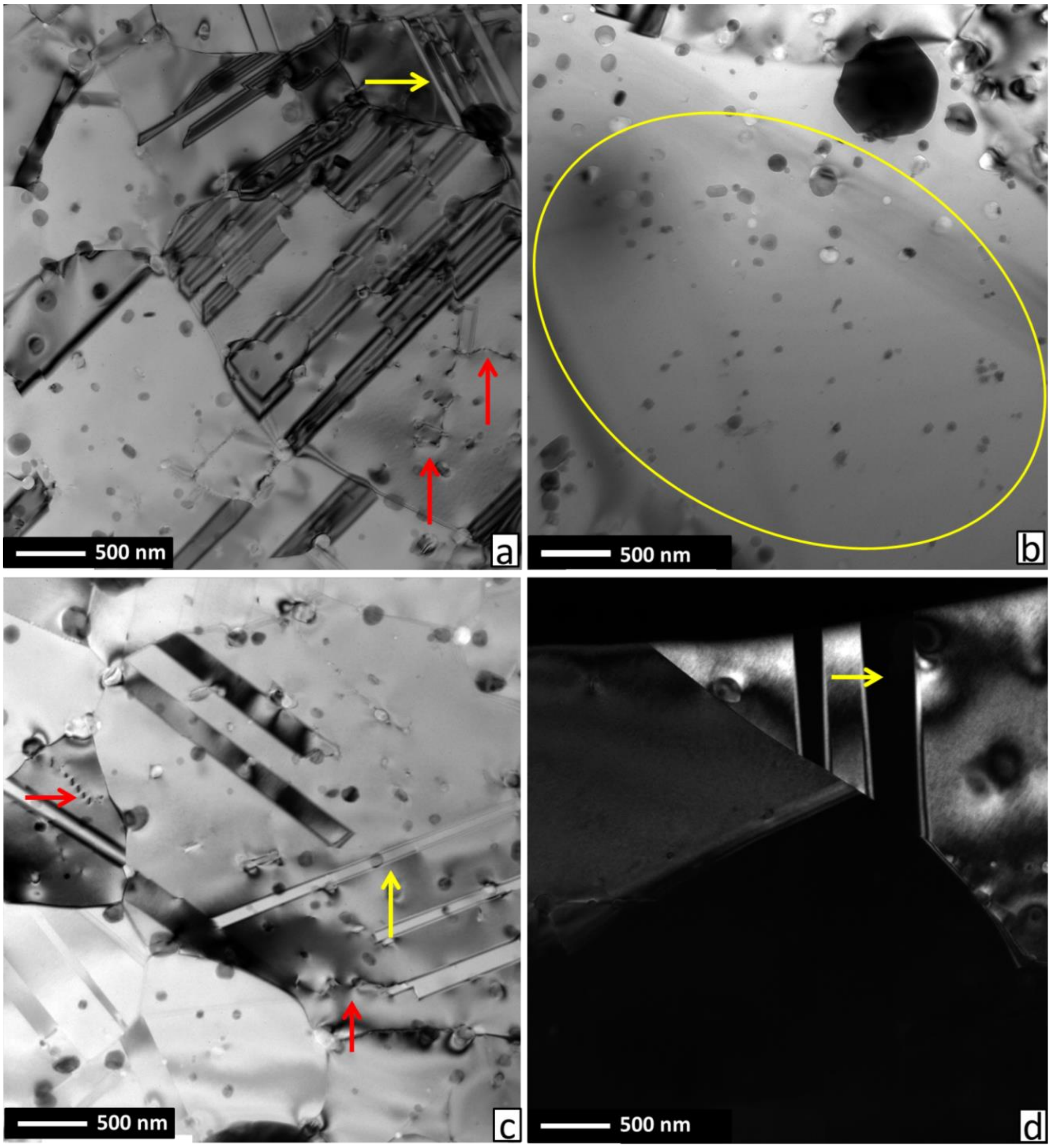

Fig. 71 TEM micrographs of $Co_{1.5}Ni_{1.5}CrFeTi_{0.5}$ bulk alloy with dislocation loops and nano-size twins denoted by red and yellow arrows respectively a), c) FCC grain microstructure; b) oxide dispersion in coarser FCC grain; d) dark contrast image with denoted twins starting on grain boundary.

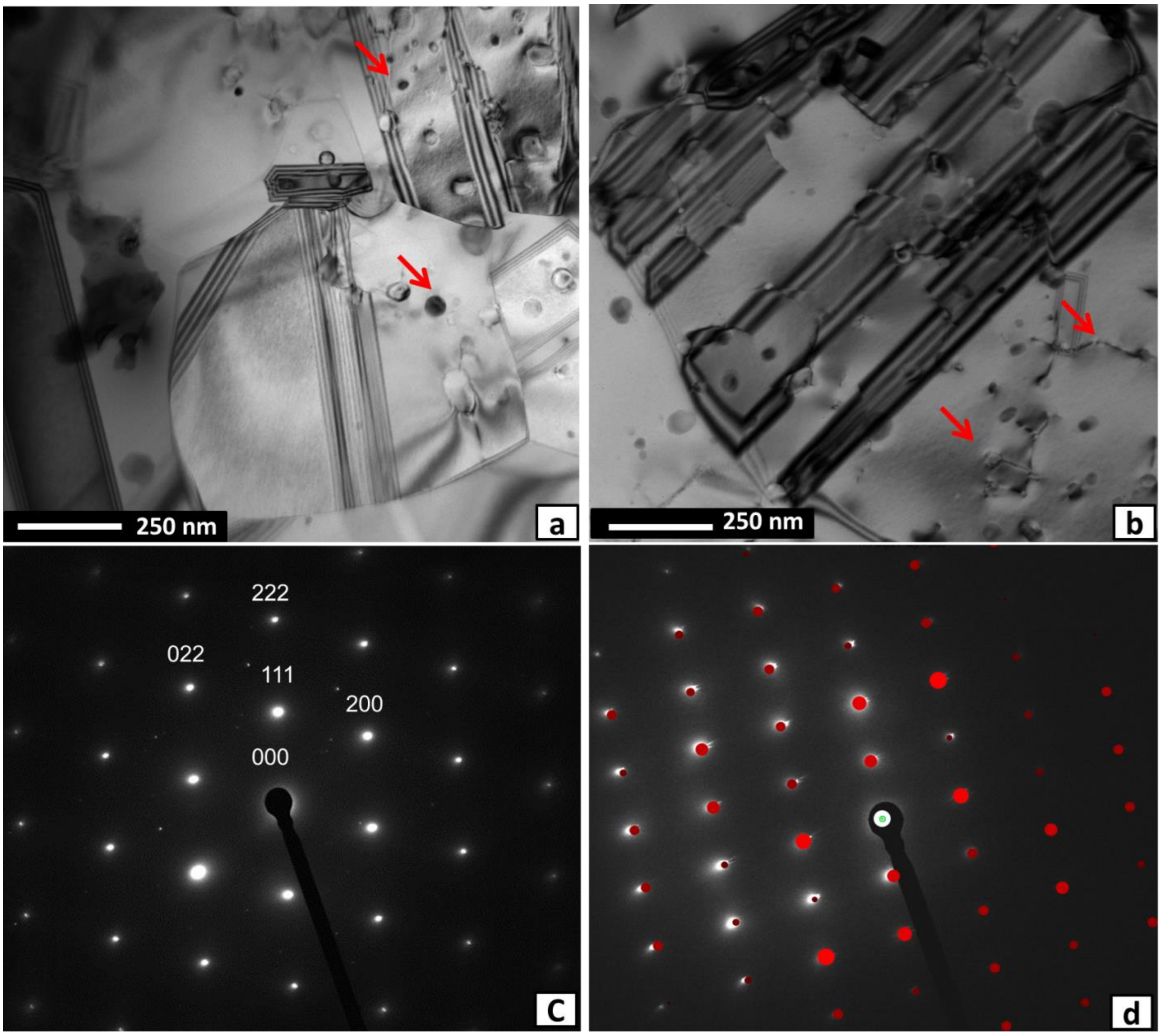

Fig. 72 TEM micrographs of a) FCC grain in 110 orientation; b) corresponding SAED pattern of FCC grain in 110; c) coarser Al_2O_3 particle; d) corresponding SAED pattern of Al_2O_3 particle with matching calculated reflections.

Fig. 73 denotes the results from DSC analysis of bulk $Co_{1.5}Ni_{1.5}CrFeTi_{0.5}$ alloy. The start of the curve has a distinctive shape. The heat flow is gradually increasing from the beginning of the test up to around 700 ºC, where the heat flow reaches the maximum value. With further increase in temperature, the heat flow decreases. This behavior is supposedly connected to the thermal behavior of the alloy (heat capacity), i.e. it does not suggest anything about the phase transformation phenomena. The DSC curve lacks any sharp change in its continuity. The small peak at 1020 ºC may correspond to the start of some sort of phase transformation, however, not very significant. The discontinuity appearing at 1280 ºC is probably attributed to start of the melting of the alloy.

In general, the alloy does not undergo any sudden significant phase transformation, revealing rather high microstructural stability. The phase changes in the material are either very slow or not present at all.

The measured hardness value is 443 ± 29 HV0.3 – a value that is relatively high for the material possessing pure FCC microstructure, suggesting the pronounced influence of extensive solid solution strengthening, coupled with strengthening by grain refinement and dispersion of present stable oxides.

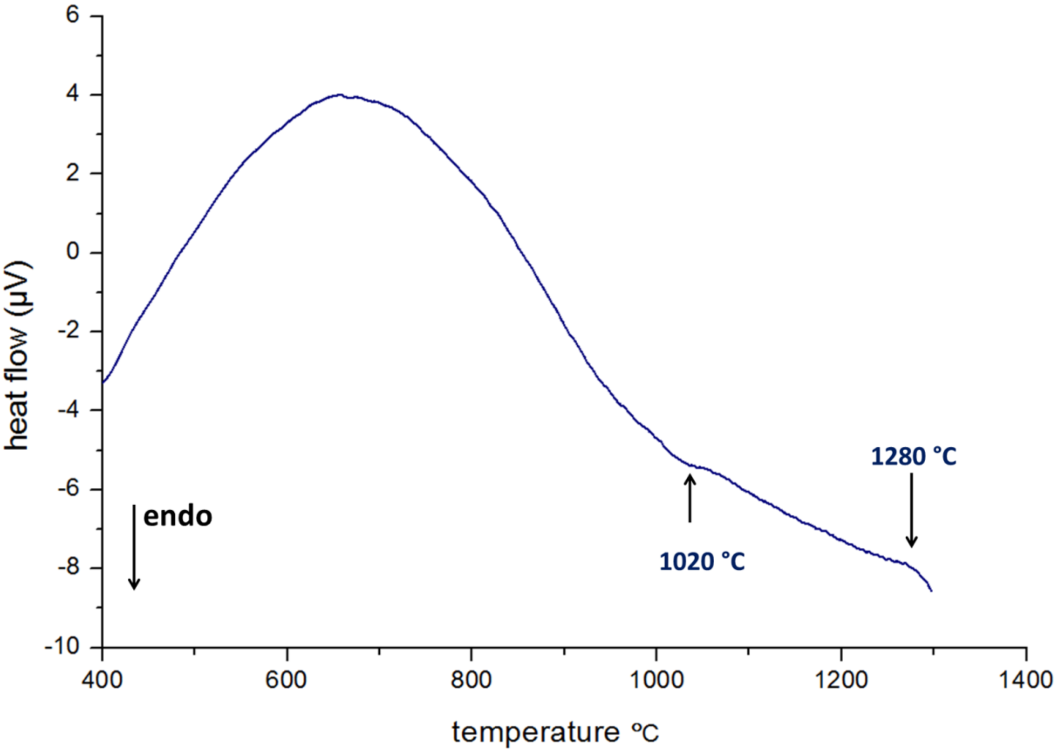

Fig. 73 DSC measurement of heat flow during heating of $Co_{1.5}Ni_{1.5}CrFeTi_{0.5}$ bulk alloy sample.

$Co_{1.5}Ni_{1.5}CrFeTi_{0.5}$ alloy bend test

The room temperature bend strength (R_{mb}) of the $Co_{1.5}Ni_{1.5}CrFeTi_{0.5}$ alloy was measured on 6 samples. Fig. 74 and Table 10 represent the determined values. In respect to previous results obtained on $AlCoCrFeNiTi_{0.5}$ bulk alloy, the $Co_{1.5}Ni_{1.5}CrFeTi_{0.5}$ alloy possesses significantly higher values of bending strength and ductility (prospective value of deflection was taken as a measure of ductility). The stress – deflection curve can be easily separated into an elastic part with deflection being directly proportional to applied force, i.e. linear response of the material, and a plastic part of the curve, deviating from linearity. The deflection corresponding to the plastic part of the curve accounts for more than 2/3 of the total deflection value, pointing out to the pronounced plastic deformation occurring before the fracture of the specimens. This is a remarkable improvement, as compared to the pure brittle fracture of previous alloys.

The R_{mb} values are statistically more consistent, showing not too high deviations from the average value. This is the consequence of significantly more ductile materials behavior. The material is able to dissipate the elastic energy generated from the applied external force by prospective plastic deformation, before the subsequent crack initiation and growth, as opposed to the abrupt rapid material fracture after elastic loading, in case of brittle fracture behavior observed in $AlCoCrFeNiTi_{0.5}$ alloys.

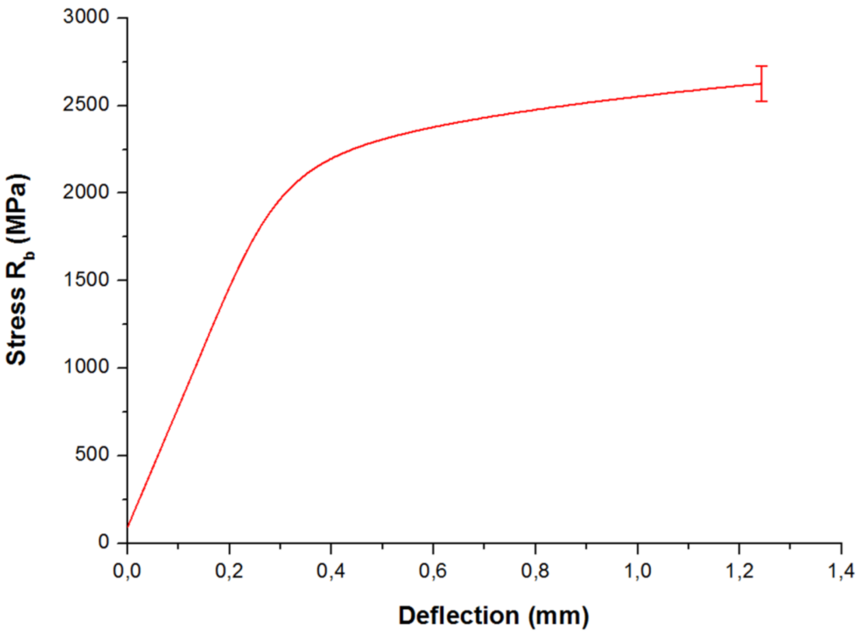

Fig. 74 Representative stress – deflection curve from three point bending test of $Co_{1.5}Ni_{1.5}CrFeTi_{0.5}$ bulk alloy at room temperature.

Table 10 results of three-point bending test on $Co_{1.5}Ni_{1.5}CrFeTi_{0.5}$ bulk alloy after SPS.

Sample	R_{mb} (MPa)	E (GPa)	Max. deflection (mm)
1-6 after SPS	2593 ±102	99.06	0.98 ± 0.19

The reason behind the dramatic increase in $Co_{1.5}Ni_{1.5}CrFeTi_{0.5}$ alloy mechanical properties (in contrast to alloy A, B and C) may be assumed from its phase composition. The absence of significant amount of B2 and TiC ordered phases should, in theory, result in the intrinsic toughening of material, but, on the other hand, decrease in the strength should be expected as well.

Experimental results suggest that the ductility of the alloy was indeed significantly improved. Interestingly, as opposed to prediction, the strength values were significantly increased as well.

SEM micrographs of the fractured bending specimens are presented in Fig. 75. The crack initiation site is located approximately in the middle of the sample side subjected to the tensile stress during bending specimen (denoted by red arrow). Therefore, the crack initiated on the surface defect, or on the microstructural defect present on the sample’s surface.

The fracture surface is composed of equiaxed ductile dimples, foreshadowing the material failure in a ductile manner, by microvoid coalescence. The mechanism of the ductile fracture is such that, at a critical point after the start of pronounced plastic deformation, the crack initiates simultaneously on several different places in the sample cross section by the interfacial decohesion, forming small voids in the process. The voids nucleate usually on present microstructural defects (e.g. non-metallic inclusions). As the stress increases, the growth of individual voids takes place. In the last stage of the prospective fracture process, the voids join and form the magistral crack.

The diameter of the individual voids is occasionally considered as a measure of the material plasticity. The voids present on the fracture surfaces, visible on higher magnification image (Fig. 75 c), are extremely small. These observations suggest that, even though the material failed in the ductile manner, the plasticity was not sufficient to support distinctive void growth. The particles that initiated the voids formation are present only in small number of dimples on the fracture surface (one such particle is denoted by yellow arrow). Therefore, there is a possibility that the void formation was initiated not solely on the oxide particles, but on the other weakening microstructural features simultaneously (triple junction of grain boundaries, intersections of slip planes, etc.). This is a consequence of the extremely fine grain size and the high material strength.

The polished side of the section perpendicular to fracture surface of the bending specimen presented in the Fig. 75 d reveals that the secondary cracks did not appear in the material throughout the bending test duration. Additionally, it seems that, some of the oxides form strings along the original boundaries of powder particle prior to densification, visible as lines of black dots. Interestingly, the crack path does not follow these strings; fact pointing out to high adhesion of oxide/FCC interface.

In summary, according to the result of later observation, it seems that the alloy fracture behavior is mixed in nature. It contains a typical morphology of ductile material, as only the dimples are present on the fracture surface. However, the crack initiates on the sample surface the behavior observed in brittle fracture cases (as opposed to non well-defined crack initiation site located in the middle of the specimen in a case of typical ductile fracture).

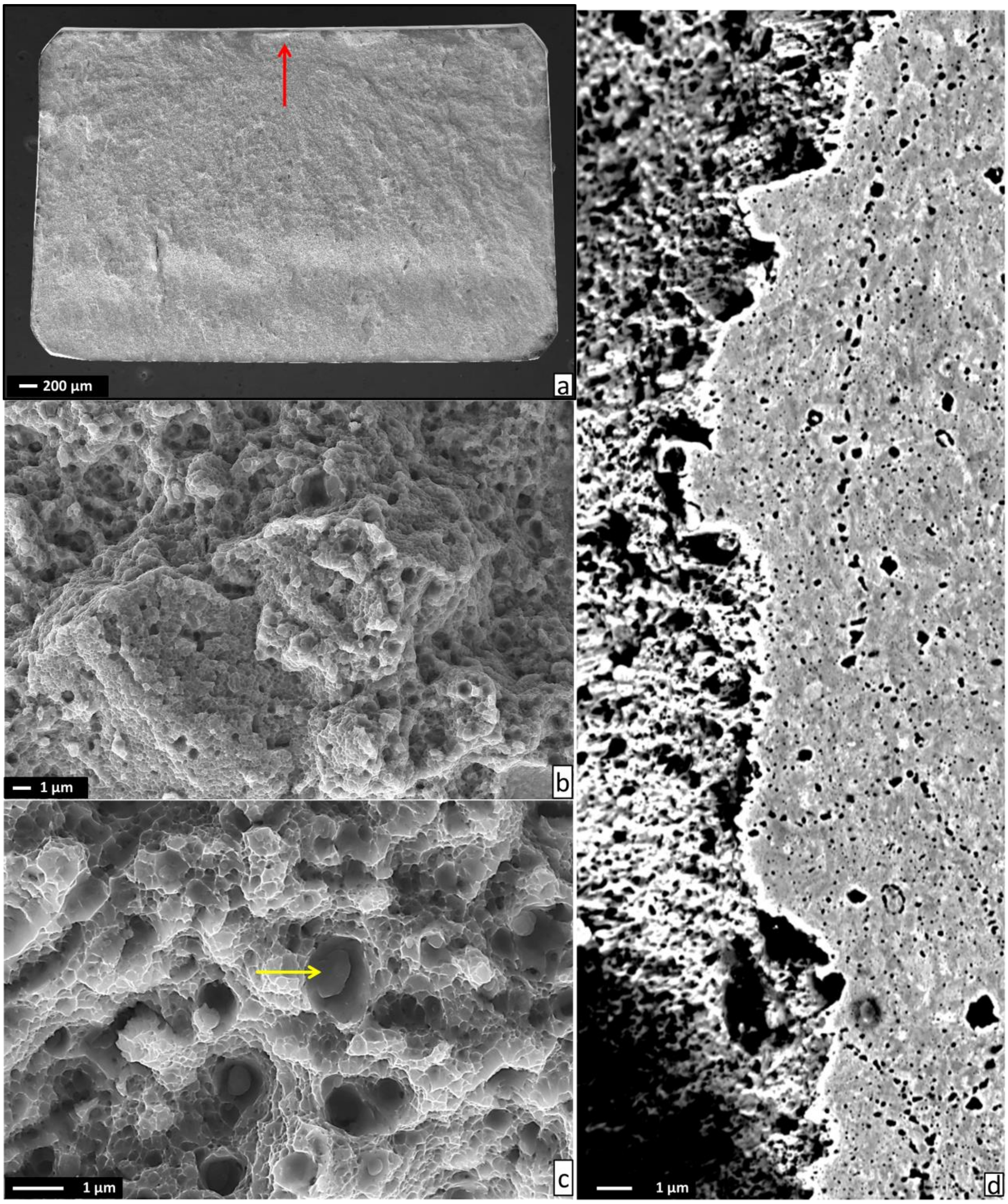

Fig. 75 SEM micrographs of a) fracture surfaces of $Co_{1.5}Ni_{1.5}CrFeTi_{0.5}$ bulk alloy bending specimens with tensile side of sample above b, c) details of fracture surface taken close to the initiation site d) view of polished fractured surface perpendicular to fracture surface specimen in ECCI mode.

An additional distinctive feature has been exposed on the fracture surfaces of some samples, presented in Fig. 76a, denoted by red arrows. It seems that an additional inclusion phase with significantly coarser grains is present in the microstructure. The phase is also visible in the microstructure of polished fractured bending specimen displayed in Fig. 76 b. Multiple cracks are visible inside the observed phase (highlighted by yellow arrow), while the surrounding FCC grains does not show any sign of sustained damage. The stress in the observed area during bending test duration was not sufficiently high to induce any observable changes in the FCC grains, while the inclusion phase has been cracked multiple times. It leads to a conclusion that the phase is significantly brittle in its nature, with greatly reduced mechanical properties, as compared to major FCC phase. The results of the performed point EBSD and EDS analysis (Fig. 76 c, d respectively) revealed that the phase contains Cr as the main element, with the corresponding BCC lattice. The determined lattice parameter is 2.88 Å e.g. close to pure Cr element.

These few inclusions appeared most probably as a consequence of the small number of present Cr particles that were not broken and mechanically alloyed in the milling process. These particles, then, reacted with the surrounding material, forming the observed BCC phase grains. However, the diffusion rate and high temperature dwell time were not sufficient to induce their complete dissolution in FCC grains. Prior to the densification procedure, MA powder cross section was checked, to ensure the demanded microstructural homogeneity (paragraph 7.3.1). Unfortunately, it seems that a very small fraction of unmilled Cr remained in the powder, causing the observed type of Cr inclusions.

The present Cr inclusions are brittle in nature. However, due to their extremely small volume and the ductile character of the surrounding FCC phase, it seems unlikely they significantly impaired the determined mechanical properties.

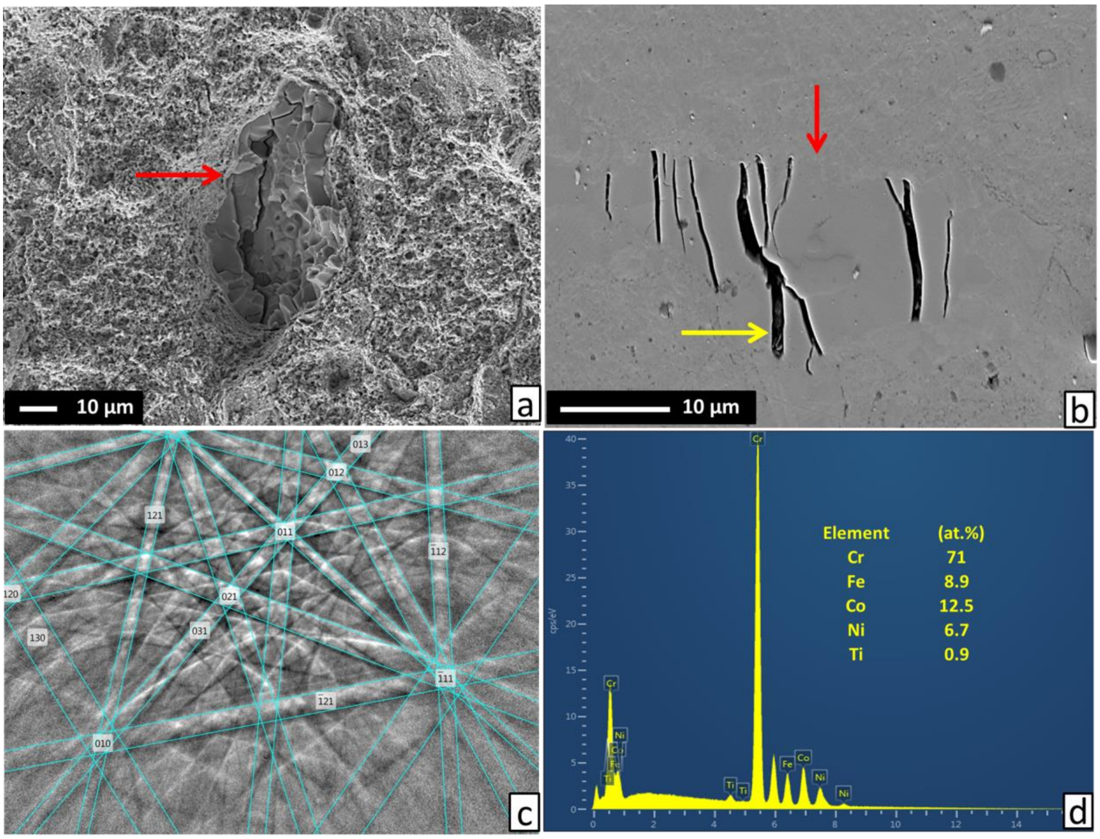

Fig. 76 Cr impurity particle embedded in FCC phase a) SEM micrographs of inclusion phase on fracture surface; b) cracked phase on the polished fractured specimen in direction perpendicular to fracture surface; c) corresponding electron diffraction pattern of cracked phase d) EDS microanalysis.

$Co_{1.5}Ni_{1.5}CrFeTi_{0.5}$ alloy tensile test

The good level of ductility possessed by the alloy, which was observed during the bend test, enabled to assess its performance in a regular tensile test. The measurement of tensile properties provides a credible data readily comparable with the commercial alloys and other HEA systems as well.

The room temperature ultimate tensile strength (R_m) was measured on 1 sample only, due to the relatively small amount of available bulk material, with the samples of with 12.5 mm gauge length (as described in 6.3). The results presented in Fig. 77, with evaluation of the test in Table 11, indicate the excellent mechanical properties of the produced alloy. It should be noted that the values of elastic constant E = 216 GPa were obtained from the impulse vibrational testing method (not from tensile test), to evaluate elastic properties more accurately.

The excellent strength properties, in combination with good ductility (for the materials of this strength level), are originated from a combination of strengthening mechanisms present in the material. The most pronounced effect on the increase in strength should originate from the extremely fine grain size of the material. The inherently ductile, fine grained FCC phase, provides the ductility, while the significant amount of grain boundaries acts as obstacles for the consecutive dislocations movement during mechanical loading and thus provide increased strength. Due to high value of atomic size misfit δ (5.04 %), FCC phase should possess high strength on its own accord, as a consequence of extreme substitutional strengthening – inherent property to all single phase HEAs. The presence of hard oxide particles should also play a role in the high strength properties directly, thanks to Orowan strengthening mechanism, and indirectly by the grain growth suppression.

The strain hardening coefficient, determined by usual hardening analysis, has relatively low value of 0.11. Low strain hardening is also exhibited by relatively small difference in the respective values of $R_{p0.2}$ (0.2% proof strength) and ultimate tensile strength R_m: only 76 MPa. The reason for this behavior is that the alloy is already extensively strengthened prior to mechanical testing, as proved by the high $R_{p0.2}$ value of 1308 MPa. The already high proof strength of the alloy has a deleterious effect on any additional strain hardening, as the dislocation density is already high (dislocation forming the grain boundaries as well as GNDs around oxides), with the new dislocations formed during tensile test unable to pass through the lattice.

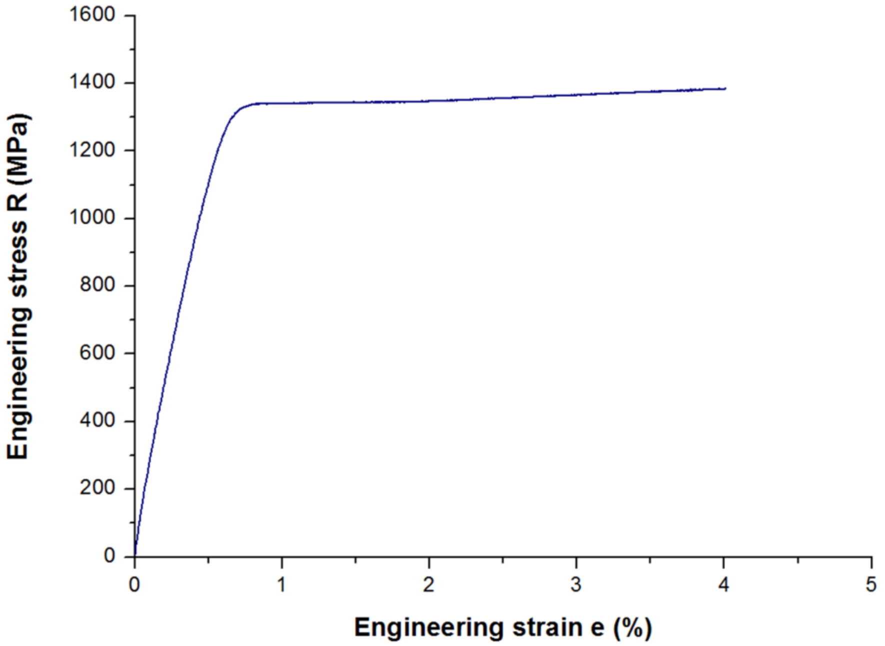

Fig. 77 representative engineering stress – strain curves from tensile test of $Co_{1.5}Ni_{1.5}CrFeTi_{0.5}$ bulk alloy at room temperature.

Table 11 Tensile strength test properties of $Co_{1.5}Ni_{1.5}CrFeTi_{0.5}$ bulk alloy.

Sample	$R_{p0.2}$ (MPa)	R_m (MPa)	Elastic modulus E (GPa)	Elongation to fracture A_t (%)	Strain hardening coefficient n (-)	Reduction Z (%)
1	1308	1384	216	4.01	0.11	5.04

Fig. 78 demonstrates the results of the fractographic and microstructural analysis of the ruptured tensile specimen. In general, the features observed on the fracture surface are identical (Fig. 78 a, b, c) with the previously presented bending test samples. The initiation site of the starting crack, denoted by red arrow in Fig. 78 a, is located on the surface of the specimen. The sample exhibited a rather ductile fracture behavior, as the fracture dimples are observed again on the whole fracture surface. The presence of Cr phase inclusions has been documented again.

The microstructure of the polished cross section of the broken tensile specimen from the vicinity of the crack reveals the extensive level of localized plastic deformation near the vicinity of the crack (presented in Fig. 78 e). The original microstructure with well-defined fine grain boundaries prior to tensile testing has been broken down to such extent, that the original grain boundaries are not visible. The white – dark contrast in the BSE mode suggests the extensive dislocation activity, taking place before the onset of cracking. Fine deformation twins are present at several places of the sample (denoted by yellow arrow in Fig. 78 e). In particular, the area delimited by a yellow rectangle shows a place plastically deformed by dislocation glide, visible from dark – white – grey contrast from left to right, crossed by a number of twins with the same direction. The green arrow is pointing out to a long deformation twin, connected to multiple shorter deformation twins with different orientation – suggesting that, at least, two separate twinning systems have been activated. The yellow arrow in the Fig. 78 e points out to the place where several smaller twins are crossing longer twin with different orientation. In this particular case, it seems that the twins are not able to penetrate each other, which may serve as an additional strengthening phenomenon contributing to the overall strength of the alloy. The analysis of the deformation twins has not been carried out due to the resolution constraints of the SEM EBSD method as a consequence of their extremely small thickness.

It seems that the plastic deformation in the alloy is carried out by a combination of dislocation glide and deformation twinning. In the most deformed FCC grains - possessing the orientation of their slip and twinning planes close to parallel in respect to the tensile stress axis - dislocation structures formed by both dislocation glide and deformation twinning are observed [26]. The grains that were in less favorable orientations are deformed only by the usual dislocation glide. The deformation twining explicitly acts as an additional deformation mechanism, activated at higher strain levels.

The black dots present in the microstructure, corresponding to oxide inclusions, appear to be well bonded to the FCC matrix, as there is no visible decohesion or crack initiation on the oxide/FCC grain boundaries in the severely plastically deformed material, as observed in the bend test specimen previously.

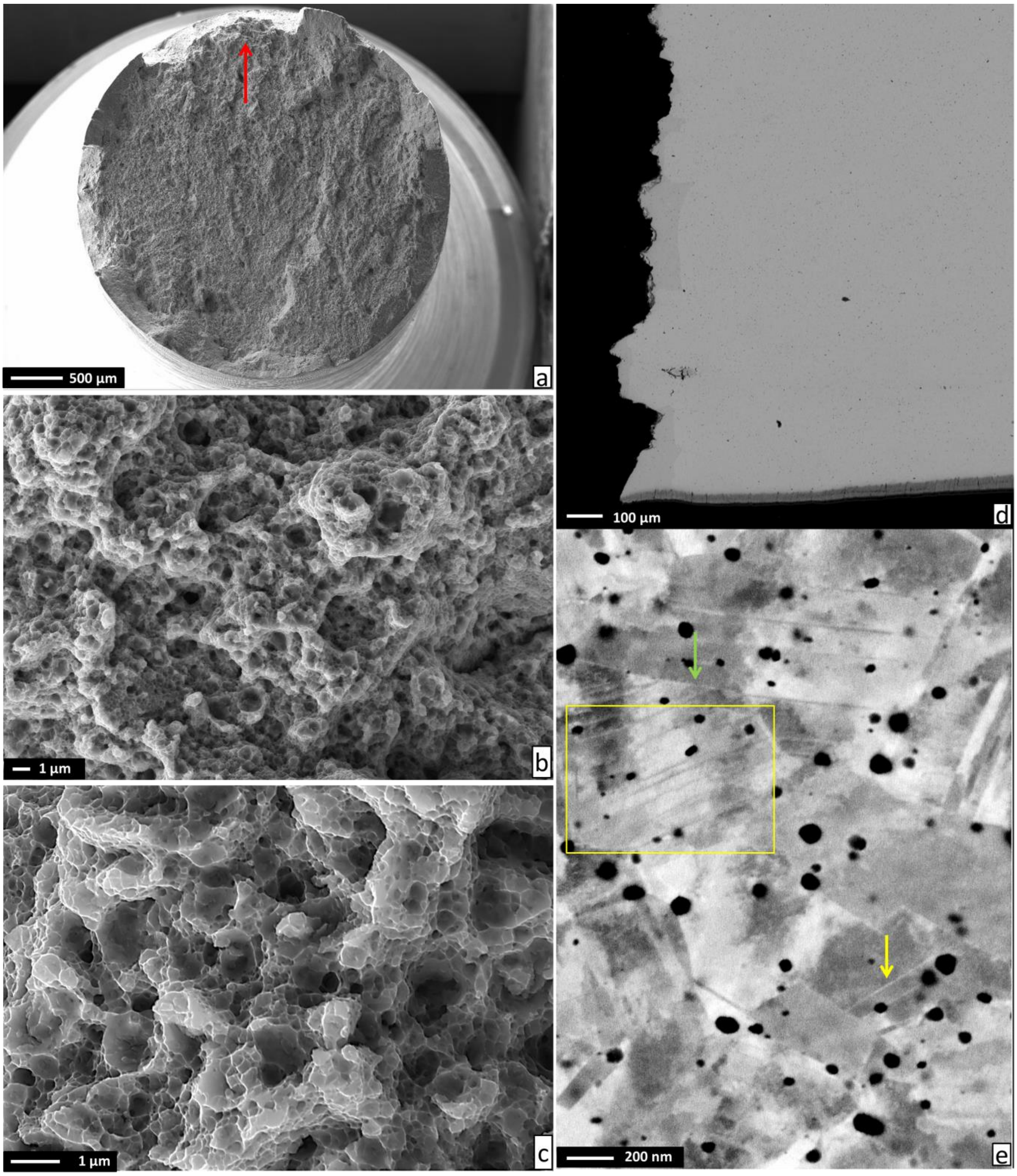

Fig. 78 SEM micrographs of a, b, c) fracture surfaces of $Co_{1.5}Ni_{1.5}CrFeTi_{0.5}$ bulk alloy tensile specimen, initiation site location is denoted by red arrow; d) view of the polished section perpendicular to fracture surface of specimen; e) the deformed microstructure from the vicinity of the crack in with twins denoted by yellow arrow.

7.4 CoCrNi alloy

The alloy composition selected for this study has been utilized with the respect to previous studies on cast materials, presented in the literature review in paragraph 2.4.1, that are pointing out to the tremendous potential of the alloy [45]. Thereby, the production of this alloy by PM route has been studied.

7.4.1 CoCrNi alloy powders

The XRD patterns of the blended and mechanically alloyed powders with CoCrNi composition are presented in Fig. 79. Peaks corresponding to the blended powders with Co, Cr and Ni elements were recognized in the patterns. In the pattern attributed to the state of the powder after the MA process (Fig. 79b), peaks corresponding to three different phases were observed. The dominant phase was an FCC Ni-based solid solution with a lattice parameter of 3.532 Å. The second and third phases are Cr-like BCC solid solution with 2.884 Å, and Co-like HCP phase with a = 2.487 Å and c = 4.132 Å, respectively. These phases are referred to as solid solutions, not the pure elements, due to a peak shift to higher angles, as compared to the corresponding pure elements. This peak shift was most probably caused by a partial dissolution of the other elements as a result of mechanical alloying reaction. All the peaks are significantly broadened as compared to the state before the milling. This is the result of the powder particles lattice distortion and high dislocation density induced by severe plastic deformation during the MA procedure. The same phenomena have been observed already in the study, in the case of AlCoCrFeNiTi$_{0.5}$ and Co$_{1.5}$Ni$_{1.5}$CrFeTi$_{0.5}$ alloy powders.

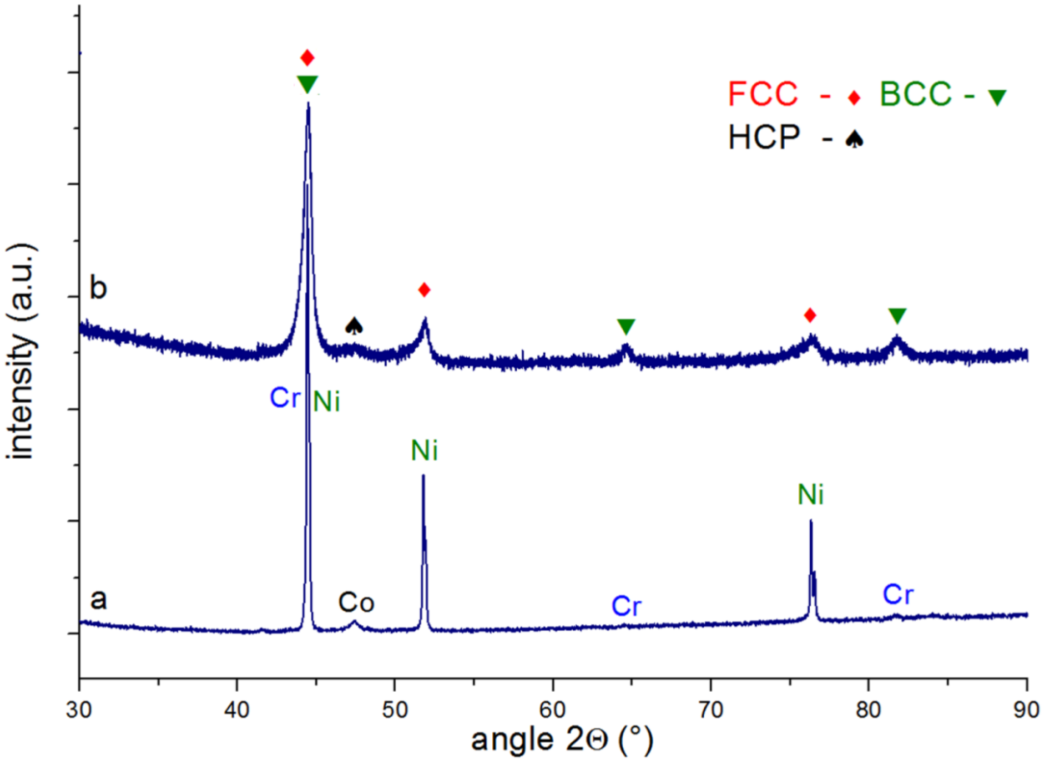

Fig. 79 XRD pattern of a) CoCrNi blended powder; b) CoCrNi mechanically alloyed powder.

Fig. 80 denotes the MA powder morphology, together with the polished cross-section micrographs of the powders. Considering the layered nature of the microstructure, the alloying process of the powders has not been fully completed after the milling, as the elemental particles have not been fully mixed – as explained beforehand in paragraph 4.1.1. Consecutive EDS mapping have been carried out (presented in the appendix in Fig. A 4), showing layers of original elements or rather their respective solid solutions.

Evidently, the prolonged milling time would result in the formation of fully alloyed powder microstructure. However, in this case, a problem of Fe contamination arises, as its amount present has been measured in the powder to be around 1 atomic % - as well as in the densified bulks (as will be presented later on). The prolonged milling would result in a more significant Fe contamination as a consequence of more conscious steel milling balls wear. As opposed to the other two studied composition containing Fe - there is no Fe present in CoCrNi alloy, therefore its presence may induce undesired phase transformations and microstructure alteration.

Nevertheless, the milling conditions were sufficient to promote mechanical activation to cause accelerated sintering, i.e. their diffusivity was increased due to a higher dislocation density and higher grain boundary area. This was later confirmed by a successful formation of a homogeneous microstructure after the SPS consolidation.

Save for the prolonged milling in toluene, applied due to a much more significant CoCrNi powder sticking to the milling media, the utilized milling conditions have been exactly the same as in the case of $Co_{1.5}Ni_{1.5}CrFeTi_{0.5}$ alloy, for which the formation of layered microstructure has not been observed. However, considering the presence of only 3 elements, as opposed to 5 for the latter alloy, it is to be expected that for the formation of perfectly mixed CoCrNi powders, longer milling times are needed with the preposition of the same weight of the powder charge.

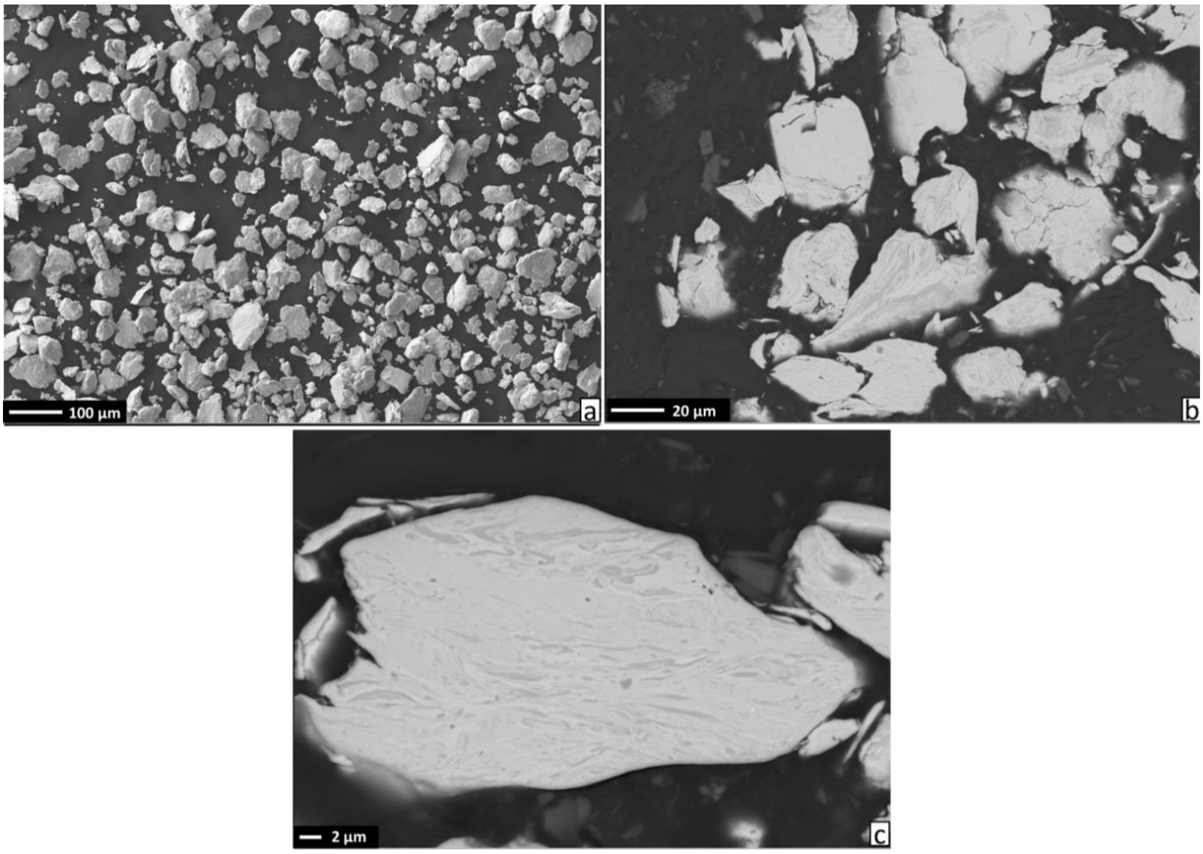

Fig. 80 SEM micrographs in BSE mode of CoCrNi powders a) powder morphology; b) powder cross-section; c) powder layered cross-section in higher magnification.

7.4.2 CoCrNi alloy bulk

The results of XRD analysis of the bulk CoCrNi alloy after SPS densification are provided in Fig. 81 together with the patterns of the milled powders, before the start of the sintering process. The major phase was an FCC solid solution with lattice parameter of 3.57 Å comprising 94.4 % of the bulk microstructure. In contrast to the expectations of pure single face microstructure (observed before in cast alloys, see 2.4.1), the minor BCC solid solution with 2.90 Å lattice parameter and 5.6 % fraction appeared as well. The peaks of the phases are much sharper and thinner as a consequence of bigger crystallite sizes. The Co-based HCP phase, observed in the milled powders, was not detected in the XRD pattern, as Co element probably dissolved in FCC solid solution.

The calculated values of δ, ΔH_{mix}, ΔS_{mix}, Ω and VEC are 0.36 %, -4.8 kJ mol^{-1}, 9.13 K^{-1} mol^{-1}, 3.53 and 8.33, respectively (formation of single solid solution microstructure predicted for $\delta \leq 4$ %, $-10 \leq \Delta H_{mix} \leq 5$ kJ.mol^{-1}, $\Delta S_{mix} > 13.38$ J.mol^{-1} and $\Omega > 1$). The theoretical density, calculated by rule of mixture, of CoCrNi composition is 8.28 g cm^{-3}. Considering the parameters, the formation of additional phase may have been expected – the value of ΔS_{mix} didn't reach the proposed minimum. It is an inevitable consequence of the alloy composition, provided that only three elements (Co, Cr and Ni) do not sufficiently increase the ΔS_{mix} values.

The Fig. 82 represents the results of area EDS chemical analysis. The CoCrNi bulk chemical composition is in very good agreement with the theoretical one. The undesired content of Fe in the alloy is explained by the abrasion wear of the steel balls during long term, high energy milling process. Given its negligible (0.8 at %) volume content and the similarity of iron atoms to chromium (both in size, properties and electron structure), such contamination should not induce any microstructural changes.

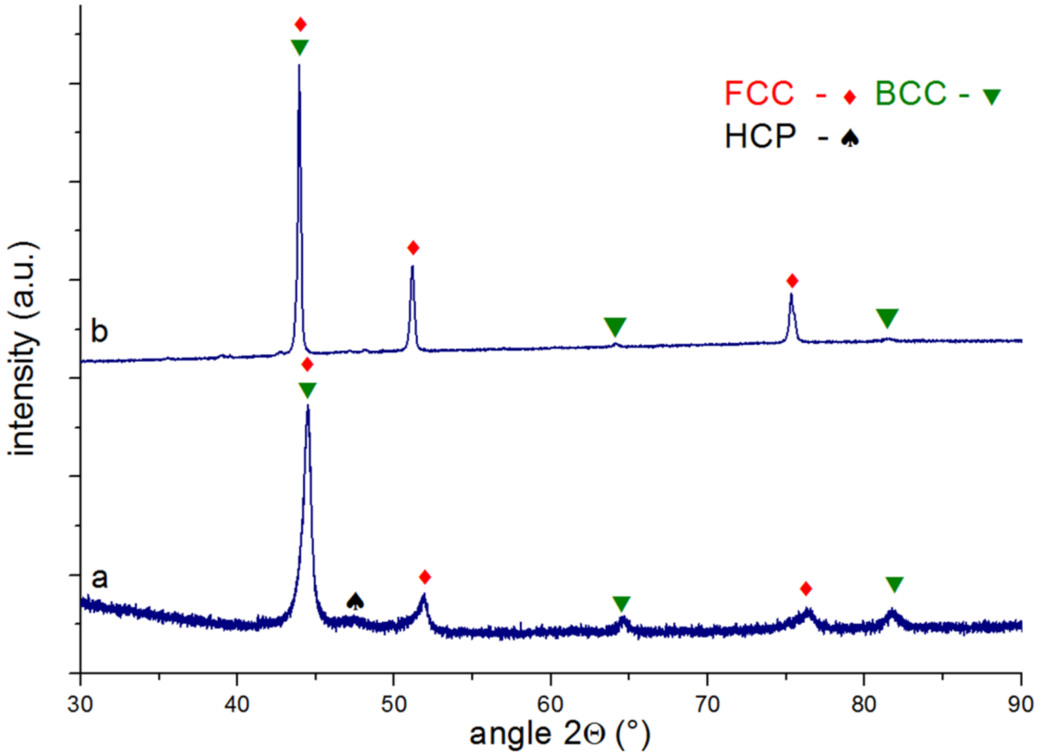

Fig. 81 XRD pattern of a) CoCrNi mechanically alloyed powder b) CoCrNi sintered bulk alloy.

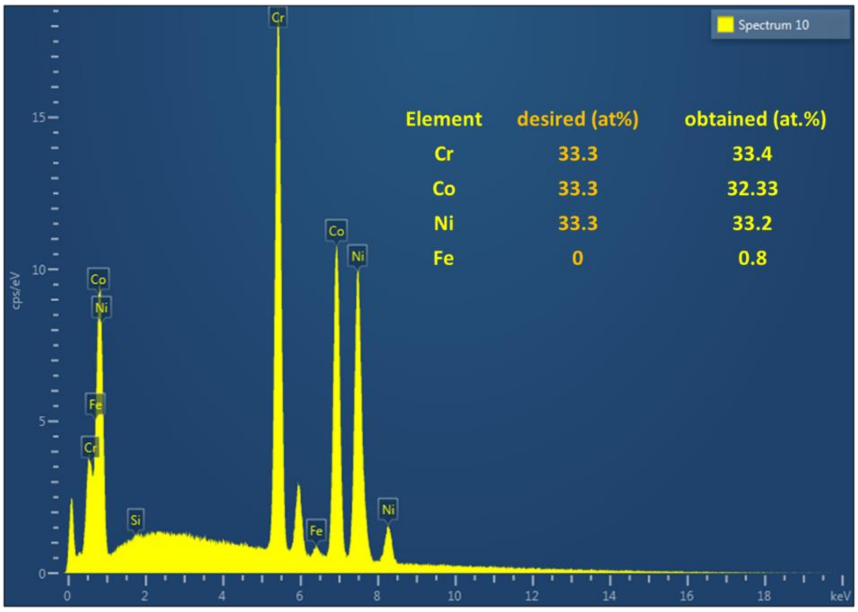

Element	desired (at%)	obtained (at.%)
Cr	33.3	33.4
Co	33.3	32.33
Ni	33.3	33.2
Fe	0	0.8

Fig. 82 chemical composition of CoCrNi bulk alloy measured by SEM EDS.

Fig. 83 reveals the microstructures of the bulk CoCrNi alloy. The bulk material was densified to full density, i.e. no porosity has been observed throughout the whole cross-section. However, the density measured by Archimedes method reached 99 % of the theoretical given by the rule of mixture (not 100 %). This small discrepancy is caused by accuracy and scatter of the Archimedes method, as well as the inaccuracy of the calculation by the rule of mixture that does not take in account the difference in lattices of the used elements.

Layers of different phases or elements that were present in the powder particles before the SPS were not observed, as mentioned in the preceding paragraph.

The most of the microstructure is composed of the grains corresponding to the major FCC phase, with high density of very fine annealing twins. The secondary phase observed solely at the FCC grain boundaries (denoted by red arrow in Fig. 83 c) should correspond to minor BCC phase detected by in the XRD patterns. The phase was too small to perform reliable accurate EDS measurements; however, it seems that it contains Cr as the base element. Considering the morphology and the emplacement of the phase, it is almost certain that it formed by the secondary precipitation process from the parental FCC phase. It is not clear if it formed during dwell time on the sintering temperature or the subsequent cooling after the SPS process. It seems that the later should be the best assumption, as the cooling time of the hot graphite die in the vacuum chamber of the SPS machine is by far longer, than relatively short heating and dwell time due to reduced heat transfer conditions - see paragraph 6.2.4.

The black dots present in the microstructure in Fig. 82 b, c pertain to oxide particles. Their size distribution is relatively wide. The ones possessing the largest sizes are usually observed on the grain boundaries, as they naturally represent areas, where the diffusion kinetics is greatly enhanced, with respect to the rest of the microstructure.

The oxides measured by the EDS analysis corresponded to the Cr and Al based oxides (Fig. A 5). The origin of the oxide phases in the microstructure is similar to the origin of oxides in $Co_{1.5}Ni_{1.5}CrFeTi_{0.5}$ alloy - they emerge as a consequence of the surface contamination of elemental powders by air atmosphere prior to start of milling process. Subsequently, they remain in the milled powders and produced bulks due to their high thermal and chemical stability.

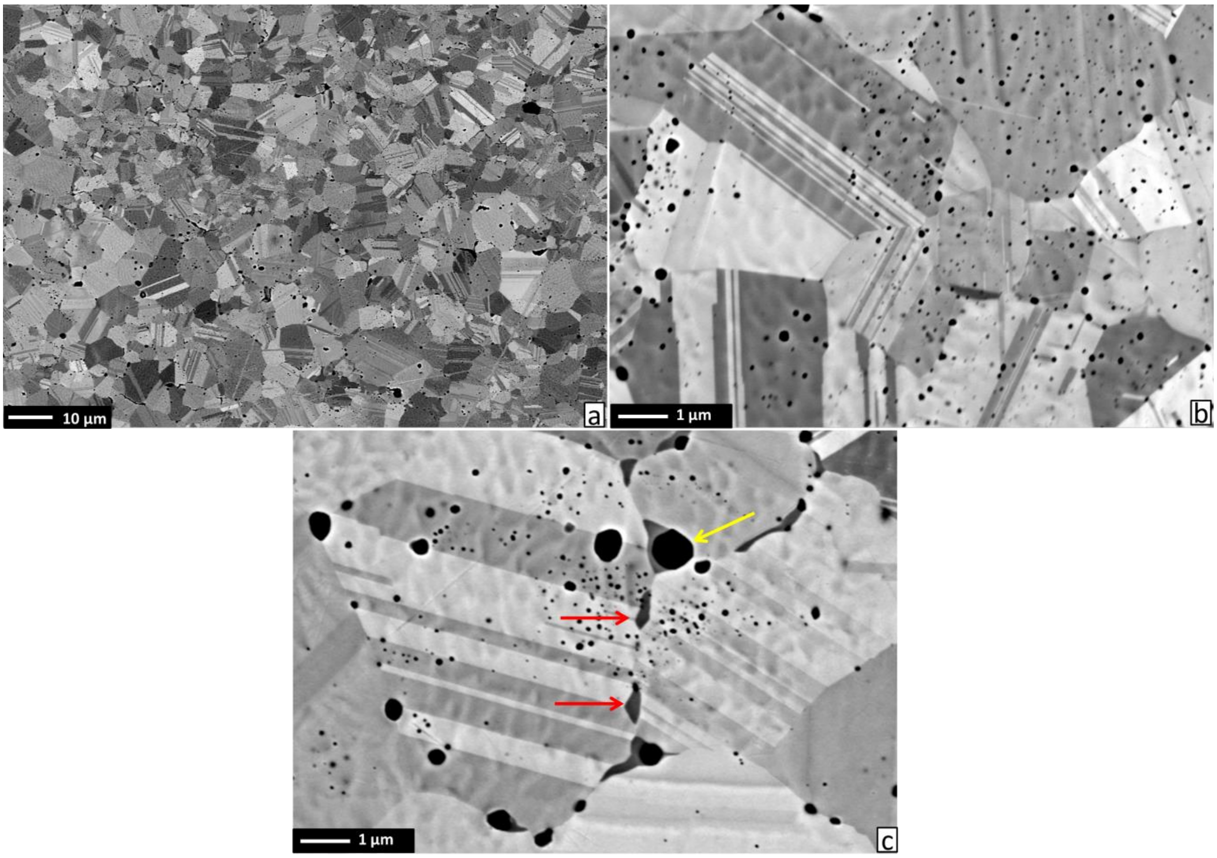

Fig. 83 SEM micrographs in back scattered mode (BSE) of CoCrNi bulk alloy showing FCC grains with BCC phase denoted by red arrows and oxides denoted by yellow arrow.

Consecutive EBSD analysis has been performed to better evaluate the grain size of the major FCC phase. The average grain size of the major FCC phase was determined to be 4.11 µm , size distribution in Fig. 84 b. The grains do not show any preferential orientation, similarly as in the case of $Co_{1.5}Ni_{1.5}CrFeTi_{0.5}$; however, even though the same processing equipment was used, the average grain size is almost 4-times larger. On one hand, this may be the influence of increase in sintering temperature (30 °C). On the other, the presence of only three elements, i.e. decrease in configurational entropy could decrease the sluggish diffusion effect in the CoCrNi alloy. Due to the very small size, the intergranular minor phase has not been detected, due to the resolution limit of performed EBSD analysis as well as the oxide phases.

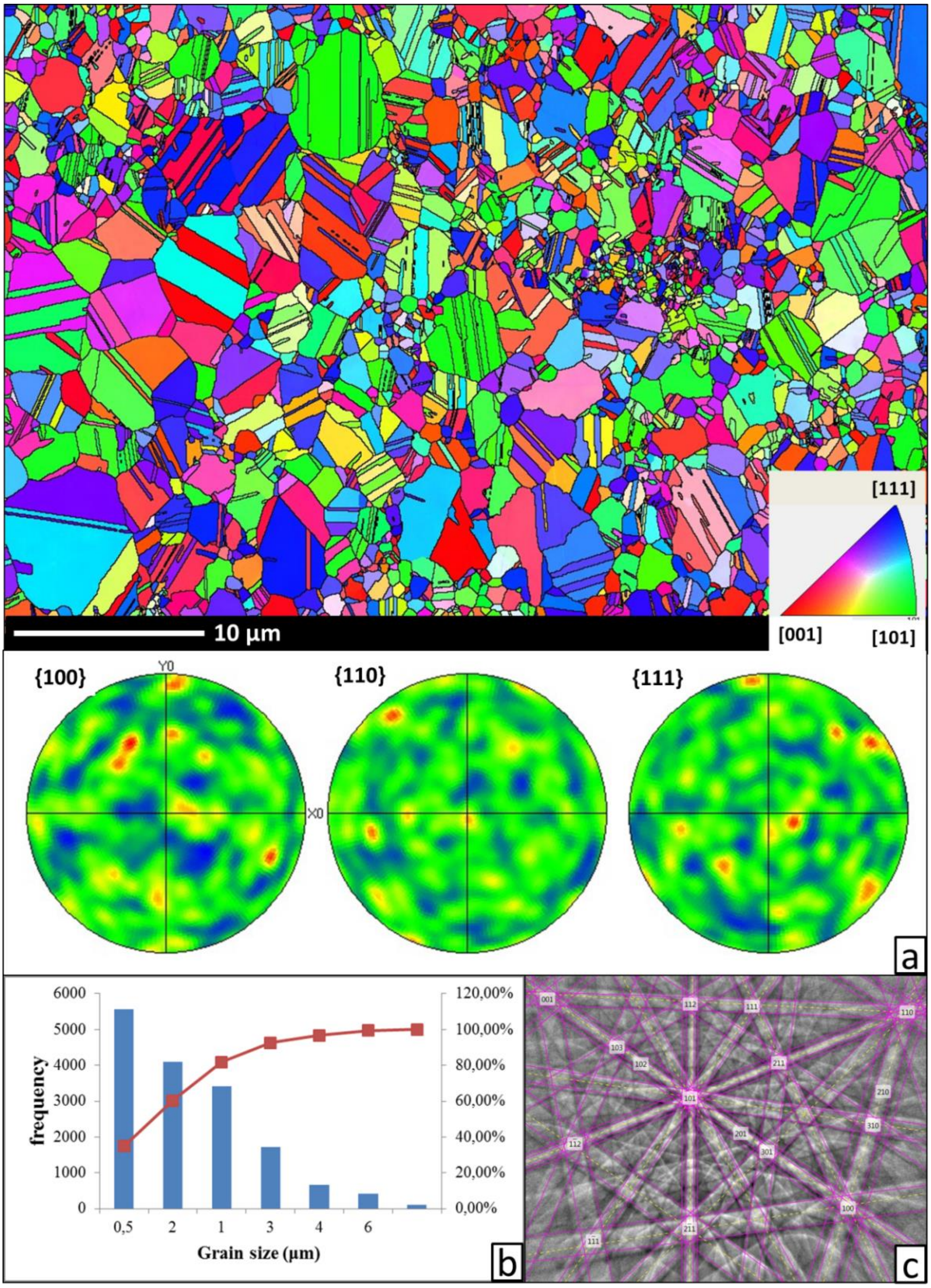

Fig. 84 SEM EBSD analysis results of CoCrNi bulk alloy representing a) color orientation map with pole figure revealing FCC phase with twin boundaries denoted by black lines showing no significant preferred orientation of grains; b) grain size distribution; c) diffraction pattern corresponding to FCC phase.

To better evaluate the nature of the microstructure and BCC intergranular phase, TEM analysis has been carried out, with the results present in Fig. 85. Dislocations pinned by oxide particles are denoted by red arrow, suggesting pronounced effect of dispersion strengthening.

The annealing twins present in the microstructure of the SPSed CoCrNi alloy are extremely fine, much finer as compared to $Co_{1.5}Ni_{1.5}CrFeTi_{0.5}$ alloy - pointing out to relatively lower values of SFE of CoCrNi alloy. Additionally, notable feature was observed in the TEM imaging (denoted by green arrow in Fig. 85 b). The feature may represent the stacking fault parallepiped, as observed previously by Zhang in CoCrFeMnNi High Entropy Alloy [48]. This volume’s structural defect is supposed to be formed by the simultaneous movement of partial dislocations on two active {111} planes and their subsequent intersection, forming an obstacle around which entangling of dislocations occurs. This defect structure should be retarding the dislocation movement, and thereby increasing the strength and strain hardening capacity of the alloy [48].

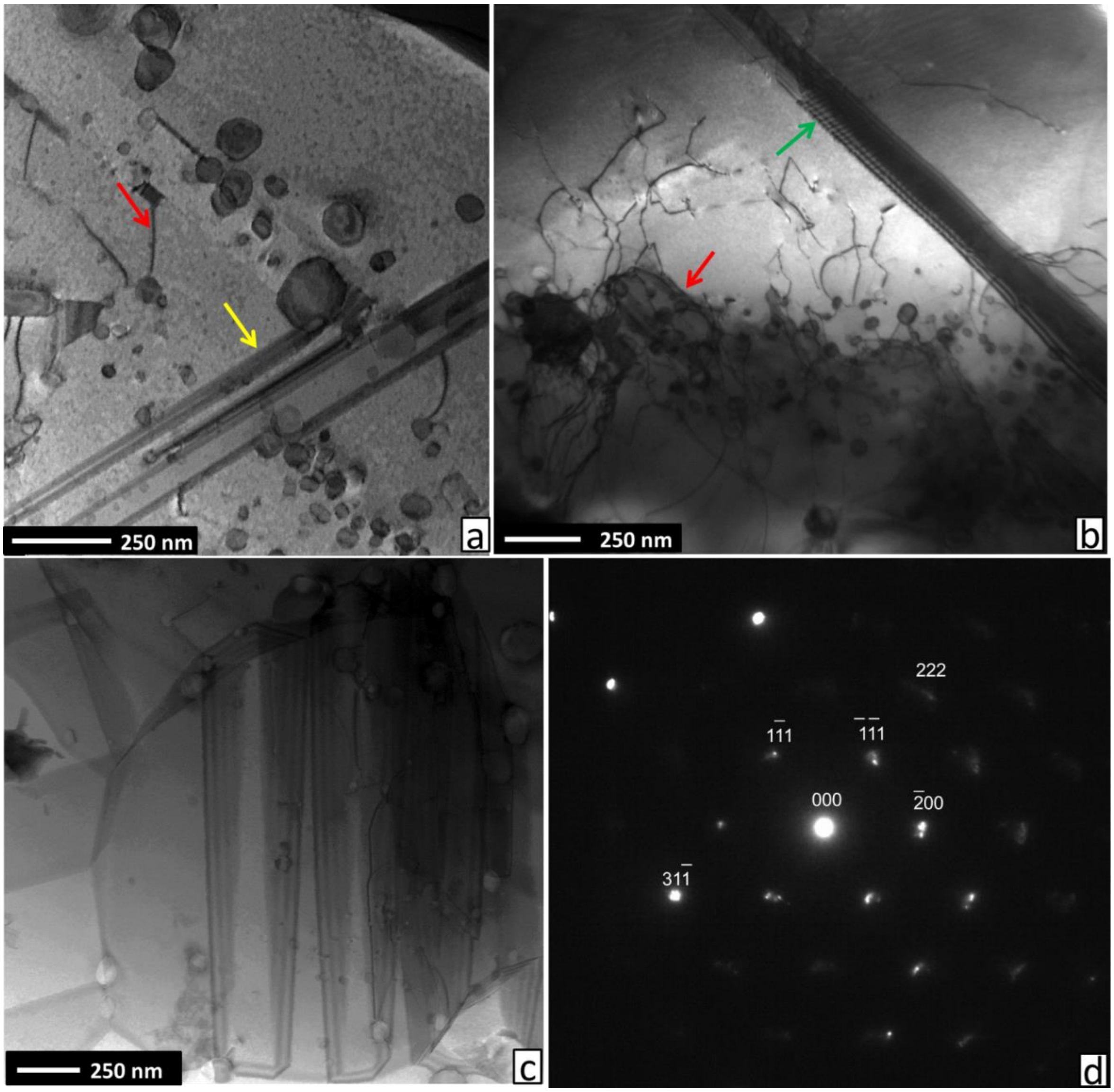

Fig. 85 TEM micrographs of a) FCC grains containing dislocation arrays pinned by oxides (red arrow) and very fine twins (yellow arrow); b) dislocation networks pinned by oxide particles and stacking-fault parallelepiped structure (denoted by green arrow) formed by slip on multiple 111 planes c) single FCC grain containing d) corresponding SAED pattern of FCC phase in 011 pole axis.

The intergranular phase TEM analysis is presented in Fig. 86. The phase is denoted by green arrow at the grain boundaries of the major FCC phase grains. The selected area diffraction pattern analysis of the feature (presented in Fig. 86 b with elemental mapping in c) revealed the phase is bearing a BCC crystal lattice. The phase possesses chemical composition of almost pure Cr element, as observed by the point EDS measurement and corresponding elemental mapping. The chemical composition and lattice of the phase perfectly corresponds to the nature of Cr-based BCC phase revealed previously by XRD and SEM analyses.

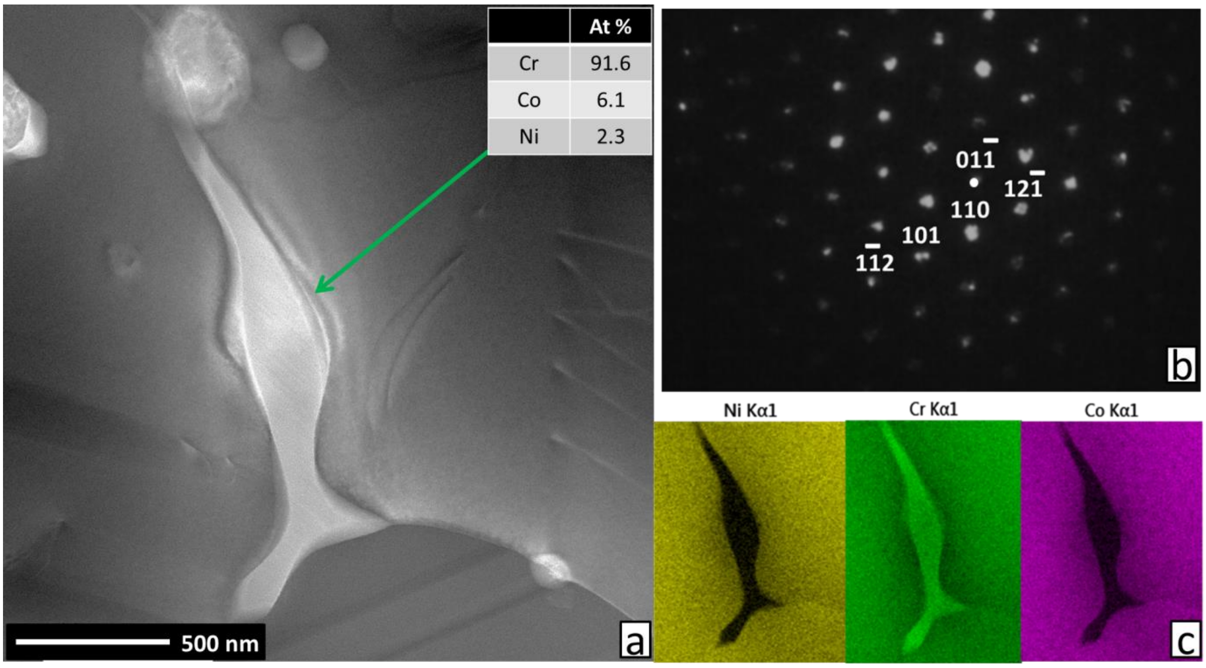

Fig. 86 TEM analysis of BCC phase that precipitated at FCC grain boundaries a) image micrograph of the precipitate (denoted by green arrow) with corresponding point EDS composition measurement; b) corresponding SAED pattern in 111 pole axis revealing BCC lattice; c) EDS elemental distribution maps.

CoCrNi alloy thermomechanical properties

As the CoCrNi alloy represents the most suitable material for substantial base of MMCs, in order to evaluate the extent of the phase transformation and measure the coefficient of thermal expansion which could be useful for the MMC design, TMA analysis has been carried out, with results presented in Fig. 87.

The CoCrNi alloy exhibited almost linear size change dependence with temperature. This fact is pointing out to the absence of pronounced phase transformation during the measurement. The measured value of CTE is $17.4\times10^{-6}\,K^{-1}$ in contrast to $10.44\times10^{-6}\,K^{-1}$, calculated as an average value of Co, Cr and Ni elements. The difference of the two values might stem from the fact that, in the alloy, the three elements are arranged in one FCC solid solution, plus minor BCC phase content, while the original elements lattices might differ (BCC Cr, HCP Co).

The measured value of CTE of the alloy is relatively high as compared to other metallic systems [108]. Therefore, the legitimacy of the idea for the utilization of this composition for production of MMCs is further supported. In fact, the high CTE value of the alloy presents a unique possibility of the alloy to be used as a matrix alloy for ceramic reinforced MMC applications. As the CTE of ceramic materials is usually low, in the range of 4×10^{-6} K^{-1} to 10×10^{-6} K^{-1}, the combination of CoCrNi MEA matrix with such reinforcements would yield a significant matrix strengthening effect through high compressive residual stresses development at the phase interfaces. The stress development due to the significant CTE mismatch is generally associated with a formation of geometrically necessary dislocations (GND) during cooling from processing temperatures, as explained in paragraph 3.3.

The as-SPSed CoCrNi alloy hardness has been determined to be 309 ± 16 HV0.3. Even in spite of the presence of the second phase, the hardness is relatively lower as compared to $Co_{1.5}Ni_{1.5}CrFeTi_{0.5}$ alloy – probably as a result of approximately 4 times bigger grain size.

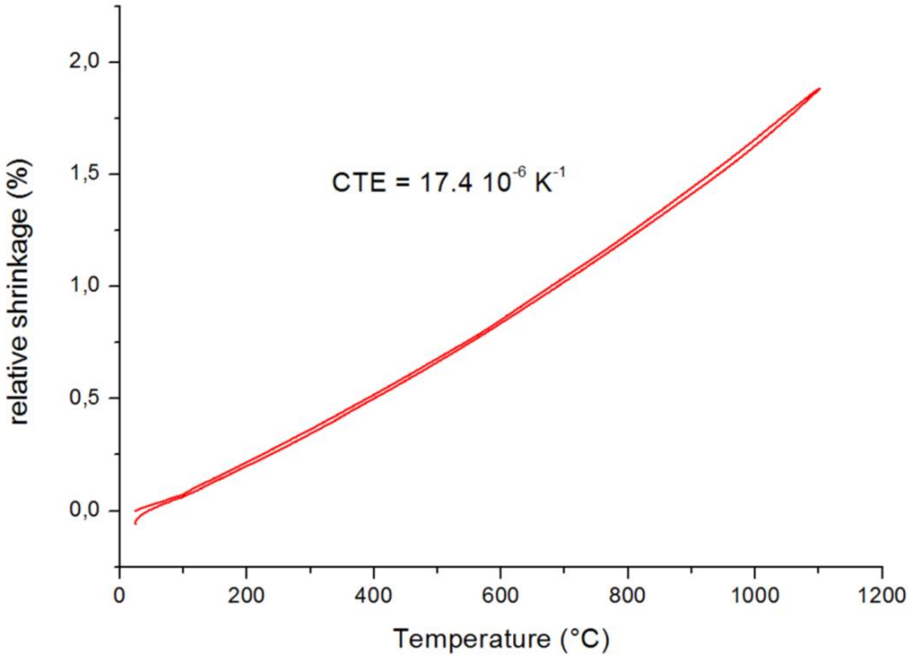

Fig. 87 TMA measurement of relative shrinkage of CoCrNi bulk alloy sample during heating.

CoCrNi alloy bend test

The room temperature bending strength (R_{mb}) was measured; Fig. 88 and Table 12 represent the determined values. However, the bending test has not been fully finished, due to the limitations given by the range of incremental sensor, i.e. max deflection of 2.5 mm in the bending jig - the sample was not broken, nor the maximum bending stress has been determined. Consequently, the value of ultimate bending strength R_{mb} is not presented in Table 12. Instead, the maximum stress value during the test before unloading is displayed, that occurred at the maximal deflection point. Considering the fact that the critical fracture conditions have not been reached during the test, the overall ductility of the alloy is relatively good.

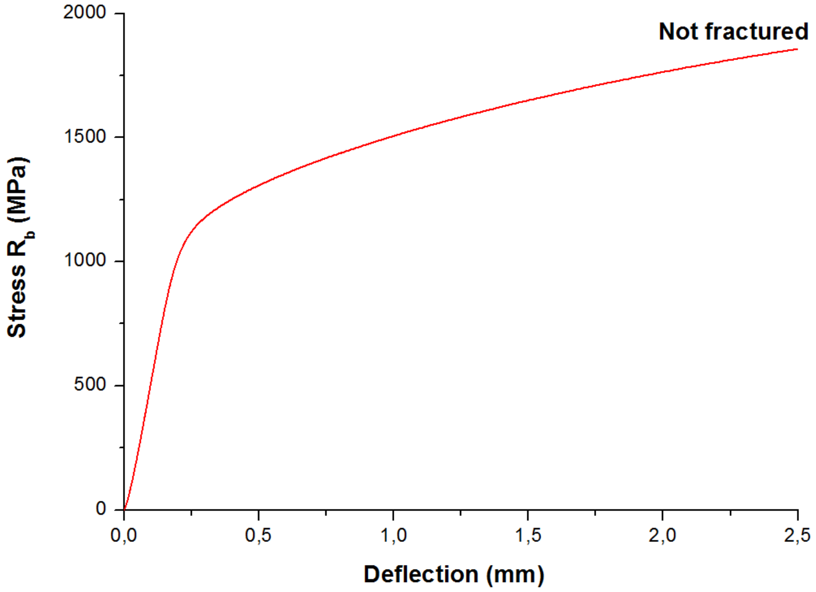

Fig. 88 Representative stress – deflection curve from three-point bending test of CoCrNi bulk alloy at room temperature test was stopped before fracture as the sensor limit has been reached.

Table 12 results of three-point bending test on CoCrNi bulk alloy after SPS.

Sample	R_{mb} (MPa)	R_b at max deflection (MPa)	E (GPa)	Max. deflection (mm)
1	-	1854	86.91	2.5

CoCrNi alloy tensile test

The room temperature tensile strength was measured on 3 samples, only with results presented in Fig. 89 with samples of 7.6 mm gauge length. The CoCrNi alloy exhibited an excellent combination of tensile strength and ductility. The very low scatter of the presented values is especially worth mentioning, pointing out to very a good homogeneity of the obtained bulk material throughout the whole cross section. The values of elastic constants E = 222 GPa and $\nu = (0.30 \pm 0.01)$ were obtained from the resonant ultrasound spectroscopy measurements (RUS), not from the tensile testing procedure, for an increased accuracy of the method. The strain hardening exponent values showed a smooth change from 0.1 to 0.28.

The strain hardening rate changed smoothly, without any sudden discontinuities, suggesting no sudden change in deformation mechanism. Therefore, deformation twinning and dislocation slip is probably employed simultaneously, depending on the grain orientations.

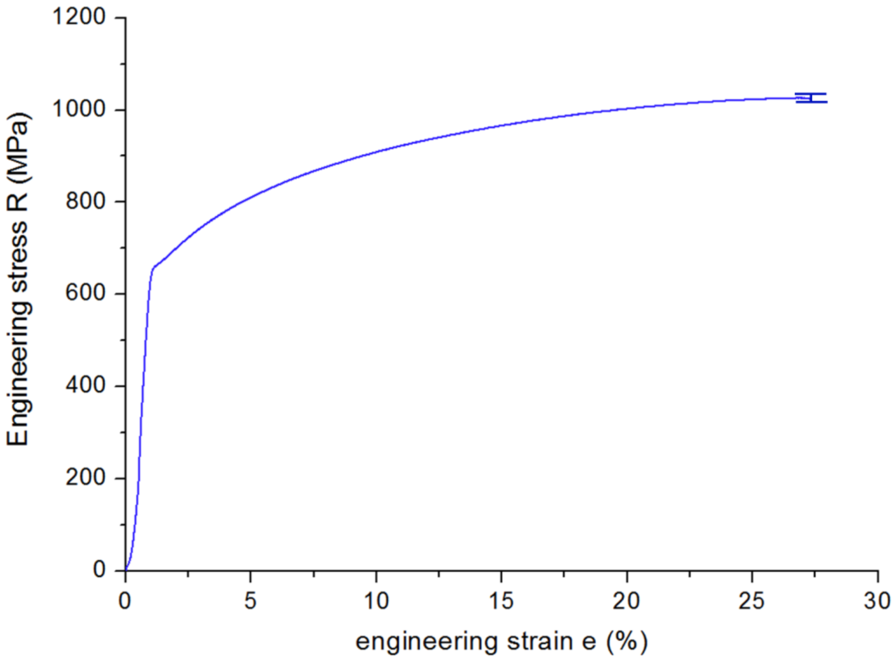

Fig. 89 Representative engineering stress - strain curve from tensile test of CoCrNi bulk alloy at room temperature.

Table 13 Average tensile strength test results of CoCrNi bulk alloy.

Sample	$R_{p0.2}$ (MPa)	R_m (MPa)	Elastic modulus E (GPa)	Elongation to fracture A_t (%)	Strain hardening coefficient n (-)	Reduction Z (%)
1-3	652±0.58	1024±6	222	25.9±0.7	0.1 – 0.28	21.5±1.4

SEM fractographic analysis of the ruptured tensile specimens is displayed in Fig. 90. Almost typical ductile fracture behavior was observed, i.e. the fracture process initiated approximately in the geometrical middle of the tensile test specimens and ended with shear tearing at the specimen edges, denoted by red arrow. Nucleation, growth and coalescence of fine microvoids is responsible for the morphology observed in Fig. 90 b and c. Oxide inclusions were located in the middle of majority of the ductile dimples as illustrated by yellow arrow. The size of the dimples is significantly increased in comparison to $Co_{1.5}Ni_{1.5}CrFeTi_{0.5}$ alloy (seen in Fig. 75) as the result of increased alloy’s ductility.

In Fig. 90 d, e and f, polished cross-section of broken tensile specimen is presented. The microstructure from the vicinity of fracture surface is showing signs of significant dislocation activity, as a consequence of plastic deformation process that is usually most extensive near the crack tip. Dislocation cells were formed by the dislocation pile – up, as observed by the change of dark grey / light grey contrast in the Fig. 90 e, d (denoted by green arrow).

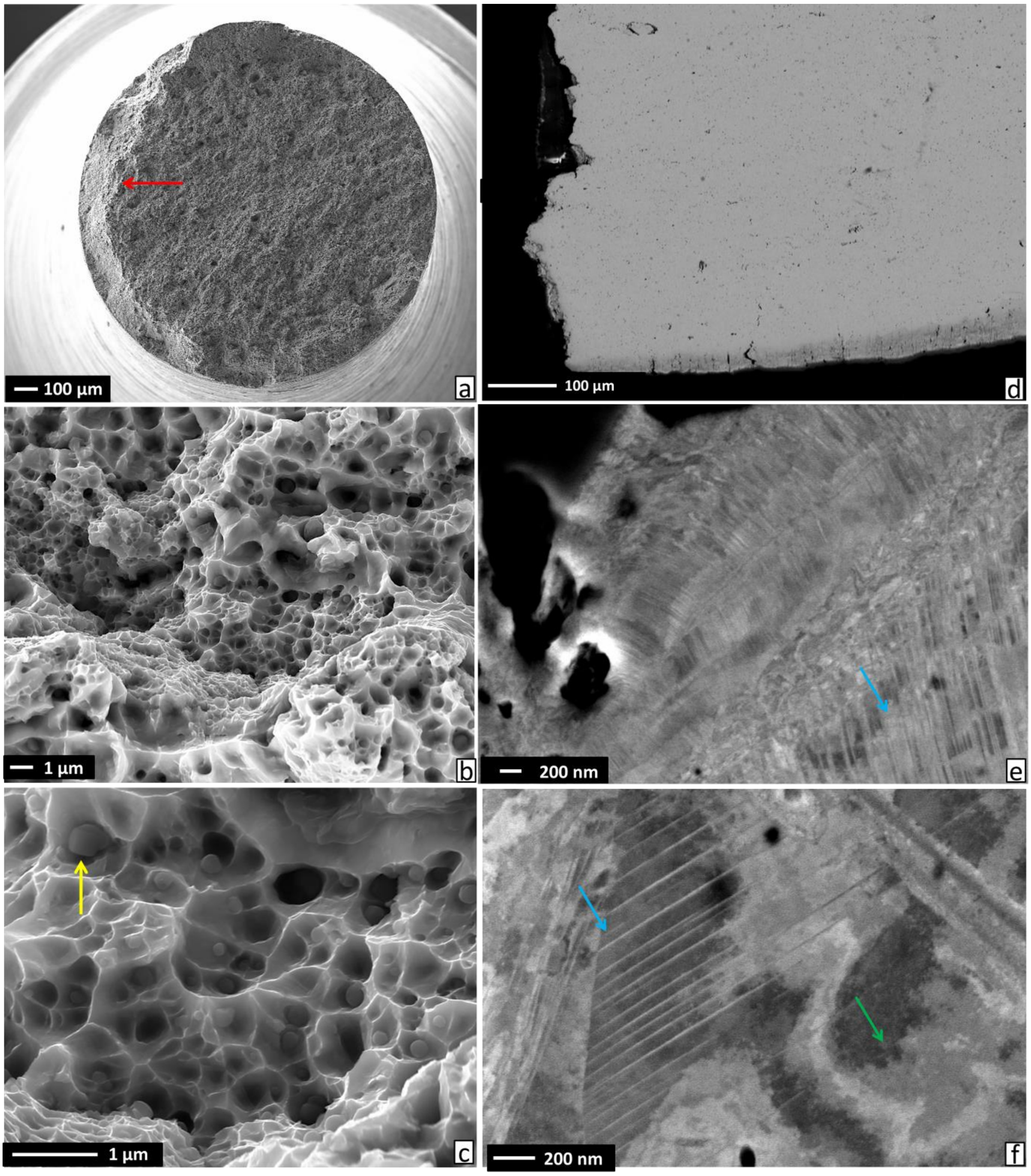

Fig. 90 SEM micrographs of a, b, c) fracture surfaces of CoCrNi bulk alloy tensile specimen, shear fringes are denoted by red arrow and oxide particles by yellow; d) side cross section view of polished fractured specimen; e, f) the deformed microstructure from the vicinity of the fracture surface with twins denoted by blue arrows and dislocation cells by green arrow.

Again, the presence of deformation twinning has been observed (as denoted by blue arrows). The density of twins is extremely high in particular places, as illustrated in Fig. 90 e. In respect to the previous alloy composition of $Co_{1.5}Ni_{1.5}CrFeTi_{0.5}$, the intensity of deformation twining is much more pronounced. This is consequence of the higher level of plastic deformation, the CoCrNi alloy has been subjected to comparing to $Co_{1.5}Ni_{1.5}CrFeTi_{0.5}$ (tensile elongation to fracture of over 4 % $Co_{1.5}Ni_{1.5}CrFeTi_{0.5}$ as compared to 26 % for CoCrNi). As a proof that the observed lines in the plastically deformed alloy's microstructure truly correspond to mechanical twinning, i.e. that they were not incorrectly interpreted as the deformation slip lines, the comprehensive HR EBSD analysis has been carried out with results displayed in Fig. 91. The deformation twins clearly possess 60° missorientation with respect to the surrounding original grain corresponding to Σ3 type special boundary. It is interesting to note that, in this particular grain, the separated twins are crossing each other. This observation points out to the fact that, at least two independent twining systems have been activated, within single the FCC grain. Dark contrast points in Fig. 91 are probably capturing the moment of the fracture void formation at the oxide phase.

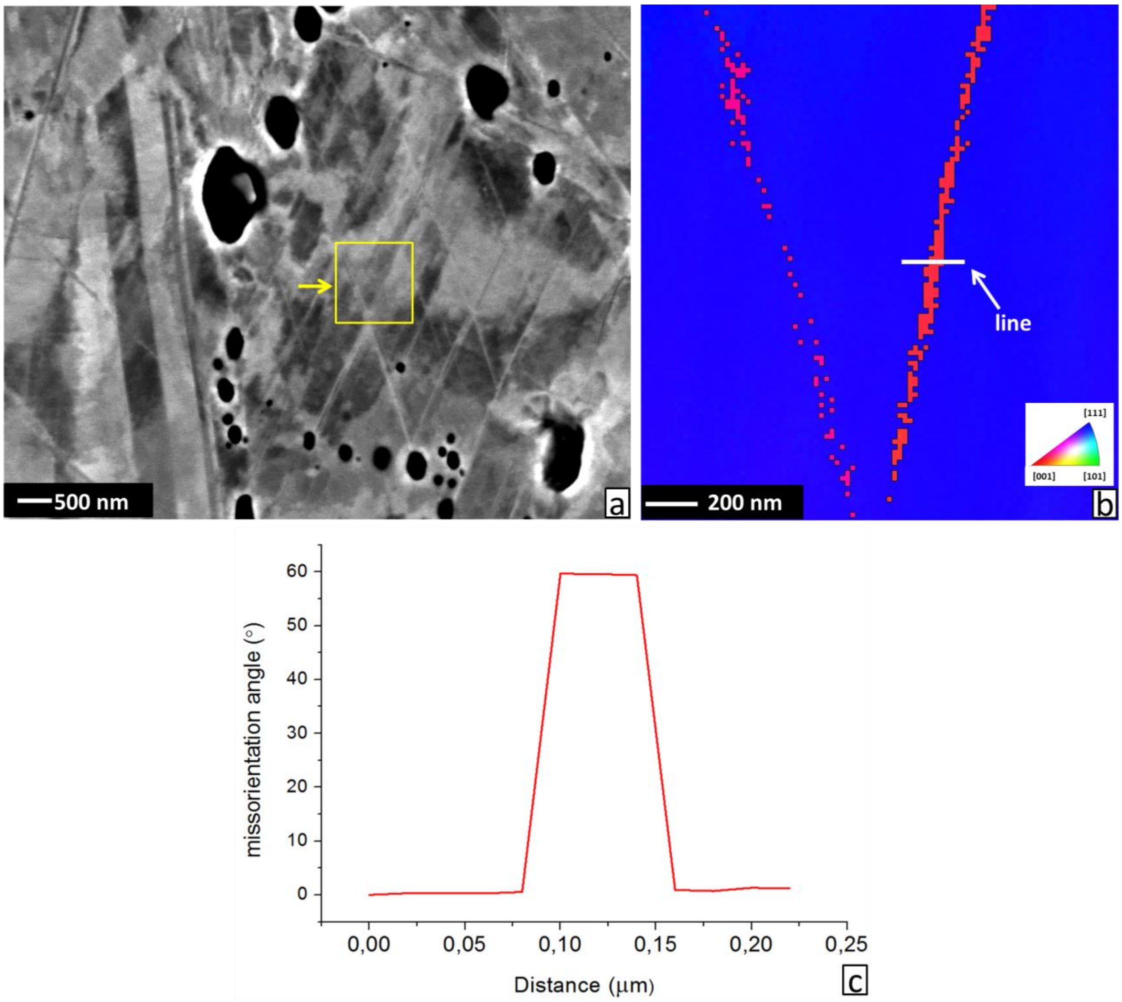

Fig. 91 Deformation nano - twinning analysis under fracture surface of tensile specimen a) SEM ECCI image of twinned grain with area subjected to HR EBSD analysis denoted by yellow square; b) orientation map of corresponding yellow square area; c) corresponding misorientation as a function of distance for the white line.

7.5 CoCrNi / B_4C composite

As explained in the preceding section, CoCrNi alloy possess an intriguing combination of properties. Amongst the tested materials, its mechanical response seemed to be the most suitable for the subsequent production of MMCs with MEA matrix. For the first trials, B_4C particles have been selected as a suitable reinforcement material, with reasons described as follows:

The properties of B_4C, very low density of 2.52 g cm^{-3}, high hardness of 3800 HV and especially elastic modulus of 441 GPa coupled with CTE of 4.5 17.4×10^{-6} K^{-1}, predetermine it for the use as a reinforcement phase in MMC [108]. In contrast to properties of CoCrNi alloy with elastic modulus of E = 222 GPa and CTE of 17.4×10^{-6} K^{-1}, the EM and CTE mismatch should generate exceptional strengthening in B_4C reinforced CoCrNi MMCs. The mechanism underlying the proposed phenomena are present in 3.3. For the trial runs, 7.5 volume % of B_4C has been introduced to CoCrNi alloy, corresponding to 2.83 atomic %. This amount of reinforcement should increase the strength of the composite, as well as other properties like wear resistance and high temperature strength, but should not diminish the alloy's ductility considerably. The average particle size of the utilized B_4C powder was selected to be as small as possible (smaller than 5 μm) to activate the corresponding strengthening mechanism, as the decrease in the reinforcement particle size correspondingly increases the strengthening extent. It should be noted that, the B_4C particle size was also decreased by powder crushing during high energy milling process – during preparation of the CoCrNi/B_4C composite powder.

7.5.1 CoCrNi / B_4C composite powders

The XRD patterns measured for the blended and milled CoCrNi / B_4C composite powder are presented in Fig. 92. While the elements and B_4C are clearly distinguishable in the blended powder, after the MA process, only peaks of FCC solid solution are visible. There may be other peaks preset in the milled powder pattern, however, due to extreme deformation induced to the powders, the corresponding phases are not recognizable; the peak-like formation at approximately 33° of 2 Θ angle may correspond to the peak of phase with extremely reduced crystallite size, but at the same time may be just a part of the background noise.

Powder particles morphology and microstructures in the state after MA process are presented in Fig. 93. As compared to the powder of pure CoCrNi alloy in Fig. 80 milled with the same parameters, the presence of B_4C resulted in comparably lower particle size (with respect to pure CoCrNi). The presence of layers of present elements has not been detected in this case.

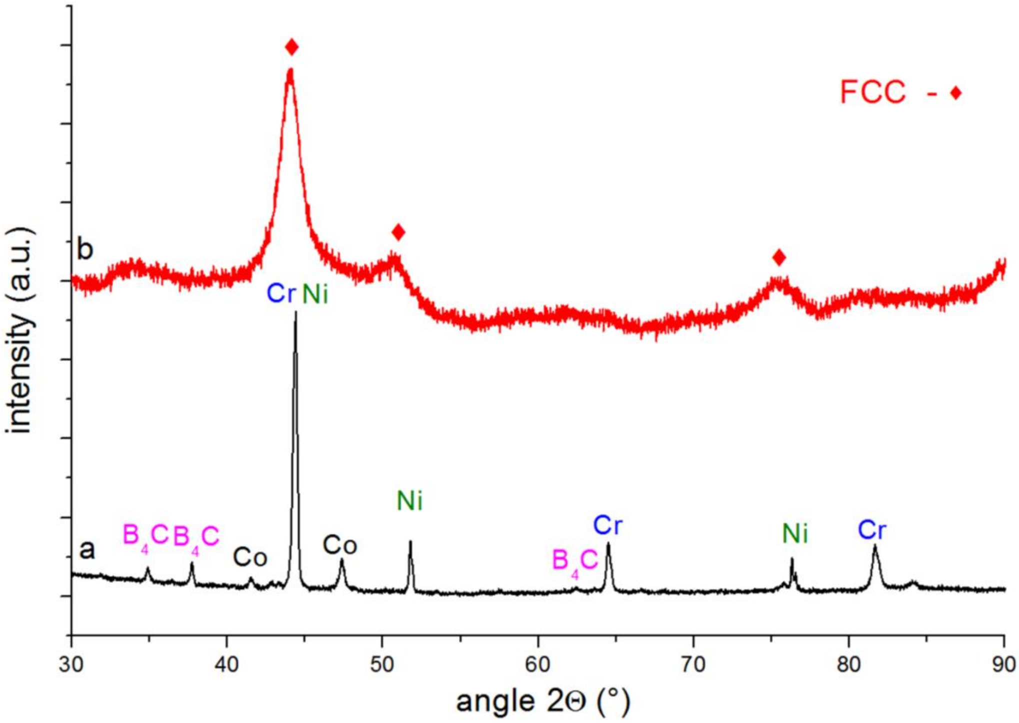

Fig. 92 XRD pattern of a) CoCrNi / B_4C blended powder; b) CoCrNi / B_4C mechanically alloyed powder.

The dispersion of B_4C has been detected by the EDS measurement in the milled powder cross section as well as some amount of Cr oxides (depicted by yellow and red arrows in Fig. 93d respectively). As compared to the original B_4C powder from Fig. 40, its particle size has been severely reduced by the constant crushing during MA.

The mechanical alloying process proceeded much more smoothly - the powders were not sticking to the milling balls and bowl as in the previous case – hence the reason why only 15 minutes in ethanol was needed as compared to 5 hours in the previous powder with only CoCrNi.

It follows from the observation that presence of hard, fine B_4C ceramic particles supports the milling process, i.e. the extent of milling, powder homogeneity and better powder behavior as well. It may be the result of more pronounced powder fracturing during milling, due to the presence of hard ceramic particles - the powder with dispersion is inherently harder and more brittle.

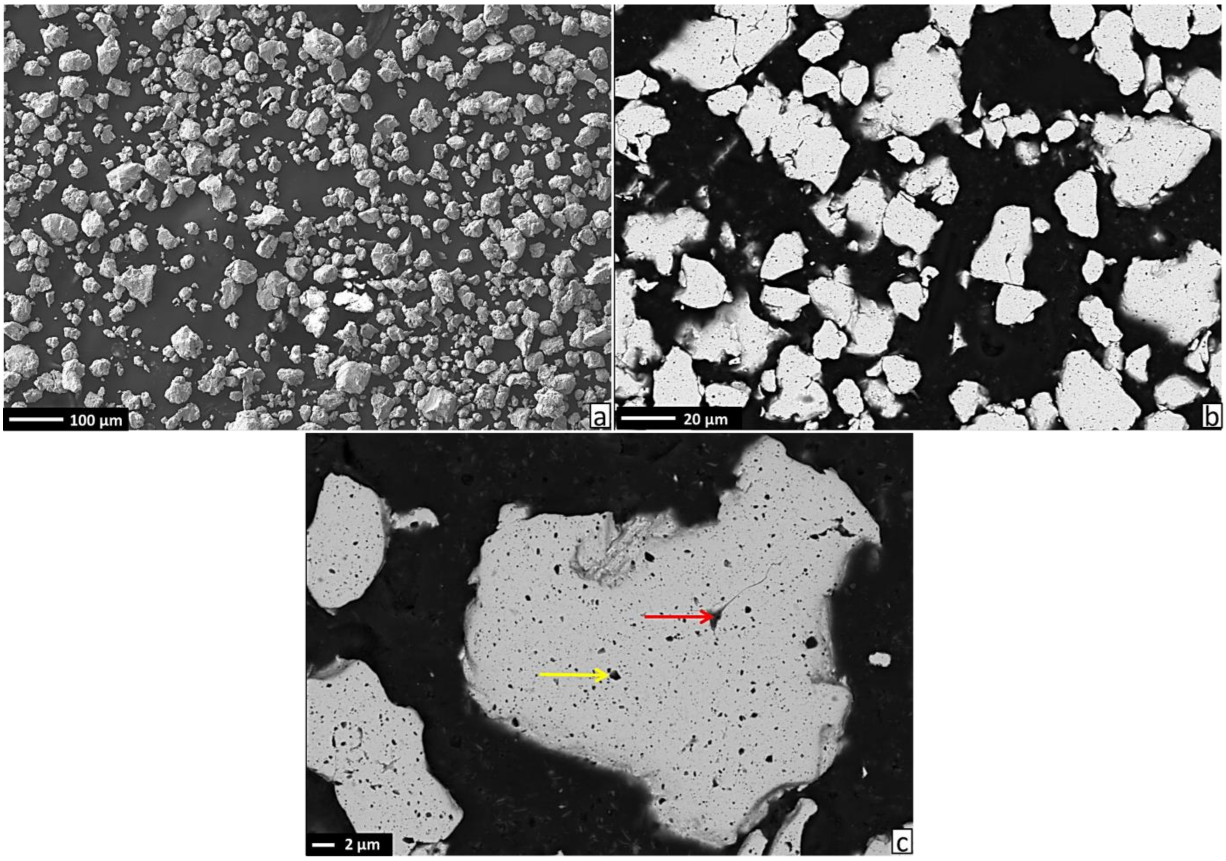

Fig. 93 SEM micrographs in BSE mode of CoCrNi / B_4C powders a) powder morphology; b) powder cross-section; c) powder cross-section detail with denoted B_4C particle (yellow arrow) and Cr oxide particle (red arrow).

7.5.2 CoCrNi / boride composite bulk

The XRD pattern analysis of the CoCrNi / B_4C alloy milled powder and bulk material produced from the powder are provided in Fig. 94. After the SPS densification, the major FCC solid solution phase with lattice parameter of 3.57 Å was formed. Surprisingly, no traces of added B_4C phase, that was observed in milled powders prior to SPS densification, were detected in the pattern of bulk materials (Fig. 94 b). Instead, the remaining peaks were attributed to tetragonal, Cr_5B_3 boride phase. It seems that the thermodynamic stability of B_4C phase in CoCrNi matrix was not sufficient, as upon high temperature sintering B reacted with Cr to for previously mentioned boride. As B_4C transformed to Cr_5B_3, these materials will be further referred to as CoCrNi / boride composite. The free C previously contained in B_4C also reacted with Cr, forming a type of Cr carbide phase, or it dissolved in the major FCC solid solution phase. However, as the amount of C is 4 times lower compared to B, the amount of formed carbides would be below the resolution limit of XRD measurement.

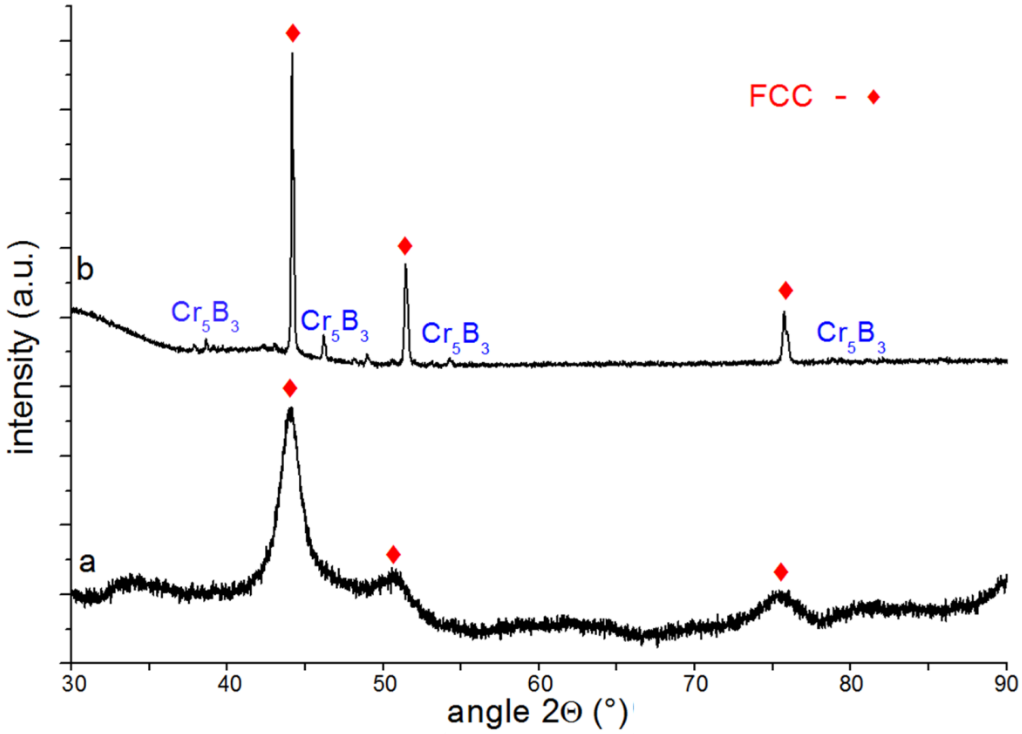

Fig. 94 XRD pattern of a) CoCrNi / B_4C mechanically alloyed powder; b) sintered bulk composite.

The alloys chemical composition is presented in Fig. 95. The ratio of the elements of Co, Cr and Ni is very close to 1:1:1, as desired. It can be seen, on the obtained EDS pattern, that the bulk material also contains amounts of C and B. However, due to the very problematic determination of true C and B concentration given by the nature of the EDS method, the presented results should be taken only as a proof of B and C presence. An interesting phenomenon occurred: the presence of hard ceramic particles most probably induced more significant wear of steel milling media – hence the reason why elevated concentration of Fe was detected.

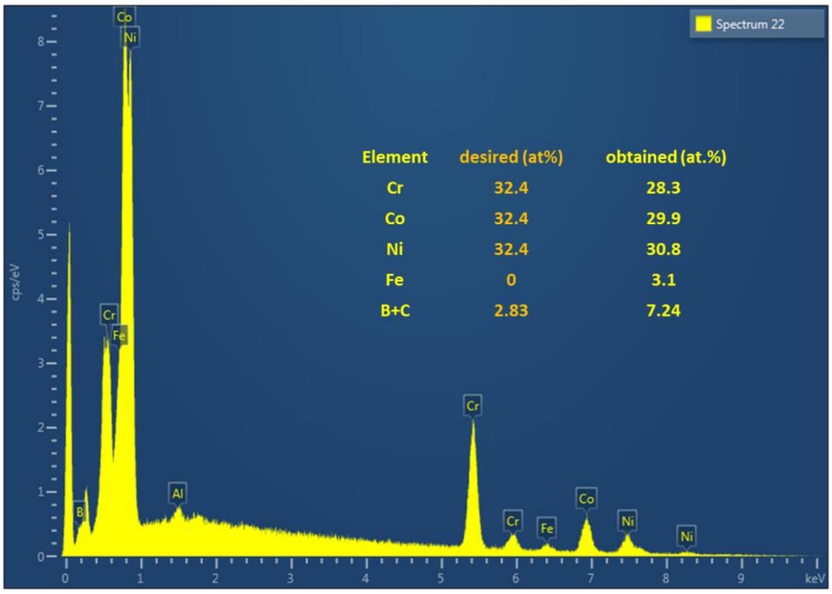

Element	desired (at%)	obtained (at.%)
Cr	32.4	28.3
Co	32.4	29.9
Ni	32.4	30.8
Fe	0	3.1
B+C	2.83	7.24

Fig. 95 chemical composition of CoCrNi / B_4C bulk alloy measured by SEM EDS.

Fig. 96 depicts the representative microstructures of the CoCrNi / boride composite. The microstructure is not completely porous free – most probably a consequence of lower sintering temperature and different SPS setup (sintering temperature of 950 °C only was used as compared to 1180 °C for CoCrNi due to problem with powder melting if higher sintering temperatures were tested). The lower processing temperature is probably the reason for the obtained extremely small grain size. The grain size could have been further suppressed by present borides and oxides. The microstructure is composed of FCC phase grains, with significant amount of Cr_5B_3 boride and remaining carbides. The comprehensive analysis of boride phase by SEM presented in Fig. 97 reveals the phase perfectly matches the Cr_5B_3 phase that was already found in XRD patterns. The grains of the Cr_5B_3 are located between the FCC grains and compose around 30 volume % of the microstructure (as measured by the image analysis). Even though only 7.5 volume % of B_4C was added, the reaction with Cr caused the total volume amount of Cr_5B_3 to be higher. The black dots (denoted by green arrow) located on the grain boundaries of all phases were determined to be oxides and carbides. Oxides have been formed as a consequence of powder contamination by oxygen. The carbides probably appear in the microstructure due to the reaction of remaining C from B_4C with chromium.

The measured hardness of the microstructure is 467 ± 21 HV0.3 – evidently higher than 303 HV for the pure CoCrNi bulk alloy.

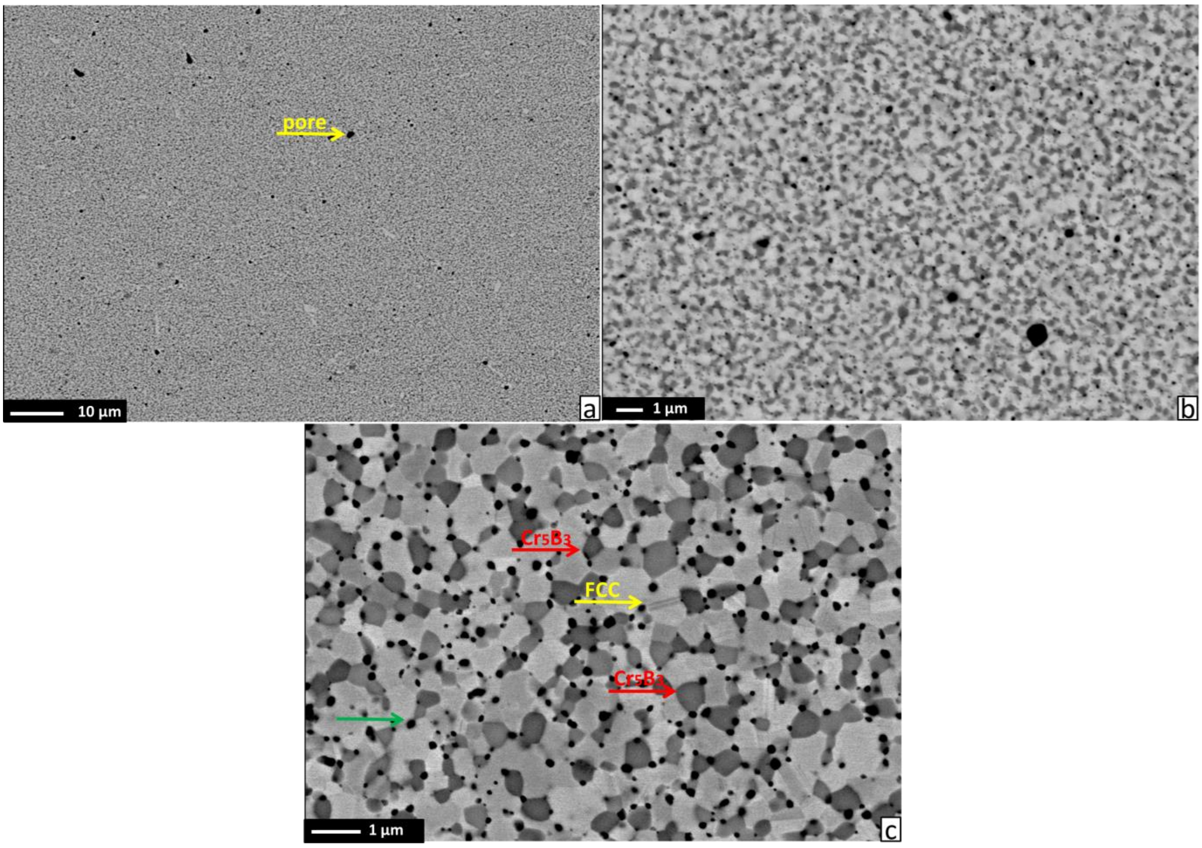

Fig. 96 SEM micrographs in BSE mode of CoCrNi/boride bulk composite showing FCC grains denoted by yellow arrow, Cr_5B_3 boride particles denoted by red arrow and oxides by green arrow respectively.

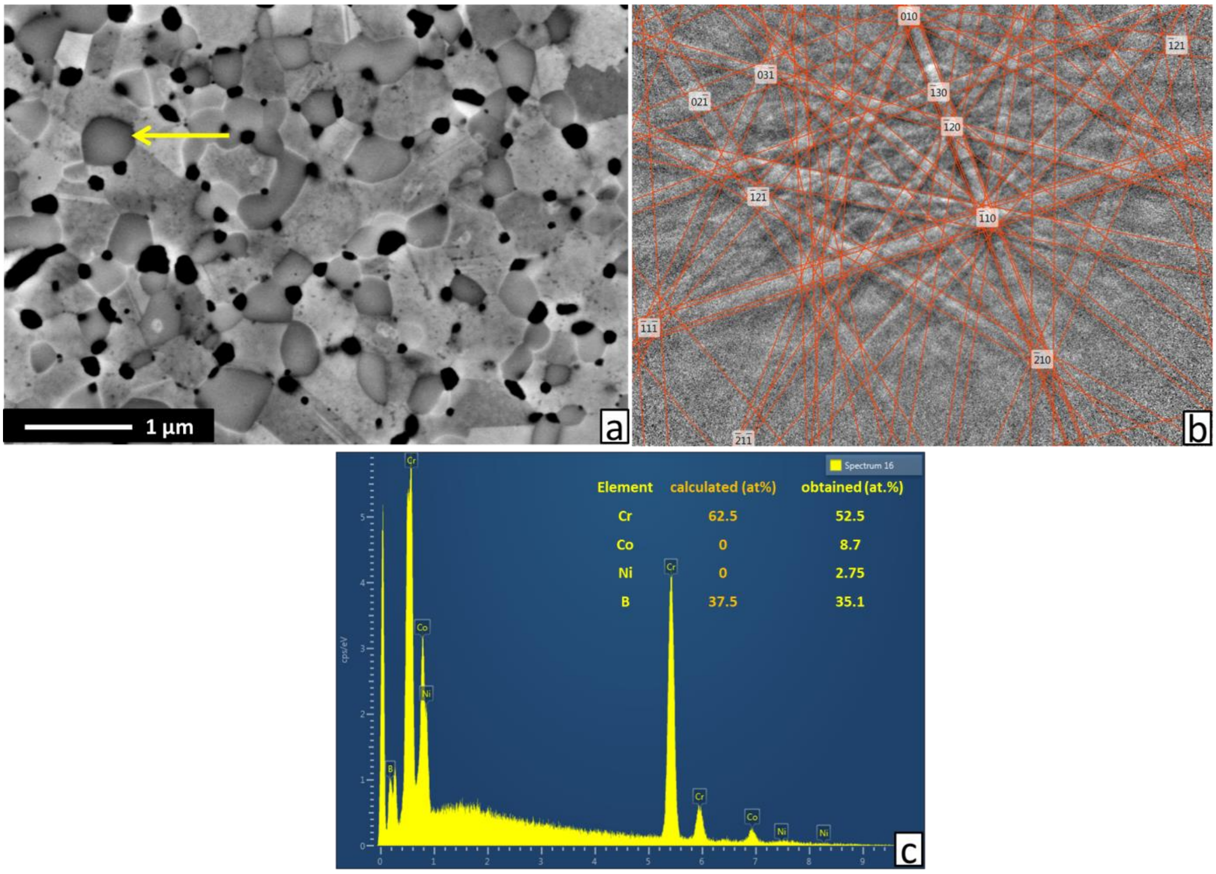

Element	calculated (at%)	obtained (at.%)
Cr	62.5	52.5
Co	0	8.7
Ni	0	2.75
B	37.5	35.1

Fig. 97 analysis of Cr_5B_3 particle a) SEM micrographs with particle denoted by yellow arrow; b) corresponding electron diffraction pattern matching tetragonal Cr_5B_3 reflections d) EDS microanalysis.

CoCrNi / boride composite tensile test

The ultimate tensile stress (R_m) of the composite was measured at room temperature on only one sample, due to the relatively limited volume of the produced material, with 12.5mm gauge length (as explained in 6.3). The evaluation of results is presented in Table 14 and Fig. 98, respectively. The presence of Cr_5B_3 boride particles resulted in the dramatic increase of tensile strength properties, as compared to pure CoCrNi; the values of both yield strength $R_{p0.2}$ and ultimate tensile strength R_m are surpassing 1400 MPa. However, very low strain hardening is also observed where the difference in the measured values of $R_{p0.2}$ and R_m reached 7 MPa only. The values of the tensile stress are decreasing after they reach the R_m value – which may look like the presented R_m is only distinguishable yield point. However, this yield point effect occurred probably due the onset of cracking instantly after R_m as consequence of crack initiation and rapid propagation. The total ductility value has been significantly reduced – it reached only 1.86 % as a consequence of the pronounced strengthening. The elastic modulus determined from elastic part of tensile curve remained relatively unchanged as compared to the pure CoCrNi alloy. It seems that the appearance of boride particles did not have significant influence on the elastic properties.

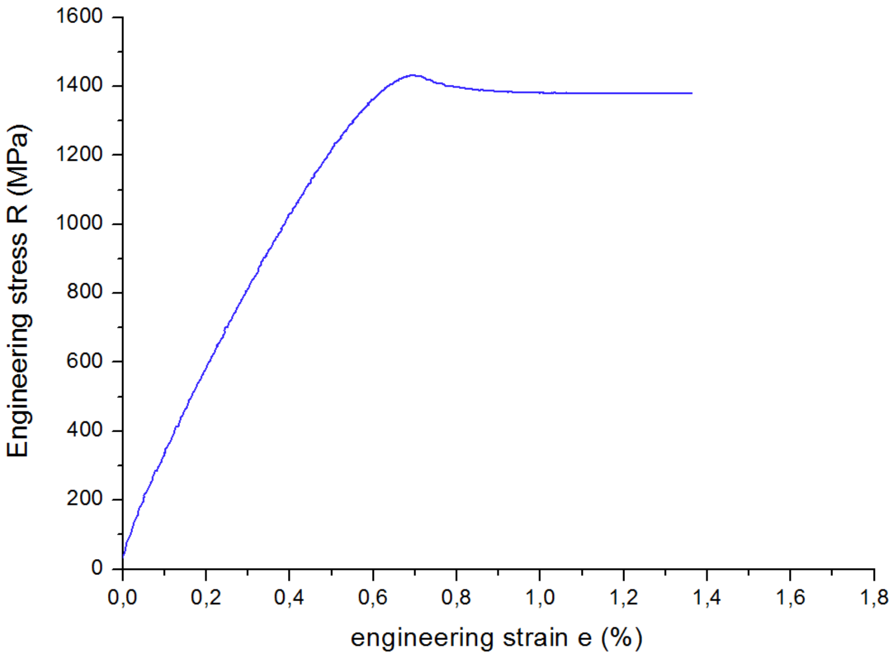

Fig. 98 Engineering stress – strain curves from tensile test of CoCrNi / B_4C composite at room temperature.

Table 14 Average tensile strength test results of CoCrNi / boride composite bulk alloy.

Sample	$R_{p0.2}$ (MPa)	R_m (MPa)	Elastic modulus E (GPa)	Elongation to fracture A_t (%)	Reduction Z (%)
1	1425	1432	226	1.86	3.9

The results of fractographic analysis of the ruptured tensile specimen are presented in Fig. 99. The fracture was initiated on the relatively large, brittle particle (as compared to the rest of microstructural features). The EDS analysis revealed that the particle is composed almost solely of pure Cr element. Most probably, some small amount of Cr element particle has not been milled, and remained in the microstructure, same as in the case of $Co_{1.5}Ni_{1.5}CrFeTi_{0.5}$ with inclusion presented in Fig. 76. Apart from the crack initiating inclusion, the morphology of the fracture surface is a mixture of ductile and brittle fracture behavior. The surface is composed of very fine ductile dimples, formed by adjacent microvoids’ coalescence, but without visible inclusions present at the dimple bottoms. However, the fracture surface contains ridges retracting towards the fracture initiation site – typical for brittle fracture behavior. In general, considering the low value of tensile ductility, the fracture should be referred to as brittle in nature with transgranular character.

In spite of that, the absence of hard boride particles or other ceramic particles in the bottoms of the dimples suggests that the dimples formed predominantly by ductile tearing of FCC phase, i.e. not by FCC / boride interphase decohesion. Probably, the dimples had formed and subsequently grew at the places of the highest stress concentration triaxiality between narrowly spaced angular boride particles [83]. At such places, the local stress overcomes the cohesive strength of the FCC phase and new free surface in the form of void is created.

The cohesive strength of the FCC phase atoms is evidently lower that the interphase cohesive strength between boride and FCC phase. Therefore, the interphase between in situ formed Cr_5B_3 borides must be inherently strong, which is the basic requirement for ductile composites with high ceramic content. The void fracture mechanism in the composite is depicted separately in Fig. 100.

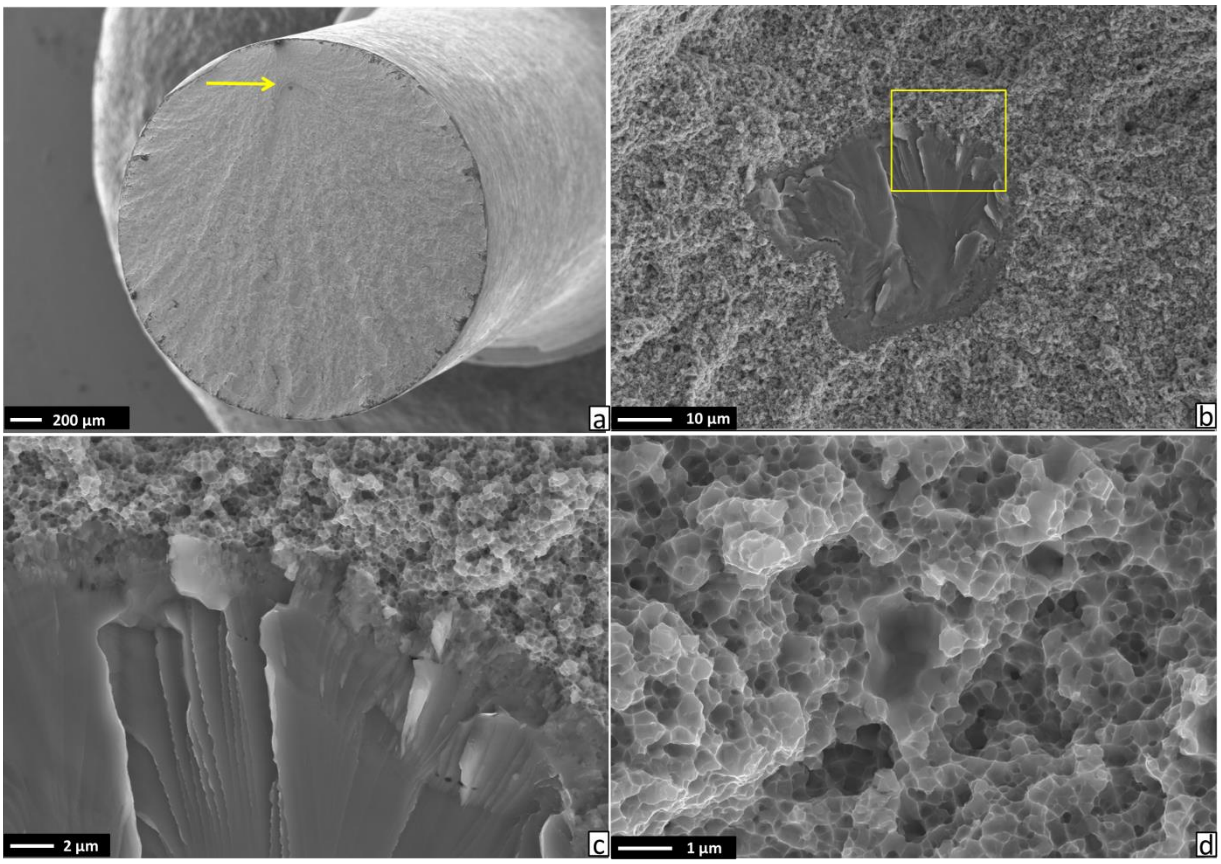

Fig. 99 SEM micrographs fracture surfaces of CoCrNi / B_4C composite tensile specimen a) fracture surface overview with crack initiation site denoted by yellow arrow; b) image of initiation site; c) image of area denoted by yellow rectangle of initiation particle interface; d) typical fracture surface morphology with fine ductile dimples.

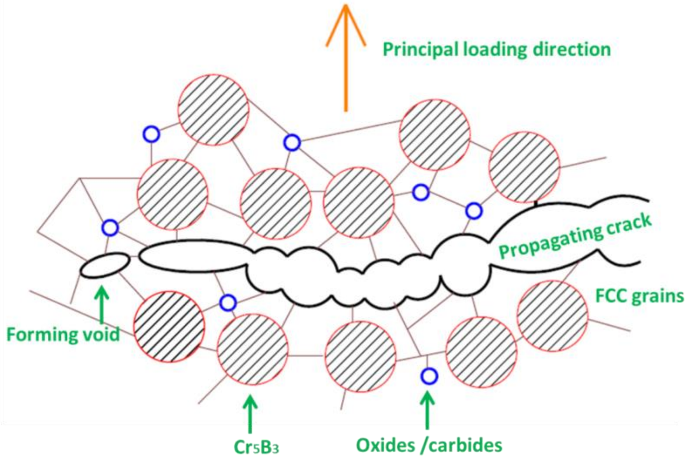

Fig. 100 Mechanism of transgranular crack formation in CoCrNi / boride composite by adjacent microvoids coalescence on the crack tip in FCC matrix phase.

8 Discussion

In the presented study, various issues related to the preparation and feasibility of HEA alloys, as well as MMCs with HEA as a matrix phase production by the means of PM manufacturing route have been investigated. The microstructures, response to mechanical loading and other selected properties of these progressive materials were characterized, to evaluate their potential for future development and application. In the following paragraphs, the main findings of the work will be discussed, regarding the varied prospects of the topic and the field.

8.1 Influence of MA parameters on process and resulting powder properties

No significant problems have been recognized during the MA process for the selected HEA and MEA alloy compositions, as well as their composites. The only issue may arise during the milling of very ductile materials. Normally, these would be wet milled in the presence of PCA. However, in such case, the powder contamination of some sort would increase significantly, just as in the case of $AlCoCrFeNiTi_{0.5}$ alloy (contaminated by C present in PCA). Should the contamination, especially carbon, ought to be avoided, the PCA cannot be used at all. Unfortunately, this leads to a very pronounced sticking of milled materials to the milling balls and milling bowl walls during MA process, to the point when most of the powder batch is mechanically attached to the bowl walls. To counter this, relatively low milling speed should be used (around 250 RPM in Pulverisette 6 mill). Usually, also consecutive wet milling period in ethanol is still needed at the end of MA procedure to decrease the average powder particle size - at least for several minutes.

As opposed to some selected published results on a range of different materials [87, 89, 101], which claim that the change in parameters of mechanical alloying process may result in formation of intermetallic phases, ceramic compounds, or even amorphization instantly during the milling, only formation of solid solutions has been observed for elemental metallic MEA and HEA powders in this work, for the whole set of used milling parameters. It seems that the intensity of milling was not sufficient to induce activation mechano-chemical and intermetallic forming reactions. The parameter administrating these reactions is the already mentioned mixing enthalpy of binary blend ΔH_{AB}. If the ΔH_{AB} of some combination of the present respective elements is very negative, the thermodynamic drive will favor their reaction, e.g. ΔH_{AB} for Ni and Al is -22 kJ mol^{-1} while for Cr and Al, the value is only -10 kJ mol^{-1} – thus ordered phase with NiAl stoichiometry will form rather that CrAl phase. The formation of such phases has been observed in this study, however, not during the milling, but rather during successive high temperature sintering – B2 NiAl-like phase. It seems that some form of thermal activation is essential for the reactions.

The formation of a solid solution in the utilized powder blends during the MA process appears to be governed only by the intensity of the MA process, given by the length of milling time and milling speed (RPM), at least within the range of used parameters. Therefore, assuming that the milling is intensive enough, the solid solution will eventually form. The higher intensity of milling can be induced either by prolonged milling time, increased milling speed or increase of both parameters, respectively. It is questionable, whether the use of milling parameters completely different than the ones used in this study would induce different milling outcomes.

Regarding the role of present elements on type of formed solid solution after the MA, it seems that very small similarities exist between milling of $AlCoCrFeNiTi_{0.5}$ where BCC have been formed, $Ni_{1.5}Co_{1.5}CrFeTi_{0.5}$ where mixture of two FCC and BCC appeared and CoCrNi alloy containing FCC and HCP, respectively. It seems that, considering the results of the study and other previous research [92, 97, 109, 110], the formation of cubic solid solutions is favored. However, the true nature of the formed solid solution is given by exact chemical composition of the alloy. Also, the nature of the MA formed solid solution seems very unstable, as different phases are usually formed upon high temperature densification, or annealing processing.

Even though the changes in MA parameters does not influence the chemical reactions in powders significantly (at least for used combinations of parameters), they affect the morphology and average particle size of the manufactured powders. It can be postulated that, in general, the increase in milling speed induces the particle size increase. However, it is extremely hard to generalize more on the influence of milling time and used milling balls diameter, as the resulting powder morphology is extremely specific in different cases.

For the purposes of the study, preparation of fully homogenous alloys after densification, even the accomplishment of perfectly homogenous solid solution in the MA powders is not necessary, as observed for the case of CoCrNi alloy. If some of the layers of original powders are present, the homogenous fine-grained microstructure will appear nevertheless as the diffusion rate during the SPS process is high enough to even out the short distance chemical gradients.

No general rule can be formulated that enables to specify MA conditions; for every particular MA case, the optimal milling conditions have to be adjusted by trial and error way.

8.2 Comparison of the mechanical properties with literature data

In the first section, PM $AlCoCrFeNiTi_{0.5}$ will be evaluated separately due to the fact that, as compared to the rest of produced materials ($Ni_{1.5}Co_{1.5}CrFeTi_{0.5}$, CoCrNi), its mechanical properties as well as phase composition are incomparably different. The produced materials of this chemical composition - Alloy A, Alloy B and Alloy C were differentiated according to their milling conditions (Alloy A -250 RPM, Alloy B 400 RPM and Alloy C 400 RPM with the absence of PCA). In general, the formation of hard, brittle phases such as B2 or σ resulted in relatively high hardness values – over 800 HV, but at the expense of plastic properties. In this regard, brittle fracture behavior has been documented in all bend test samples, even after the utilized heat treatment that was performed to decrease the brittle nature of the alloys. In the particular case of this composition, the use of PCA is crucial for its performance, as it resulted in the formation of more favorable microstructure containing TiC and FCC ductile phase. The alloy milled without the addition of PCA; alloy C was extremely brittle due to the appearance of considerable quantity of σ phase and suppression of ductile FCC phase formation.

However, it should be noted that, for alloy B, the bending strength reached almost 2000 MPa with 546 HV after the HT procedure at 1250 °C - a good performance comparable to some tool steels [111]. The alloy also exhibited good microstructural stability during HT. Considering the phase composition of alloy B that contains dispersion of TiC particles, there is a reasonable premise for good abrasive wear resistance.

Considering all its properties, it seems that the alloy could find an application as a tool material, either used as a bulk or coating. For the application as a traditional, load bearing structural material, the ductility and damage resistance properties does not seems satisfactory at the moment, in the light of results obtained herein and the published works [5, 66, 112].

The comprehensive comparison of the mechanical properties obtained by tensile test of the PM alloys $Ni_{1.5}Co_{1.5}CrFeTi_{0.5}$, CoCrNi and CoCrNi/boride composite produced in this work, with the available published results of alloys produced by casting is presented in Fig. 101; the data for comparison has been taken from references [43-46, 102, 113-120]. Note that some HEA compositions are present multiple times due to the difference in the last processing step, e.g. as-cast state, as-cast and hot rolled, as-cast and cold rolled – that resulted in different tensile properties.

It should be noted that, even though there are several examples of the produced PM HEAs (be it combination of MA + SPS or other), their absence in the comparison chart in Fig. 101 stems from the fact that the HEAs produced by PM route didn’t exhibit satisfactory level of ductility, to perform credible tensile test. As such, this work represents one of the first successful attempts to produce ductile PM HEA and MEA. PM $AlCoCrFeNiTi_{0.5}$ alloy is not present, as its tensile test has not been performed. In this fashion, the PM $AlCoCrFeNiTi_{0.5}$ alloy is too brittle to be used as a structural material, as mentioned earlier in the section.

It is obvious that, in terms of room temperature tensile properties, many of the HEAs easily outperform the ferrous alloy - steels. In addition, they usually possess excellent secondary properties, especially corrosion resistance given by the passivating influence of Cr and Al element in their compositions – as mentioned in paragraph 2.4. The $Fe_{40}Ni_{11.3}Mn_{34.8}Al_{7.5}Cr_6C_1$ HEA is present in Fig. 101 once in as cast + homogenized condition, and second time in as-cast, homogenized and cold rolled condition as 120 μm and 4.7 μm, respectively. The decrease in grain size clearly increases the strength of the alloy. Therefore, as proposed in the reference [121, 122], the HEAs and MEAs comply with Hall – Petch relation in the same way as the traditional polycrystalline systems.

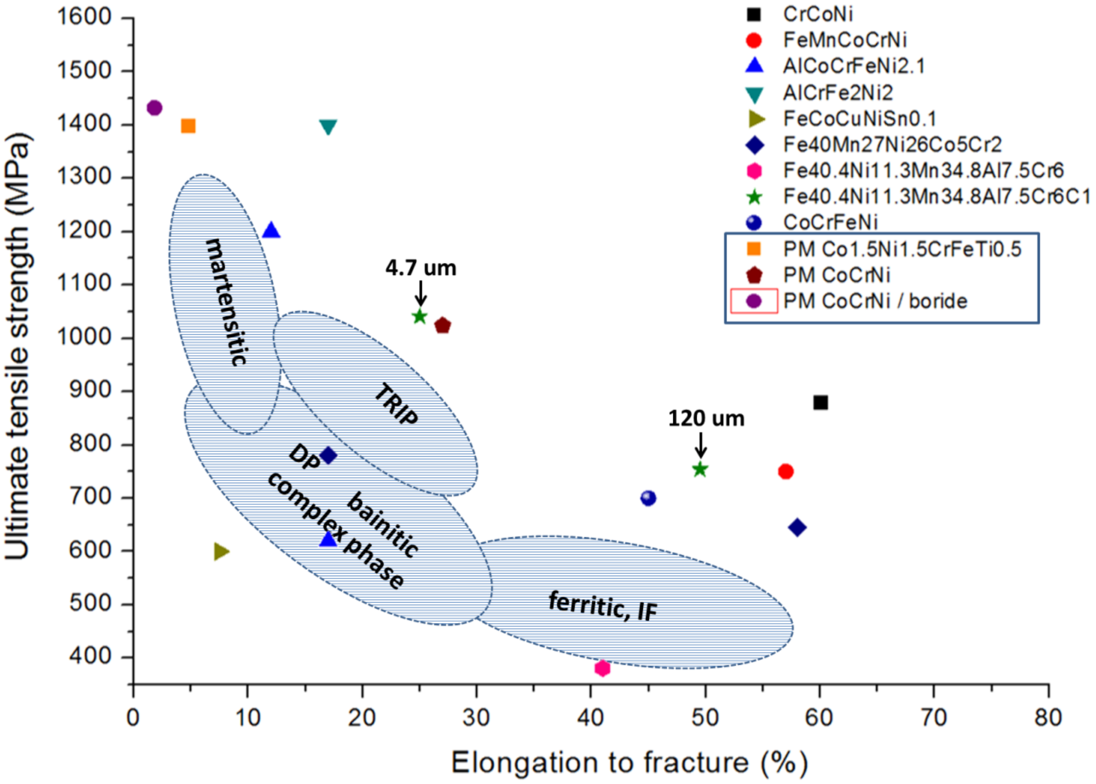

Fig. 101 Comparison of strength and deformation of conventional steels, high and medium entropy alloys, with materials produced in this study highlighted by blue rectangle, the MEA composite is marked by red rectangle. Some HEA compositions are present multiple times due to their different last manufacturing step.

Comparing the properties of the produced PM CoCrNi and PM $Co_{1.5}Ni_{1.5}CrFeTi_{0.5}$ alloy, one can see that the latter possesses much higher strength properties, but its ductility is significantly lower. In fact, the whole set of available results from mechanical testing are supporting this claim, especially the fractographic analysis. The increase in the strength is most probably associated with multiple strengthening phenomena acting concurrently. One of them emerges from the average grain size of the $Co_{1.5}Ni_{1.5}CrFeTi_{0.5}$ alloy being approximately ¼ of the CoCrNi. The significantly reduced grain size of the 5 elements alloy may be associated to slower diffusion kinetics – sluggish diffusion effect intrinsic to all HEAs, induced by the presence of 5 elements as compared to only 3 in CoCrNi. The increase in grain size should not be notably affected by the slightly higher sintering temperature used for CoCrNi alloy preparation, as the total difference was only 30 °C.

Another phenomenon greatly affecting the total strength is the much more pronounced atomic size mismatch δ - 5.04% of $Co_{1.5}Ni_{1.5}CrFeTi_{0.5}$ alloy, in contrast to δ value of 0.36% in 3 element CoCrNi alloy.

The introduction of hard boride particles of in-situ formed Cr_5B_3 - result of B_4C reaction with present Cr – caused more than two-fold increase in the ultimate tensile strength and hardness of PM CoCrNi / boride composite, but notably decreased the total elongation, i.e. to only 1.86 %. However, it is very interesting to note that the interface between the boride reinforcement and the matrix FCC phase exhibited very high bonding strength, as no direct interfacial decohesion has been observed in fracture surfaces. Instead, the ductile tearing of the

FCC matrix phase has been observed, probably at the places of high stress triaxiality, which is a requirement for development of ductile fracture behavior [83].

The $Co_{1.5}Ni_{1.5}CrFeTi_{0.5}$ is closely matching the CoCrNi / boride composite in terms of strength. On the other hand, it exhibits the tensile elongation exceeding 4 %. Therefore, in the overall comparison, the $Co_{1.5}Ni_{1.5}CrFeTi_{0.5}$ alloy comes on top of all materials produced in this study.

Regarding the $AlCoCrFeNiTi_{0.5}$ alloy, the presence of Al element induced the formation of microstructure with unfavorable mechanical properties, especially very high brittleness. As compared to $Co_{1.5}Ni_{1.5}CrFeTi_{0.5}$, the Al presence in relatively high atomic concentration induces the formation of ordered, Al-rich B2 phase. Also, the higher atomic concentration of Cr and Fe elements probably caused the appearance of Cr-rich σ phase, which possess properties that are very detrimental to the overall alloy ductility. However, considering very high hardness values, even after heat treatment procedure, the high wear resistance can be expected from the alloy even at high temperatures.

8.3 Production of TiC reinforced in-situ composites

One of the most important contributions of the work is seen in the finding of the possibility to produce in-situ composites with nano-grained dispersion of TiC (as displayed in Fig. 102). The in-situ reaction enabled during high temperature exposure after powder mechanical alloying in the presence of liquid organic PCA. The PCA (e.g. toluene C_6H_5-CH_3, hexane C_6H_{14}) serves as the source of carbon and, at the same time support the mechanical alloying process. In this fashion, bulk materials, as well as powders with TiC dispersion may be conveniently manufactured.

The simple chemical reaction governing the TiC formation goes as presented below:

$$Ti + C = TiC \tag{27}$$

The alloy should, therefore, contain atomic concentration of Ti element that correlates with the atomic fraction of C, added in the form of PCA. The key element of the successful production is the mechanical alloying process, which enables the dissolution of C into the milled powders. Therefore, the powders should be extensively milled to enable the incorporation of PCA present on the powder particles surfaces into the powders cross section. The Ti element introduced in the form of pure powder should be homogenously dispersed correspondingly. It should be noted that the same procedure could be used to produce different kind of carbide dispersion, as the Ti may be replaced by other element with high affinity for C (e.g. Nb, Zr).

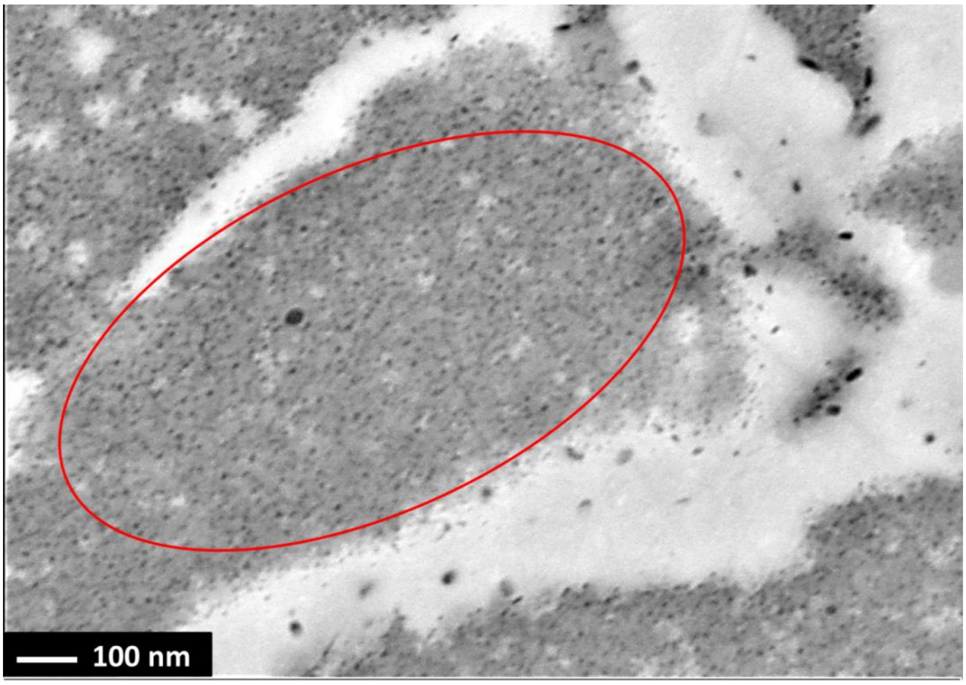

Fig. 102 Area with in-situ formed TiC nano dispersion (small black dots) in B2 phase grey area observed in bulk $AlCoCrFeNiTi_{0.5}$ alloy observed by SEM BSE, white area correspond to FCC phase.

Assuming the MA powders are manufactured in this way, the nano-grained TiC dispersion will form in the phase that contains the Ti element, after the high temperature exposure. In the case of $AlCoCrFeNiTi_{0.5}$, it happened to be Ti-rich B2 phase.

The volume of the formed TiC can be adjusted by the calculation of required quantity of PCA and Ti, respectively; however, this should be also correlated with the appropriate milling conditions. The research on the TiC in situ composites, therefore, carries challenges, as the volume of formed TiC seems to be significantly altered by changes in milling parameters, that are probably connected to the PCA dissolution kinetics.

The role of H present in the organic PCA has not been fully understood. It seems that it evaporates either already during the MA process prior to the described reaction of C and Ti or after the subsequent heating, as no traces of H-rich phases has been documented by performed analytical methods. However, it should be noted that, to assess the presence of H-rich phases precisely, different characterization methods should be employed. Ultimately, the presence of H in PCA seems to not have detrimental effect on the microstructure and mechanical properties.

One of the future topics of the ongoing research in this area is to evaluate the influence of different milling time on the dissolution of PCA in the powder cross section, as well as its influence on TiC dispersion formation and morphology. The composites with FCC HEA or MEA matrix and TiC dispersion will be subsequently prepared and studied, in comparison with the same ex-situ composites.

8.4 Pros and cons of the selected manufacturing process vs casting

As mentioned in 3.2.1, the grain boundary strengthening described by Hall-Petch equation represents one of the most feasible way to increase the yield strength of the materials.

Considering this fact, one of the most eloquent benefit of the use of the selected manufacturing route, i.e. combination of MA and SPS, is deduced in the following section.

In conventional cast alloys, the grain size refinement in single phase alloys is imposed by the cold deformation processes, resulting in significant level of property anisotropy (e.g. cold rolling etc.). Additionally, there is rather limited end product shape variability – usually alloy sheet is produced with additional cutting and machining operations required.

As opposed to this, utilizing the combination of MA and SPS, the extremely fine-grained microstructure may be achieved in the state directly after SPS. The possible variability of the shapes is given by the geometry of the SPS die. The amplitude of grain refinement is simply adjusted by the intensity of the milling process. In addition to this, also different types of densification processes may be applied for the MA powders, including the standard cold-press and sinter, where shape variability is greatly increased.

Unfortunately, there are also drawbacks to the MA + SPS manufacturing route. By far, the greatest hindrance is the formation of undesired oxide inclusions in the powder cross section and the final bulk materials.

In the matter of contamination, the cast materials claim superiority over their PM counterparts, due to possibility to decrease the contamination of all kinds by several tried and tested industrial processes (inert gas purging, vacuum remelting, desoxidation, etc.)

Oxide formation has been observed in all of the PM materials in the study. The way to counter their formation has not been discovered throughout the work. The oxide contamination is induced by the presence of oxides on the original elemental powder particles. These oxides then become dispersed into the cross section of MA powders. The surfaces of the powder particles may be treated in a reduction atmosphere, to chemically turn the metal oxides back into pure metals. However, this reduction process takes place on the powder particle surfaces only. The oxides that are dispersed during MA inside the powder particles will not be affected much.

The surfaces of the reduced powders will be subsequently corrupted by atmospheric oxygen again, as soon as the powders are removed from the reduction furnace. This becomes inevitable, as they need to be fed to the SPS machine die manually in the air.

The performance of SPS in the reduction atmosphere could solve the problem partially. However, the SPS process would be probably almost impossible to perform in reduction atmosphere containing significant amounts of hydrogen gas, due to problem with explosions. Additionally, it would not solve the problems of oxides present inside the powder particles.

Another way would be an introduction of trace amount of active metals. This would affect the surface energy of the oxides, thus altering their morphology to form finer, more homogenous dispersion.

The effect of the oxide dispersion (inclusions) in the manufactured materials is in a way questionable; their effect is on one hand beneficial, as oxides they retard the dislocation movement, thus increasing the strength levels. The oxides also indirectly provide grain boundary strengthening, bearing in mind their beneficial effect on the grain growth suppression during the high temperature exposure (see paragraph 3.3.1). On the other hand, presence of oxide inclusion is generally apprehended as detrimental, as they may cause the void nucleation and following crack growth.

Nevertheless, their presence is somewhat inevitable in the materials produced by PM manufacturing route, as a consequence of enormous free surfaces, especially in alloys containing elements susceptible to oxidation (Al, Ti, Cr, Mg…), as shown in previous results on commercial alloys [123-125].

9 Conclusions

The presented work has been focused on the preparation and feasibility of production of Medium and High Entropy Alloys and their composites by utilization of powder metallurgy processes; namely a combination of mechanical alloying and spark plasma sintering. The properties of the manufactured materials have been evaluated, with a special focus on their prospective mechanical response. The main results of the work can be summarized as follows:

1. The HEAs and MEAs powders with extremely fine crystallite sizes can be produced by mechanical alloying of elemental powders. The resulting powder microstructures are considerably affected by the mechanical alloying process parameters selection.
2. The presence of process control agent containing carbon is important to prevent agglomeration of powders. However, it may cause the formation of in-situ carbides after mechanical alloying. The process may be exploited to produce in-situ reinforced composites.
3. The mechanically alloyed powders can be readily densified to full density bulk materials by spark plasma sintering process.
4. The manufactured bulks possess very fine grain sizes and isotropic properties.
5. The oxides present at the surfaces of powders are retained and produce homogenous dispersion after the mechanical alloying process that is retained in the final bulks. The parameters δ, ΔH_{mix}, ΔS_{mix}, Ω and VEC for microstructural prediction have shown relatively poor validity for the HEAs prepared by PM route.
6. The best mechanical properties have been attributed to the $Co_{1.5}Ni_{1.5}CrFeTi_{0.5}$, exhibiting the ultimate tensile strength R_m of 1384 MPa and 4% of tensile elongation.
7. For the use as a matrix for composite materials, the PM CoCrNi alloy possessed best properties with ultimate tensile strength R_m of 1024 MPa and 26% tensile elongation
8. CoCrNi alloy reinforced by in-situ formed Cr boride exhibited and exceptional increase in strength properties at the expense of plasticity.

10 Future work

The results presented in the study exposed many unanswered questions regarding the nature of the mechanical alloying processes, as well as the regarding properties of the High

Entropy Alloys, their prospects and future application. Some of the topics considered for the future research are outlined below:

1. The microstructural stability of the HEAs and MEAs during high temperature exposure, to assess their prospective high temperature application potential.
2. The role of oxides on the properties of alloys, as well as possible ways to decrease the oxide contamination.
3. The influence of interstitial elements (H, N) on behavior of HEA produced by PM process.
4. The differences in TiC reinforced composites produced by in-situ reaction and traditional ex-situ composites.

References:

[1] J.-W. Yeh, Alloy Design Strategies and Future Trends in High-Entropy Alloys, JOM 65(12) (2013) 1759-1771.

[2] J.W. Yeh, S.K. Chen, S.J. Lin, J.Y. Gan, T.S. Chin, T.T. Shun, C.H. Tsau, S.Y. Chang, Nanostructured High-Entropy Alloys with Multiple Principal Elements: Novel Alloy Design Concepts and Outcomes, Advanced Engineering Materials 6(5) (2004) 299-303.

[3] B. Cantor, I.T.H. Chang, P. Knight, A.J.B. Vincent, Microstructural development in equiatomic multicomponent alloys, Materials Science and Engineering: A 375–377(0) (2004) 213-218.

[4] E. Munch, M.E. Launey, D.H. Alsem, E. Saiz, A.P. Tomsia, R.O. Ritchie, Tough, Bio-Inspired Hybrid Materials, Science 322(5907) (2008) 1516.

[5] U.G.K. Wegst, H. Bai, E. Saiz, A.P. Tomsia, R.O. Ritchie, Bioinspired structural materials, Nat Mater 14(1) (2015) 23-36.

[6] S. Fang, W. Chen, Z. Fu, Microstructure and mechanical properties of twinned Al0.5CrFeNiCo0.3C0.2 high entropy alloy processed by mechanical alloying and spark plasma sintering, Materials & Design (1980-2015) 54 (2014) 973-979.

[7] P.W. Lee, e. all, ASM Metal Handbook: Volume 7 Powder Metal Technologies and Applications, ASM International, 1997.

[8] L. Jiang, Z. Li, G. Fan, L. Cao, D. Zhang, Strong and ductile carbon nanotube/aluminum bulk nanolaminated composites with two-dimensional alignment of carbon nanotubes, Scripta Materialia 66(6) (2012) 331-334.

[9] B.S. Murty, J.W. Yeh, S. Ranganathan, High-Entropy Alloys, Elsevier, Butterworth-Heinemann, London, 2014.

[10] Y. Zhang, T.T. Zuo, Z. Tang, M.C. Gao, K.A. Dahmen, P.K. Liaw, Z.P. Lu, Microstructures and properties of high-entropy alloys, Progress in Materials Science 61(0) (2014) 1-93.

[11] J.W. Gibbs, On the Equilibrium of Heterogeneous Substances, In: The Scientific Papers of J. Willard Gibbs, vol. 1, 1993, 1906.

[12] A. Nowotnik, Nickel-Based Superalloys, Reference Module in Materials Science and Materials Engineering, Elsevier2016.

[13] X. Yang, Y. Zhang, Prediction of high-entropy stabilized solid-solution in multi-component alloys, Materials Chemistry and Physics 132(2–3) (2012) 233-238.

[14] Y.J. Lv, M. Chen, Thermophysical Properties of Undercooled Alloys: An Overview of the Molecular Simulation Approaches, International Journal of Molecular Sciences 12(1) (2011).

[15] A. Takeuchi, A. Inoue, Classification of Bulk Metallic Glasses by Atomic Size Difference, Heat of Mixing and Period of Constituent Elements and Its Application to Characterization of the Main Alloying Element, MATERIALS TRANSACTIONS 46(12) (2005) 2817-2829.
[16] C. Zhang, F. Zhang, S. Chen, W. Cao, Computational Thermodynamics Aided High-Entropy Alloy Design, JOM 64(7) (2012) 839-845.
[17] Y. Zhang, Y.J. Zhou, J.P. Lin, G.L. Chen, P.K. Liaw, Solid-Solution Phase Formation Rules for Multi-component Alloys, Advanced Engineering Materials 10(6) (2008) 534-538.
[18] K.Y. Tsai, M.H. Tsai, J.W. Yeh, Sluggish diffusion in Co–Cr–Fe–Mn–Ni high-entropy alloys, Acta Materialia 61(13) (2013) 4887-4897.
[19] Z. Balogh, G. Schmitz, 5 - Diffusion in Metals and Alloys A2 - Laughlin, David E, in: K. Hono (Ed.), Physical Metallurgy (Fifth Edition), Elsevier, Oxford, 2014, pp. 387-559.
[20] D. Li, Y. Zhang, The ultrahigh charpy impact toughness of forged AlxCoCrFeNi high entropy alloys at room and cryogenic temperatures, Intermetallics 70 (2016) 24-28.
[21] J.-W. Yeh, S.-Y. Chang, Y.-D. Hong, S.-K. Chen, S.-J. Lin, Anomalous decrease in X-ray diffraction intensities of Cu–Ni–Al–Co–Cr–Fe–Si alloy systems with multi-principal elements, Materials Chemistry and Physics 103(1) (2007) 41-46.
[22] S. Ranganathan, Alloyed pleasures: Multimetallic cocktails, Current Science 85(10) (2003) 1404-1406.
[23] X. Yang, Y. Zhang, P.K. Liaw, Microstructure and Compressive Properties of NbTiVTaAlx High Entropy Alloys, Procedia Engineering 36 (2012) 292-298.
[24] Y. Dong, K. Zhou, Y. Lu, X. Gao, T. Wang, T. Li, Effect of vanadium addition on the microstructure and properties of AlCoCrFeNi high entropy alloy, Materials & Design 57 (2014) 67-72.
[25] S.G. Ma, Y. Zhang, Effect of Nb addition on the microstructure and properties of AlCoCrFeNi high-entropy alloy, Materials Science and Engineering: A 532 (2012) 480-486.
[26] P.K. Huang, J.W. Yeh, T.T. Shun, S.K. Chen, Multi-Principal-Element Alloys with Improved Oxidation and Wear Resistance for Thermal Spray Coating, Advanced Engineering Materials 6(1-2) (2004) 74-78.
[27] W.-R. Wang, W.-L. Wang, J.-W. Yeh, Phases, microstructure and mechanical properties of AlxCoCrFeNi high-entropy alloys at elevated temperatures, Journal of Alloys and Compounds 589 (2014) 143-152.
[28] B.D. Miracle, D.J. Miller, N.O. Senkov, C. Woodward, D.M. Uchic, J. Tiley, Exploration and Development of High Entropy Alloys for Structural Applications, Entropy 16(1) (2014).
[29] S. Guo, Q. Hu, C. Ng, C.T. Liu, More than entropy in high-entropy alloys: Forming solid solutions or amorphous phase, Intermetallics 41(0) (2013) 96-103.
[30] W.-R. Wang, W.-L. Wang, S.-C. Wang, Y.-C. Tsai, C.-H. Lai, J.-W. Yeh, Effects of Al addition on the microstructure and mechanical property of AlxCoCrFeNi high-entropy alloys, Intermetallics 26(0) (2012) 44-51.
[31] W.-R. Wang, W.-L. Wang, J.-W. Yeh, Phases, microstructure and mechanical properties of AlxCoCrFeNi high-entropy alloys at elevated temperatures, Journal of Alloys and Compounds 589(0) (2014) 143-152.
[32] E.J. Pickering, R. Muñoz-Moreno, H.J. Stone, N.G. Jones, Precipitation in the equiatomic high-entropy alloy CrMnFeCoNi, Scripta Materialia 113 (2016) 106-109.
[33] E.J. Pickering, N.G. Jones, High-entropy alloys: a critical assessment of their founding principles and future prospects, International Materials Reviews 61(3) (2016) 183-202.
[34] W. Hume-Rothery, B.R. Coles, The transition metals and their alloys, Advances in Physics 3(10) (1954) 149-242.
[35] U. Mizutani, Hume-Rothery rules for structurally complex alloy phases, MRS Bulletin 37(2) (2012) 169-169.

[36] Y.-F. Kao, T.-J. Chen, S.-K. Chen, J.-W. Yeh, Microstructure and mechanical property of as-cast, -homogenized, and -deformed AlxCoCrFeNi ($0 \leq x \leq 2$) high-entropy alloys, Journal of Alloys and Compounds 488(1) (2009) 57-64.

[37] K. Zhang, Z. Fu, Effects of annealing treatment on phase composition and microstructure of CoCrFeNiTiAlx high-entropy alloys, Intermetallics 22 (2012) 24-32.

[38] B. Schuh, F. Mendez-Martin, B. Völker, E.P. George, H. Clemens, R. Pippan, A. Hohenwarter, Mechanical properties, microstructure and thermal stability of a nanocrystalline CoCrFeMnNi high-entropy alloy after severe plastic deformation, Acta Materialia 96 (2015) 258-268.

[39] Y.-J. Chang, A.-C. Yeh, The evolution of microstructures and high temperature properties of AlxCo1.5CrFeNi1.5Tiy high entropy alloys, Journal of Alloys and Compounds.

[40] F. Tian, L.K. Varga, N. Chen, J. Shen, L. Vitos, Empirical design of single phase high-entropy alloys with high hardness, Intermetallics 58(0) (2015) 1-6.

[41] Z. Wu, H. Bei, F. Otto, G.M. Pharr, E.P. George, Recovery, recrystallization, grain growth and phase stability of a family of FCC-structured multi-component equiatomic solid solution alloys, Intermetallics 46 (2014) 131-140.

[42] O.N. Senkov, J.M. Scott, S.V. Senkova, F. Meisenkothen, D.B. Miracle, C.F. Woodward, Microstructure and elevated temperature properties of a refractory TaNbHfZrTi alloy, Journal of Materials Science 47(9) (2012) 4062-4074.

[43] M.J. Yao, K.G. Pradeep, C.C. Tasan, D. Raabe, A novel, single phase, non-equiatomic FeMnNiCoCr high-entropy alloy with exceptional phase stability and tensile ductility, Scripta Materialia 72–73 (2014) 5-8.

[44] B. Gludovatz, A. Hohenwarter, D. Catoor, E.H. Chang, E.P. George, R.O. Ritchie, A fracture-resistant high-entropy alloy for cryogenic applications, Science 345(6201) (2014) 1153-1158.

[45] B.H. Gludovatz, A. Thurston, KV. Bei. H. Wu. Z. George, EP. Ritchie, RO., Exceptional damage-tolerance of a medium-entropy alloy CrCoNi at cryogenic temperatures, Nature communications, 2016.

[46] Z. Wu, H. Bei, G.M. Pharr, E.P. George, Temperature dependence of the mechanical properties of equiatomic solid solution alloys with face-centered cubic crystal structures, Acta Materialia 81 (2014) 428-441.

[47] Z. Wu, C.M. Parish, H. Bei, Nano-twin mediated plasticity in carbon-containing FeNiCoCrMn high entropy alloys, Journal of Alloys and Compounds 647 (2015) 815-822.

[48] Z. Zhang, M.M. Mao, J. Wang, B. Gludovatz, Z. Zhang, S.X. Mao, E.P. George, Q. Yu, R.O. Ritchie, Nanoscale origins of the damage tolerance of the high-entropy alloy CrMnFeCoNi, Nat Commun 6 (2015).

[49] D.T. Pierce, J.A. Jiménez, J. Bentley, D. Raabe, J.E. Wittig, The influence of stacking fault energy on the microstructural and strain-hardening evolution of Fe–Mn–Al–Si steels during tensile deformation, Acta Materialia 100 (2015) 178-190.

[50] N. Kumar, Q. Ying, X. Nie, R.S. Mishra, Z. Tang, P.K. Liaw, R.E. Brennan, K.J. Doherty, K.C. Cho, High strain-rate compressive deformation behavior of the Al0.1CrFeCoNi high entropy alloy, Materials & Design 86 (2015) 598-602.

[51] Z. Fu, W. Chen, S. Fang, X. Li, Effect of Cr addition on the alloying behavior, microstructure and mechanical properties of twinned CoFeNiAl0.5Ti0.5 alloy, Materials Science and Engineering: A 597(0) (2014) 204-211.

[52] S. Huang, W. Li, S. Lu, F. Tian, J. Shen, E. Holmström, L. Vitos, Temperature dependent stacking fault energy of FeCrCoNiMn high entropy alloy, Scripta Materialia 108 (2015) 44-47.

[53] P. Behjati, A. Kermanpur, A. Najafizadeh, H. Samaei Baghbadorani, J.G. Jung, Y.K. Lee, Enhanced mechanical properties in a high-manganese austenitic steel through formation of

nano grains, nanotwinned austenite grains, nano carbides and TRIP, Materials Science and Engineering: A 610 (2014) 273-278.
[54] Y. Deng, C.C. Tasan, K.G. Pradeep, H. Springer, A. Kostka, D. Raabe, Design of a twinning-induced plasticity high entropy alloy, Acta Materialia 94 (2015) 124-133.
[55] Y. Yu, J. Wang, J. Li, H. Kou, W. Liu, Characterization of BCC phases in AlCoCrFeNiTix high entropy alloys, Materials Letters 138(0) (2015) 78-80.
[56] M.-H. Chuang, M.-H. Tsai, W.-R. Wang, S.-J. Lin, J.-W. Yeh, Microstructure and wear behavior of AlxCo1.5CrFeNi1.5Tiy high-entropy alloys, Acta Materialia 59(16) (2011) 6308-6317.
[57] Y.Y. Chen, U.T. Hong, H.C. Shih, J.W. Yeh, T. Duval, Electrochemical kinetics of the high entropy alloys in aqueous environments—a comparison with type 304 stainless steel, Corrosion Science 47(11) (2005) 2679-2699.
[58] X.-W. Qiu, Microstructure and properties of AlCrFeNiCoCu high entropy alloy prepared by powder metallurgy, Journal of Alloys and Compounds 555 (2013) 246-249.
[59] Z. Tang, L. Huang, W. He, K.P. Liaw, Alloying and Processing Effects on the Aqueous Corrosion Behavior of High-Entropy Alloys, Entropy 16(2) (2014).
[60] Y.-J. Chang, A.-C. Yeh, The evolution of microstructures and high temperature properties of AlxCo1.5CrFeNi1.5Tiy high entropy alloys, Journal of Alloys and Compounds 653 (2015) 379-385.
[61] H.M. Daoud, A.M. Manzoni, N. Wanderka, U. Glatzel, High-Temperature Tensile Strength of Al10Co25Cr8Fe15Ni36Ti6 Compositionally Complex Alloy (High-Entropy Alloy), JOM 67(10) (2015) 2271-2277.
[62] M.A. Manzoni, S. Singh, M.H. Daoud, R. Popp, R. Völkl, U. Glatzel, N. Wanderka, On the Path to Optimizing the Al-Co-Cr-Cu-Fe-Ni-Ti High Entropy Alloy Family for High Temperature Applications, Entropy 18(4) (2016).
[63] U. Roy, H. Roy, H. Daoud, U. Glatzel, K.K. Ray, Fracture toughness and fracture micromechanism in a cast AlCoCrCuFeNi high entropy alloy system, Materials Letters 132 (2014) 186-189.
[64] A. Meyers, K. Chawla, Mechanical Behaviour of Materials, Cambridge University Press, Cambridge, 2009.
[65] A. Adams, ASM Metals handbook Composites, Materials information company, ASM International, 2001.
[66] R.O. Ritchie, The conflicts between strength and toughness, Nat Mater 10(11) (2011) 817-822.
[67] Q. Chen, N.M. Pugno, Bio-mimetic mechanisms of natural hierarchical materials: A review, Journal of the Mechanical Behavior of Biomedical Materials 19 (2013) 3-33.
[68] N. Chawla, Y.L. Shen, Mechanical Behavior of Particle Reinforced Metal Matrix Composites, Advanced Engineering Materials 3(6) (2001) 357-370.
[69] B. Harris, ENGINEERING COMPOSITE MATERIALS The Institute of Materials, London, 1999.
[70] I.A. Ibrahim, F.A. Mohamed, E.J. Lavernia, Particulate reinforced metal matrix composites — a review, Journal of Materials Science 26(5) (1991) 1137-1156.
[71] R. Casati, M. Vedani, Metal Matrix Composites Reinforced by Nano-Particles—A Review, Metals 4(1) (2014).
[72] T.G. Nieh, J. Wadsworth, Hall-petch relation in nanocrystalline solids, Scripta Metallurgica et Materialia 25(4) (1991) 955-958.
[73] O. Bouaziz, S. Allain, C.P. Scott, P. Cugy, D. Barbier, High manganese austenitic twinning induced plasticity steels: A review of the microstructure properties relationships, Current Opinion in Solid State and Materials Science 15(4) (2011) 141-168.

[74] A.F. Mirza, L.D. Chen, A Unified Model for the Prediction of Yield Strength in Particulate-Reinforced Metal Matrix Nanocomposites, Materials 8(8) (2015).
[75] Z. Zhang, D.L. Chen, Consideration of Orowan strengthening effect in particulate-reinforced metal matrix nanocomposites: A model for predicting their yield strength, Scripta Materialia 54(7) (2006) 1321-1326.
[76] A. Sanaty-Zadeh, Comparison between current models for the strength of particulate-reinforced metal matrix nanocomposites with emphasis on consideration of Hall–Petch effect, Materials Science and Engineering: A 531 (2012) 112-118.
[77] S.F. Hassan, M.J. Tan, M. Gupta, High-temperature tensile properties of Mg/Al2O3 nanocomposite, Materials Science and Engineering: A 486(1–2) (2008) 56-62.
[78] G.I. Taylor, The Mechanism of Plastic Deformation of Crystals. Part I. Theoretical, Proceedings of the Royal Society of London. Series A 145(855) (1934) 362.
[79] Z. Zhang, D.L. Chen, Contribution of Orowan strengthening effect in particulate-reinforced metal matrix nanocomposites, Materials Science and Engineering: A 483–484 (2008) 148-152.
[80] Q.B. Nguyen, M. Gupta, Enhancing compressive response of AZ31B magnesium alloy using alumina nanoparticulates, Composites Science and Technology 68(10–11) (2008) 2185-2192.
[81] M. Kouzeli, A. Mortensen, Size dependent strengthening in particle reinforced aluminium, Acta Materialia 50(1) (2002) 39-51.
[82] A. Miserez, A. Rossoll, A. Mortensen, Investigation of crack-tip plasticity in high volume fraction particulate metal matrix composites, Engineering Fracture Mechanics 71(16–17) (2004) 2385-2406.
[83] A. Miserez, R. Müller, A. Rossoll, L. Weber, A. Mortensen, Particle reinforced metals of high ceramic content, Materials Science and Engineering: A 387–389 (2004) 822-831.
[84] L. Jiang, Z. Li, G. Fan, D. Zhang, A flake powder metallurgy approach to Al2O3/Al biomimetic nanolaminated composites with enhanced ductility, Scripta Materialia 65(5) (2011) 412-415.
[85] C. Suryanarayana, E. Ivanov, V.V. Boldyrev, The science and technology of mechanical alloying, Materials Science and Engineering: A 304–306 (2001) 151-158.
[86] C. Suryanarayana, Mechanical alloying and milling, Progress in Materials Science 46(1–2) (2001) 1-184.
[87] B.S. Murty, M. Mohan Rao, S. Ranganathan, Milling maps and amorphization during mechanical alloying, Acta Metallurgica et Materialia 43(6) (1995) 2443-2450.
[88] J. Joardar, S.K. Pabi, B.S. Murty, Milling criteria for the synthesis of nanocrystalline NiAl by mechanical alloying, Journal of Alloys and Compounds 429(1–2) (2007) 204-210.
[89] L. Takacs, Self-sustaining reactions induced by ball milling, Progress in Materials Science 47(4) (2002) 355-414.
[90] S. Nouari, Spark Plasma Sintering of Metals and Metal Matrix Nanocomposites: A Review, in: I. Zafar (Ed.) Hindawi Publishing Corporation, Journal of Nanomaterials, 2012, p. 13.
[91] S.r.A.F.n. M, J.L. Menéndez, R. Torrecillas, H. U. Kessel, J. Hennicke, R. Kirchner and T. Kessel (2013). Challenges and Opportunities for Spark Plasma Sintering: A Key Technology for a New Generation of Materials, Sintering Applications, Dr. Burcu Ertug (Ed.), InTech, DOI: 10.5772/53706. in: F.n. A (Ed.) Burcu Ertug (Ed.), InTech, 2013, p. 20.
[92] Z. Fu, W. Chen, H. Xiao, L. Zhou, D. Zhu, S. Yang, Fabrication and properties of nanocrystalline Co0.5FeNiCrTi0.5 high entropy alloy by MA–SPS technique, Materials & Design 44 (2013) 535-539.

[93] F. Lomello, G. Bonnefont, Y. Leconte, N. Herlin-Boime, G. Fantozzi, Processing of nano-SiC ceramics: Densification by SPS and mechanical characterization, Journal of the European Ceramic Society 32(3) (2012) 633-641.

[94] I. Sulima, P. Putyra, P. Hyjek, T. Tokarski, Effect of SPS parameters on densification and properties of steel matrix composites, Advanced Powder Technology 26(4) (2015) 1152-1161.

[95] H. Zhang, J. Ye, S.P. Joshi, J.M. Schoenung, E.S.C. Chin, G.A. Gazonas, K.T. Ramesh, Superlightweight Nanoengineered Aluminum for Strength under Impact, Advanced Engineering Materials 9(5) (2007) 355-359.

[96] J. Ye, B.Q. Han, Z. Lee, B. Ahn, S.R. Nutt, J.M. Schoenung, A tri-modal aluminum based composite with super-high strength, Scripta Materialia 53(5) (2005) 481-486.

[97] S. Fang, W. Chen, Z. Fu, Microstructure and mechanical properties of twinned Al0.5CrFeNiCo0.3C0.2 high entropy alloy processed by mechanical alloying and spark plasma sintering, Materials & Design 54(0) (2014) 973-979.

[98] W. Chen, Z. Fu, S. Fang, Y. Wang, H. Xiao, D. Zhu, Processing, microstructure and properties of Al0.6CoNiFeTi0.4 high entropy alloy with nanoscale twins, Materials Science and Engineering: A 565 (2013) 439-444.

[99] R.G.L.a.F.A. Willis, Resonant ultrasound spectroscopy, Journal of Physics: Condensed Matter 9(28) (1997) 6001.

[100] M. Umemoto, K. Tsuchiya, Z.G. Liu, S. Sugimoto, Tensile stress-strain analysis of single-structure steels, Metallurgical and Materials Transactions A 31(7) (2000) 1785-1794.

[101] N.C. Abhik, R. Vivek, V. Udhayabanu, B.S. Murty, Influence of heat of formation of B2/L12 intermetallic compounds on the milling energy for their formation during mechanical alloying, Journal of Alloys and Compounds 465(1–2) (2008) 106-112.

[102] Y. Dong, X. Gao, Y. Lu, T. Wang, T. Li, A multi-component AlCrFe2Ni2 alloy with excellent mechanical properties, Materials Letters 169 (2016) 62-64.

[103] Z. Tang, M. Gao, H. Diao, T. Yang, J. Liu, T. Zuo, Y. Zhang, Z. Lu, Y. Cheng, Y. Zhang, K. Dahmen, P. Liaw, T. Egami, Aluminum Alloying Effects on Lattice Types, Microstructures, and Mechanical Behavior of High-Entropy Alloys Systems, JOM 65(12) (2013) 1848-1858.

[104] Y. Wang, S. Ma, X. Chen, J. Shi, Y. Zhang, J. Qiao, Optimizing mechanical properties of AlCoCrFeNiTi x high-entropy alloys by tailoring microstructures, Acta Metallurgica Sinica (English Letters) 26(3) (2013) 277-284.

[105] A.A. Popov, A.S. Bannikova, S.V. Belikov, Precipitation of the sigma phase in high-alloy austenitic chromium-nickel-molybdenum alloys, The Physics of Metals and Metallography 108(6) (2009) 586-592.

[106] M.-H. Tsai, K.-Y. Tsai, C.-W. Tsai, C. Lee, C.-C. Juan, J.-W. Yeh, Criterion for Sigma Phase Formation in Cr- and V-Containing High-Entropy Alloys, Materials Research Letters 1(4) (2013) 207-212.

[107] J.D. Giallonardo, U. Erb, K.T. Aust, G. Palumbo, The influence of grain size and texture on the Young's modulus of nanocrystalline nickel and nickel–iron alloys, Philosophical Magazine 91(36) (2011) 4594-4605.

[108] H. Holleck, Material selection for hard coatings, J. Vac. Sci. Technol. A **4**, 2661 1986.

[109] H. Hadraba, Z. Chlup, A. Dlouhy, F. Dobes, P. Roupcova, M. Vilemova, J. Matejicek, Oxide dispersion strengthened CoCrFeNiMn high-entropy alloy, Materials Science and Engineering: A 689 (2017) 252-256.

[110] S. Praveen, B.S. Murty, R.S. Kottada, Alloying behavior in multi-component AlCoCrCuFe and NiCoCrCuFe high entropy alloys, Materials Science and Engineering: A 534(0) (2012) 83-89.

[111] R.K. George Adam Roberts, G. Krauss, Tool Steels, ASM International2000.

[112] A. Hohenwarter, B. Völker, M.W. Kapp, Y. Li, S. Goto, D. Raabe, R. Pippan, Ultra-strong and damage tolerant metallic bulk materials: A lesson from nanostructured pearlitic steel wires, Scientific Reports 6 (2016) 33228.
[113] Z. Tang, O.N. Senkov, C.M. Parish, C. Zhang, F. Zhang, L.J. Santodonato, G. Wang, G. Zhao, F. Yang, P.K. Liaw, Tensile ductility of an AlCoCrFeNi multi-phase high-entropy alloy through hot isostatic pressing (HIP) and homogenization, Materials Science and Engineering: A 647 (2015) 229-240.
[114] A.V. Kuznetsov, D.G. Shaysultanov, N.D. Stepanov, G.A. Salishchev, O.N. Senkov, Tensile properties of an AlCrCuNiFeCo high-entropy alloy in as-cast and wrought conditions, Materials Science and Engineering: A 533 (2012) 107-118.
[115] I.S. Wani, T. Bhattacharjee, S. Sheikh, Y.P. Lu, S. Chatterjee, P.P. Bhattacharjee, S. Guo, N. Tsuji, Ultrafine-Grained AlCoCrFeNi2.1 Eutectic High-Entropy Alloy, Materials Research Letters (2016) 1-6.
[116] J.Y. He, H. Wang, H.L. Huang, X.D. Xu, M.W. Chen, Y. Wu, X.J. Liu, T.G. Nieh, K. An, Z.P. Lu, A precipitation-hardened high-entropy alloy with outstanding tensile properties, Acta Materialia 102 (2016) 187-196.
[117] L. Liu, J.B. Zhu, C. Zhang, J.C. Li, Q. Jiang, Microstructure and the properties of FeCoCuNiSnx high entropy alloys, Materials Science and Engineering: A 548 (2012) 64-68.
[118] Z. Wang, I. Baker, Interstitial strengthening of a f.c.c. FeNiMnAlCr high entropy alloy, Materials Letters 180 (2016) 153-156.
[119] H. Dong, Y.X. Gan, Y. Weng, SpringerLink, Advanced steels the recent scenario in steel science and technology, (2011).
[120] G. Dini, A. Najafizadeh, R. Ueji, S.M. Monir-Vaghefi, Tensile deformation behavior of high manganese austenitic steel: The role of grain size, Materials & Design 31(7) (2010) 3395-3402.
[121] C. Varvenne, A. Luque, W.A. Curtin, Theory of strengthening in fcc high entropy alloys, Acta Materialia 118 (2016) 164-176.
[122] S. Yoshida, T. Bhattacharjee, Y. Bai, N. Tsuji, Friction stress and Hall-Petch relationship in CoCrNi equi-atomic medium entropy alloy processed by severe plastic deformation and subsequent annealing, Scripta Materialia 134 (2017) 33-36.
[123] F.H. Froes, M. Qian, 31 - A perspective on the future of titanium powder metallurgy, Titanium Powder Metallurgy, Butterworth-Heinemann, Boston, 2015, pp. 601-608.
[124] J. Keskinen, A. Pogany, J. Rubin, P. Ruuskanen, Carbide and hydride formation during mechanical alloying of titanium and aluminium with hexane, Materials Science and Engineering: A 196(1–2) (1995) 205-211.
[125] C.C. Eiselt, H. Schendzielorz, A. Seubert, B. Hary, Y. de Carlan, P. Diano, B. Perrin, D. Cedat, ODS-materials for high temperature applications in advanced nuclear systems, Nuclear Materials and Energy 9 (2016) 22-28.

Used abbreviations and symbols

v_b	Single milling ball speed
v_p	Reinforcement volume fraction
ρ^{CTE}	Dislocation density by CTE missmatch

ρ^{EM}	Dislocation density by EM mismatch
σ_{Orowan}	Strengthening by particles
σ_{dCTE}	Strengthening by CTE mismatch
σ_{dEM}	Strengthening by EM mismatch
σ_y	Strengthening by grain boundaries
$\emptyset$	Milling efficiency factor
$\Delta\sigma_l$	Increase of stress from load transfer strengthening
$\Delta\tau$	Increase of shear lattice friction stress
$\Delta\sigma$	Sum of all strengthening contributions
2D	2 Dimensional
B	Burger’s vector
BCC	Body Centered Cubic
BSE	Backscattered electrons
c	Atomic concentration
CALPHAD	Calculation Phase Diagram
c_i	Atomic fraction of i-th element
CMC	Ceramic matrix composites
CTE	Coefficient of Thermal expansion
D	Diffusion coefficient
d	Average grain size
d_m	Zener type strengthening final grain size
d_p	Average reinforcement particle size
DSC	Differential Scanning Calorimetry
E	Tensile Elastic modulus
E_b	Kinetic Energy
EBSD	Electron Backscattered Diffraction
ECCI	Electron Channeling Contrast Imaging
EDM	Electric Discharge Machining
EDS	Energy-Dispersive X-ray Spectroscopy
EM	Elastic Modulus
F	Number of systems in equilibrium coexisting phases
FCC	Face Centered Cubic
G	Shear Elastic Modulus

GND	Geometrically Necessary Dislocations
HCP	Hexagonal Closed Packed
HEA	High Entropy Alloy
HT	Heat treatment
I_t	Milling Intensity
k	Boltzmann’s constant ($1{,}38\times10^{-23}$ J K^{-1})
K_{IC}	Fracture Toughness
L_{12}	Ordered lattice type
ln	Natural Logarithm
MA	Mechanical Alloying
m_b	Single milling ball weight
MEA	Medium Entropy Alloy
MMC	Metal Matrix Composites
MPEA	Multi-Principal Element Alloy
N	Number of system component
n	Strain hardening exponent
PCA	Process control agent
PIPS	Precision Ion Polishing System
PM	Powder Metallurgy
PMC	Polymer Matrix Composites
R	Engineering Tensile stress
r_b	Planetary mill milling ball radius
R_b	Bending stress
R_g	Gas constant (8.314 J K^{-1} mol^{-1}
r_i	Atomic radius of i-th element
R_m	Ultimate engineering tensile stress
R_{mb}	Ultimate bending strength
R_p	Planetary mill plate radius
RPM	Rounds per minute
RUS	Resonant Ultrasound Spectroscopy
R_v	Planetary mill bowl radius
SAED	Selected Area Electron Diffraction
SFE	Stacking Fault Energy

SPS	Spark Plasma Sintering
T	Thermodynamic temperature
t	Thickness of the reinforcement particles
TEM	Transmission Electron Microscopy
TGS	Trimodal Grain Size
t_m	Total Milling Time
TMA	Thermo-Mechanical Analysis
T_{mi}	Temperature of Melting of the i-th element
TCC	Topologically Close Packed
V	Number of systems thermodynamic degrees of freedom
VEC	Valence Electron Concentration
W	Number of States in the system
W_p	Total weight of milled powder
XRD	X-ray Diffraction
XRD	X-ray Diffraction Analysis
δ	Atomic Size Difference
ΔG	Gibbs free energy change
ΔG_{mix}	Gibbs free energy of mixing change
ΔH	Enthalpy change
ΔH_{AB}	Mixing Enthalpy of Binary Blend change
ΔH_{mix}	Enthalpy of mixing change
ΔS	Entropy Change
ΔS_{mix}	Entropy of Mixing Change
λ	Interparticle Spacing
σ_o	Tensile Lattice Friction stress
ω	Angular velocity of the bowl in planetary mill
Ω	Angular velocity of the plate in planetary mill
A	Proportionality constant
l	Reinforcement phase dimension parallel to the loading direction
μ	Poisson constant
π	Ludolph’s number

Appendix A

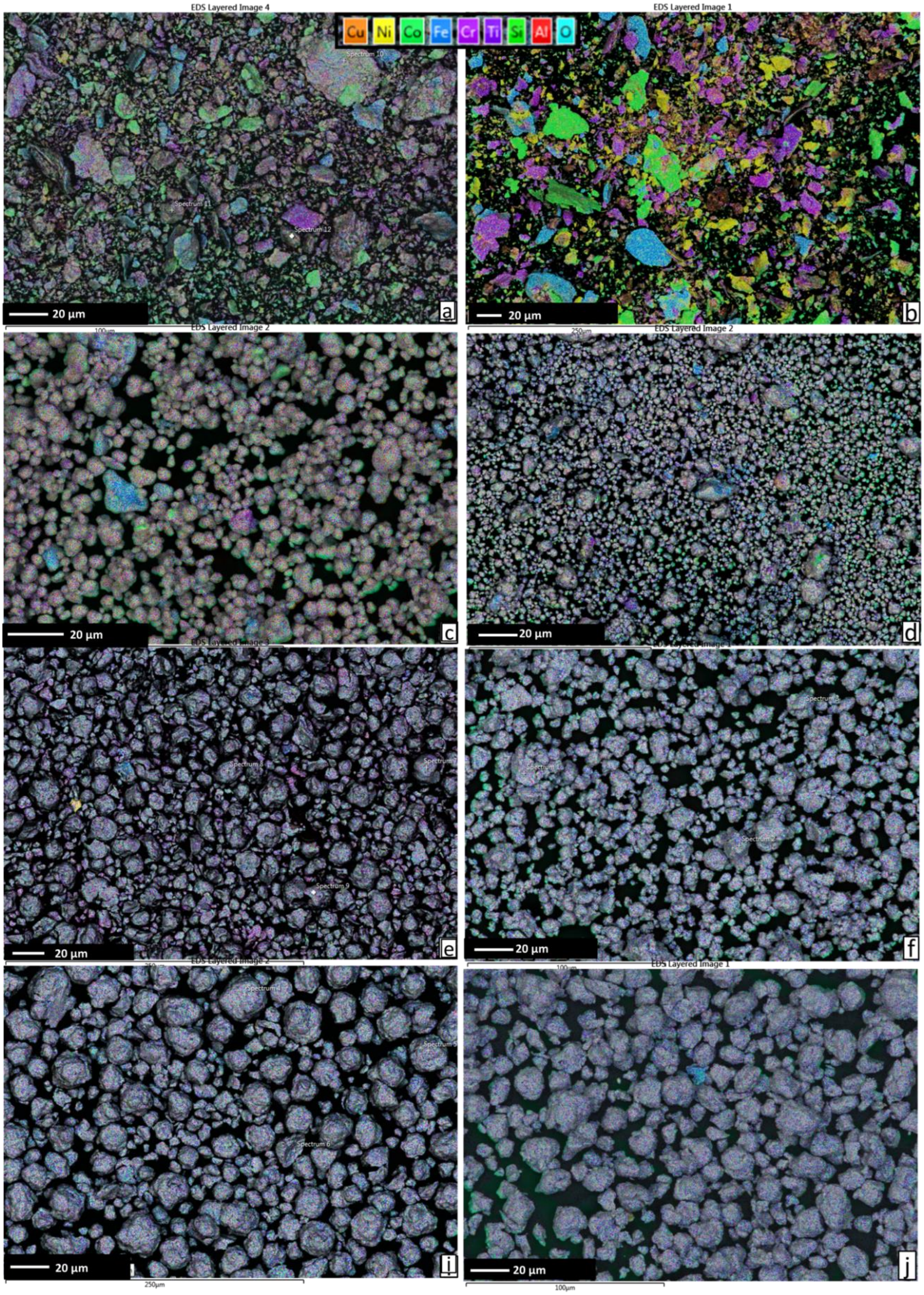

Fig. A 1 EDS SEM maps of milled powder morphologies with parameters of a) 250 RPM, 10h, 10mm balls b) 250 RPM, 10h, 15mm balls c) 250 RPM, 24h, 10mm balls d) 250 RPM, 24h, 15mm balls e) 400 RPM, 10h, 10mm balls g) 400 RPM, 10h, 15mm balls i) 400 RPM, 24h, 10mm balls g) 400 RPM, 24h, 15mm balls.

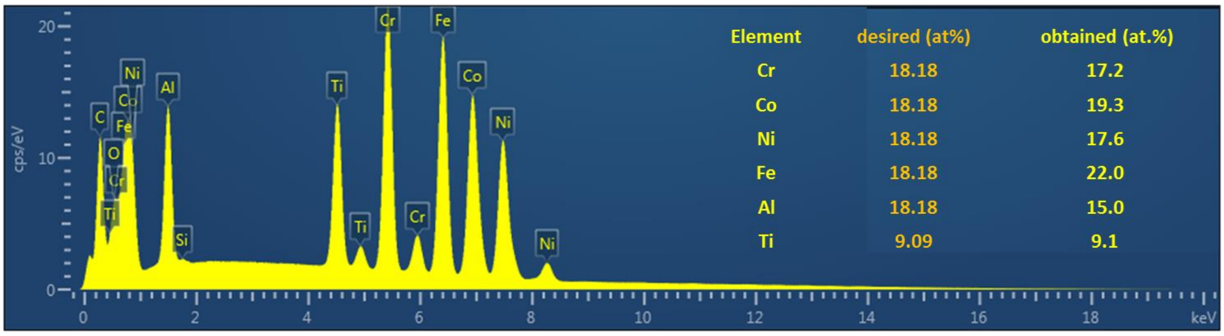

Element	desired (at%)	obtained (at.%)
Cr	18.18	17.2
Co	18.18	19.3
Ni	18.18	17.6
Fe	18.18	22.0
Al	18.18	15.0
Ti	9.09	9.1

Fig. A 2 The SEM area EDS measurement of AlCoCrNiFe$Ti_{0.5}$ powders milled with 400 RPM with evident increase in Fe concentration, as compared to rest of the elements.

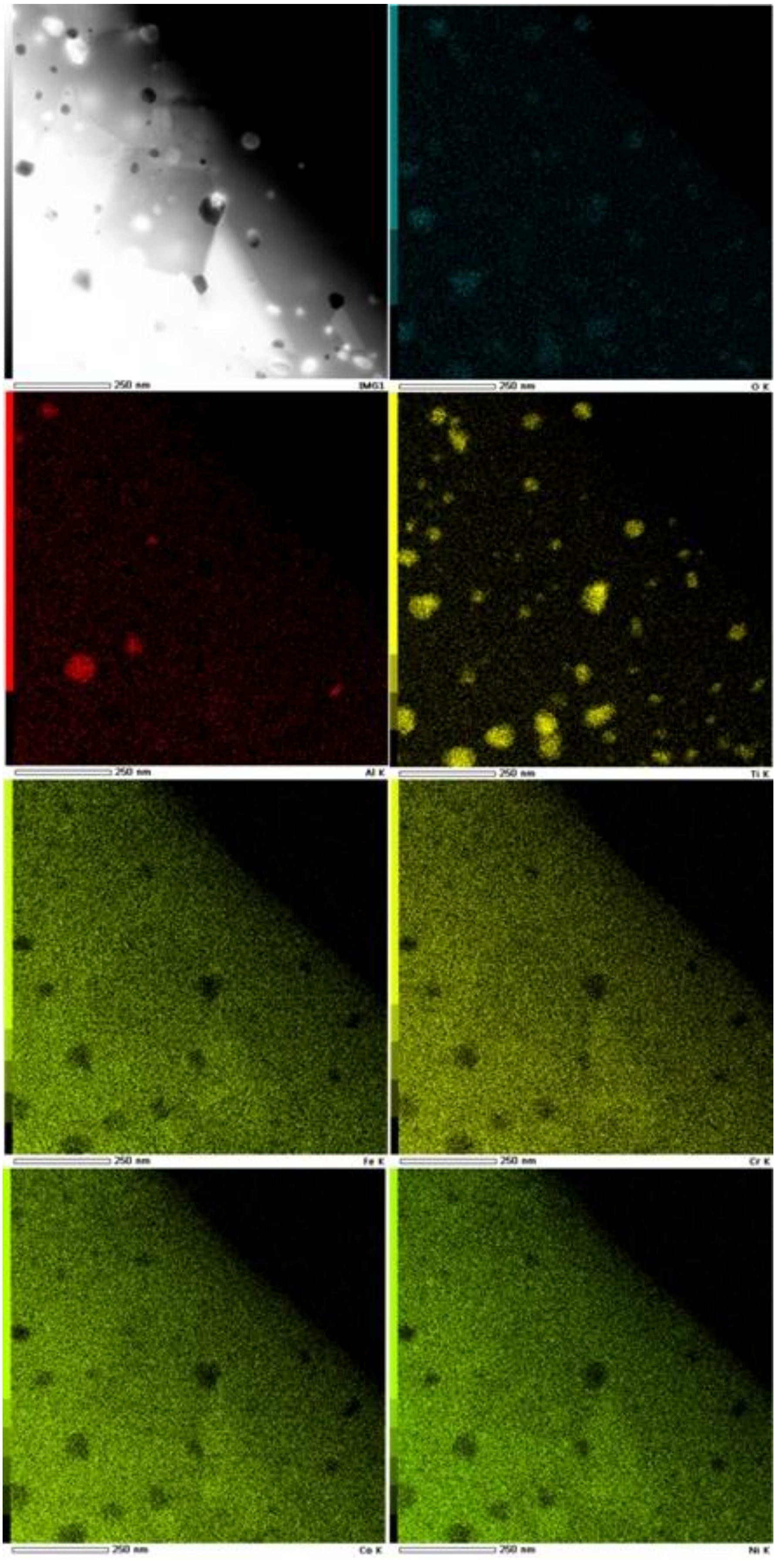

Fig. A 3 TEM EDS maps of Co$_{1.5}$Ni$_{1.5}$CrFeTi$_{0.5}$ alloy revealing Ti and Al oxides, with the rest of the elements homogenously dispersed in grains.

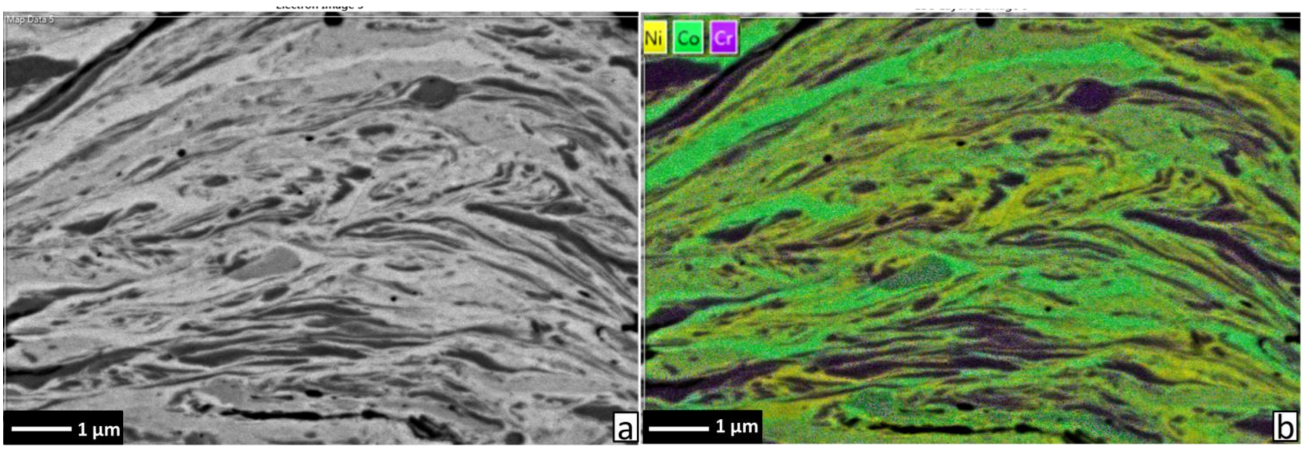

Fig. A 4 Layered microstructure of CoCrNi powder after mechanical alloying a) BSE mode b) EDS map spectrum.

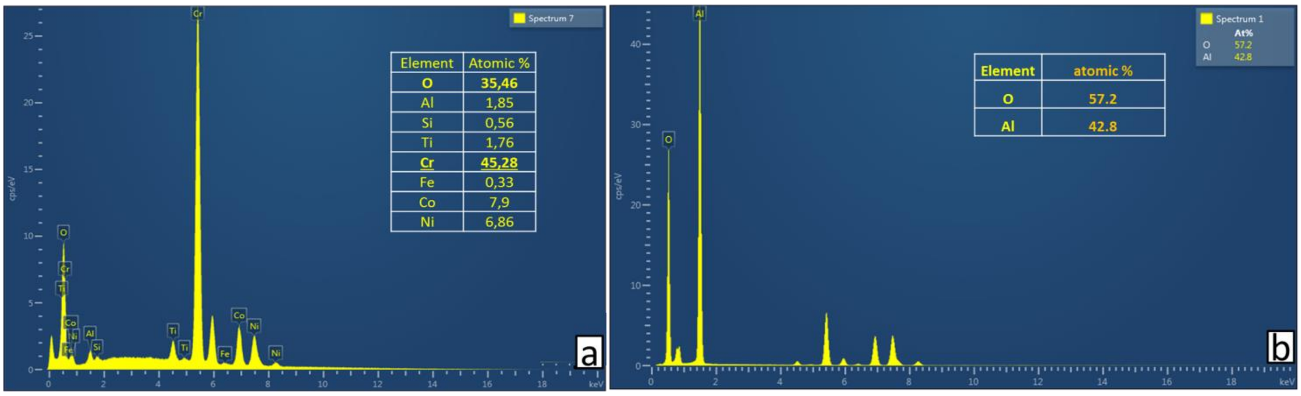

Element	Atomic %
O	**35,46**
Al	1,85
Si	0,56
Ti	1,76
Cr	**45,28**
Fe	0,33
Co	7,9
Ni	6,86

Element	atomic %
O	**57.2**
Al	**42.8**

Spectrum 1
At%
O 57.2
Al 42.8

Fig. A 5 EDS measurement of bigger oxide particle in CoCrNi alloy microstructure.

List of publications:

Journal papers:

I. I. Moravcik, J. Cizek, Z. Kovacova, J. Nejezchlebova, M. Kitzmantel, E. Neubauer, I. Kubena, V. Hornik, I. Dlouhy. Mechanical and microstructural characterization of powder metallurgy CoCrNi medium entropy alloy. Materials Science and Engineering: A 701 (2017) 370-380.
https://doi.org/10.1016/j.msea.2017.06.086

II. I. Moravcik, J. Cizek, J. Zapletal, Z. Kovacova, J. Vesely, P. Minarik, M. Kitzmantel, E. Neubauer, I. Dlouhy. Microstructure and mechanical properties of Ni1,5Co1,5CrFeTi0,5 high entropy alloy fabricated by mechanical alloying and spark plasma sintering. Materials & Design 119 (2017) 141-150.
http://dx.doi.org/10.1016/j.matdes.2017.01.036

III. I. Moravcik, J. Cizek, P. Gavendova, S. Sheikh, S. Guo, I. Dlouhy. Effect of heat treatment on microstructure and mechanical properties of spark plasma sintered $AlCoCrFeNiTi_{0.5}$ high entropy alloy. Materials Letters 174 (2016) 53-56.
http://dx.doi.org/10.1016/j.matlet.2016.03.077

IV. I. Moravcik, P. Hanusova, J. Cupera, I. Dlouhy. Effect of milling agent (methanol) on phase composition and structure of $AlCoCrFeNiTi_{0.5}$ high entropy alloy powders. Materials Engineering 23 (2016) 20-26. ISSN: 1338-6174.
http://ojs.mateng.sk/index.php/Mateng/article/view/194/368

Conference papers:

I. I. Moravcik, J. Cizek, E. Hryha, I. Dlouhy. Preparation of $AlCoCrFeNiTi_{0.5}$ high entropy alloy by SPS from Mechanically Alloyed Powders. EURO PM 2015 Proceedings. Reims France: European powder metallurgy association, 2015. s. 1-6. ISBN: 978-1-899072-47.
http://www.epma.com/publications/euro-pm-abstracts-proceedings/abstracts-individual-paper-downloads/product/ep150541

II. I. Moravcik, J. Cizek, P. Krajnakova, I. Dlouhy. Influence of sintering temperature on microstructure and hardness of $AlCoCrFeNiTi_{0.5}$ high entropy alloy. METAL 2016 Brno: TANGER Ltd., 2016. s. 64-65. ISBN: 978-80-87294-66- 6.

III. I. Moravcik, J. Cizek, I. Dlouhy. Multicomponent alloy powders preparation by mechanical alloying. METAL 2015 Brno: TANGER Ltd., 2015. s. 195-205. ISBN: 978-80-87294-62- 8.